Neotectonic Significance of the Mae Hong Son and Thoen Faults, Northern Thailand

May 2014

Weerachat WIWEGWIN

Neotectonic Significance of the Mae Hong Son and Thoen Faults, Northern Thailand

A Dissertation Submitted to

the Graduate School of Life and Environmental Sciences,

the University of Tsukuba

in Partial Fulfillment of the Requirements

for the Degree of Doctor of Philosophy in Science

(Doctoral Program in Earth Evolution Sciences)

Weerachat WIWEGWIN

Contents

Abstract

The collision between the Indian and Eurasian plates since the late Paleogene causes the NW–SE and NE–SW strike-slip faults and the N–S dip-slip faults in the Indochina region. In the Mae Hong Son region, northern Thailand, several fault lines trend in the NE–SW, NW–SE and N–S directions. Theses faults are called the Mae Hong Son Fault. In the southeastern margin of the Lampang basin, northern Thailand, fault lines trend in the NE–SW and ENE–WSW directions. Theses faults are called the Thoen Fault. The Mae Hong Son and Thoen Faults are temporally and spatially associated with the Cenozoic basin formation. Previous remote sensing investigation reveals many lines of morphotectonic evidence along the Mae Hong Son and Thoen Faults which suggest an active tectonic zone. In order to clarify tectonic activity of these regions, the Mae Hong Son and Thoen Faults were selected for this study.

Remote sensing and aerial photographic techniques were applied to a study of the Mae Hong Son Fault, located in the Mae Hong Son region, northern Thailand. Several fault lines are recognized in the region, trending mainly NE–SW, NW–SE, and N–S. The main morphotectonic landforms associated with the Mae Hong Son Fault are fault scarps, offset streams, linear valleys, triangular facets, offset ridge crests, beheaded streams, hot springs, and linear mountain fronts. A trench, a quarry, and a road cut in Cenozoic strata were used to analyse fault geometries in the area. Eight paleoearthquake events were identified from trenching, quarry, and road-cut data, and from optically stimulated luminescence (OSL) and thermoluminescence (TL) dating. The OSL and TL ages of the events are: (1) 78,000 yr BP; (2) 68,000 yr BP; (3) 58,000 yr BP; (4) 48,000 yr BP; (5) 38,000 yr BP; (6) 28,000 yr BP; (7) 18,000 yr BP; and (8) 8,000 yr BP. The recurrence interval of seismic events on the Mae Hong Son Fault appears to be *ca.* 10,000 years, and the slip rate was estimated as *ca.* 0.03–0.13 mm/yr.

To the southeast of the Mae Hong Son region, remote sensing and aerial photographic techniques were also applied to a study of the NE–SW trending Thoen Fault, located in the southeastern margin of the Lampang basin. Morphotectonic landforms caused by normal faulting in the Lampang basin are well represented by fault scarps, triangular facets, wine-glass canyons, linear valleys, and linear mountain fronts. On the other hand, morphotectonic landforms that would indicate strike-slip faulting are not found. Three paleoearthquake events were identified in the Lampang basin based on trenching data, AMS radiocarbon, OSL and TL ages (first event: 3,700 yr BP; second event: 1,800 yr BP, and the most recent event: more than 960 yr BP).

The Eocene–Oligocene collision of the Indian and Eurasian plates resulted in N–S compressive stresses in the Indochina region. The N–S compressive stresses possibly caused dextral motion on major NW–SE trending faults and sinistral motion on the NE–SW trending faults in northern Thailand. The movement on faults accompanying regional E–W extension during the late Oligocene–Miocene initiated the formation of Neogene basins. It is possible that the onset of Cenozoic basin formation in the Mae Hong Son region and the Lampang basin occurred during this time. It is also proposed that strike-slip fault movements and E–W extensional tectonics in the Neogene played a critical role in the generation of neotectonic patterns and active faulting in these areas.

The level of activity on the Mae Hong Son Fault seems low by comparison with the timing of the latest fault movement and slip rates on other active faults in northern Thailand. Moreover, it is inferred that the Thoen Fault is more active than the Mae Hong Son Fault. Although no large earthquake has occurred within the Mae Hong Son region and Lampang basin, micro-earthquakes are recorded by seismographs of the Thai Meteorological Department and the Royal Thai Navy Seismic Research Station. These micro-earthquakes, which are quite scattered

in their distribution, indicate that these regions may be in a low-seismicity zone. The micro-earthquakes may represent low-level activity on the Mae Hong Son and Thoen Faults. There is a low possibility of a large earthquake on the Mae Hong Son and Thoen Faults in the near future.

***Keywords**:* Mae Hong Son Fault, Thoen Fault, Active fault, Quaternary dating, Paleoseismology, Mae Hong Son, Lampang basin, Northern Thailand.

List of figures

List of tables

1. Introduction

1.1. Introduction

Several large earthquakes (Richter magnitude ≥ 6) have been reported from northern Thailand in a region east of the Sagaing Fault in Myanmar (Fig. 1). Northern Thailand has experienced micro-earthquakes (Richter magnitude ≤ 3) and moderate earthquakes (Richter magnitude 3–6) since at least 63 BC [Nutalaya *et al.*, 1985; Bott *et al.*, 1997]. Several micro- to moderate earthquakes have been detected along major fault traces in northern Thailand (i.e., the Mae Ping, Mae Chan, Thoen, and Mae Hong Son Faults; see Fig. 1); morphotectonic landforms have also been observed in this region [Kosuwan *et al.*, 1999; Pailoplee *et al.*, 2009]. Based on earthquake data recorded in this region and morphotectonic landforms, the Mae Hong Son and Thoen Faults can be delineated and classified to active fault [Hinthong, 1995, 1997; Department of Mineral Resources (DMR), 2006; Charusiri *et al.*, 2007].

The Mae Hong Son Fault in the Mae Hong Son region trends mainly N–S and NW–SE, as inferred from a Landsat image (Fig. 1). Micro-earthquakes were recently recorded in the Mae Hong Son region (for locations, see Fig. 3). The Mae Hong Son Fault (Figs 1 and 9) is important because it is the only fault in Thailand with a trend parallel to that of the Sagaing Fault, occurs near the Sagaing Fault and is considered an active fault zone [Hinthong, 1995, 1997; DMR, 2006; Charusiri *et al.*, 2007].

Earlier work shows that the Mae Hong Son Fault trends mainly N–S and NW–SE, and is associated with Cenozoic basin formation [Baum et *al.*, 1970; Charusiri *et al.*, 1993; Hinthong, 1997; DMR, 2006]. The only detailed studies of the stratigraphy and geology of this region are those reported by Hahn *et al.* [1986] and Srinak *et al.* [2003, 2007]. Reconnaissance studies on neotectonics and paleoearthquakes were conducted by Takashima and Maneenai [1995], Hinthong [1997], DMR [2007], and Charusiri *et al.* [2007]. However, no systematic or detailed surveys have so far been conducted to examine paleoearthquakes in

the Mae Hong Son region. Moreover, existing data are insufficient to constrain the paleoseismological history and characteristics of the region. Thus, quarry and trenching studies across the fault segments are necessary to reconstruct the history of displacement.

In 1975, a moderate earthquake of Richter magnitude 5.6 and Mercalli intensity VI occurred along the southern part of the Mae Hong Son Fault (Fig. 3); this event caused minor damage in the Mae Hong Son region. Seismicity in northern Thailand is, however, generally considered to be low, and there is no clear association between seismicity and mapped faults [Bott *et al.*, 1997; Fenton *et al.*, 2003]. Therefore, to better understand and clarify the nature of seismicity in this region, the paleoseismicity of faults along the Mae Hong Son Fault was examined.

For the Thoen Fault in the southeastern margin of the Cenozoic Lampang basin, although no large earthquake has occurred within the Lampang basin, micro-earthquakes are also recorded by seismographs of the Thai Meteorological Department (TMD) and the Royal Thai Navy Seismic Research Station (RTNSRS). Seismogenic faults in this area have not been identified, and it is not certain whether micro-earthquakes in the Lampang basin are caused by basement tectonics or active faulting. Therefore, to better understand and clarify the nature of seismicity, the paleoseismicity of faults along the Thoen fault was also examined. Some of the Thoen Fault segments were examined as part of a paleoearthquake study (e.g., Pailoplee *et al.* [2009]); however, paleoearthquake data are insufficient in terms of determining the timing of the most recent event. Trenching studies across the fault segments are necessary to reconstruct the history of displacement.

As explained above, two active faults, including the Mae Hong Son and Thoen Faults in northern Thailand, were selected for a paleoearthquake study. The main objectives of this study were to (1) identify and characterize morphotectonic landforms resulting from fault movements, (2) determine the numbers of paleoearthquake events, (3) estimate slip rates and

recurrence intervals of the faults, and (4) compare the activity on the Mae Hong Son and Thoen Faults.

In this study, fault segments and their senses of movement along the Mae Hong Son Fault were identified using field work and remote sensing techniques. Optically stimulated luminescence (OSL) and thermoluminescence (TL) dating were used to determine the depositional ages of sediment layers involved in paleoearthquake events. Geophysical data from the Electricity Generating Authority of Thailand (EGAT) [2012] were reinterpreted, and used to locate subsurface structures in some areas. Faults and sediments in trenches and exposures crossing fault segments (Mae La Noi School quarry, Phra That Chom Kitti road cut, Nong Mae La, Huai Kia, and Mok Chum Pae trenches; Fig. 9c) were mapped and their stratigraphy determined to reconstruct displacement histories.

For the Thoen Fault, fault segments and their senses of movement along the fault were identified using remote sensing techniques. Quaternary dating methods, including optically stimulated luminescence (OSL) and accelerator mass spectrometry (AMS) radiocarbon dating, were used to determine the ages of sedimentary layers in the trench. Normal faulting along the Ban Don Fai segment has produced distinct morphotectonic landforms that represent the most important data in terms of site selection for a paleoearthquake study. Thus, this study focuses on the Ban Don Fai segment.

1.2. Location of the study area

The Mae Hong Son Fault is located in the Mae Hong Son region in northwestern Thailand (17°38'–19°48'N, 97°20'–98°39'E), and at its furthest point is approximately 924 km north of Bangkok (Figs 1 and 8).

The Thoen Fault is located in the southeastern margin of the Lampang basin in northern Thailand (17°45'–18°32'N, 99°07'–99°50'E), and at its furthest point is approximately 599 km north of Bangkok (Figs 1 and 21).

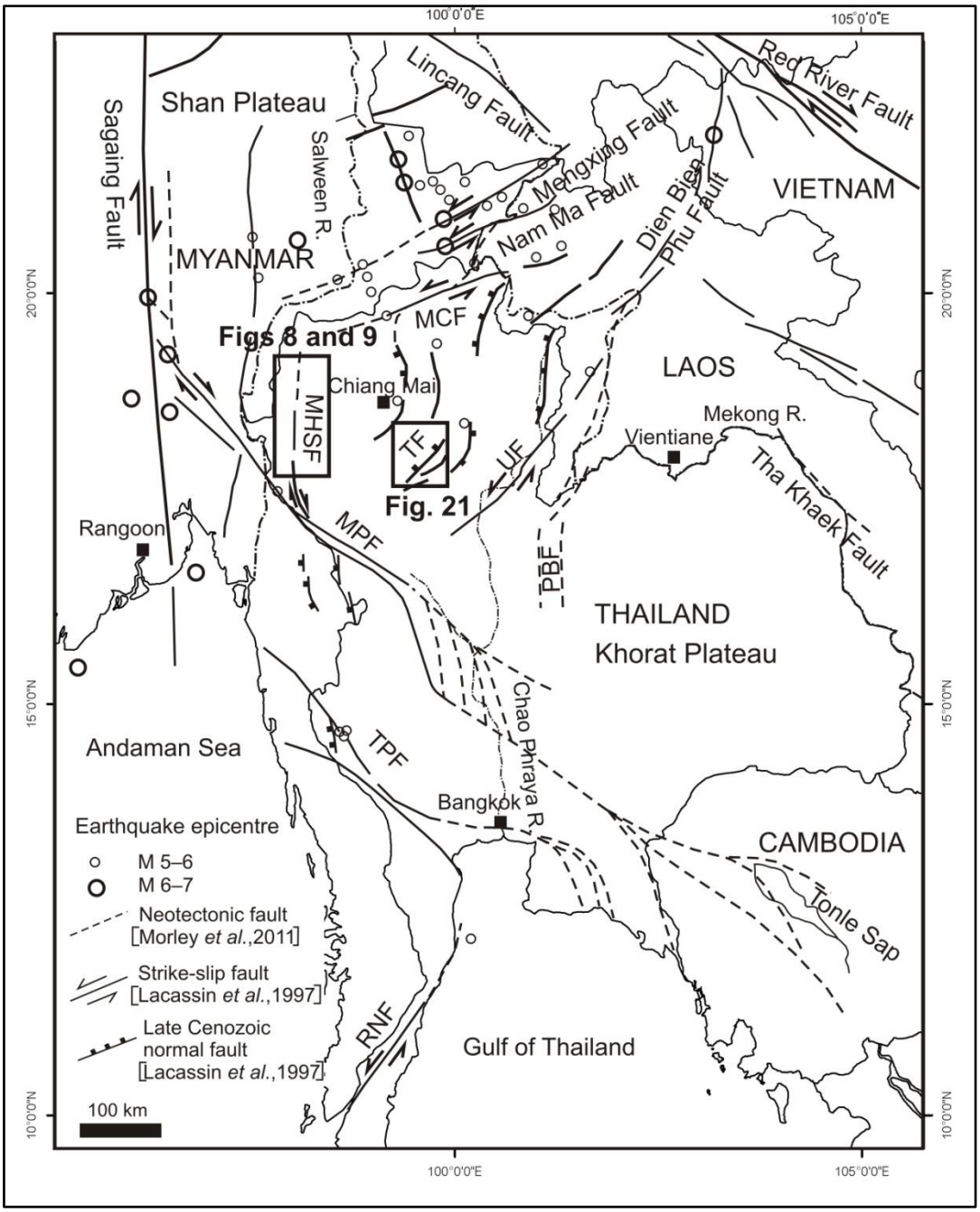

Fig. 1. Map of Thailand and adjacent areas showing major active and neotectonic faults [modified from Lacassin *et al.*, 1997, 1998; Morley *et al.*, 2011; DMR, 2006] and the epicentres of large earthquakes; the rectangle shows the location of the study area. MPF, Mae Ping Fault; MCF, Mae Chan Fault; MHSF, Mae Hong Son Fault; RNF, Ranong Fault; TPF, Three Pagoda Fault; UF, Uttaradit Fault; TF, Thoen Fault; PBF, Phetchabun Fault.

1.3. Methodology

The detailed methodology of this study can be described in terms of six steps (Fig. 2).

1.3.1. Planning and preparation

The first step was to put together all the available and relevant data on the study area, and arrange it appropriately to help facilitate the rest of the work. This involved surveying the previous literature, finding base maps (topographic and geological), earthquake epicentres, acquiring satellite images and aerial photographs, collecting records of historical earthquakes, and bringing together a number of other related technical and nontechnical documents.

1.3.2. Field reconnaissance

The second step involved a general reconnaissance of the field area in order to construct general guidelines for the more detailed investigations. Assessing the conditions of transportation routes and the ease of access into the study area was a necessary step, because this information was then used for selecting the locations of trenching sites.

1.3.3. Remote sensing interpretation

The third step concerned remote sensing interpretations. Landsat 7, the shuttle radar topography mission (SRTM), and digital elevation models (DEMs) have all been applied in the interpretation of Cenozoic basins in the study area and in analyses of the attitudes and orientations of lineaments and Quaternary faults. Faults were divided into segments during this step, and the characteristics of individual fault segments were defined using aerial photographs and IKONOS images. Morphotectonic landforms associated with the faults were also assessed and interpreted.

1.3.4. Field investigations

This step involved verification in the field of the results of remote sensing interpretation. Morphotectonic landforms related to neotectonics were used for evaluating the locations of active faults, and then used for selecting locations for further geophysical investigation. The geophysical data (i.e., the results of resistivity and radon investigations) have been used to locate subsurface structures and to decide on appropriate trenching sites. Subsequently, trenches were excavated across fault traces, and the stratigraphic units and the faults exposed were recorded and mapped.

1.3.5. Geochronological investigation

For this step, soil samples that could be related to the faulting visible in the trenches were collected for AMS radiocarbon, OSL and TL dating. Quartz grains from soil samples are necessary materials for both OSL and TL dating. Carbonaceous clay samples are necessary materials for AMS radiocarbon dating.

1.3.6. Discussion and conclusions

During this step, all the data and results from this and previous work are used to determine the nature, timing, and sequence of paleoearthquake events. The goals were to identify morphotectonic landforms that resulted from fault movements, determine the number of paleoearthquake events on the Mae Hong Son and Thoen Faults, and estimate slip rates and recurrence intervals for the fault. With this information, it is then possible to discuss the history of the Mae Hong Son and Thoen Faults, the neotectonics of the fault, and fault activity in northern Thailand generally.

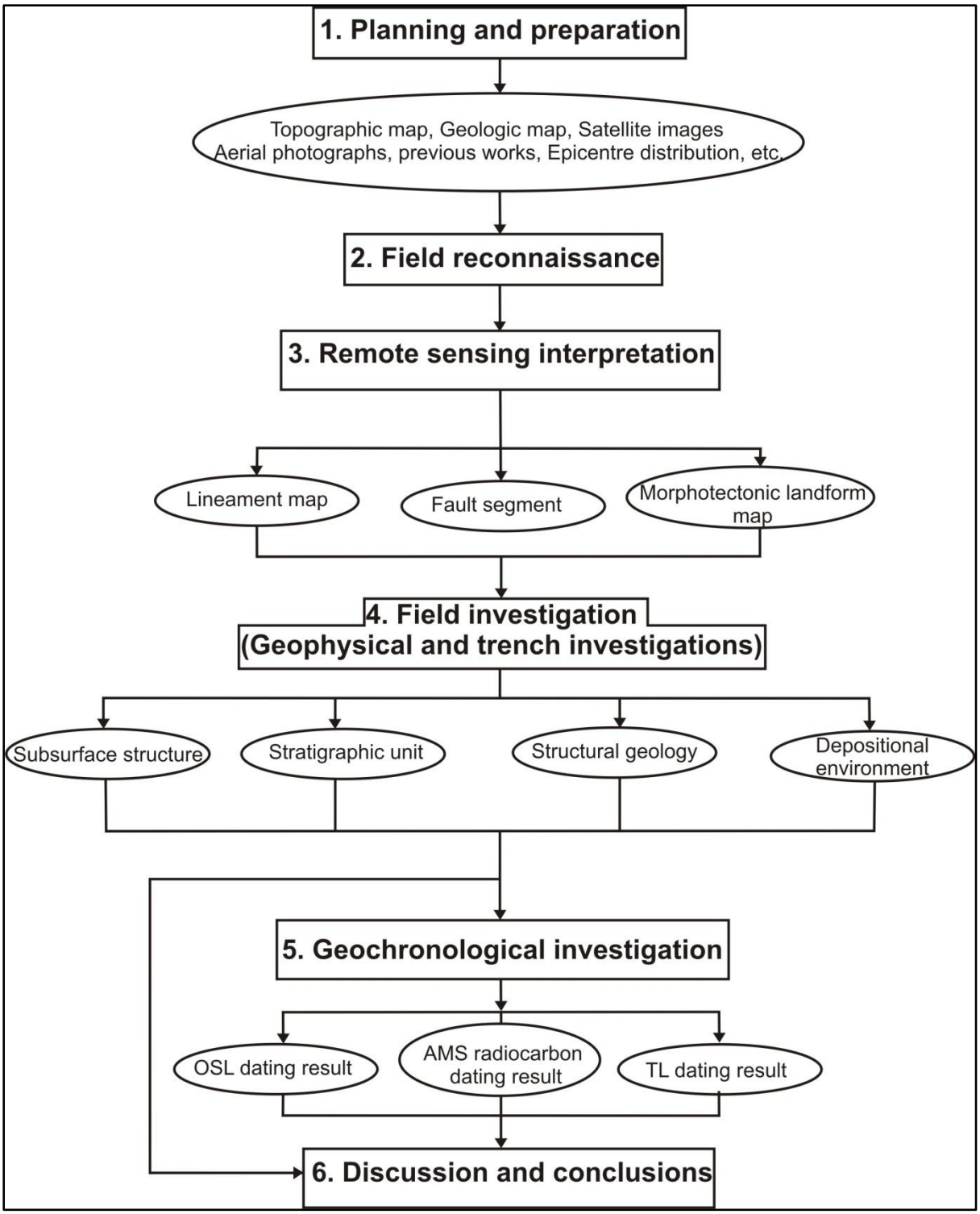

Fig. 2. Simplified flow chart of procedures adopted in this study.

2. Tectonic Setting

The tectonic framework of SE Asia is dominated by the interaction of three major adjoining lithospheric plates: the continental–oceanic Indian Plate to the west and south, the continental Eurasian Plate in a central location, and the oceanic Philippine Plate to the east [Fenton *et al.,* 2003]. Thailand is part of the Eurasian Plate and lies to the east of an active east-dipping subduction zone that extends from north India, passes through west Myanmar and west of the Andaman and Nicobar Islands, and then swings eastwards along the Sumatra–Java trench [Reading, 1980]. Major neotectonic events in the Indochina region are likely related to progressive northward and northeastward movement of the Indian plate and collision with the Eurasian plate [Peltzer and Tapponnier, 1988; Charusiri *et al.*, 2007].

In the Indochina region, collision of the Indian and Eurasian plates since the late Palaeogene has resulted in strike-slip faults that strike mainly NW–SE and NE–SW, and dip-slip faults that strike N–S [Tapponnier *et al.*, 1986; Peltzer and Tapponnier, 1988]. During the late Eocene, collision of the Indian and Eurasian plates resulted in left-lateral displacements along the NW–SE trending Red River Fault, the Mae Ping Fault (MPF; Fig. 1), and the Three Pagoda Fault (TPF; Fig. 1) [Lacassin *et al.*, 1997]. Left-lateral displacement along the Red River Fault amounted to hundreds of kilometres during the Eocene–Oligocene, caused by extension within the South China Sea [Morley, 2002]. The Gulf of Thailand was also opening during this time [Srisuwan, 2002]. During the early Oligocene–early Miocene, as the Indian plate collided with the southern margin of the Eurasian plate, the Southeast Asia region was rotated clockwise by *ca*. 25° and was extruded southeastwards [Peltzer and Tapponnier, 1988; Fenton *et al.*, 2003]. The clockwise rotation of SE Asia resulted in a reversal in the sense of movement along the Mae Ping and Three Pagoda Faults during the Oligocene–early Miocene, when these faults changed from left-lateral to right-lateral NW–SE trending strike-slip faults, and the Uttaradit Fault (UF; Fig. 1) became a left-lateral NE–SW trending strike-

slip fault. At the same time, the Red River Fault remained a left-lateral strike-slip fault [Huchon *et al.*, 1994; Polachan *et al.*, 1991]. By the middle Miocene, all of the NW–SE trending strike-slip faults in the Indochina region (Red River, Mae Ping, and Three Pagoda Faults) had become right-lateral strike-slip faults [Longley, 1997; Srisuwan, 2002]. Taken together, these major faults form a transtensional regime related to the opening of Cenozoic basins in Southeast Asia [Ducrocq *et al.*, 1992; Charusiri *et al.*, 2007].

Thailand lies mainly in a zone of strike-slip deformation, between the Red River Fault to the east and the compressive Sagaing Fault to the west [Morley, 2007; Morley *et al.*, 2011]. In the southwestern part of northern Thailand, the Mae Ping Fault, a NW–SE trending strike-slip fault, connects to the Sagaing Fault. Several seismic profiles show that in the southeastern part of northern Thailand, the NE–SW trending Uttaradit Fault has a left-lateral sense of movement [Bal *et al.*, 1992]. The movement on these strike-slip faults during the Cenozoic has resulted in extensional and transtensional stresses in northern Thailand, leading to the formation of a number of basins in this region [Uttamo *et al.*, 1999, 2003]. The Cenozoic basins in northern Thailand are mainly N–S trending grabens and half-grabens, with sediment thicknesses in the range of 1,000–3,000 m [Polachan *et al*., 1991]. The geometries of the Cenozoic basins and the locations of faults may possibly be controlled by pre-existing fabrics in basement rocks [O'Leary and Hill, 1989; Morley, 2007]. A combination of both dip-slip and lateral strike-slip (i.e., oblique-slip) movement is required to explain the evolution of these basins [Morley *et al.*, 2001, 2004; Morley, 2002, 2007] and the triggering of the faulting observed in this region.

3. Seismicity of northern Thailand and vicinity

The seismotectonic character of northern Thailand is similar to that of the Basin and Range Province of the western United States (i.e., a region of extended crust and basin-and-range topography [MacDonald *et al*., 1993]), and thus, this region has been called the Northern Basin and Range Province [Fenton *et al.*, 1997]. Several micro- to moderate earthquakes have been detected dispersedly in northern Thailand (Fig. 3). Seismicity in this region is generally considered to be low, and there is no clear association between seismicity and mapped faults [Bott *et al.*, 1997; Fenton *et al.*, 2003].

Approximately 51 earthquake events with Richter magnitudes (M_L) of 2–5 have been reported nearby and within the Mae Hong Son region (Fig. 3) [RTNSRS, 2012; TMD, 2012; United States Geological Survey (USGS), 2006]. Several of these micro-earthquakes occurring near towns have been felt; however, no damage has been reported. The largest known earthquake, with a magnitude of Richter 5.6, occurred on the southern section of the Mae Hong Son Fault on 17 February 1975 (Fig. 3). Damage was reported from this event, particularly in the southern part of the Mae Hong Son region. Although no large earthquakes have been recorded within the Mae Hong Son region, farther to the northeast in easternmost Myanmar, a large-scale earthquake on 24 March 2011 (Mw 6.8) occurred on the Nam Ma Fault (Fig. 3). Farther to the north, a few intermediate earthquakes causing minor damage have been reported, including a Mw 5.1 event on 1 March 1989. These observations indicate that present-day seismicity is, at least to an extent, related to the Mae Hong Son Fault. Present-day hot spring data (stars, Fig. 9a) also suggest on-going activity along the fault.

For the Thoen Fault, from 1990 to the present day, more than two dozen earthquakes with Richter magnitudes (M_b) of 3–5 have been reported nearby and within the Lampang basin (Fig. 3) [RTNSRS, 2012; TMD, 2012; USGS, 2006]. Several of these micro-earthquakes occurring near towns have been felt; however, no damage has been reported. The

largest known earthquake, with a magnitude of Richter 4.4, occurred on the northeastern section of the Thoen Fault on 2 February 1997 (Fig. 3). These observations indicate that present-day seismicity is, at least to an extent, related to the Thoen Fault.

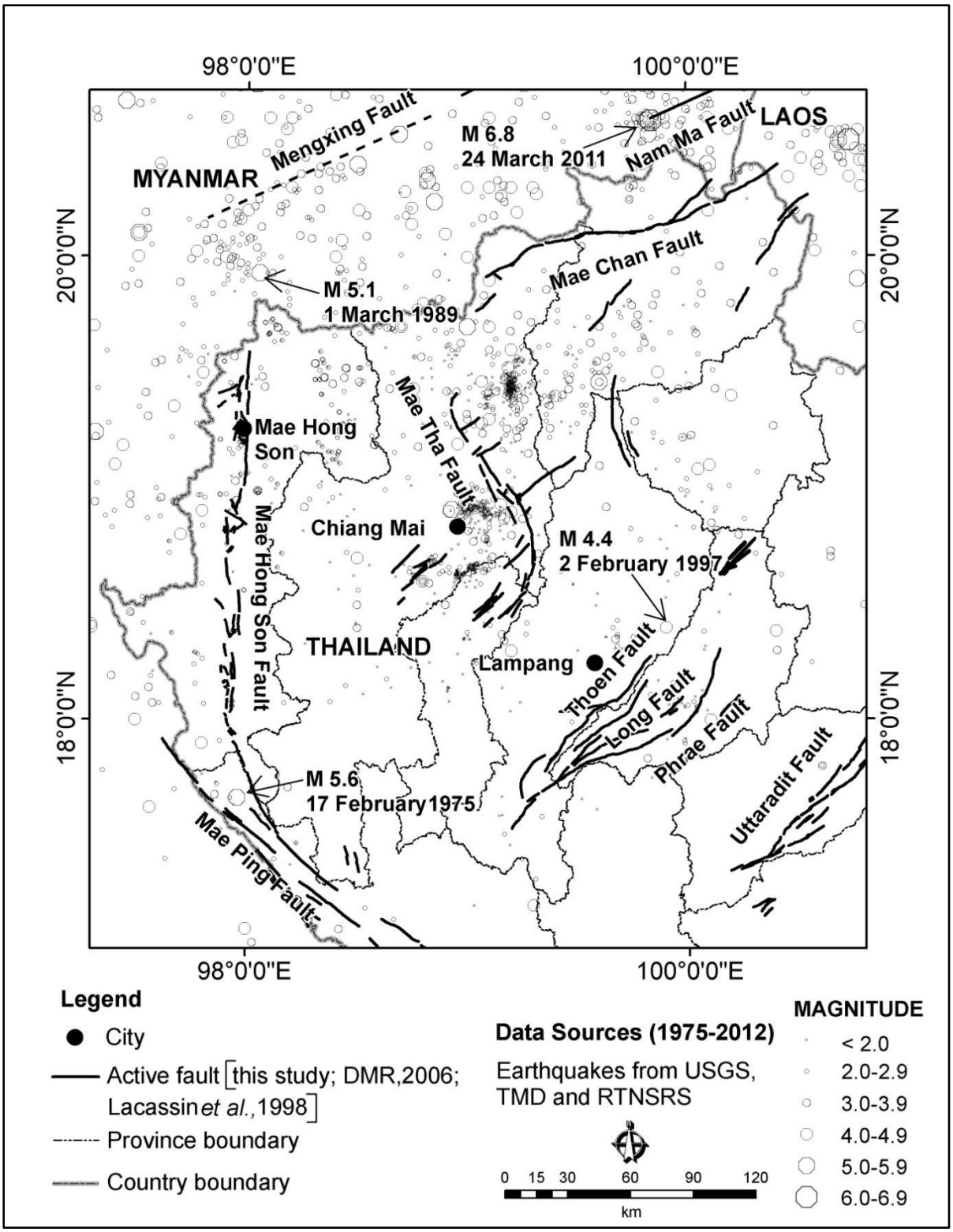

Fig. 3. Active faults and historical seismicity (1975–2012) of northern Thailand and surrounding areas [RTNSRS, 2012; TMD, 2012; USGS, 2006].

4. Active Fault in Thailand

Paleoearthquake studies aim to determine the occurrence of past earthquakes on active faults. In this paper, an active fault can be defined as one that has moved at least once during the late Pleistocene and extending to the present day [Geological Survey of Japan, 1983], and that has the potential to generate another earthquake in the near future [Slemmons, 1982]. The movements of active fault might have resulted from neotectonics. The neotectonics can be broadly described as tectonic events and processes that have occurred in post Miocene time [Slemmons, 1991], or neotectonic is defined as the tectonics occurring in the current tectonic regime [Wood and Mallard, 1992].

Based on seismological and geological evidence, Nutalaya *et al.* [1985] were the first to introduce the concept of seismic source zones in Thailand and neighboring countries (Fig. 4). Hinthong [1995, 1997] conducted a project titled "Study of Active Faults in Thailand", and used geological, historical, and seismological data to identify 22 active or suspected active faults in Thailand (1–22 in Fig. 5), and later the Bang Pa Kong Fault (23 in Fig. 5) was added into the map by Woodward-Clyde Federal Services [1996]. Siribhakdi [1986] studied seismogenic regimes in Thailand, and reported on the earthquakes that had occurred in Thailand throughout the past 1,500 years. Many of these earthquakes were closely related to the Three Pagoda Fault (TPF in Fig. 1; 13 in Fig. 5), the Mae Ping Fault (MPF in Fig. 1 or Moei Fault of Hinthong [1995]; 11 in Fig. 5), and the Mae Hong Son Fault (Mae Sariang Fault of Hinthong [1995]; 3 in Fig. 5). Thiramongkol [1986] provided evidence of Holocene movement on the Bang Pa Kong Fault (23 in Fig. 5) along the eastern margin of the lower central plain of Thailand (Fig. 6). Charusiri *et al.* [1996] applied several remote sensing techniques to a study of earthquakes in Thailand and neighboring countries. A seismotectonic (or seismic source) map was compiled by Charusiri *et al.* [1996].

Rhodes *et al.* [2004] studied the kinematics of the Mae Kuang Fault in northeastern Chiang Mai, northern Thailand, and identified offset contacts and slickenlines on the surface of the fault, indicating a left-lateral slip of 3.5 km and a dip-slip of 600 m (Fig. 7). The authors suggested that the fault was initiated between 20 and 5 Ma, simultaneous with a reversal in the movement direction on the Mae Ping and Red River Faults, and that it terminates at the northeastern margin of the Chiang Mai basin. The Mae Kuang Fault does not extend to the western side of the Chiang Mai basin because it is truncated by the right-lateral Mae Tha Fault. The ENE–WSW trending Mae Chan Fault in northern Thailand (MCF in Fig. 1; 1 in Fig. 5) is a left-lateral strike-slip fault [Fenton *et al.*, 1997]. Strong geomorphological evidence is present for late Quaternary left-lateral displacement along this fault, and recent trench investigations have confirmed late Quaternary faulting [DMR, 2009; Fenton *et al.*, 1997, 2003; Kosuwan *et al.*, 1999]. Based on remote sensing data, trenching, and geochronological investigations along the Mae Ping Fault, western Thailand, Saithong [2006] identified three paleoearthquake events (at 80,000, 65,000, and 15,000 yr BP) involving dextral movement along the fault. Le Dain *et al.* [1984] reported a focal plane solution for a 1975 earthquake on the Mae Ping Fault consistent with right-lateral slip. In the southeastern part of northern Thailand, remote sensing investigations and Quaternary dating have revealed that the Uttaradit Fault (UF; Fig. 1) is located within an active tectonic zone [Saithong *et al.*, 2011]. Based on trench investigations, slip rates on the Uttaradit Fault have been calculated as between 0.19 and 0.21 mm/yr [Saithong *et al.*, 2011].

Earlier work has demonstrated that the Mae Hong Son Fault strikes mainly N–S and NW–SE. Hot springs are present along the fault trace, and may be the result of movement along the fault [Sasada *et al.*, 1987]. Based on field and geochronological evidences, Charusiri *et al.* [1993] suggested that the Mae Hong Son Fault may have been active during the period of 27.3–1.6 Ma. A fault in the Mae Sariang basin has been interpreted as a splay

fault of the active Mae Ping Fault to the south [Morley *et al.*, 2007]. Age dating by TL has revealed that the Mae Hong Son Fault was active from 0.89 to 0.32 Ma [Takashima and Maneenai, 1995; Hinthong, 1997]. Recently, Wiwegwin *et al.* [2014] also reported the most recent movement upon Mae La Noi segment no. 1 of the Mae Hong Son Fault occurred several thousand years ago; the fault has been classified as active by Hinthong [1995, 1997], DMR [2007], Charusiri *et al.* [2007], and Wiwegwin *et al.* [2014].

The NE–SW trending Thoen Fault (TF in Fig. 1; 8 in Fig. 5), a sinistral fault located in the Lampang basin, has been regarded as active [Fenton *et al.*, 1997, 2003; Hinthong, 1997; DMR, 2006]. Quartz-rich samples from fault-related colluviums, and charcoal samples, provide displacement ages of 4,000, 3,000, and 2,000 yr BP using thermoluminescence (TL) dating and the ^{14}C method, respectively [DMR, 2006]. Moreover, from 1990 to the present day, more than two dozen earthquakes with magnitudes of M_b 3.0–5.0 have been detected near this fault. Danphaiboonphon [2005] studied the characteristics of the Thoen Fault, using remote sensing, petrographic analysis, and geophysical investigation, and suggested that it is an oblique strike-slip fault. Several lines of evidence, including geomorphic and stratigraphic, indicate that the Thoen Fault was an extensional structure during the Holocene [Fenton *et al.*, 2003] and that current displacements involve mainly normal dip-slip and subordinate left-lateral slip movement [Fenton *et al.*, 2003; Morley, 2007]. Based on morphotectonic landform observations in the Lampang basin, Wiwegwin *et al.* [2011] suggested that the Thoen Fault was a normal dip-slip fault, without any significant component of strike-slip movement. Fenton *et al.* [2003] calculated a slip rate on the Thoen Fault of 0.6 mm/yr, using total offset of youngest geomorphic feature or stratigraphic unit divided by its relative age. Pailoplee *et al.* [2009] excavated two trenches on the Ban Mai and Doi Ton Ngun segments of the Thoen Fault in the Lampang Basin. Based on trench-log interpretations, the Ban Mai segment records a single main paleoearthquake, at 3,800 yr BP; the slip rate is approximately

0.06 mm/yr. The Doi Ton Ngun segment records evidence for two paleoearthquake events at 3,500 and 1,800 yr BP; the average slip rate since the last fault movement is 0.18 mm/yr, and the recurrence interval for earthquakes is 1,700 years. Wiwegwin *et al.* [2011] also reported that the most recent movement on the Ban Don Fai segment of the Thoen Fault occurred more than 960 years ago. Based on the current study of seismicity (i.e., the *b* value of the Gutenberg–Richter (G–R) relationship, where a low value indicates high earthquake activity) upon the Thoen Fault (Lampang basin) and upon the Phrae Fault (Phrae basin), the *b* value for the Thoen Fault is lower than that for the Phrae Fault [Pailoplee *et al.*, 2009]. Pailoplee *et al.* [2009] also suggested that the Thoen Fault in the Lampang basin is capable of generating more earthquake activity than the Phrae Fault.

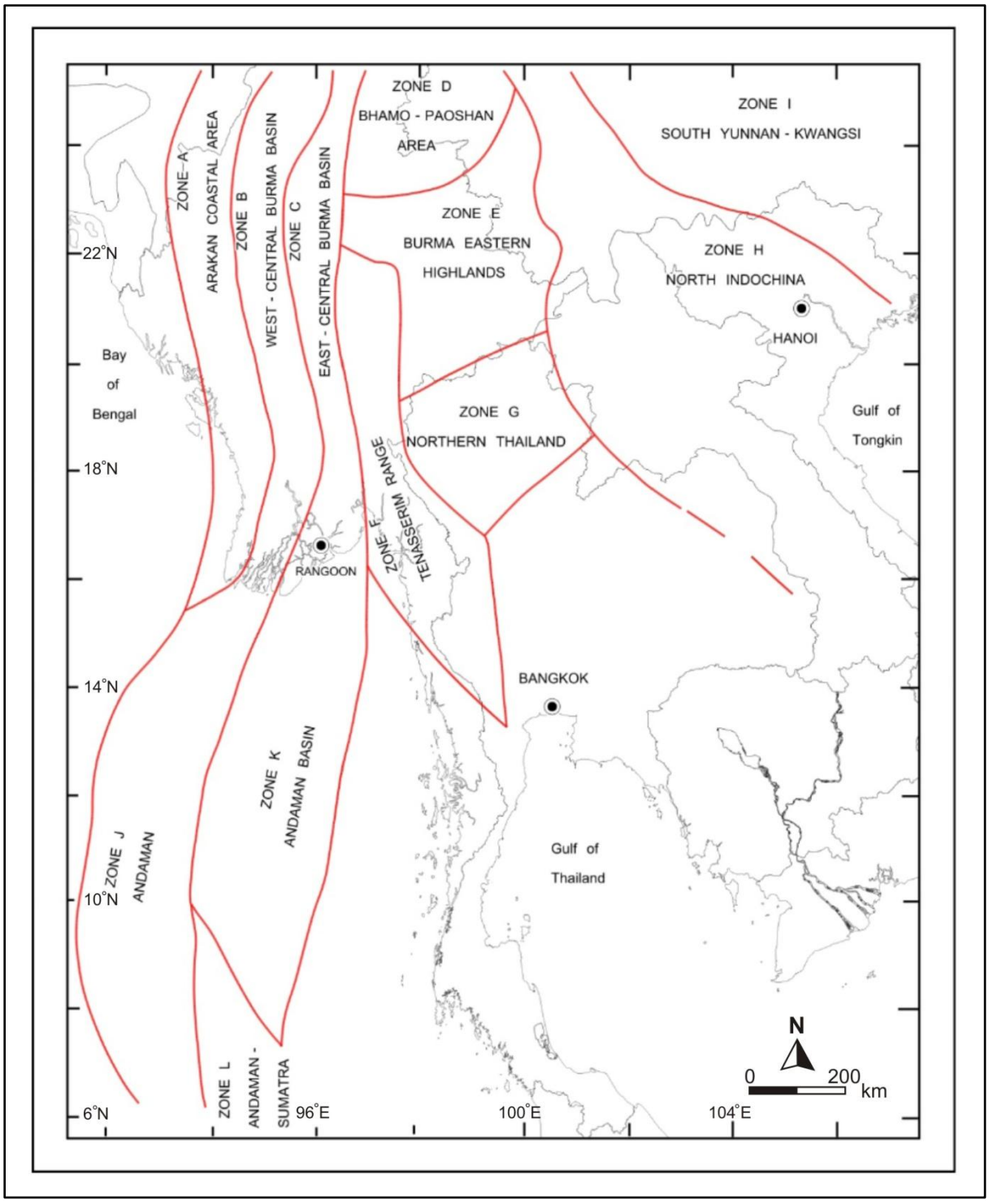

Fig. 4. Seismic source zones in the Indochina region [Nutalaya *et al.*, 1985]. Note that two study areas (Mae Hong Son region and the Lampang basin) are located in zone G.

Fig. 5. Map of Thailand showing the active faults identified by Hinthong [1995] and Woodward-Clyde Federal Services [1996], based on geomorphic expression and thermoluminescence ages obtained from fault gouges.

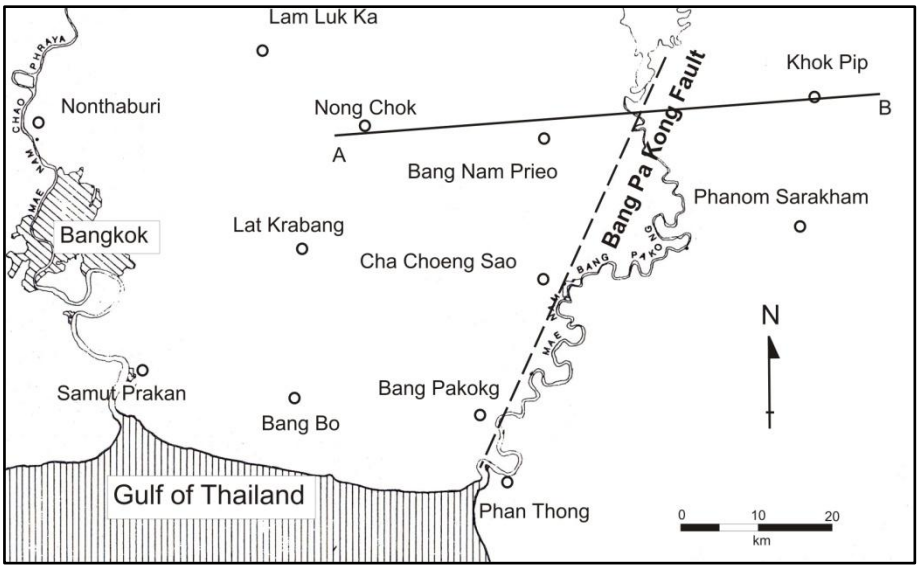

(a)

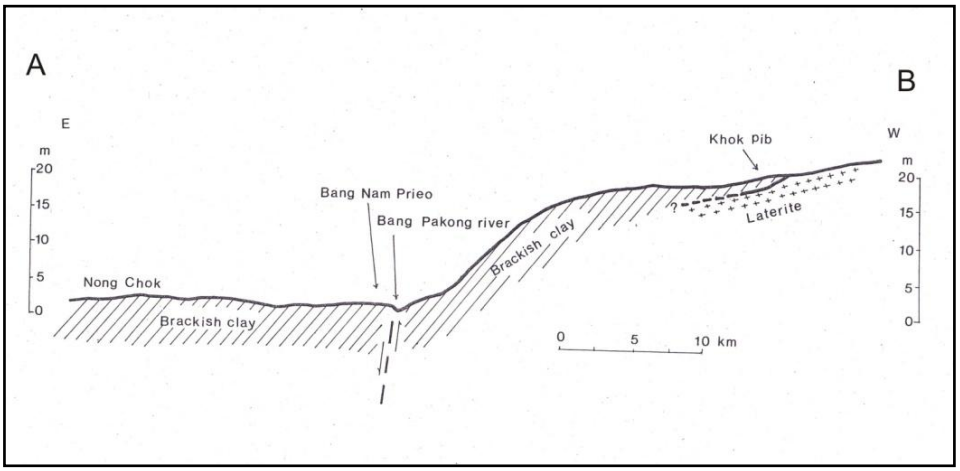

(b)

Fig. 6. Map showing the location of the Bang Pa Kong Fault at the eastern margin of the lower central plain of Thailand (a). Cross-section from Nong Chok through Bang Nam Prieo to Ban Khok Pip showing the area of tectonic uplift (b), the location of section b is shown in a. This figure is modified from Thiramongkol [1986].

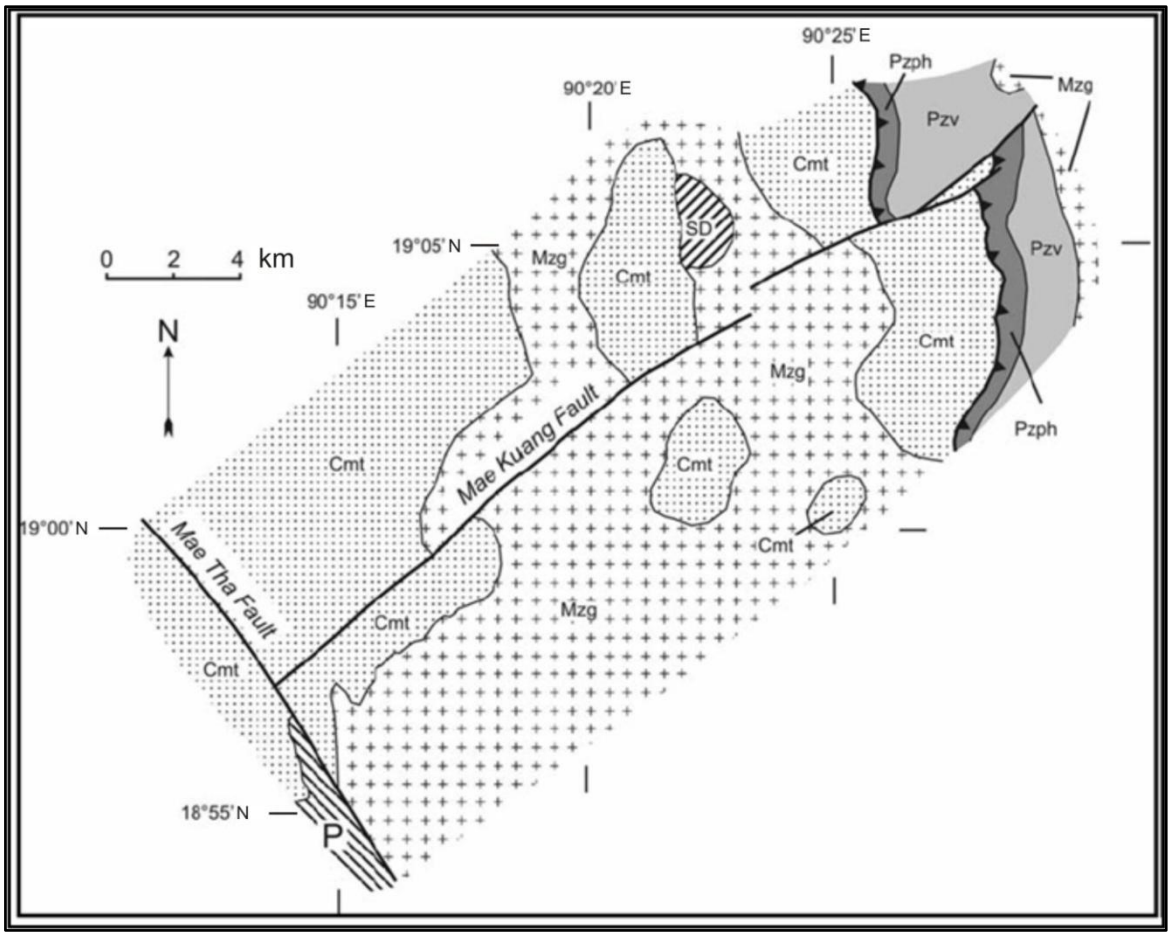

Fig. 7. Map showing the location of the Mae Kuang Fault, located in the northeastern Chiang Mai Basin, and the geology of the area that surrounds the trace of this fault. P, undifferentiated Permian rocks; Cmt, Carboniferous rocks of the Mae Tha Formation; SD, Silurian and Devonian rocks; Pzph, Paleozoic phyllite; Pzv, Paleozoic metabasalt; Mzg, granitic rocks of the Fang–Mae Suai batholiths [Rhodes *et al.*, 2004].

5. Results of Remote Sensing Analysis

5.1. Mae Hong Son Fault in the Mae Hong Son region

5.1.1. Lineaments and fault segments

Landsat 7 imaging (Fig. 8) has been applied to the interpretation of lineaments and Quaternary faults in the study area. Lineaments were identified based on morphological features, their correlation with tectonic elements, and available geological maps. The orientations of faults at 767 locations along these lineaments are shown in Fig. 9b.

The Mae Hong Son Fault is well defined and is visible as a sharp lineament on aerial photographs and satellite images (see Fig. 8). The Mae Hong Son Fault strikes mainly N–S, with conjugate faults trending NW–SE and NE–SW. The N–S faults show normal dip-slip movement, and they delineate the margins of elongate N–S basins. The NW–SE faults show right-lateral strike-slip movement. On the other hand, the NE–SW faults show left-lateral strike-slip movement. The Mae Hong Son Fault, which has a total length of *ca*. 202 km, can be divided into four major segments based on fault geometries and the distribution of Cenozoic basins (Fig. 9c). Fault traces are visible along the boundaries between Paleozoic–Mesozoic units and unconsolidated Quaternary sediments; such faults mainly occur within Cenozoic basins. From north to south, the four major segments of the Mae Hong Son Fault are the Mae Hong Son, Khun Yuam, Mae La Noi, and Mae Sariang segments (Fig. 9c). These segments can be subdivided into 49 smaller segments (all showing clear traces of Quaternary faulting, as interpreted from remote sensing observations); the segments were investigated to determine fault geometries and orientations, associations with morphotectonic landforms, and their seismicity history.

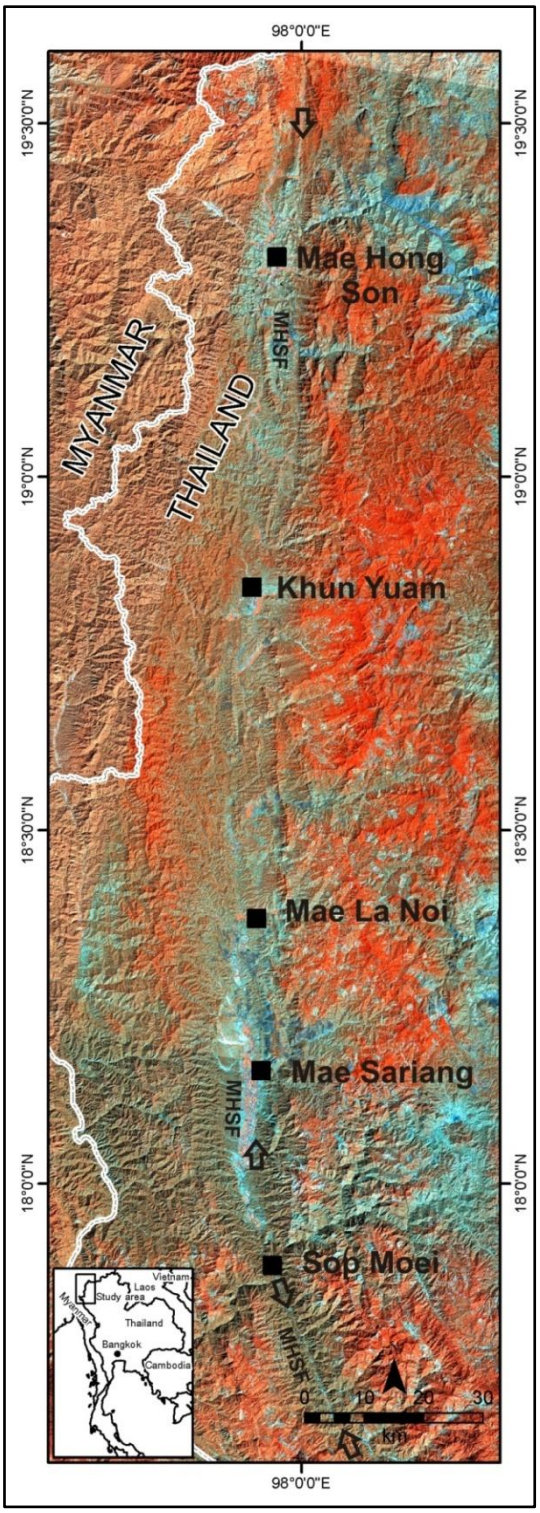

Fig. 8. Landsat image showing the location of the study area (Mae Hong Son region) and prominent N–S and NW–SE trending faults (MHSF: Mae Hong Son Fault; arrows). This image was analyzed to identify lineaments and Quaternary faults. The area covered by this image is shown in Fig. 1.

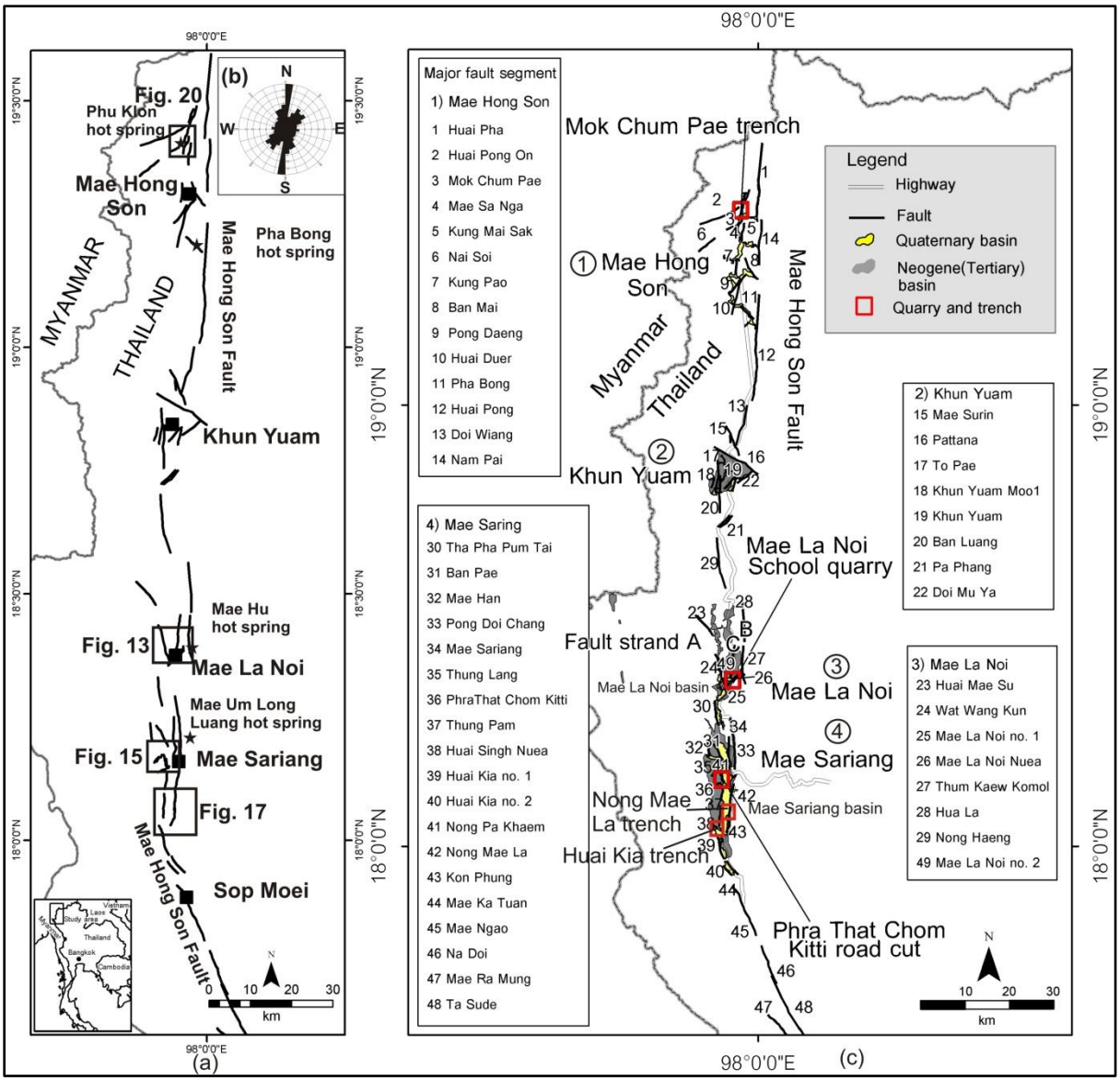

Fig. 9. The Mae Hong Son Fault (MHSF; see location map, Fig. 1) of northern Thailand and its four major fault segments as interpreted from Landsat 7 images (a and c), the principle orientations of faults shown as a rose diagram (b, inset in a), and the locations of Cenozoic basins in the Mae Hong Son region (c). The names and locations of individual segments are also displayed (c). The black stars represent hot spring locations.

5.1.2. Morphotectonic landform interpretation

5.1.2.1. Morphotectonic landforms and faulting

Active faulting produces a variety of landform features (i.e., morphotectonic landforms), including fault scarps, warped and tilted ground, subsidence features such as sag ponds, and offset stream channels. These morphotectonic landforms can be classified into three groups that are associated with strike-slip, normal, and reverse faulting, respectively. However, many faults show oblique displacements that involve both strike-slip and vertical movements. For this study, the landform features associated with the three main types of faulting are briefly explained.

Within a strike-slip fault zone, a variety of structures and landforms can originate by simple shear, including fractures, folds, normal faults, thrust faults, and reverse faults [Christie–Blick and Biddle, 1985]. Naturally, within a broad shear zone, different generations of motion produce various kinds of these structures, all of which can be superimposed, producing an array of structural complexity [Sylvester, 1988]. In many strike-slip faults, a bending of the fault trace can be observed in overlapping areas among adjacent blocks. Therefore, strike-slip fault movements can create both compressive and tensile stresses in the curved areas of fault segments. For instance, as shown in Fig. 10, releasing bends and restraining bends can cause pull-apart basins and uplift features related to tension and compression stresses, respectively [Biddle and Christie–Blick, 1985; Keller and Pinter, 1996]. In many cases, both pull-apart basins and uplift highs may be explained in term of step-overs where two fault segments occur, and with both showing the same sense of movement [Keller and Pinter, 1996].

In conclusion, strike-slip faulting is capable of producing many kinds of morphotectonic landforms, as shown in Fig. 11. These features include linear valleys, offset

or deflected streams, shutter ridges, sag ponds, beheaded streams, benches, scarps, and springs [Keller and Pinter, 1996].

Within a normal fault zone, the morphotectonic landforms that often result from an extensional regime include linear mountain fronts, fault scarps, triangular facets, horsts and grabens, escarpments, and rift valleys and axial rifts in oceanic ridge systems [Keller and Pinter, 1996]. Fault scarps are the typical indicator of normal faulting. Triangular facets can also be used for indicating a normal fault system, and they are formed by a combination of vertical movement on range-bounding normal faults and stream incision in the valleys. Triangular facets are roughly planar surfaces with broad bases and upwards-pointing apices, and they typically occur on ridge crests between valleys [Keller and Pinter, 1996]. A time sequence of displacements along a normal fault can produce a vertically stepped series of triangular facets [Hamblin, 1976; Fenton *et al.*, 2003].

Morphotectonic landforms associated with reverse faulting include belts of active folding and faulting, steep mountain fronts, and fault scarps. The long axis of these structures is usually perpendicular to the direction of maximum compressive stress. The most common geomorphic products of compressional tectonism in a continent are fault scarps [Carver and McCalpin, 1996] and active folding [Keller and Pinter, 1996]. Based on historical surface ruptures associated with the Armenian 1988 earthquake, seven types of reverse fault scarp morphology have been identified by Philip *et al.* [1992], and these are shown in Fig. 12.

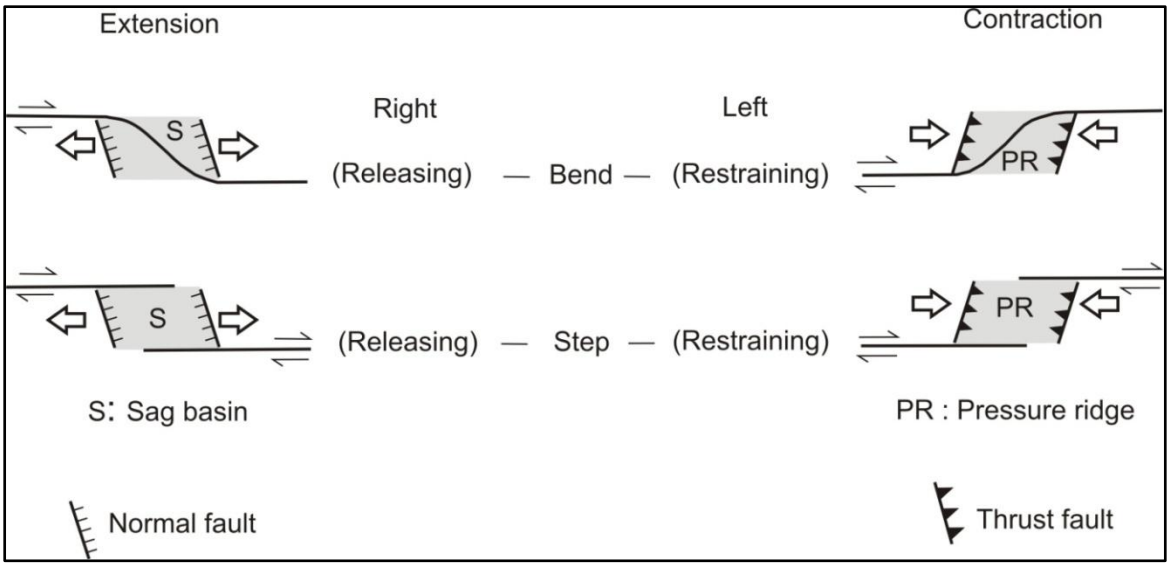

Fig. 10. Sags and pressure ridges associated with bends and steps along strike-slip faults [Keller and Pinter, 1996].

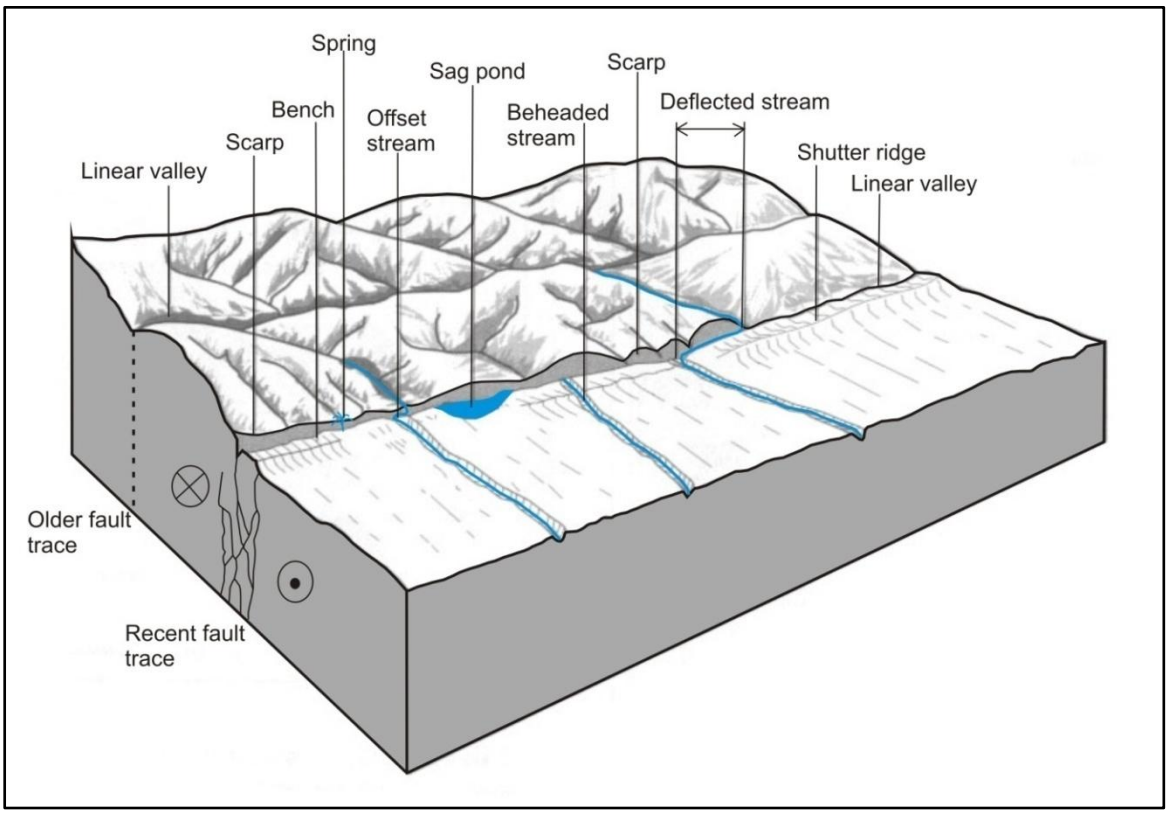

Fig. 11. Morphotectonic landforms associated with active strike-slip faulting [modified from Keller and Pinter, 1996].

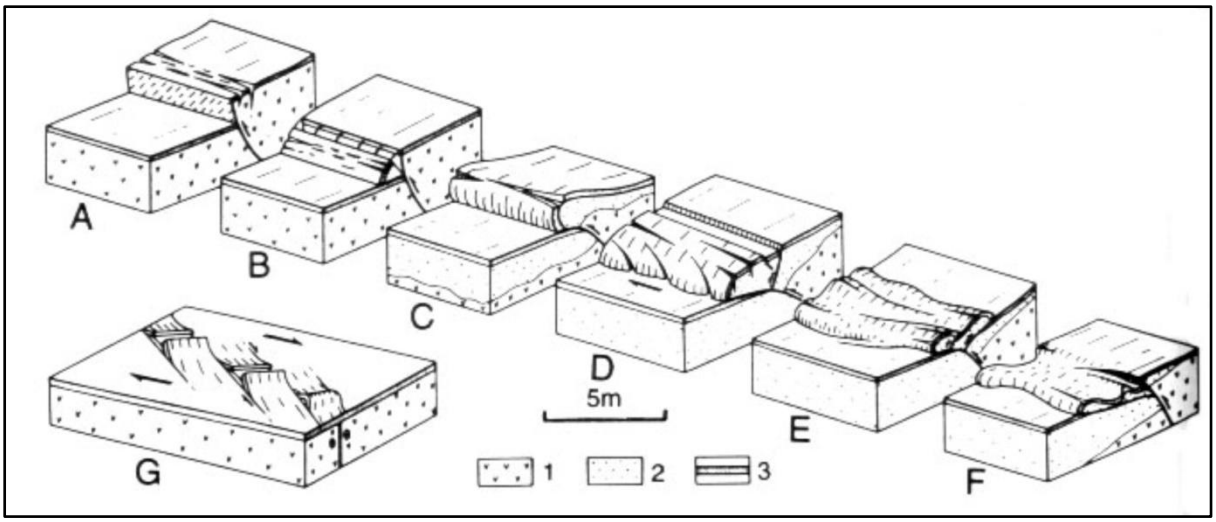

Fig. 12. Seven types of reverse fault scarps. A: Simple reverse (or thrust) scarp; B: Hanging-wall collapse scarp; C: Simple pressure ridge; D: Dextral pressure ridge; E: Back-thrust pressure ridge; F: Low-angle ridge; G: *En echelon* pressure ridge; 1: bedrock; 2: unconsolidated Quaternary sediments, and 3: turf [after Philip *et al*., 1992].

5.1.2.2. Results of aerial photograph interpretation

The morphotectonic landforms observed in the study area include fault scarps, triangular facets, offset streams, hot springs (stars in Fig. 9a), linear valleys, and linear mountain fronts. Based on aerial photographic interpretations, the Mae La Noi and Mae Sariang basins (Fig. 9c) are bounded to the east and west by N–S trending segments and to the north and south by NE–SW and NW–SE trending segments, respectively.

In the Mae La Noi basin, detailed interpretations of aerial photographs reveal small fault scarps, offset streams, and linear valleys along the fault trace (Figs 13 and 14). To the north of Mae La Noi School, a westward flowing stream channel shows a sinistral offset of *ca*. 70 m (the stream flows southward along the fault trace before returning to its westward course; Fig. 14a and b); this offset stream indicates left-lateral strike-slip along the Mae La Noi segment no. 2. This fault segment has a total length of *ca.* 1.8 km. Small fault scarps are

also present on the piedmont behind Mae La Noi School (on Mae La Noi segment no. 1; Figs 13 and 14). Mae La Noi segment no.1 has a total length of *ca.* 1.4 km.

Morphotectonic landforms observed in the Mae Sariang basin include fault scraps, offset streams, triangular facets, offset ridge crests, benches, and linear mountain fronts (Figs 15–19). The N–S trending faults show normal dip-slip displacement. The NW–SE and NNW–SSE trending faults show right-lateral strike-slip displacement. However, the NE–SW trending fault segments frequently show left-lateral strike-slip displacement. The ridge crest to the northeast of Phra That Chom Kitti temple shows left-lateral offsets across the fault (Fig. 16), indicating left-lateral strike-slip movement on the Phra That Chom Kitti segment. This fault segment has a total length of *ca.* 1.0 km. To the north of Phra That Chom Kitti temple (Fig.16), an eastward flowing stream channel is offset dextrally by *ca*. 100 m; the stream flows southwards along the fault trace before returning to its eastward course (Fig. 16). The ridge crest to the south of this offset stream also shows right-lateral offset across the fault (Fig. 16). These features indicate right-lateral strike-slip movement on the Nong Pa Khaem segment (2.0 km length).

Triangular facets, scarps, beheaded stream, and linear mountain fronts can be observed along the eastern margin of the Mae Sariang basin (the Kon Phung area in Figs 17 and 18). These morphotectonic landforms support the interpretation of normal displacement along the fault trace on the basin's eastern margin. The triangular facets represent a combination of vertical movements on range-bounding N–S normal faults and stream incision in valleys. A series of triangular facets is present in the Mae Sriang basin along a W-facing escarpment (Fig. 17c). It is suggested that such features are the result of episodic fault movement, and that the facets formed as a result of fault movement, while the benches formed during intervening periods of tectonic stability. Therefore, it is possible that movement along the Mae Hong Son Fault resulted in the development of several sets of

triangular facets in the Mae Sariang basin. The locations of triangular facets are also consistent with the locations of surface traces of the Mae Hong Son Fault. Series of triangular facets have been reported from other well-studied active fault zones, and they are considered as indicative of mountain fronts bounded by active faults [e.g., Hamblin, 1976; Bull and McFadden, 1977; Wallace, 1978; Fenton *et al.*, 2003; Ganas *et al.*, 2005; Picotti *et al.*, 2009; Wiwegwin *et al.*, 2011]. Thus, triangular facets in the N–S trending Mae Sariang basin are considered to be the result of vertical movements of the Mae Hong Son Fault.

To the west of the 9.2-km Nong Mae La and 4.0-km Kon Phung segments (Fig. 18), eastwards flowing stream channels are offset dextrally by *ca*. 20–70 m; the streams flow southwards along the fault trace before returning to their eastwards course (Fig. 18). These features indicate right-lateral strike-slip movement on the Huai Singh Nuea segment (5.3 km length).

Fault traces in the Huai Kia area, in the southern part of the Mae Sariang basin, change orientation from trending N–S to trending NW–SE (Fig. 19). Significant morphotectonic landforms, such as scarps, offset streams, benches, and linear mountain fronts, can be observed along the fault traces. Streams are offset dextrally. These features are interpreted, therefore, to indicate right-lateral strike-slip movement along these NW–SE trending fault segments (e.g., 2.16-km Huai Kia segment no.1). These segments have the same orientation as the Mae Ping Fault to the south, and they may actually merge with that fault.

In the north of the Mae Hong Son region, morphotectonic landforms observed in the Mok Chum Pae area include fault scarps, offset streams, triangular facets, hot springs, and linear mountain fronts (Fig. 20). The N–S trending fault segments show normal dip-slip displacements, and the NE–SW trending fault segments show left-lateral strike-slip displacements. However, the NW–SE and NNW–SSE trending fault segments frequently

show right-lateral strike-slip displacements. A hot spring occurs along the southwestern part of the Mok Chum Pae segment, and streams are offset across the fault segment (Fig. 20). To the northeast of the hot spring, a southeastwards flowing stream channel shows a sinistral offset of *ca*. 150 m (the stream flows northeastwards along the fault trace before returning to its southeastwards course; Fig. 20). Indeed, all the offset streams observed along the Mok Chum Pae segment indicate left-lateral strike-slip movements. The Mok Chum Pae segment has a total length of *ca.* 8.3 km. A series of triangular facets is present in the Mok Chum Pae area on the escarpments that face E and W (Fig. 20). Based on morphotectonic landforms observed in this area, it is possible that these faults of the Mae Hong Son Fault have produced both vertical and lateral movements.

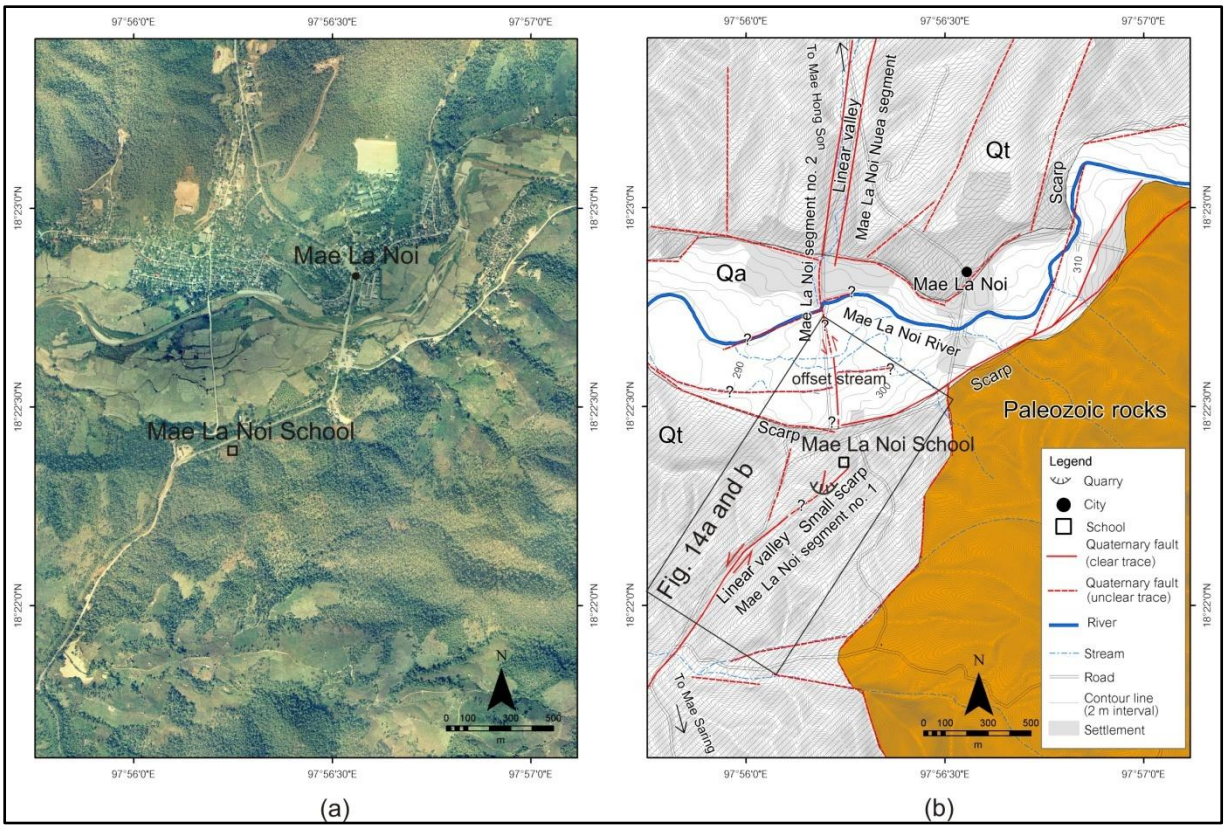

Fig. 13. Morphotectonic landforms of the Mae La Noi area. (a) Aerial photograph of the Mae La Noi area, Mae Hong Son region (see Fig. 9a for location of the image), and (b) results of remote sensing investigations and the distribution of geological units (Qa: alluvial sediments; Qt: terrace sediments, and Paleozoic rocks), showing morphotectonic landforms along Mae La Noi segment nos 1 and 2 (see Fig. 9c).

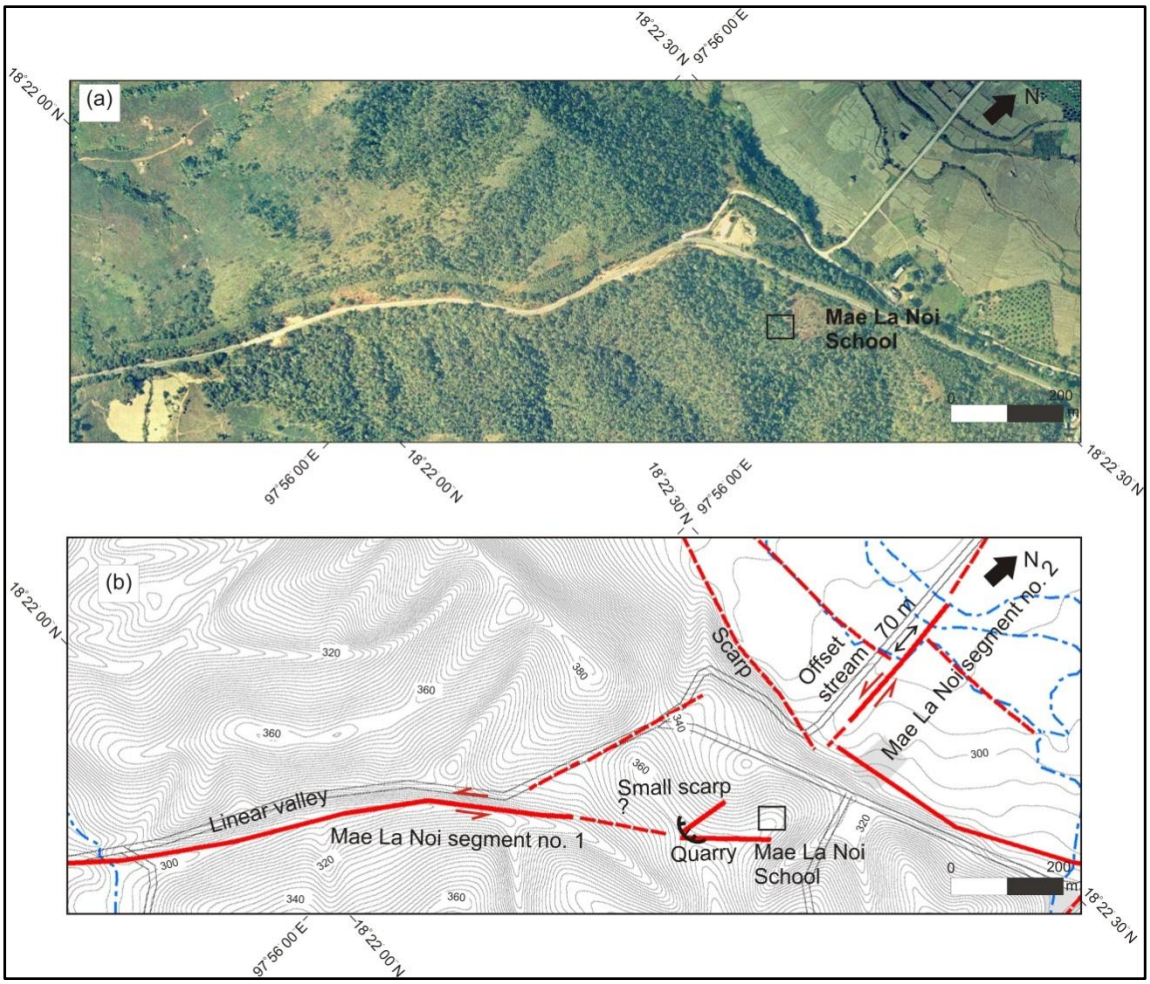

Fig. 14. Morphotectonic landforms of the Mae La Noi School area. (a) Aerial photograph showing a linear valley in the southwestern part of Mae La Noi segment no. 1 and an offset stream along Mae La Noi segment no. 2. (b) Topographic map showing the fault traces and morphotectonic landforms in plate a. The displacement of the offset stream is *ca*. 70 m. The locations of plates a and b are shown in Fig. 13b. (c) A small scarp at Mae La Noi School (on Mae La Noi segment no.1). The location of this scarp is at the quarry site shown in Fig. 14b.

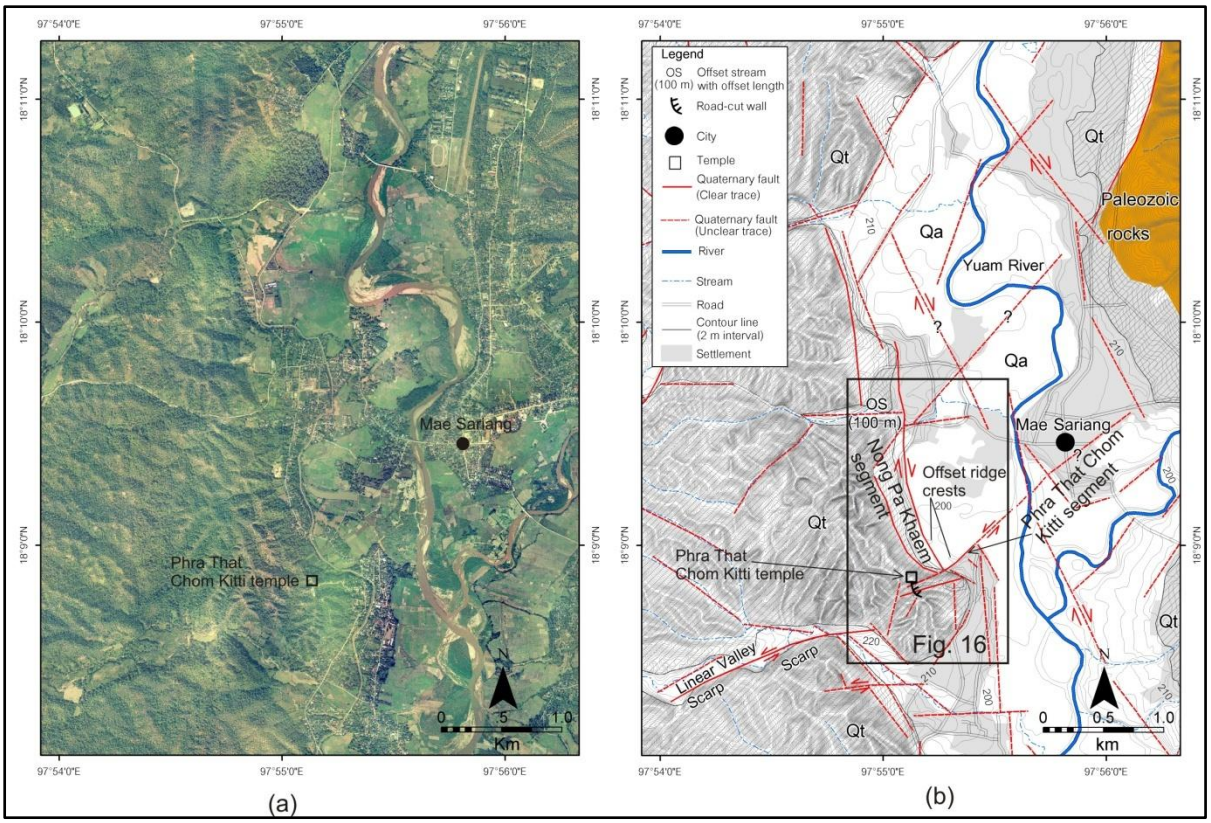

Fig. 15. Morphotectonic landforms of the Mae Sariang area. (a) Aerial photograph of the Mae Sariang area (location shown in Fig. 9a), and (b) the results of remote sensing investigations and distribution of geological units (Qa: alluvial sediments; Qt: terrace sediments, and Paleozoic rocks), showing morphotectonic landforms along Phra That Chom Kitti segment no. 36 (see Fig. 9c) and Nong Pa Khaem segment no. 41 (see Fig. 9c).

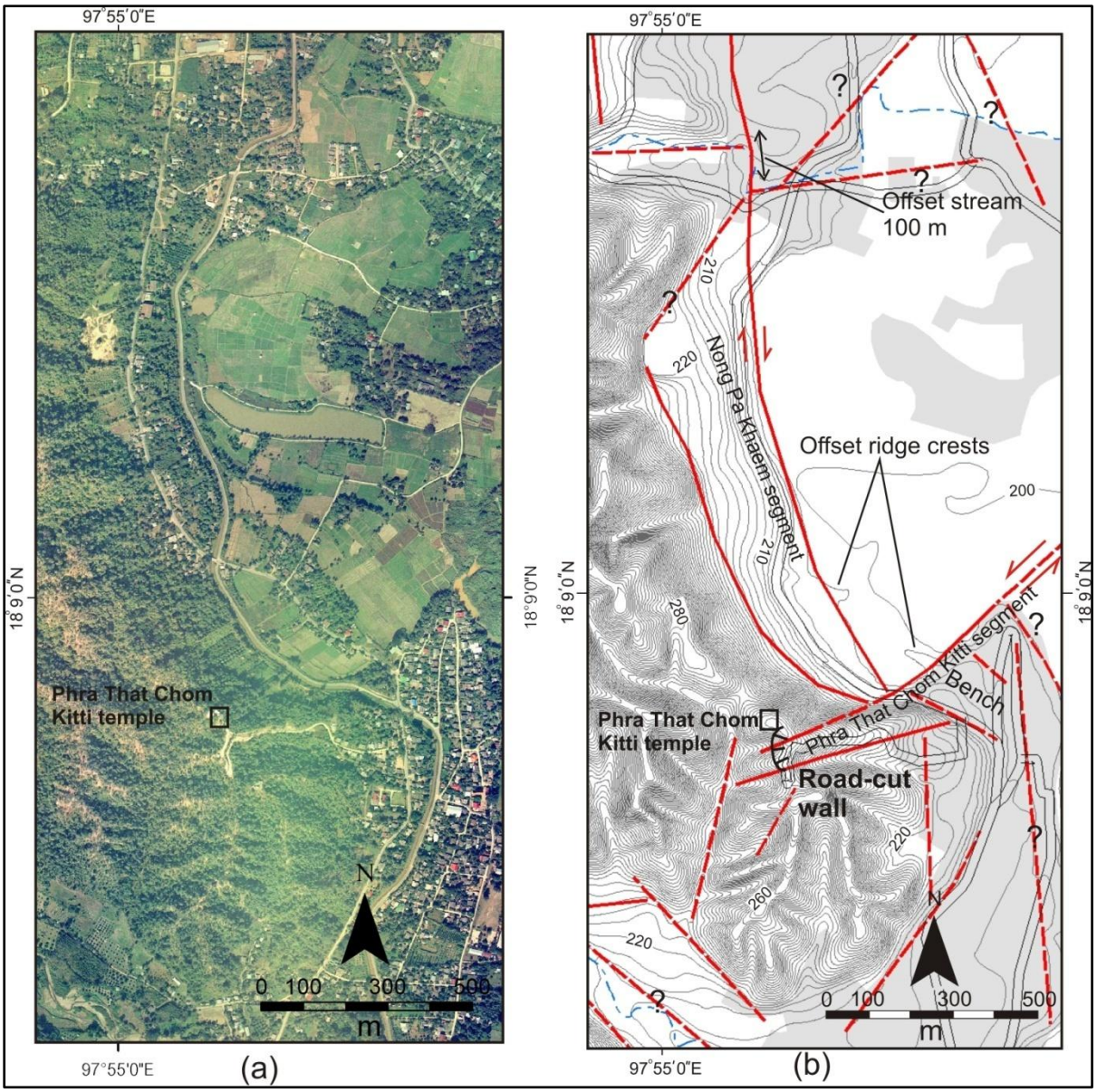

Fig. 16. Morphotectonic landforms of the Phra That Chom Kitti area. (a) Aerial photograph showing features along Nong Pa Khaem segment no. 41 and Phra That Chom Kitti segment no. 36 (for locations, see Fig. 9c). (b) Topographic map showing fault traces and an offset stream. The displacement of the offset stream is *ca.* 100 m. Offset ridge crests observed along the Nong Pa Khaem segment indicate right-lateral strike-slip movement, but the offset ridge crest observed along the NE–SW trending Phra That Chom Kitti segment indicates left-lateral strike-slip movement. The location of the figure is shown in Fig. 15b.

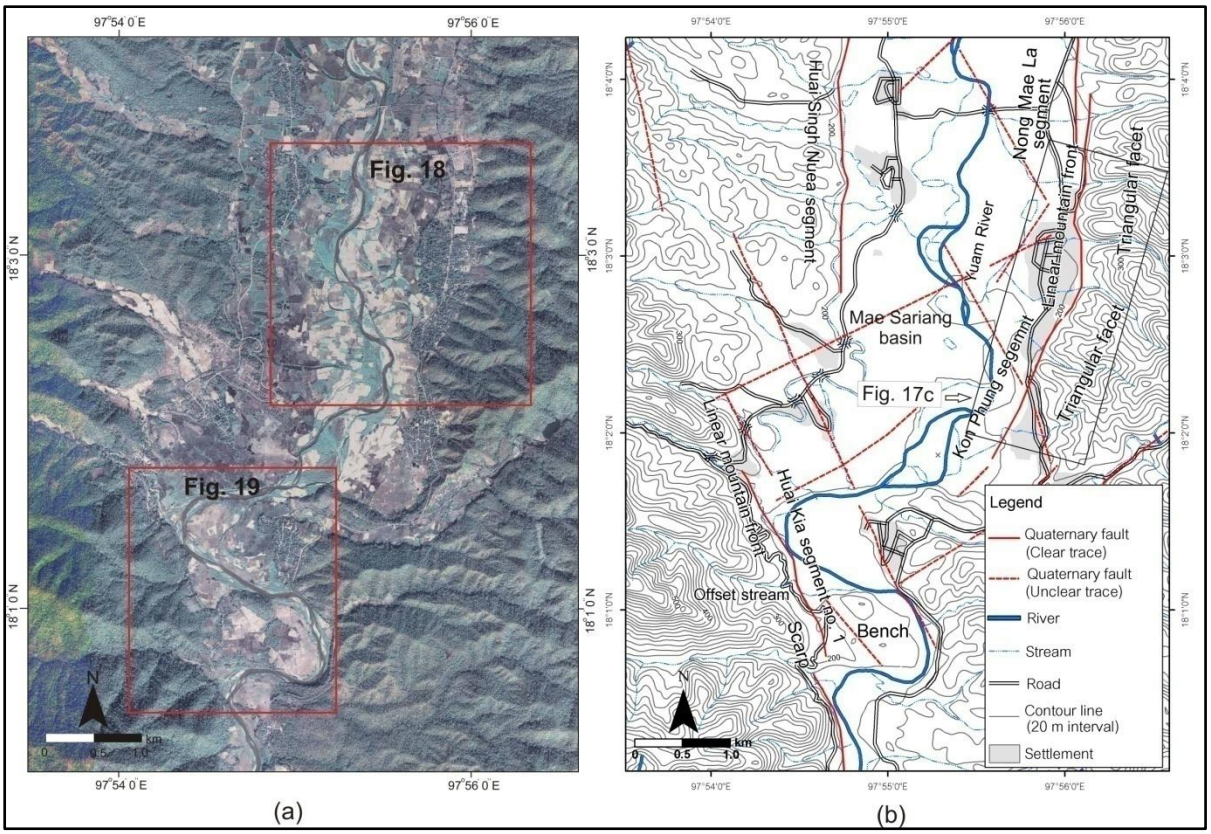

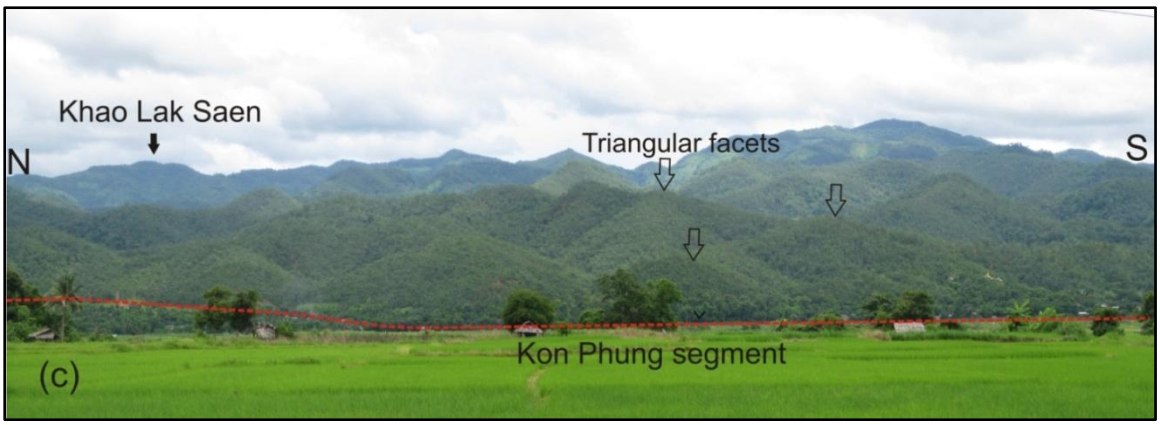

Fig. 17. Morphotectonic landforms of the southern Mae Sariang basin. (a) An IKONOS image of the southern part of the Mae Sariang basin (location shown in Fig. 9a), (b) an interpretation of morphotectonic landforms in the Mae Saring basin, and (c) a panoramic view of the west-facing escarpment in the Mae Sariang basin showing three lateral series of triangular facets (arrows; locations of the triangular facets are shown in Fig. 17b).

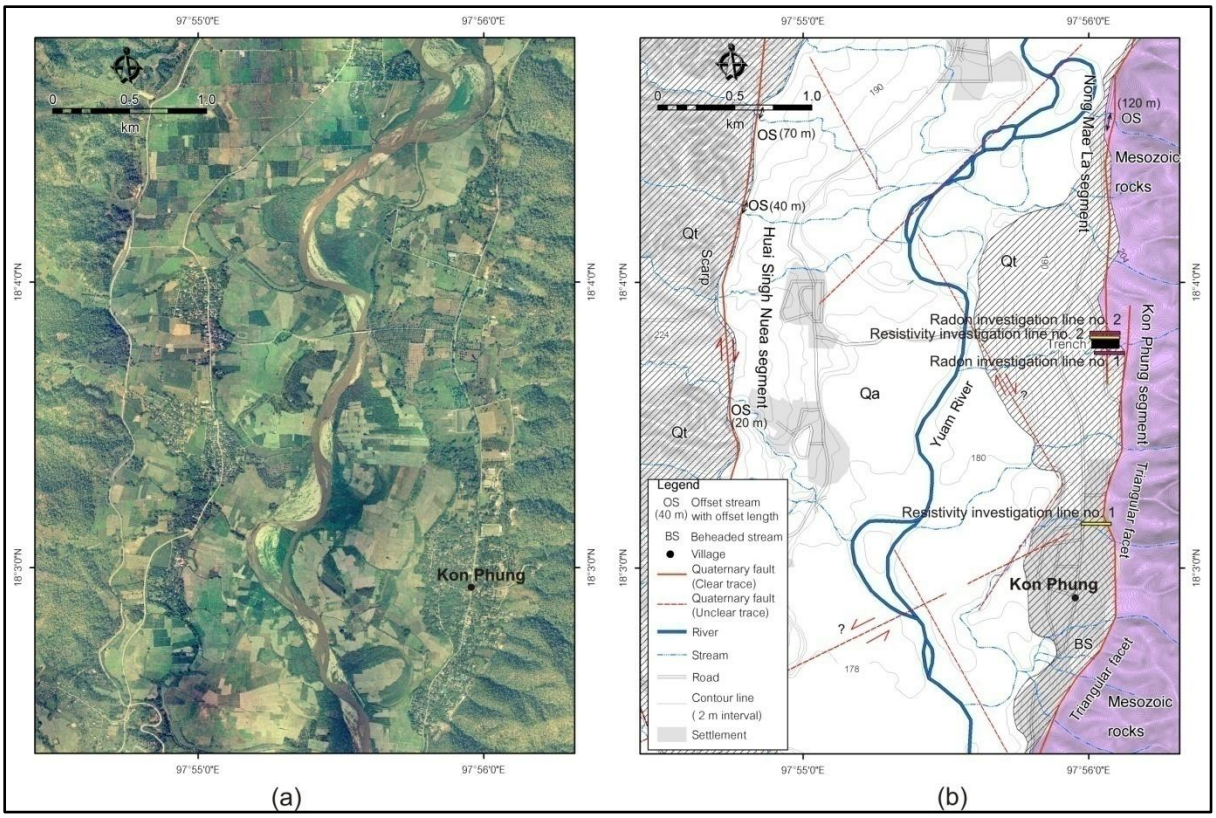

Fig. 18. Morphotectonic landforms of the Kon Phung area. (a) Aerial photograph showing features along Kon Phung segment no. 43, Nong Mae La segment no. 42, and Huai Singh Nuea segment no. 38 (for locations, see Fig. 9c). (b) Topographic map showing fault traces, an offset stream and distribution of geological units (Qa: alluvial sediments; Qt: terrace sediments, and Mesozoic rocks). Offset streams observed along the Huai Singh Nuea segment indicate right-lateral strike-slip movements. Triangular facets observed along the Kon Phung segment indicate normal dip-slip movements. The location of the figure is shown in Fig. 17a.

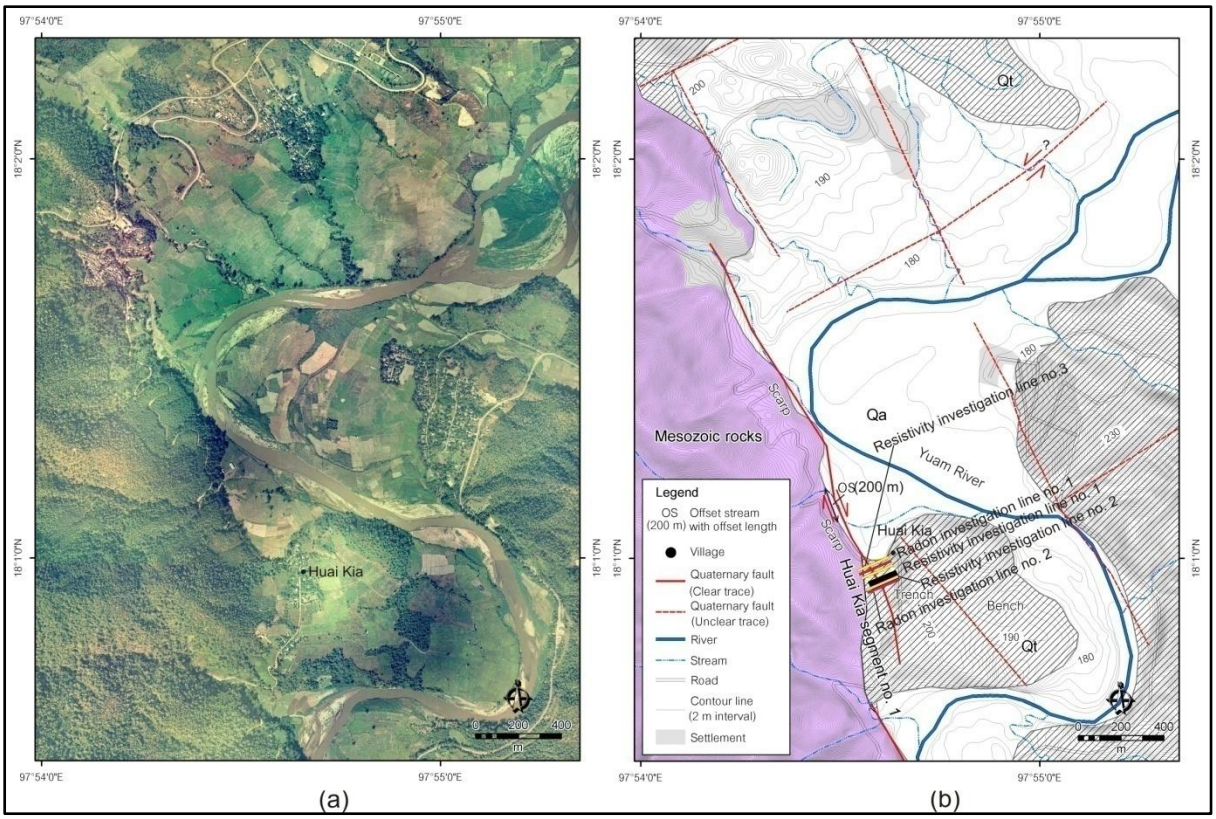

Fig. 19. Morphotectonic landforms of the Huai Kia area. (a) Aerial photograph showing features along Huai Kia segment no. 1 (labelled no. 39 in Fig. 9c). (b) Topographic map showing fault traces, an offset stream and distribution of geological units (Qa: alluvial sediments; Qt: terrace sediments, and Mesozoic rocks). Offset stream observed along Huai Kia segment no. 1 indicates right-lateral strike-slip movement. The location of the figure is shown in Fig. 17a.

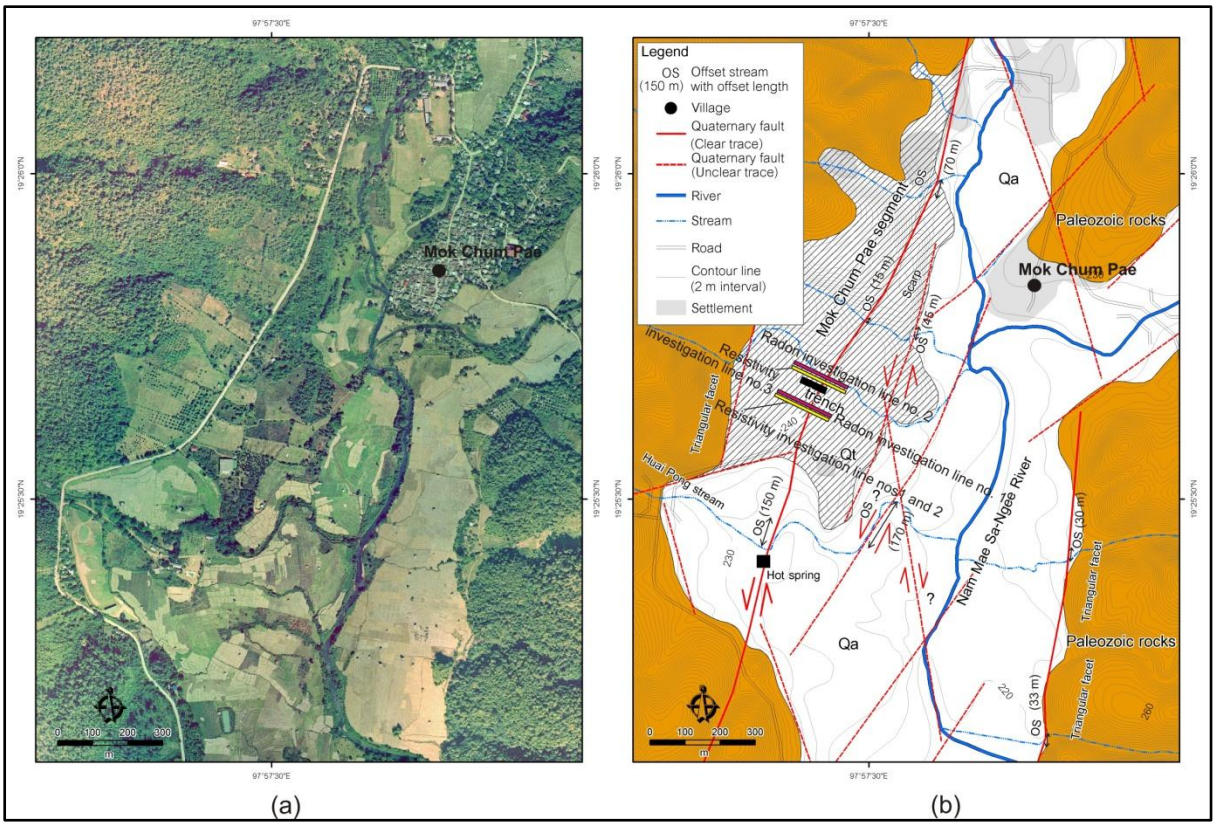

Fig. 20. Morphotectonic landforms of the Mok Chum Pae area. (a) Aerial photograph of the Mok Chum Pae area (location shown in Fig. 9a), and (b) the results of remote sensing investigations and the distribution of geological units (Qa: alluvial sediments; Qt: terrace sediments, and Paleozoic rocks), showing morphotectonic landforms along Mok Chum Pae segment no. 3 (see Fig. 9c).

5.2. Thoen Fault in the Lampang basin

5.2.1. Lineaments and fault segments

Lineaments and fault segments in the Lampang basin and adjacent areas are clearly visible on enhanced Landsat 7 images (Fig. 21a), mainly oriented NE–SW, with conjugate structures oriented NW–SE, along with some minor N–S structures (Fig. 21b). The NE–SW-striking fault that bounds the Lampang Basin is clearly visible along the southeastern side of the basin (Fig. 21c). The total length of the Thoen Fault in the Lampang basin is approximately 75 km. The fault can be traced along the boundary between Triassic marine sandstone and unconsolidated Quaternary sediments that are mainly fluvial, colluvial, and alluvial deposits.

The Thoen Fault is well defined, visible as a sharp lineament on aerial photographs and satellite images (Figs 21 and 22). Detailed interpretations of aerial photographs reveal fault scarps at Ban Mai, Ban Don Fai, and Ban Samai Nuea (a and c in Fig. 22), and reveal the following six geometrical fault segments along the southeastern margin of the Lampang basin: Ban Don Fai, Ban Mai, Ban Mae Ip, Doi Ton Ngun, Mae Than, and Sop Prap (Fig. 21c).

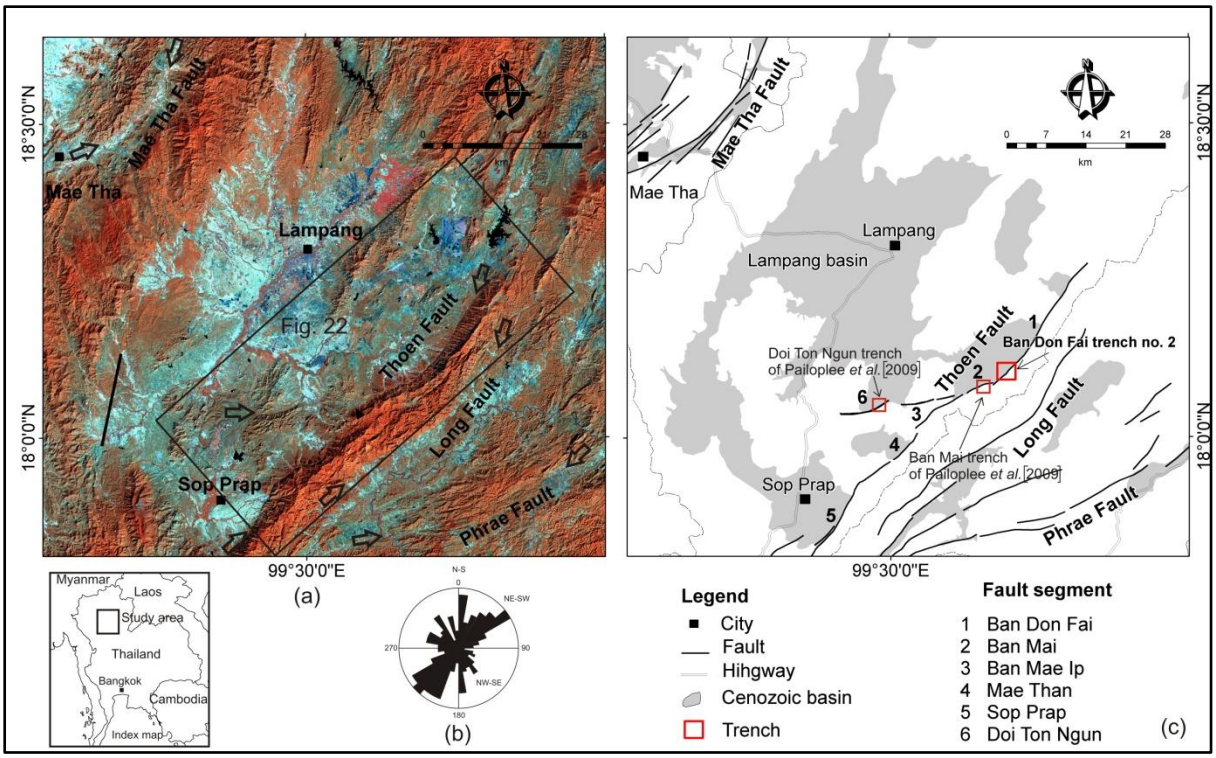

Fig. 21. Landsat image showing the location of the Lampang basin and the prominent NE–SW trending Thoen Fault (arrows) (a), the principle orientations of faults shown as a rose diagram (b), and location of the Thoen Fault in the Lampang basin (c). The names and locations of individual segments are also displayed. The area covered by this image is shown in Fig. 1.

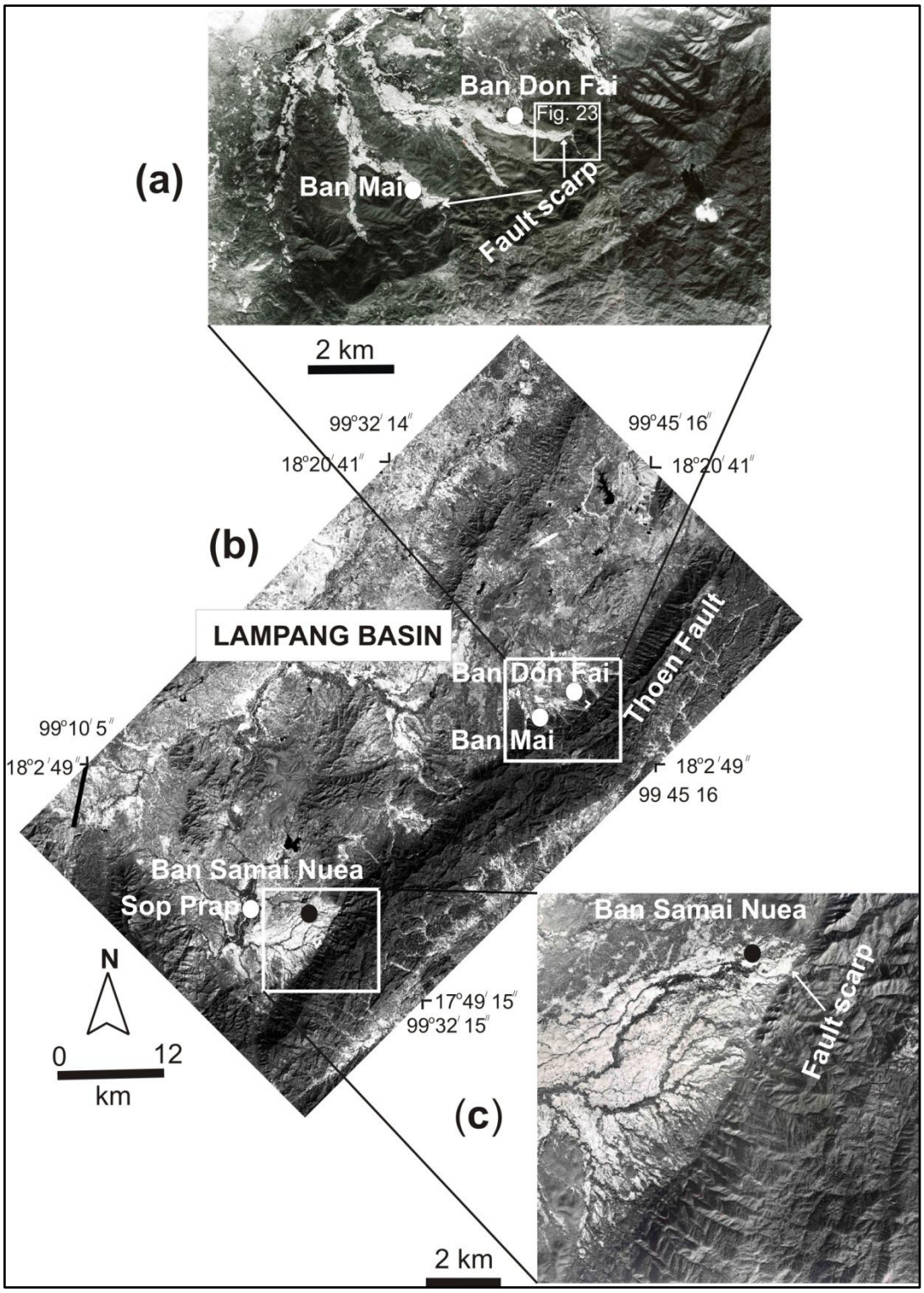

Fig. 22. Panchromatic Landsat image of the Thoen Fault in the Lampang basin, showing a sharp lineament near Ban Mai, Ban Don Fai, and Ban Samai Nuea (b), and aerial photographs of the Thoen Fault showing the fault scarps at Ban Mai, Ban Don Fai, and Ban Samai Nuea (a and c). The location of this image is shown in Fig. 21a.

5.2.2. Results of aerial photograph interpretation

The morphotectonic landforms observed in the Lampang basin include fault scarps, triangular facets, wine-glass canyons, linear valleys, and linear mountain fronts. In the Ban Don Fai area, detailed interpretations of aerial photographs reveal small fault scarps, linear mountain fronts, and linear valleys along the fault trace (Fig. 23). The NE–SW trending faults show normal dip-slip displacement. Small fault scarps on the Ban Don Fai segment are present on the piedmont to the west of the reservoir (Fig. 23). The Ban Don Fai segment has a total length of *ca.* 27.5 km.

Triangular facets, scarps, wine-glass canyon, and linear mountain fronts can be observed along the southeastern margin of the Lampang basin (Figs 22c and 24). These morphotectonic landforms support the interpretation of normal displacement along the fault trace on the basin's southeastern margin. The triangular facets represent a combination of vertical movements on range-bounding NE–SW normal faults and stream incision in valleys. A series of triangular facets is found in the Lampang basin along the NW-facing escarpment (Fig. 24a and c). Triangular facets may be caused by lateral erosion or by differential erosion acting on a lithologic boundary between resistant and non-resistant rocks; however, several streams that cross the Ban Don Fai, Sop Prap, and Ban Mai segments pass through wine-glass canyons (Fig. 25) and V-shaped valleys. The presence of wine-glass canyons indicates steepening of the faceted spurs at the base of the escarpment, suggesting in turn that the Ban Don Fai and Ban Mai segments, and possibly other segments, are currently undergoing renewed or increasing vertical displacement. Rapid down-cutting results in the formation of a narrow slot in a wine-glass canyon. A line of small, triangular facets at the base of the range front coincides with the locations of a narrow slot in a wine-glass canyon, and with the surface trace of the Thoen Fault. A NW-facing escarpment of triangular facets is developed in Triassic marine sandstone, with slope angles (50°–60°) steeper than the dip of bedding

(45°–50°). These morphotectonic landforms (i.e., triangular facets, V-shaped valleys, and wine-glass canyons) have been reported from other well-studied active fault zones and are considered to indicate mountain fronts bounded by active faults [e.g., Hamblin, 1976; Bull and McFadden 1977; Wallace, 1978; Fenton *et al.,* 2003; Ganas *et al.,* 2005; Picotti *et al.,* 2009; Wiwegwin *et al.*, 2011]. This explanation of the origin of triangular facets is consistent with the findings of previous studies that linked facet formation to periods of active faulting.

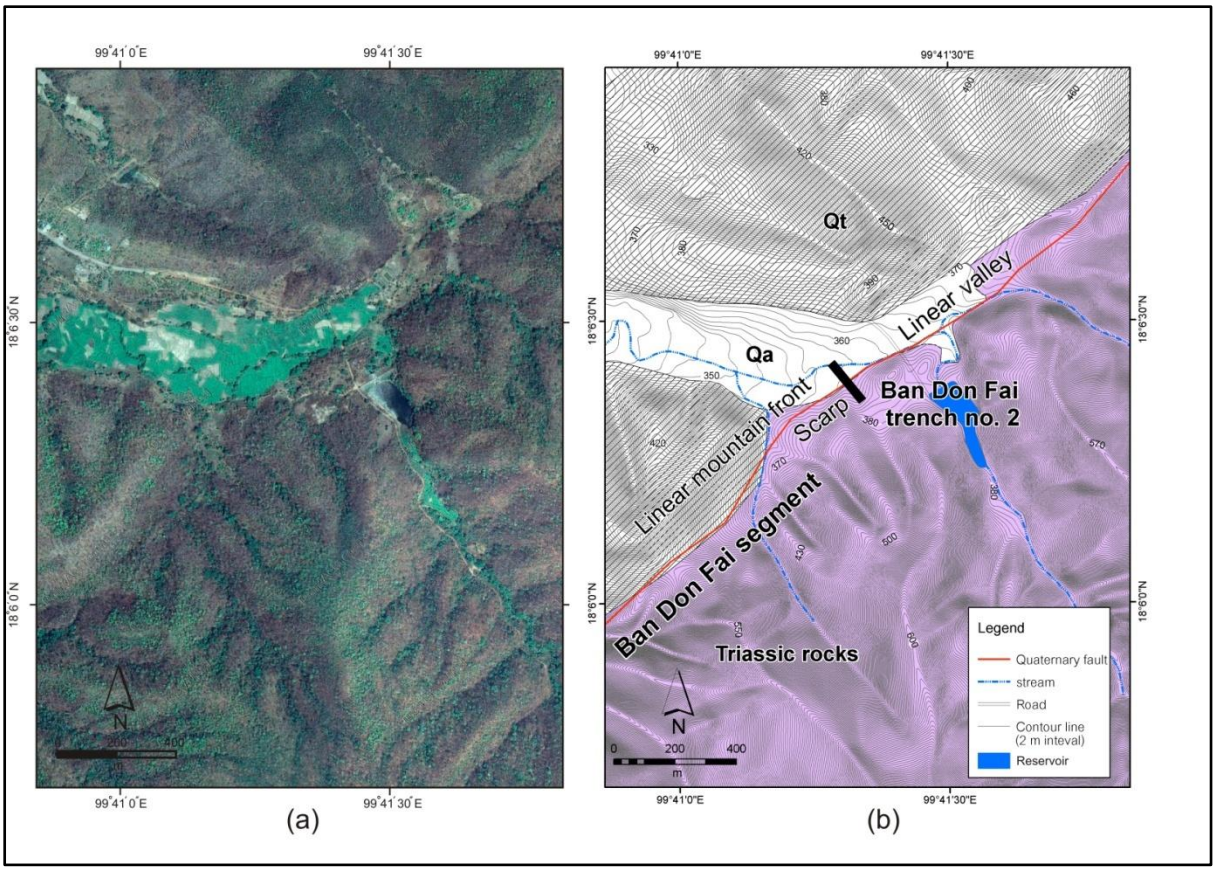

Fig. 23. Morphotectonic landforms of the Ban Don Fai area, Lampang basin. (a) Aerial photograph of the Ban Don Fai area (location shown in Fig. 22a), and (b) the results of remote sensing investigations and the distribution of geological units (Qa: alluvial sediments; Qt: terrace sediments, and Triassic rocks), showing morphotectonic landforms along the Ban Don Fai segment of the Thoen Fault (1 in Fig. 21c).

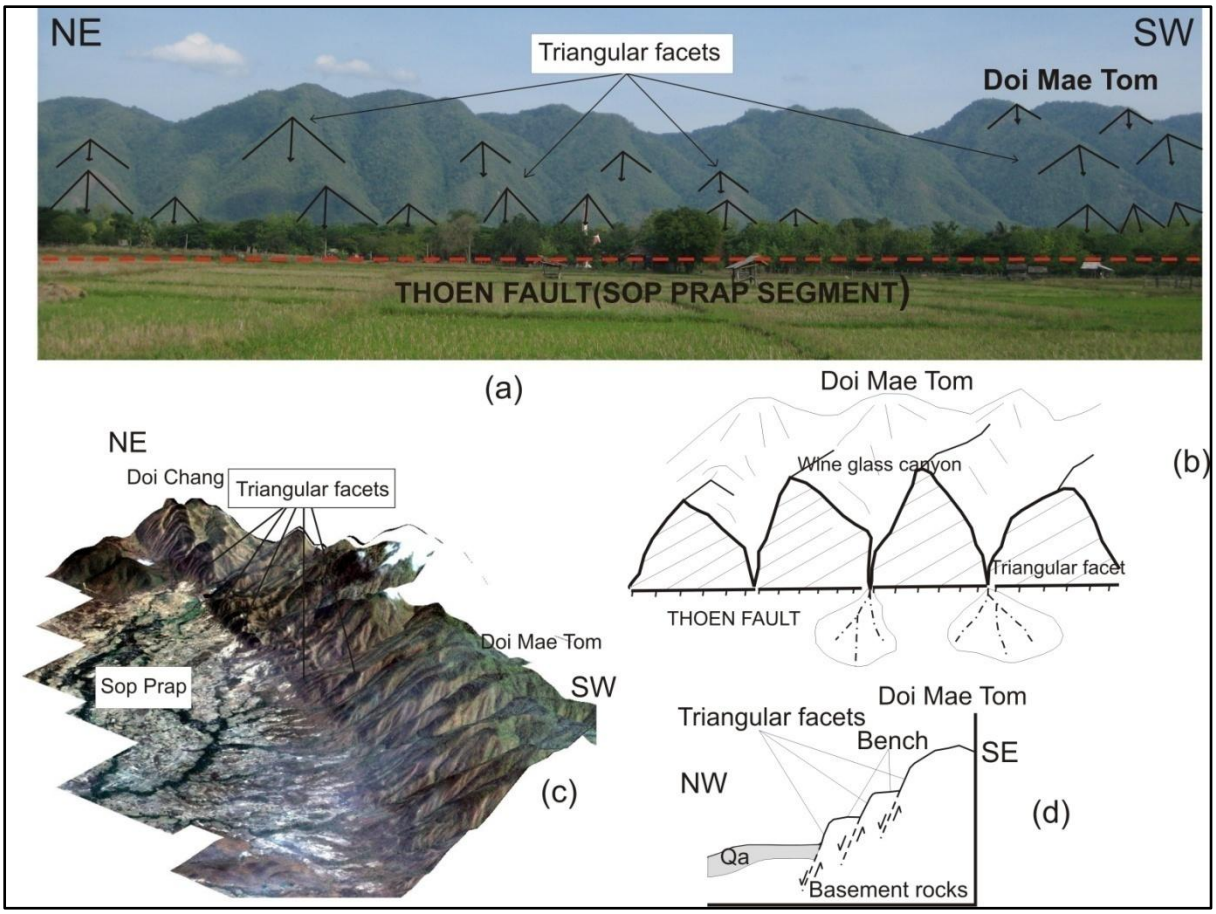

Fig. 24. Panoramic view of the NW-facing escarpment with three lateral series of triangular facets at Doi Mae Tom in the Ban Samai Nuea, Sop Prap area (a); an idealized model showing triangular facets of the Lampang basin (b); a three-dimensional model of the IKONOS image of the Sop Prap area, showing a series of triangular facets (c); and a NW–SE cross-section across Doi Mae Tom (d).

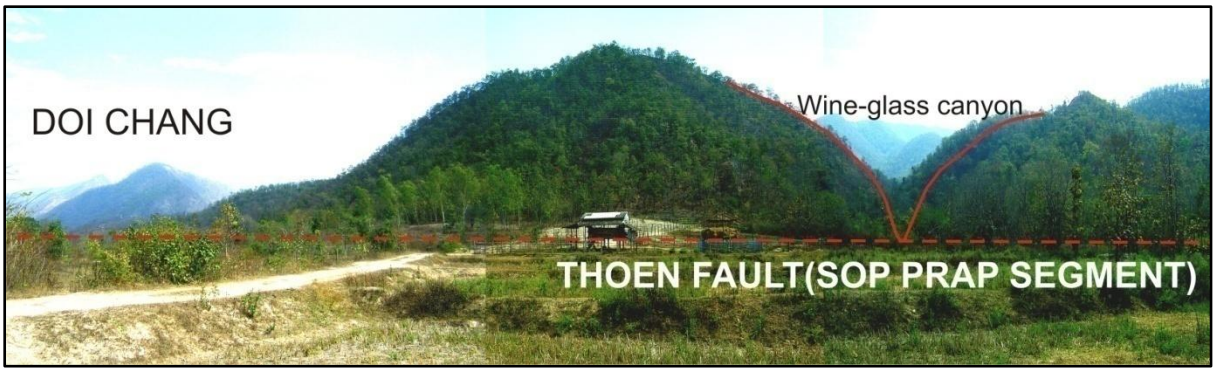

Fig. 25. Panoramic view of Doi Chang mountain, looking towards the SE, showing a wine-glass canyon along the Sop Prap segment of the Thoen Fault.

6. Results of geophysical investigations across the Mae Hong Son Fault

6.1. Radon investigations

Radon (^{222}Rn), a naturally occurring radioactive gas, is produced by the decay of radium (^{236}Ra) within the uranium (^{238}U) decay series. High radon anomalies can often be related to the upwards migration of gas along active fault zones [Abodoh and Pilkington, 1989], and this is because an active fault zone exhibits a high permeability compared to the surrounding country rock, thus providing an easy route for subsurface gases (i.e., methane, CO_2, He, radon, etc.) to escape into the atmosphere. Thus, radon has been used both to locate buried faults and to monitor faults in the hope of predicting earthquake activity [Moussa and El Arabi, 2003]. Anomalously high radon concentrations have been measured along many active faults in the world [Tanner, 1980; King *et al*., 1996]. For example, the Chinese State Seismological Bureau reported high concentrations of radon and other gases not only along major faults but also above some buried faults in China [Wang *et al.*, 1991]. Israel and Bjornsson [1967] reported high concentrations of radon and thoron in soil at 1 m depth along a transect perpendicular to the strike of several faults near Aachen, Germany.

A few radon investigations have been applied to detecting active faults in Thailand. Atyotha [2007] was the first to use the portable radonmeter (model RAD 7: Electronic Radon Detector) for measuring radon concentrations in soils across the Khlong Marui Fault (15 in Fig. 5). He found that high radon concentrations in soils (measured by RAD 7) can locate the fault traces of the Khlong Marui Fault, and he confirmed that the radon gas measurement technique is a suitable tool for detecting and mapping active fault zones in Thailand. Pispak *et al*. [2010] measured radon concentrations in soil gases across the Khlong Marui Fault, using an automatic soil gas radon monitoring system, and an anomalously high radon concentration was observed along the fault. Pispak *et al*. [2010] also reported that an increase in the number of local earthquakes along the Khlong Marui Fault and related faults in

southern Thailand was detected several days after an anomalously high radon concentration was observed. Most of these local earthquakes were located along the Khlong Marui Fault. Thus, Pispak *et al*. [2010] suggested that there was a possibility of using radon monitoring in soil gases for providing a warning of earthquakes in the region. Recently, Bhongsuwan *et al*. [2011] applied alpha track detection for measuring radon concentrations in soils across the Khlong Marui Fault. They confirmed that the radon emanations observed are anomalously high [Bhongsuwan *et al*., 2011], and their conclusions are similar to those of Pispak *et al*. [2010].

For this study, radon concentrations were measured across the fault traces in three areas (the Mok Chum Pae, Kon Phung, and Huai Kia areas; see locations in Figs 18–20) following the method of Atyotha [2007], and radon investigations were performed by EGAT [2012]. For this paper, the data have been re-examined to find the locations of faults. Two traverses across the faults in all three areas have been conducted, with the radon measured. Along each traverse (100–140 m) there were at least five sampling sites at approximately 5–20 m intervals. The traverses crossed the assumed lines of the faults at approximately 90° (pink bars in Figs 18–20). These traverses are in Quaternary sediments that are possibly cut by the fault, as indicated by the remote sensing interpretation.

Radon concentrations measured in the Kon Phung area are shown in Tables 1 and 2. Figure 26 shows the results of radon investigations along the 100 m survey lines across the Nong Mae La segment of the Mae Hong Son Fault. The results of the radon analyses show peak radon emissions at position 20 m along the survey line no. 1 (Fig. 26a), and at position 60 m on survey line no. 2 (Fig. 26b). These peak radon emissions are interpreted as indicating the presence of fractures or fault zones, possibly caused by movement of the Nong Mae La segment.

Radon concentrations measured in the Huai Kia area are shown in Tables 3 and 4. Figure 27 shows the results of radon investigations along the two 100 m survey lines across the Huai Kia segment no. 1 of the Mae Hong Son Fault. The results of the radon analyses show peak radon emissions at the position located 20 m along survey line no. 1 (Fig. 27a), and at 60 m along survey line no. 2 (Fig. 27b). These peak radon emissions are interpreted to indicate the presence of fractures or fault zones, possibly caused by movement of the Huai Kia segment no. 1.

Radon concentrations measured in the Mok Chum Pae area are shown in Tables 5 and 6. Figure 28 shows the results of radon investigations along the two 140 m survey lines across the Mok Chum Pae segment of the Mae Hong Son Fault. The results of the radon analyses show three peaks of radon emissions at positions 40, 95, and 110 m along survey line no. 1 (Fig. 28a), while two peaks can be observed at positions 40 and 120 m on survey line no. 2 (Fig. 28b). These peak radon emissions are interpreted to indicate the presence of fractures or fault zones, possibly caused by movement of the Mok Chum Pae segment.

Table 1. Radon concentrations measured along radon investigation line no. 1 in the Kon Phung area.

Distance (m)	**Location (UTM)**	**Radon concentration (kBq/m^3) ± S.D.**	**Remark**
0	0387261E/1997429N	10.20 ± 9.04	
20	0387279E/1997429N	20.32 ± 11.57	peak
40	0387298E/1997430N	16.10 ± 8.66	
60	0387315E/1997431N	13.66 ± 7.93	
80	0387332E/1997430N	9.28 ± 5.03	
100	0387353E/1997432N	3.70 ± 1.89	

Table 2. Radon concentrations measured along radon investigation line no. 2 in the Kon Phung area.

Distance (m)	**Location (UTM)**	**Radon concentration (kBq/m^3) ± S.D.**	**Remark**
0	0387170E/1997527N	13.40 ± 7.51	
20	0387192E/1997518N	0.24 ± 0.13	
40	0387214E/1997523N	3.95 ± 2.34	
60	0387233E/1997521N	11.94 ± 5.67	peak
80	0387254E/1997520N	8.85 ± 4.40	
100	0387273E/1997519N	6.89 ± 4.06	

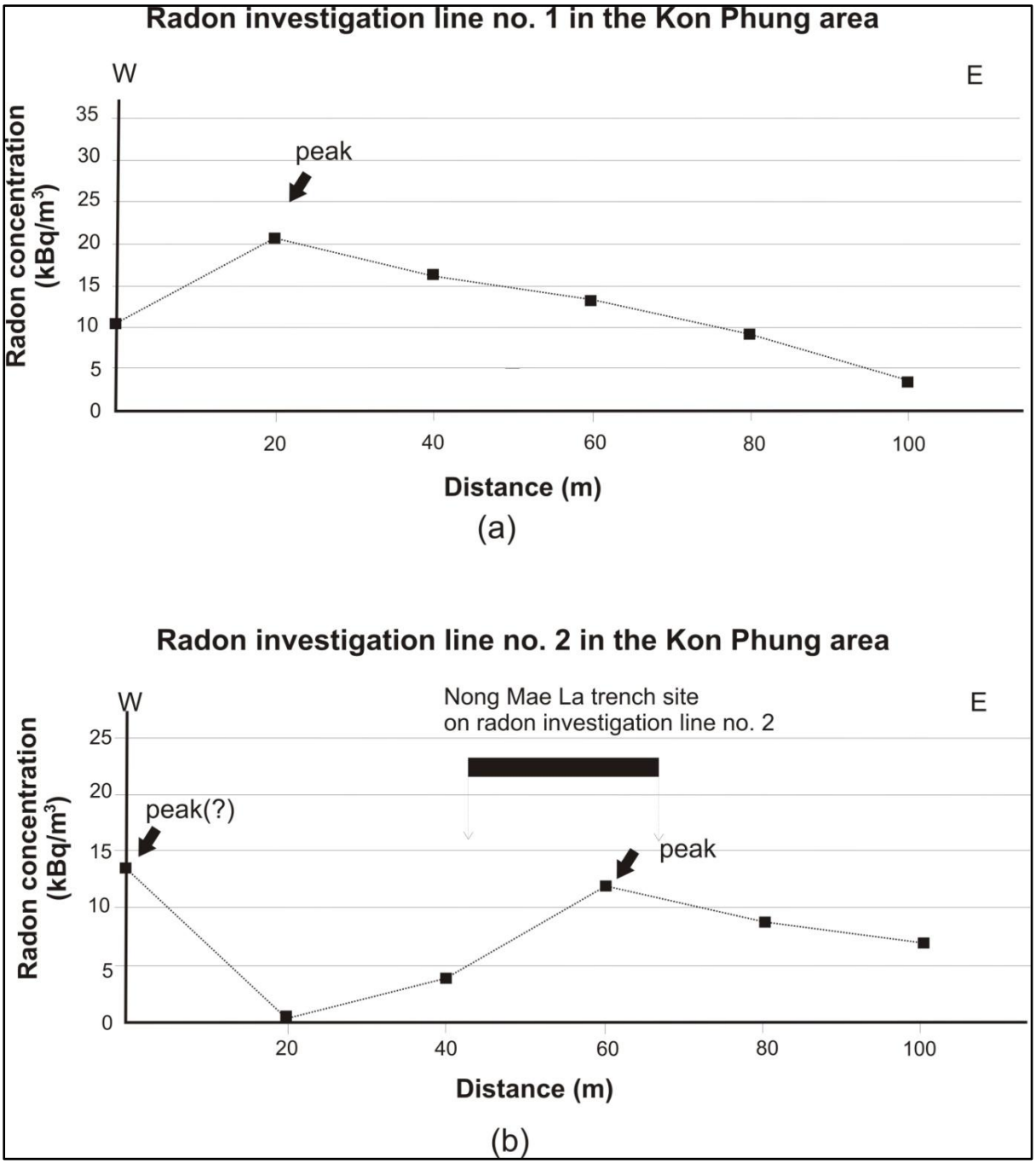

Fig. 26. Results of radon analyses in the Kon Phung area showing peak radon emissions at position 20 m on survey line no. 1 (a), and at position 60 m on survey line no. 2 (b). These indicate that faults cut through the Quaternary sediments in this area. The locations of the survey lines are shown in Fig. 18b. The location of the Nong Mae La trench is indicated in Figs 9c and 18b, and is shown by a dark bar on radon investigation line no. 2.

Table 3. Radon concentrations measured along radon investigation line no. 1 in the Huai Kia area.

Distance (m)	**Location (UTM)**	**Radon concentration (kBq/m^3) ± S.D.**	**Remark**
0	0384547E/1992223N	0.03 ± 0.03	
20	0384563E/1992233N	13.14 ± 7.84	peak
30	0384570E/1992237N	10.02 ± 5.23	
40	0384581E/1992243N	8.38 ± 4.03	
60	0384598E/1992253N	5.94 ± 3.32	
80	0384615E/1992263N	5.70 ± 3.12	
100	0384631E/1992272N	6.52 ± 4.00	

Table 4. Radon concentrations measured along radon investigation line no. 2 in the Huai Kia area.

Distance (m)	**Location (UTM)**	**Radon concentration (kBq/m^3) ± S.D.**	**Remark**
20	0384538E/1992189N	4.89 ± 2.92	
40	0384556E/1992196N	6.93 ± 3.71	
60	0384573E/1992206N	13.08 ± 6.49	peak
80	0384591E/1992216N	4.23 ± 2.43	
100	0384608E/1992227N	10.16 ± 6.09	

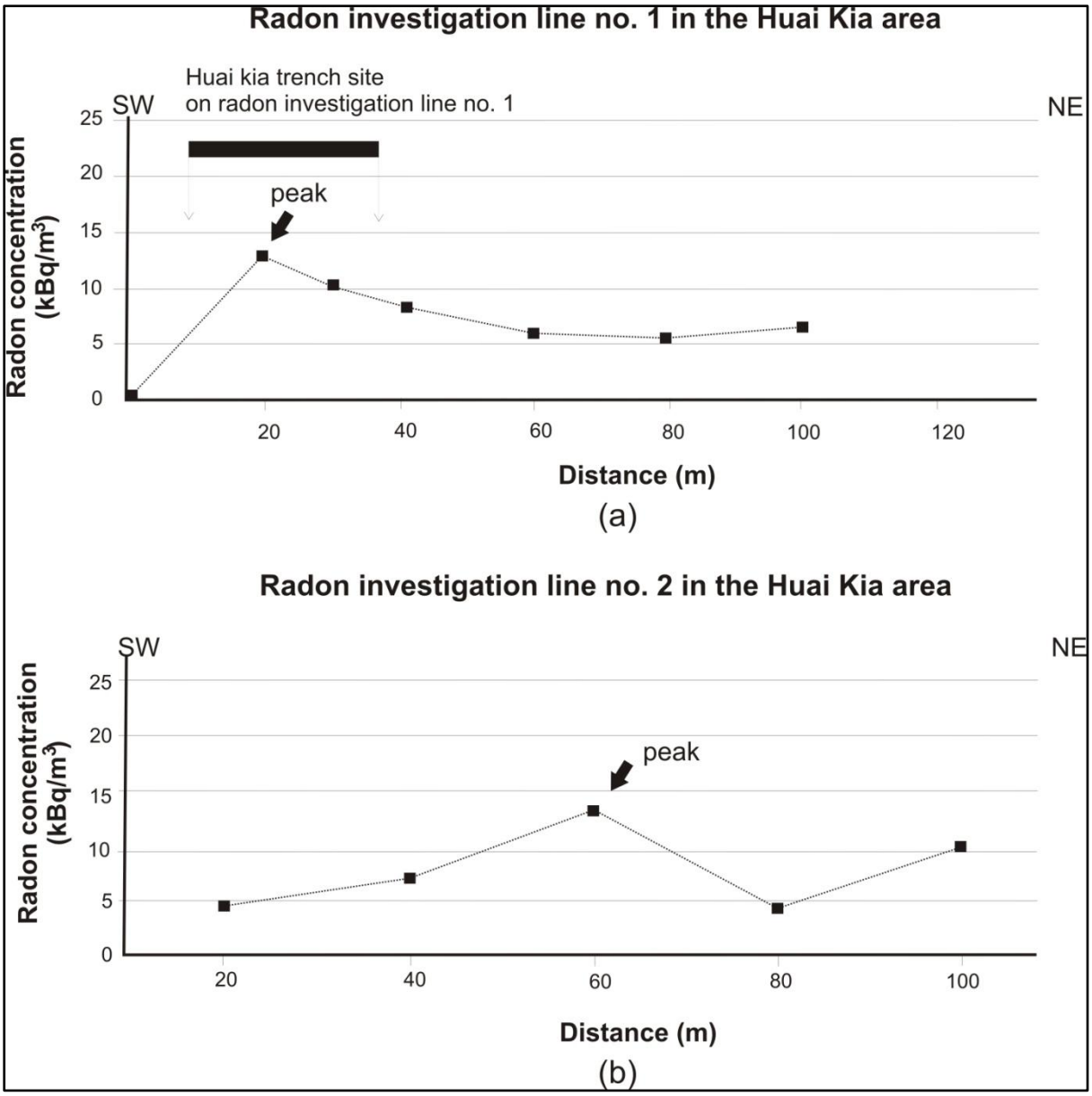

Fig. 27. Results of radon analyses in the Huai Kia area showing peak radon emissions at position 20 m on survey line no. 1 (a), and at position 60 m on survey line no. 2 (b). These indicate that faults cut through the Quaternary sediments in this area. The locations of the survey lines are shown in Fig. 19b. The location of the Huai Kia trench is indicated in Figs 9c and 19b, and is shown by a dark bar on radon investigation line no. 1.

Table 5. Radon concentrations measured along radon investigation line no. 1 in the Mok Chum Pae area.

Distance (m)	**Location (UTM)**	**Radon concentration (kBq/m^3) ± S.D.**	**Remark**
0	0390369E/2148536N	7.29 ± 5.29	
20	0390389E/2148531N	13.02 ± 6.93	
25	0390395E/2148528N	6.32 ± 3.30	
30	0390398E/2148528N	12.15 ± 6.21	
35	0390403E/2148523N	8.76 ± 4.41	
40	0390410E/2148522N	13.98 ± 7.29	peak
60	0390431E/2148514N	0.06 ± 0.04	
80	0390446E/2148505N	2.23 ± 2.92	
90	0390455E/2148502N	14.72 ± 8.02	
95	0390460E/2148501N	19.11 ± 10.30	peak
100	0390464E/2148498N	16.99 ± 10.65	
105	0390464E/2148494N	6.78 ± 3.69	
110	0390470E/2148493N	13.39 ± 7.27	peak
120	0390479E/2148487N	2.27 ± 3.00	
140	0390498E/2148479N	0.02 ± 0.03	

Table 6. Radon concentrations measured along radon investigation line no. 2 in the Mok Chum Pae area.

Distance (m)	**Location (UTM)**	**Radon concentration (kBq/m^3) ± S.D.**	**Remark**
0	0390394E/2148580N	13.03 ± 7.19	
20	0390412E/2148572N	9.73 ± 5.27	
40	0390431E/2148562N	15.49 ± 8.15	peak
60	0390451E/2148553N	6.17 ± 3.26	
80	0390466E/2148547N	12.38 ± 6.77	
100	0390482E/2148536N	10.68 ± 5.79	
120	0390501E/2148528N	13.70 ± 8.21	peak
140	0390519E/2148517N	10.75 ± 7.90	

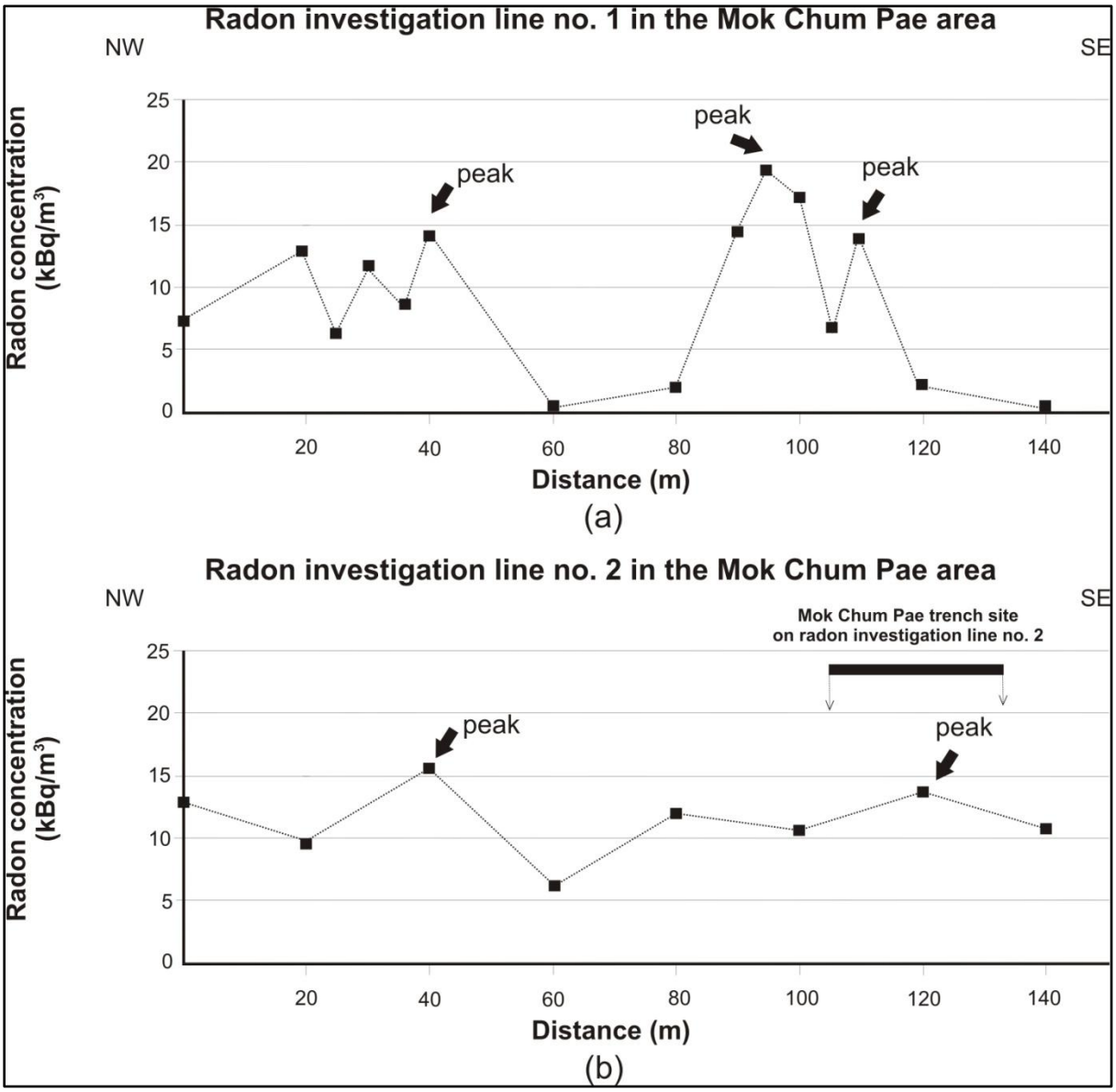

Fig. 28. Results of radon analyses in the Mok Chum Pae area showing peak radon emissions at positions 40, 95, and 110 m on survey line no. 1 (a), and at positions 40 and 120 m on survey line no. 2 (b). These indicate that faults cut through the Quaternary sediments in this area. The locations of the survey lines are shown in Fig. 20b. The location of the Mok Chum Pae trench is indicated in Figs 9c and 20b, and is shown by a dark bar on radon investigation line no. 2.

6.2. Electrical resistivity investigations

Electrical resistivity quantifies how strongly a given material opposes the flow of an electric current. A low resistivity indicates a material that readily allows the movement of an electric charge. The basic concept is that the resistance (R) is proportional to the length (L) of the resistive material divided by area (A); this can be written as $R = \rho L/A$, where ρ is the true resistivity. According to Ohm's Law, for an electrical circuit, Ohm's Law gives $R = V/I$, where V and I respectively are the potential difference across a resistor and the current passing through it. These two expressions can be combined to form the product of resistance (Ω) and distance (area/length; meters), which is defined as the resistivity (units: ohm.m, Ωm).

Electrical resistivity surveys measure variations in the resistivity of the ground by applying small electric currents across arrays of ground electrodes. These data are processed to produce graphic depth sections of the thickness and resistivity of subsurface layers, and they are used to interpret earth material types [Burger *et al.*, 2006]. The resistivity sections are correlated with ground interfaces such as soil and fill layers or soil–bedrock interfaces. Resistivities of some minerals and rocks are listed in Table 7. Igneous rocks tend to have the highest resistivities, whereas sedimentary rocks tend to be most conductive, largely due to their high pore fluid content, and metamorphic rocks have intermediate resistivities [Reynolds, 2011]. Measuring the electrical resistivity has several advantages over other methods of investigating the subsurface geology [McCalpin, 2009]. First, its depth penetration is not limited by moisture, salinity, or clays, as is the case with ground penetrating radar (GPR). Second, interpreting the resistivity values with respect to the effects of the water table (i.e., the saturated zone) is easier than with P-wave seismic surveys. However, a disadvantage is that metals in the ground and electrical wires can induce false signals. Therefore, this geophysical method is applied extensively for searching groundwater sources, and for locating subsurface cavities and faults [Reynolds, 2011].

In Japan, Fujita and Ikuta [2000] successfully applied electrical resistivity surveying to the complex structures of the Yamasaki Fault. Moreover, 2D electrical resistivity surveying has been widely used to locate subsurface structures prior to trenching investigations in Europe. For example, Caputo *et al.* [2007] applied electrical resistivity tomography (ERT, also called electrical resistivity imaging) to trace a normal fault in southern Italy. Although this method of geophysical surveying has been successfully used for tracing active faults in Europe, it has not been widely applied for this purpose in North America [McCalpin, 2009].

A few electrical resistivity investigations have been used for detecting active faults in Thailand. Danphaiboonphon *et al.* [2007] applied ground geophysical methods, including magnetic, electromagnetic, and electrical resistivity investigations, to locate active faults in Kanchanburi, western Thailand. The results of these electrical resistivity investigations can delineate the orientations of faults and the dips of fault planes. It also seems that the results of electrical resistivity investigations are consistent with those of magnetic and electromagnetic investigations. Danphaiboonphon *et al.* [2007] suggested that electrical resistivity investigations could be used for detecting fault traces in the subsurface.

For this study, electrical resistivity imaging data were collected using a Syscal R1 Plus (IRIS Instruments). A dipole–dipole array configuration was used with an electrode spacing of 1–2 m. The resistivity cross-sections are almost perpendicular to the strikes of the faults (yellow bars in Figs 18–20). These electrical resistivity investigations were conducted by EGAT [2012]. The data were re-examined here in order to locate the faults. As a result, two survey lines have been investigated in the Kon Phung area, three in the Huai Kia area, and farther to the north, three in the Mok Chum Pae area where two main survey lines were investigated using an electrode spacing of 2 m (resistivity investigation line nos 1 and 3 in

Fig. 20), and the other survey line was selected from positions 40 to 90 m along survey line no. 1, using an electrode spacing of 1 m.

Figure 29 shows the results of electrical resistivity investigations across the Kon Phung and Nong Mae La segments (resistivity investigation line nos 1 and 2, respectively, in Fig. 18b). Resistivity values measured along both lines are similar to those of the normal values for common sediments and sedimentary rocks, and the resistivity results and field surveys indicate that sand, gravel, and alluvial sediments possibly overlie Triassic sandstones. The positions of fractures or faults can be determined using the discontinuities in resistivity values in the horizontal layers. Thus, faults or fractures are put at positions 47 and 64 m on investigation line no. 1. Similarly, along line no. 2, fractures or faults can be put at positions 56 and 72 m.

Figure 30 shows the results of electrical resistivity investigations across Huai Kia segment no. 1 (resistivity investigation line nos 1, 2, and 3 in Fig. 19b). Resistivity values measured along all three lines are similar to those of the normal values for common sediments and sedimentary rocks, and again the results indicate that sand, gravel, and alluvial sediments possibly overlie Triassic sandstones. The fractures or faults can be determined from the discontinuities in resistivity values in the horizontal layers. Thus, positions 16 and 23 m on investigation line no. 1 are interpreted as fractures or faults. For line no. 2, fractures or faults can be put at positions 22, 40, 52, and 72 m, and for line no. 3, the fractures or faults can be put at positions 22, 32, and 60 m.

Figure 31 shows the results of resistivity investigations across the Mok Chum Pae segment (resistivity investigation line nos 1, 2, and 3 in Fig. 20b). Resistivity values measured along all three lines are similar to those of the normal values for common sediments and sedimentary rocks. The results indicate that sand, gravel, and alluvial sediments possibly overlie Paleozoic sandstones. The positions of fractures or faults can be

determined using the discontinuity of resistivity values in the horizontal layers. Thus, positions 64 and 68 m on line no. 1 are interpreted to be fractures or faults. For the resistivity investigation of line no. 2, an electrode spacing of 1 m was used from points 40 to 90 m, and fractures or faults can be put in at positions 64, 71, 78, and 82 m. The resistivity investigation of line no. 3 suggests fractures or faults at positions 36 and 70 m.

Table 7. Resistivities of some geological materials [Reynolds, 2011]

Material	**Nominal resistivity (Ωm)**
Sulphides:	
Chalcopyrite	1.2×10^{-5}–3×10^{-1}
Pyrite	2.9×10^{-5}–1.5
Galena	3.0×10^{-5}–3×10^{2}
Oxides:	
Haematite	3.5×10^{-3}–10^{7}
Limonite	10^{3}–10^{7}
Magnetite	5×10^{-5}–5.7×10^{3}
Ilmenite	10^{3}–50
Quartz	300–10^{6}
Rock salt	30–10^{13}
Granite	300–1.3 × 106
Granite (weathered)	30–500
Diorite	10^{4}–10^{5}
Basalt	10–1.3×10^{7}
Schist (calcareous and micaceous)	20–10^{4}
Slates	600–4×10^{7}
Marble	100–2.5×10^{8}
Consolidated shales	20–2000
Sandstones	1–7.4×10^{8}
Limestones	50–10^{7}
Clays	1–100
Alluvium and sand	10–800
Quaternary/Recent sands	50–100
Topsoil	270–1700
Sand and gravel	30–225
Dry sandy soil	80–1050
Sand clay/clayey sand	30–215
Gravel (dry)	1400
Gravel (saturated)	100

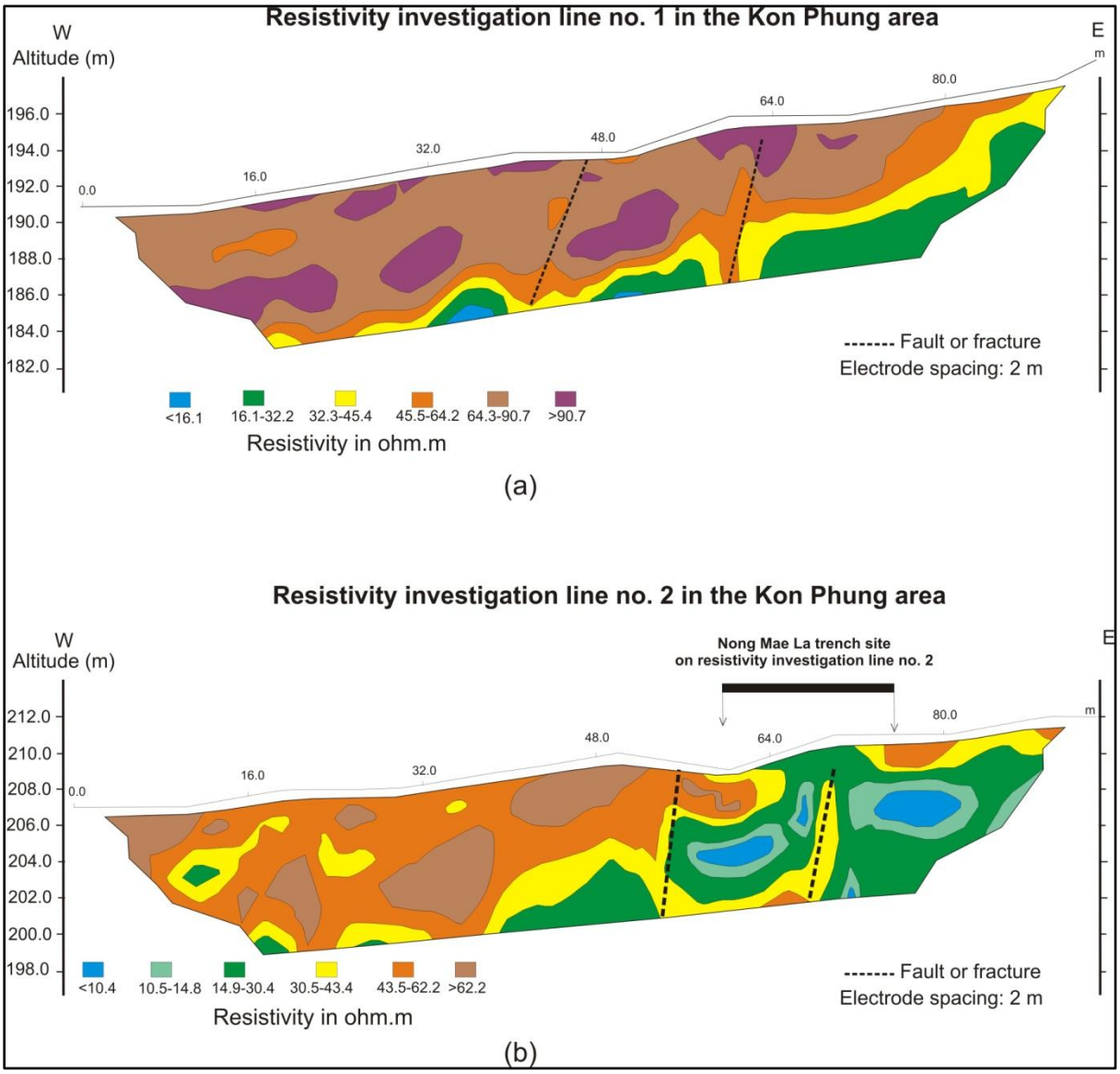

Fig. 29. Resistivity results in the Kon Phung area showing the locations of faults or fractures at positions 47 and 64 m along investigation line no. 1 (a), and at positions 56 and 72 m on investigation line no. 2 (b). The results of the resistivity investigations indicate that the faults cut through Quaternary sediments in this area. The locations of the survey lines are shown in Fig. 18b. The location of the Nong Mae La trench is indicated in Figs 9c and 18b, and is shown by a dark bar on resistivity investigation line no. 2.

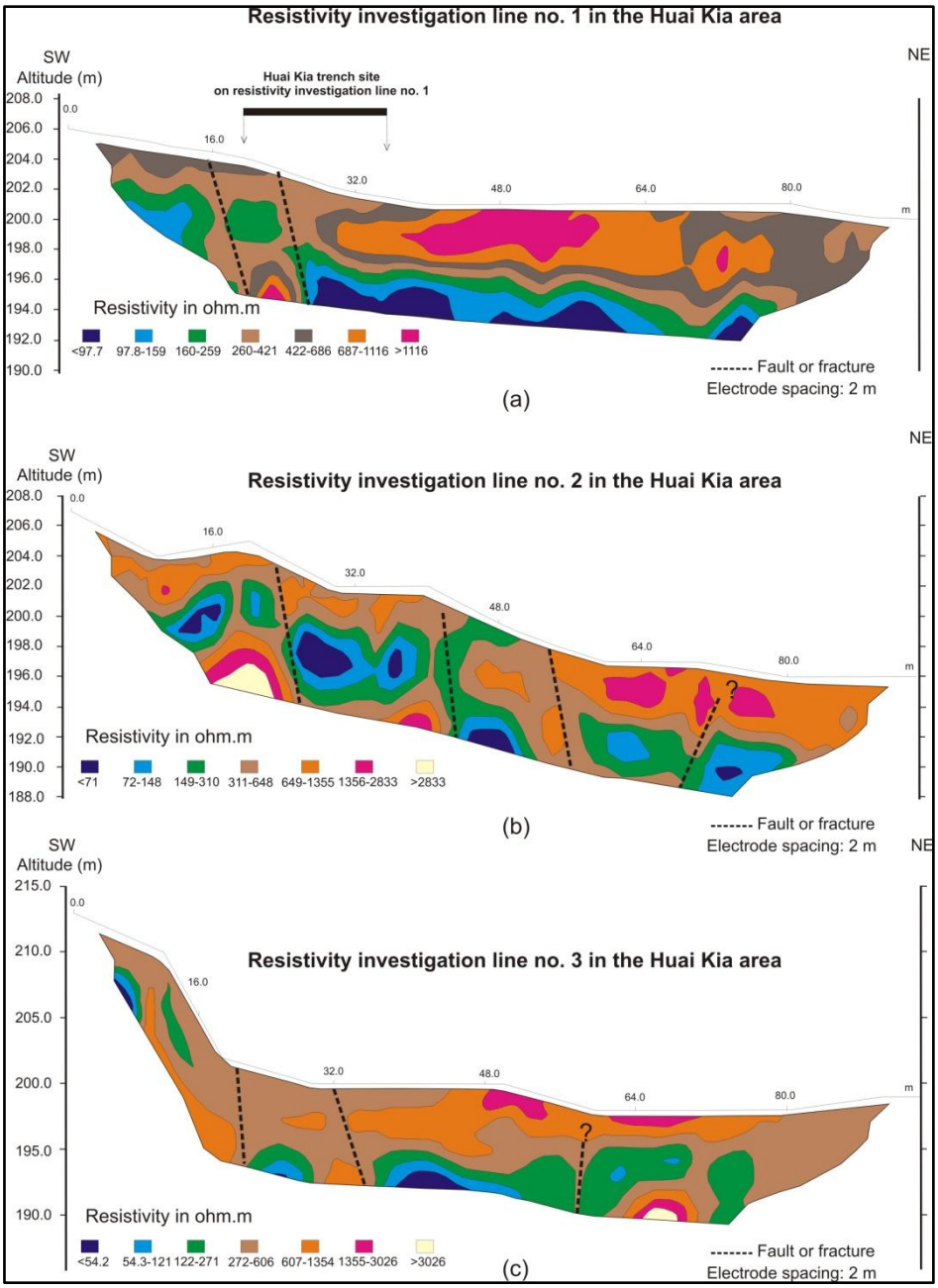

Fig. 30. Resistivity results in the Huai Kia area showing the locations of faults or fractures at positions 16 and 23 m on investigation line no. 1 (a), at positions 22, 40, 52, and 72 m on investigation line no. 2 (b), and at positions 22, 32, and 60 m on investigation line no. 3 (c). The results of the resistivity investigations indicate that the faults cut through the Quaternary sediments in this area. The locations of the survey lines are shown in Fig. 19b. The location of the Huai Kia trench is indicated in Figs 9c and 19b, and is shown by a dark bar on resistivity investigation line no. 1.

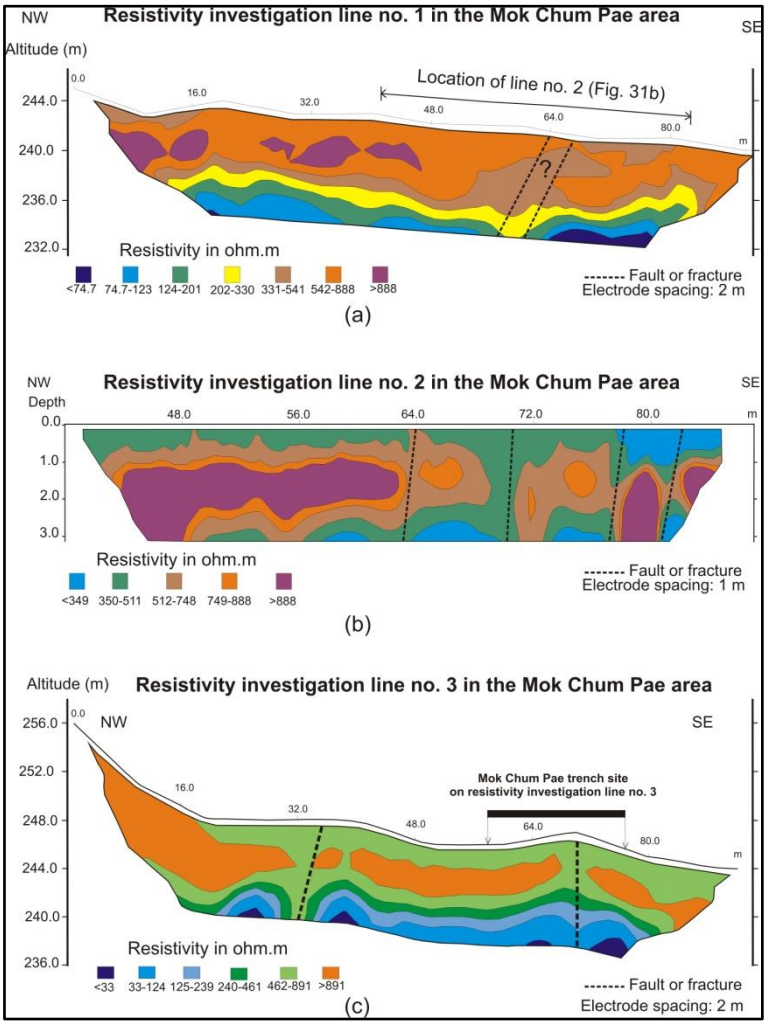

Fig. 31. Resistivity results in the Mok Chum Pae area showing the locations of faults or fractures at positions 64 and 68 m on investigation line no. 1 (a), and at positions 36 and 70 m on investigation line no. 3 (c). Positions from 40 to 90 m on survey line no. 1 were selected for detailed resistivity investigations (1 m electrode spacing), and the results indicate fractures or faults at positions 64, 71, 78, and 82 m (b). The results of the resistivity investigations indicate that the faults cut through the Quaternary sediments in this area. The locations of the survey lines are shown in Fig. 20b. The location of the Mok Chum Pae trench is indicated in Figs 9c and 20b, and is shown by a dark bar on resistivity investigation line no. 3.

7. Results of paleoearthquake investigations

Evidences of offset stratigraphic units of Quaternary sediments and deformed sediment layers recorded in the road cut, quarry and trenching are the most important data for interpreting the faulting events. Therefore, quarry and trenching studies across the fault segments of the Mae Hong Son and Thoen Faults are selected for a paleoearthquake study. Details of this study are shown below.

7.1. Paloearthquake investigations of the Mae Hon Son Fault

Three trenches, one quarry, and one road-cut exposure were examined for a paleoearthquake study (see Fig. 9c), based on the integration of results from remote sensing interpretations, geophysical investigations, digital elevation models, geological maps, and field studies. The quarry traverses the NE–SW Mae La Noi segment no. 1, and the road-cut exposure traverses the NE–SW Phra That Chom Kitti segment. The first of the three excavated trenches traversed the N–S Nong Mae La segment, the second trench traversed the NW–SE Huai Kia segment no. 1, and the third traversed the NE–SW Mok Chum Pae segment. All segments are parts of the Mae Hong Son Fault.

7.1.1. Mae La Noi segment no. 1

Significant morphotectonic landforms, such as offset streams and scarps, are present in the Mae La Noi area (Figs 13 and 14). Quaternary faults in the quarry (for location, see Fig. 14b; 18°22'17.40"N, 97°56'11.74"E) adjacent to the Mae La Noi School cut Cenozoic strata (terrace sediments, Qt, of Chindasut *et al.* [1990]). Two reverse faults are visible in the quarry wall (F1 and F2; Fig. 32); the faults strike N0°E–N40°E and dip 85°E–70°SE. Slickensides can be observed on fault planes (Fig. 33a and b) with pitches of 15° (on the F1 fault plane)

and 60°(F2) (Fig. 33c). Based on their sedimentological characteristics, the stratigraphy of the quarry wall can be described in terms of nine unconsolidated units; units A to I (Fig. 32).

Unit A, which is the oldest in the quarry, is an alluvial unit with a thickness of greater than 6 m; the unit is a clast-supported gravel consisting mainly of gravel, sand, and clay. The gravel clasts are mainly subangular to rounded in shape (maximum diameter, *ca.*15 cm), and consist mostly of quartz, sandstone, granite, and shale.

Unit B is an alluvial unit consisting of light brown clay and sand layers, and with a thickness ranging from 1 to 3 m. Clasts of iron concretions, quartz, and shale are found in the unit.

Unit C is an alluvial/colluvial unit containing gravel and sand lenses; it is 2 m thick and consists of a clast-supported river gravel unit. The gravel clasts are mainly subangular to rounded in shape (maximum diameter, *ca*. 10 cm) and consist mostly of quartz, sandstone, granite, and shale. Graded beds of 30–50 cm thickness are intercalated in the unit, and coarse to very coarse grained sand lenses are present in the middle part of the unit.

Unit D is an alluvial unit comprising light brown sandy clay with small amounts of gravel; its thickness is 30 cm. Most of the gravel clasts are of pebble size and consist of sandstone and quartz.

Unit E is an alluvial unit consisting of reddish-brown clayey sand and gravel. The unit is *ca*. 50–70 cm thick. Most clasts are subrounded and consist of sandstone, shale, and quartz.

Unit F is an alluvial/colluvial unit consisting mostly of sand, silt, and clay, and gravel. This unit is clast-supported and consists of subangular to rounded clasts of quartz, sandstone, and shale (maximum diameter, *ca.* 5 cm). The thickness of the unit ranges from 50 cm to 2 m.

Unit G is an alluvial/colluvial complex with a thickness of 2–2.5 m; it consists mainly of reddish-brown sandy clay and minor amounts of gravel. Most of the clasts are subangular

to subrounded, and consist of sandstone, shale, and quartz (maximum diameter, *ca*. 3 cm). The upper part of unit G is not cut by faulting (X3 in Fig. 32a and c).

Unit H is a clast-supported colluvial unit characterized by gravel and sand. Most clasts in the unit are subangular to subrounded (maximum diameter, *ca*. 5 cm) and the sediments consist of quartz, sandstone, and shale. The unit is approximately 50 cm to 1 m thick.

Unit I is a top soil consisting of sand and silt with a few gravel beds. Plant roots and debris with organic matter are common in the unit, and are somewhat disturbed by human activity. The unit is *ca*. 20 cm to 1 m thick.

Overall, the grain sizes of sediments in the quarry range from clay to cobble. The sediments in the clast-supported gravel units (units A, C, F, and H) are moderately to poorly sorted. Clasts in the gravel layers are subangular to rounded; they are randomly oriented, with some elongate gravel clasts oriented with their long axes at a high angle to bedding. The sedimentary structures suggest that the gravel units were deposited by clast-rich debris flows. Sediments of clast-rich debris flow origin are typically very poorly sorted, and with clast-supported gravels within a fine-grained matrix [Larsen and Steel, 1978; Steel and Gloppen, 1980]. Matrix-supported (i.e., matrix-rich) gravels deposited by debris flows have been reported in India by Shukha [2009] and in northern Thailand by Rhodes *et al.* [2005]. The sediments in the matrix-supported gravel units (units B, D, E, and G) are poorly sorted and consist of mixed sand, silt, clay, and gravel. The sedimentary structures suggest that these units were deposited by matrix-rich debris flows.

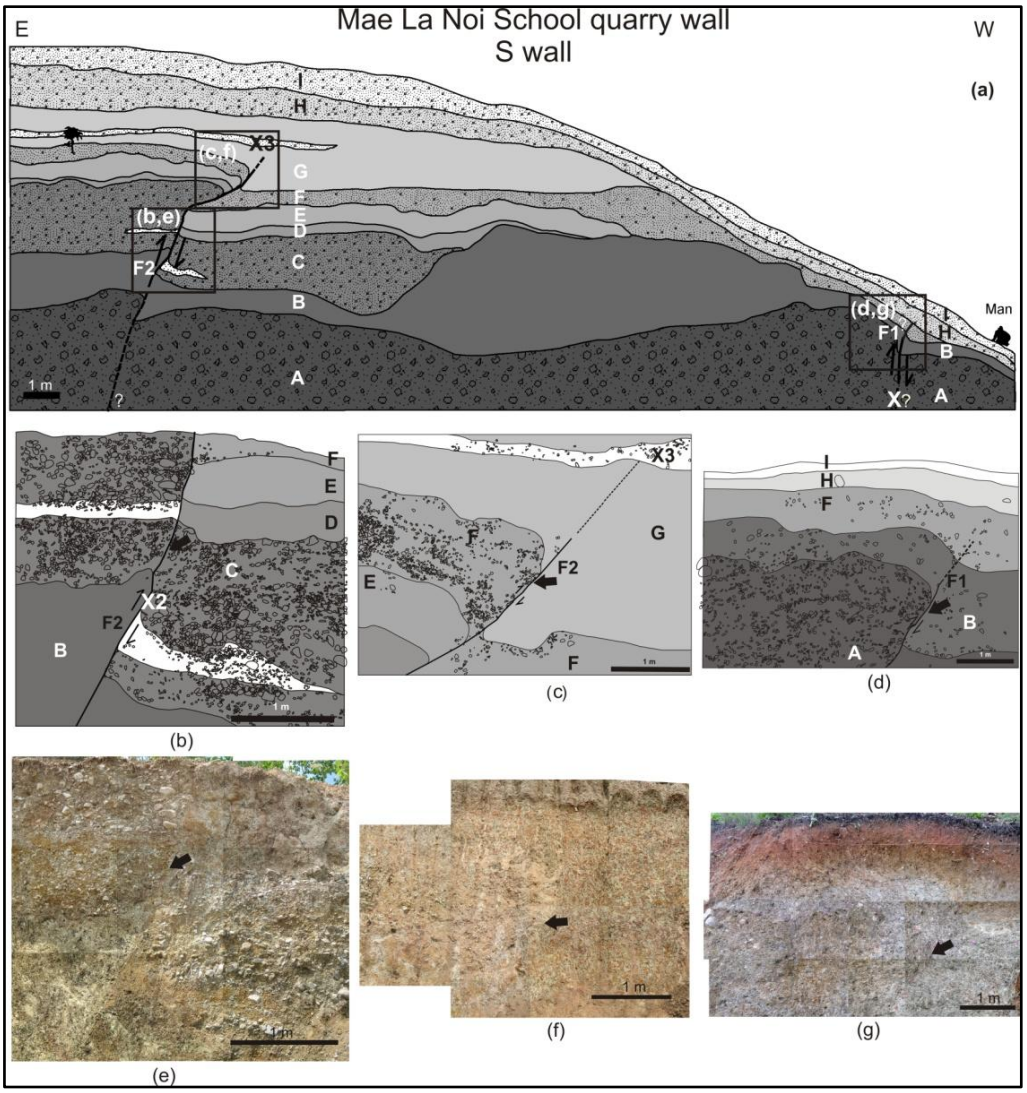

Fig. 32. Stratigraphic units of Quaternary sediments along an E–W transect in the Mae La Noi School quarry (a–d). Close-up photographs of plates b, c, and d are presented in plates e, f, and g, respectively. The faults identified in the quarry wall are F1 and F2. Black arrows indicate fault traces and half arrows show sense of movement. The location of the quarry is shown in Figs 13b and 14b. Unit A: gravel sand and clay; Unit B: clay and sand; Unit C: gravel, sand, clay, with sand lens; Unit D: sandy clay with gravel; Unit E: clayey sand with gravel; Unit F: gravel, sand, and clay; Unit G: sandy clay with gravel; Unit H: gravel and sand, and Unit I: top soil. The points marked “X” and “X2” indicate the locations of slickensides on fault planes. The point marked “X3” indicates the location where the fault terminates in unit G.

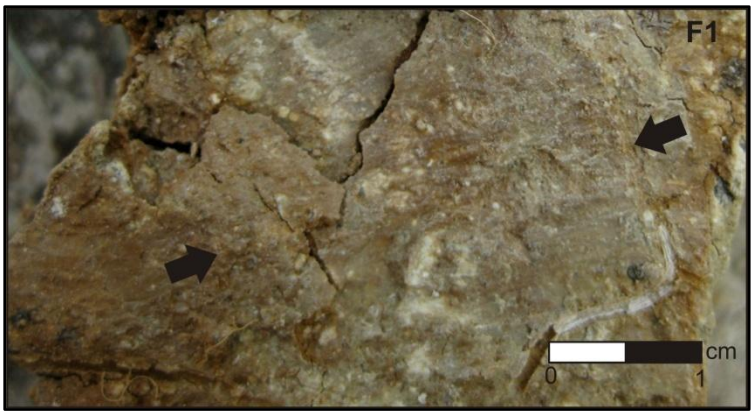

(a)

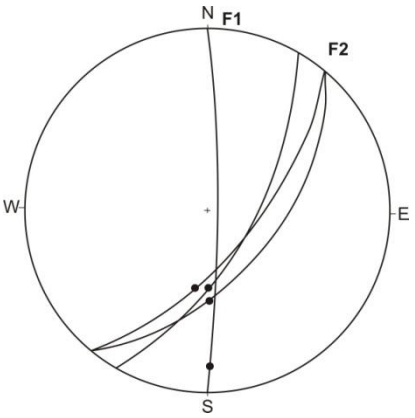

(c)

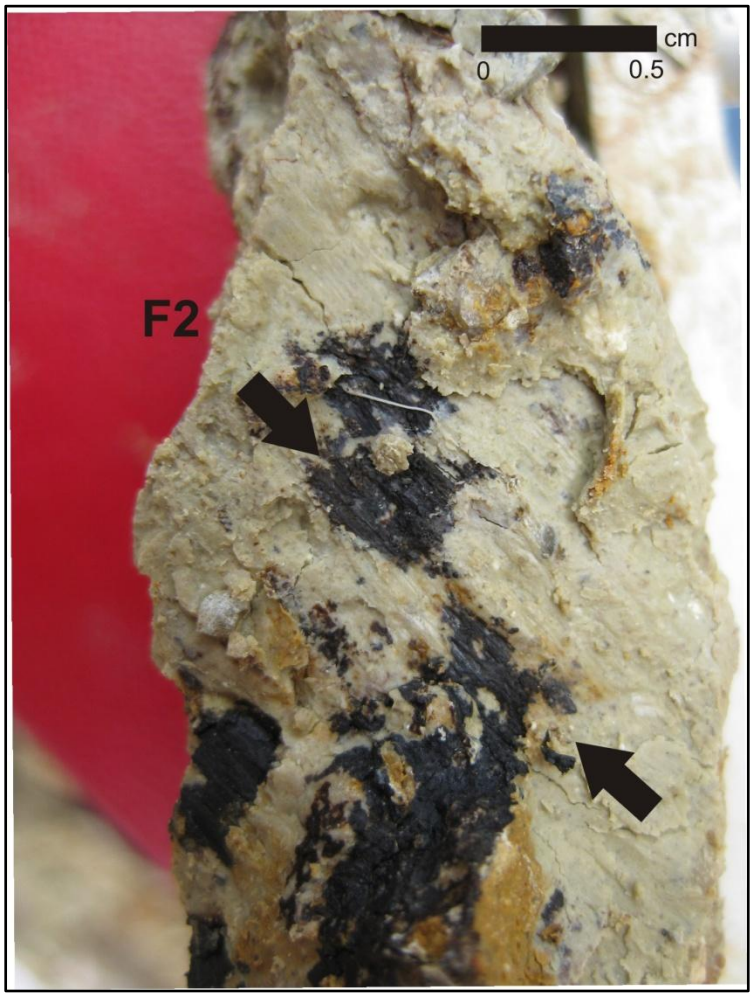

(b)

Fig. 33. Photographs showing slickensides (black arrows) on fault planes at Mae La Noi School quarry. (a) Slickensides resulting from movement on F1 in Fig. 32. (b) Slickensides resulting from movement on F2 in Fig. 32. (c) Stereonet showing the orientations of fault planes and their pitches. Slickensides on the fault plane of F1 can be observed at the point marked "X" in Fig. 32a, while slickensides on the fault plane of F2 can be observed at the point marked "X2" in Fig. 32b.

7.1.2. Phra That Chom Kitti segment

Quaternary faults cutting Cenozoic terrace deposits (Qt of Bunkanpai [2005]) have been observed at the road cut on the road to the pagoda of Phra That Chom Kitti temple (location shown in Figs 15 and 16; 18°08'47.26"N, 97°55'08.55"E). The mapped faults (F1–F4 in Fig. 34) strike N50°E–N72°E and dip 70°NW–80°SE. The Quaternary stratigraphy and structural geology of the road-cut wall are depicted in Fig. 34b; the identification of units and structures was based on field data and sedimentological characteristics of the strata.

Unit A, the oldest unit in the road cut, is an alluvial unit consisting mainly of moderately sorted, brown to yellowish very fine to coarse sand. The minimum thickness of the unit is 1.5 m.

Unit B is an alluvial unit consisting of silty clay and clasts of feldspar and quartz. The thickness of the unit ranges from 50 cm to 1 m.

Unit C is an alluvial/colluvial unit containing brown to yellowish sand with gravel. Grain sizes range from very coarse to fine sand. Most clasts are angular to subrounded, pebble sized, and comprised of sandstone and quartz. Thin layer of Fe oxide serves as a marker for the contact between unit C and the overlying unit D. The thickness of the unit ranges from 50 cm to 1.2 m.

Unit D, with an average thickness of 80 cm, is an alluvial unit comprised of light brown to yellowish sand. Grain sizes vary from coarse to fine sand; pebbles of quartz and sandstone are sparsely distributed in the unit.

Unit E, with an average thickness of 2 m, is an alluvial unit comprised of clayey sand and sandy clay with minor gravel. The lower part consists principally of clay and sand; gravels are sparsely distributed in the upper part.

Unit F, with an average thickness of 2.5 m, is an alluvial unit comprised of gravel, sand, and clay. The gravel beds in unit F are clast-supported. The gravel clasts are mainly

subrounded to rounded and consist mostly of quartz, sandstone, and shale; their maximum diameter is *ca*. 6 cm. Sand layers are prominent in the unit. The unit consists of intercalated graded beds with thicknesses of 30–50 cm.

Unit G is a 30-cm thick colluviul/alluvial complex consisting of poorly sorted gravels and sands. Most clasts are subangular to rounded (maximum diameter, *ca*. 4 mm), and are comprised of quartz, sandstone, and shale.

Unit H, the youngest units, is the topmost soil layer; it is approximately 10 cm thick and consists of organic rich silt/clay with some gravel and sand.

The sediments of units B and E are chiefly clay and silt with minor sand; they are considered to represent fluviolacustrine environments. The sediments of units A, C, D, and G are poorly sorted and subangular, and are characterized by mixtures of sand, silt, clay, and gravel. The geometries of the sedimentary packages and structures indicate that these units were possibly deposited by matrix-rich debris flow, similar to those reported by Shukha [2009] and Rhodes *et al.* [2005]. The clast-supported gravel of unit F, however, contains mostly subrounded clasts, and the sediments are poorly to moderately sorted; graded beds have been encountered in this unit. The sediments of unit F were possibly deposited by clast-rich debris flows similar to those reported by Larsen and Steel [1978], Steel and Gloppen [1980], and Rhodes *et al.* [2005], as well as by occasional channel flood deposits.

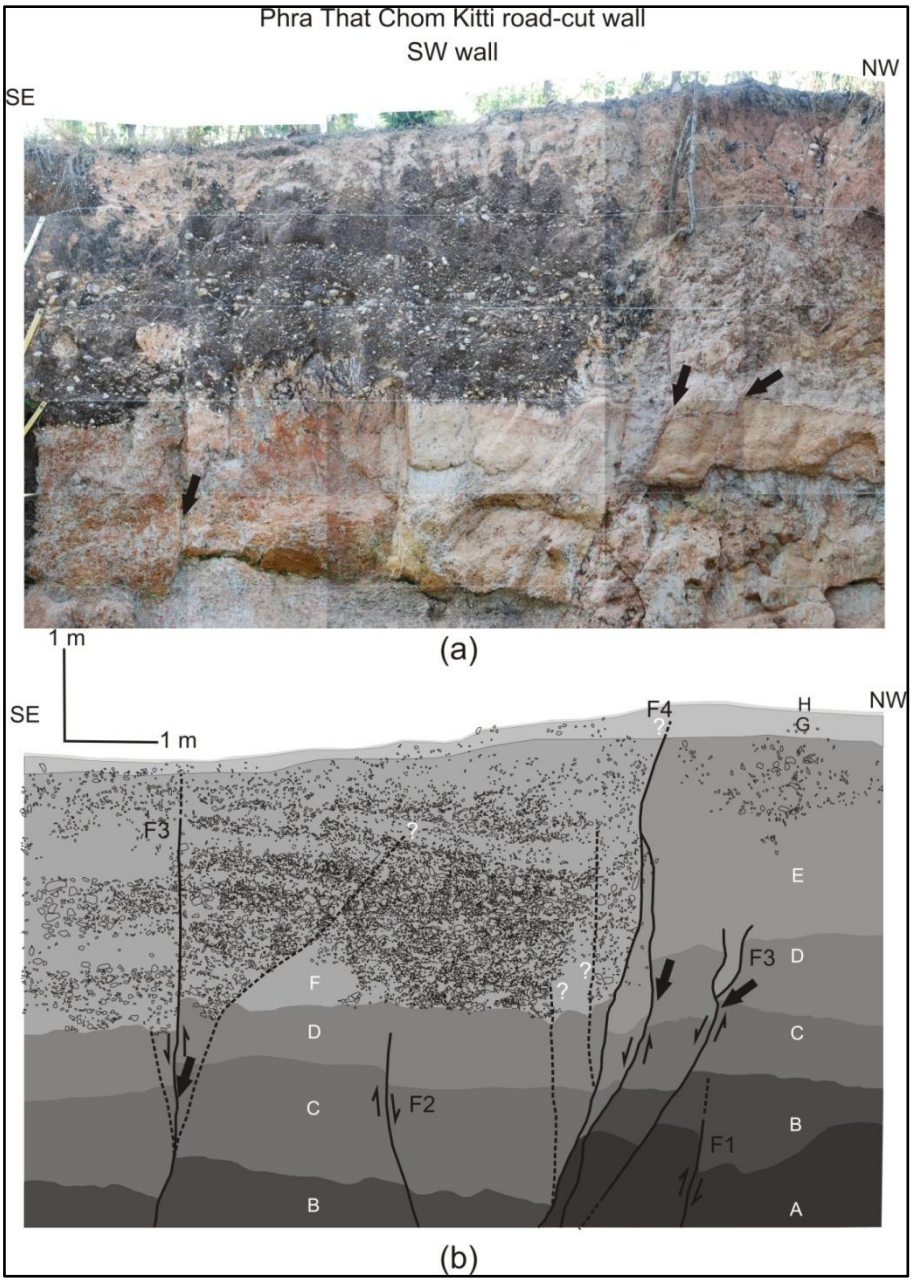

Fig. 34. Stratigraphic units of Quaternary sediments along the SE–NW transect in the Phra That Chom Kitti road-cut exposure (a–b). Faults identified in the road-cut wall are F1–F4. Black arrows indicate fault traces and half arrows show the sense of movement. The location of the wall is shown in Figs 15b and 16b. Unit A: brown to yellowish sand; Unit B: clay with clasts of feldspar and quartz; Unit C: brown to yellowish sand with gravel; Unit D: light brown to yellowish sand; Unit E: clay, sand and with some gravel; Unit F: gravel, sand, and clay; Unit G: gravel with sand; Unit H: top soil.

7.1.3. Nong Mae La segment

A trench at Ban Nong Mae La (Kon Phung area) across the Nong Mae La segment of the Mae Hong Son Fault was selected for a paleoearthquake study (Nong Mae La trench in Fig. 18b; 18°03'48.11"N, 97°56'04.03"E) on the basis of morphotectonic landforms, detailed topographical and geological maps, and geophysical data (radon and resistivity results). The excavated trench was 20 m long, 2 m wide, and 4 m deep, and the sediments exposed can be divided into seven unconsolidated units (excluding sandstone and shale of the basement rock unit). The sediments are exposed in both sidewalls. The fault can be observed in the basement rock unit, unit A, and the lower–middle parts of unit B (F1 in Figs 35 and 36; strike N5°E and dip 40° NW). However, the younger sediments (i.e., upper part of unit B and units C–G) in this trench are laterally continuous, and no faults were observed to cut these layers. A detailed trench log is shown in Figs 35 and 36. Details of the individual units are described below.

Unit A is a clast-supported colluvial unit characterized by gravel and sand. Most clasts in the unit are subangular to subrounded (maximum diameter, *ca*. 10 cm), and the sediments consist of quartz grains, sandstone, and shale. The unit is approximately 20–80 cm thick.

Unit B is an alluvial unit composed of reddish-brown sandy clay with small amounts of iron-rich concretions; its thickness is approximately 20 cm to 1 m.

Unit C is an alluvial unit consisting of reddish-brown sandy clay and gravel. The unit is *ca*. 10–60 cm thick. Most clasts are subrounded and consist of sandstone, shale, and quartz grains.

Unit D is an alluvial unit consisting of reddish-brown sandy clay and gravel. The unit is *ca*. 50 cm to 1.3 m thick. Most clasts are subrounded and consist of sandstone, shale, iron-rich concretions, and quartz grains.

Unit E is an alluvial unit consisting of reddish-brown clayey sand and gravel. The unit is *ca*. 50 cm to 1 m thick. Most clasts are subrounded and consist of sandstone, shale, and quartz grains.

Unit F is an alluvial unit consisting of reddish-brown clayey sand with small amounts of gravel. Most clasts in the unit are subangular to subrounded (maximum diameter, *ca*. 5 cm), and the sediments consist of quartz grains, sandstone, and shale. The unit is approximately 50 cm to 1 m thick.

Unit G, the youngest unit, is the topmost soil layer; it is approximately 10–25 cm thick, and consists of an organic rich silt/clay with some gravel and sand.

The sediments of units B–F are poorly sorted and subangular to subrounded, and are characterized by mixtures of sand, silt, clay, and gravel. The geometries of the sedimentary packages and structures indicate that these units were possibly deposited by matrix-rich debris flows, similar to those reported by Shukha [2009] and Rhodes *et al.* [2005]. However, the clast-supported gravel of unit A contains mostly subangular to subrounded clasts, and the sediments are poorly to moderately sorted. The sediments of unit A were possibly deposited by clast-rich debris flows similar to those reported by Larsen and Steel [1978] and Steel and Gloppen [1980].

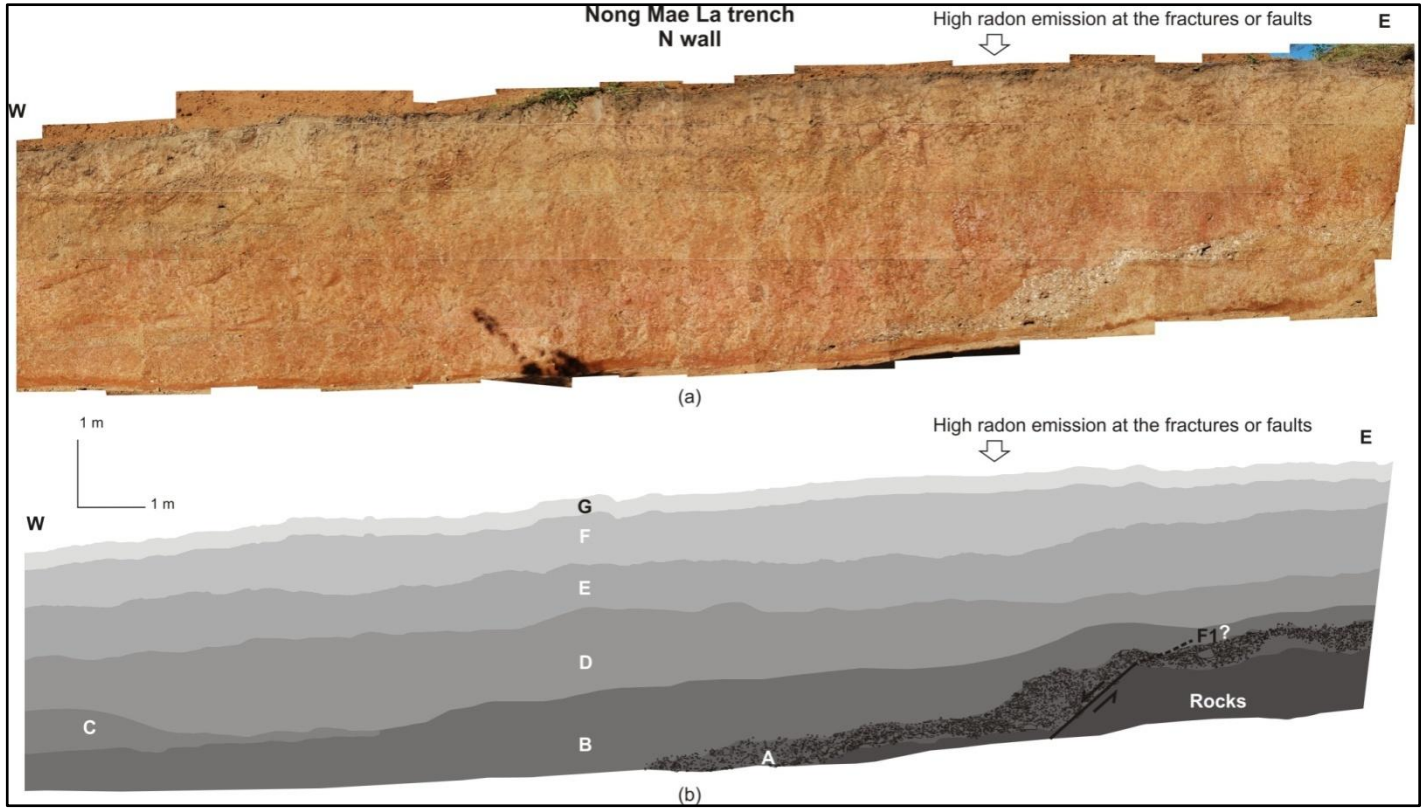

Fig. 35. Stratigraphic units of the Quaternary sediments along the north wall of the Nong Mae La trench (a–b). Fault indentified in the trench wall is F1.The location of the wall is shown in Fig. 18b. Unit A: gravel and sand; Unit B: reddish-brown sandy clay; Unit C: reddish-brown sandy clay and gravel; Unit D: reddish-brown sandy clay and gravel with clasts of iron-rich concretions; Unit E: reddish-brown clayey sand and gravel; Unit F: reddish-brown clayey sand with small amounts of gravel; Unit G: top soil.

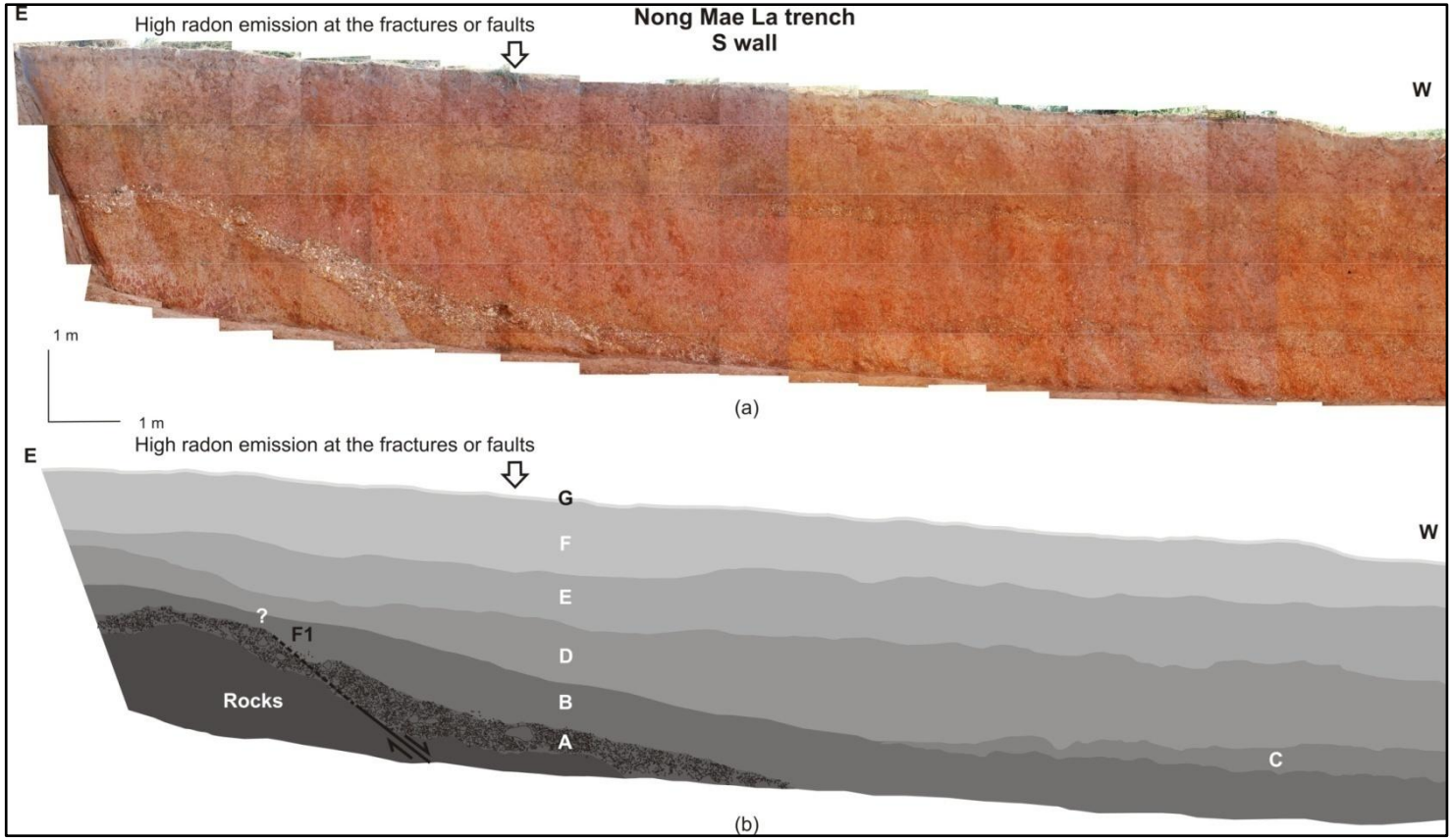

Fig. 36. Stratigraphic units of the Quaternary sediments along the south wall of the Nong Mae La trench (a–b). Fault indentified in the trench wall is F1.The location of the wall is shown in Fig. 18b. Unit A: gravel and sand; Unit B: reddish-brown sandy clay; Unit C: reddish-brown sandy clay and gravel; Unit D: reddish-brown sandy clay and gravel with clasts of iron-rich concretions; Unit E: reddish-brown clayey sand and gravel; Unit F: reddish-brown clayey sand with small amounts of gravel; Unit G: top soil.

7.1.4. Huai Kia segment no. 1

A trench at Ban Huai Kia across Huai Kia segment no. 1 of the Mae Hong Son Fault was selected for a paleoearthquake study (Huai Kia trench in Fig. 19b; 18°00'55.65"N, 97°54'34.25"E) on the basis of morphotectonic landforms, detailed topographical and geological maps, and geophysical data (radon and resistivity results). The excavated trench was 24 m long, 2 m wide, and 4 m deep, and the sediments exposed can be divided into six unconsolidated units, visible in both sidewalls. The sediments in this trench are laterally continuous, and no faults were observed cutting them. A detailed trench log is shown in Figs 37 and 38. Details of the individual units are described below.

Unit A, with a minimum thickness of 1 m, is an alluvial unit composed of gravel, sand, and clay. The gravel beds in unit A are clast-supported. The gravel clasts are mainly subrounded to rounded, and consist mostly of quartz, sandstone, and shale; the maximum clast diameter is *ca*. 6 cm.

Unit B is an alluvial unit consisting of reddish-brown to gray sandy clay with a little gravel. The unit is *ca*. 40 cm to 1.50 m thick. Most clasts are subrounded and consist of sandstone, shale, and quartz.

Unit C is an alluvial/colluvial unit consisting mostly of sand, silt, clay, and gravel. This unit is made up of subangular to rounded clasts of quartz, sandstone, and shale (maximum diameter, *ca.* 4 cm). The thickness of the unit ranges from 20 to 80 cm.

Unit D is an alluvial unit consisting of reddish-brown sandy clay with a little gravel. The unit is *ca*. 10–80 cm thick. Most clasts are subrounded and consist of sandstone, shale, and quartz.

Unit E is an alluvial/colluvial unit consisting of gravel and sand. Most clasts in the unit are subangular to subrounded (maximum diameter, *ca*. 4 cm) and consist of quartz, sandstone, and shale. The unit is approximately 50 cm to 1 m thick.

Unit F, the youngest unit, is the topmost soil layer; it is approximately 40 cm thick and consists of an organic rich silt/clay with some gravel and sand.

The sediments of units B–E are poorly sorted and subangular to rounded, and are characterized by mixtures of sand, silt, clay, and gravel. The geometries of the sedimentary packages and structures indicate they were possibly deposited by matrix-rich debris flows, similar to those reported by Shukha [2009] and Rhodes *et al.* [2005]. The clast-supported gravel of unit A, however, contains mostly subangular to subrounded clasts, and the sediments are poorly to moderately sorted. The sediments of unit A were possibly deposited by clast-rich debris flows similar to those reported by Larsen and Steel [1978] and Steel and Gloppen [1980].

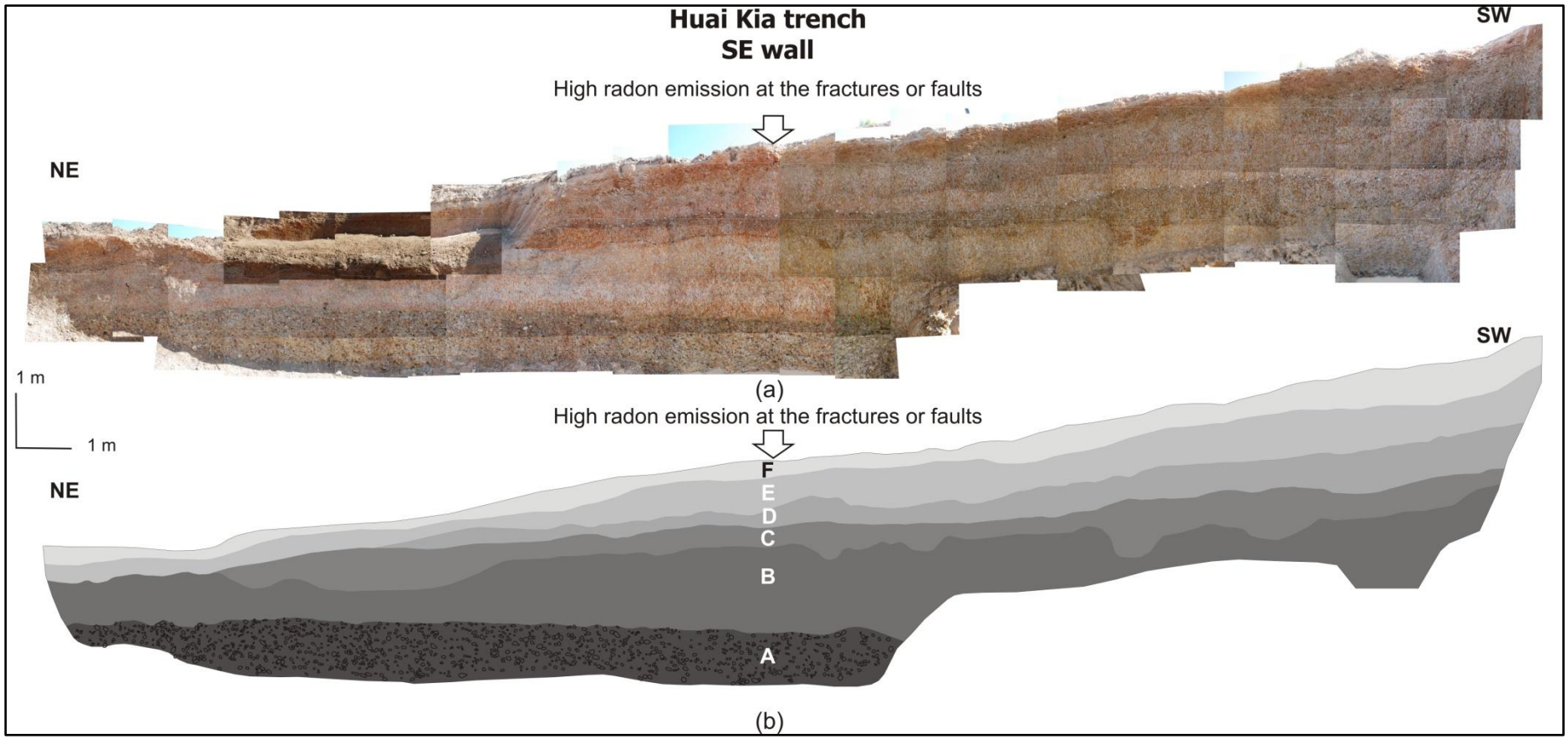

Fig. 37. Stratigraphic units of the Quaternary sediments along the southeast wall of the Huai Kia trench (a–b). The location of the wall is shown in Fig. 19b. Unit A: gravel, sand, and clay; Unit B: reddish-brown to gray sandy clay with a little gravel; Unit C: sand, silt, clay, and gravel; Unit D: reddish-brown sandy clay with a little gravel; Unit E: gravel and sand; Unit F: top soil.

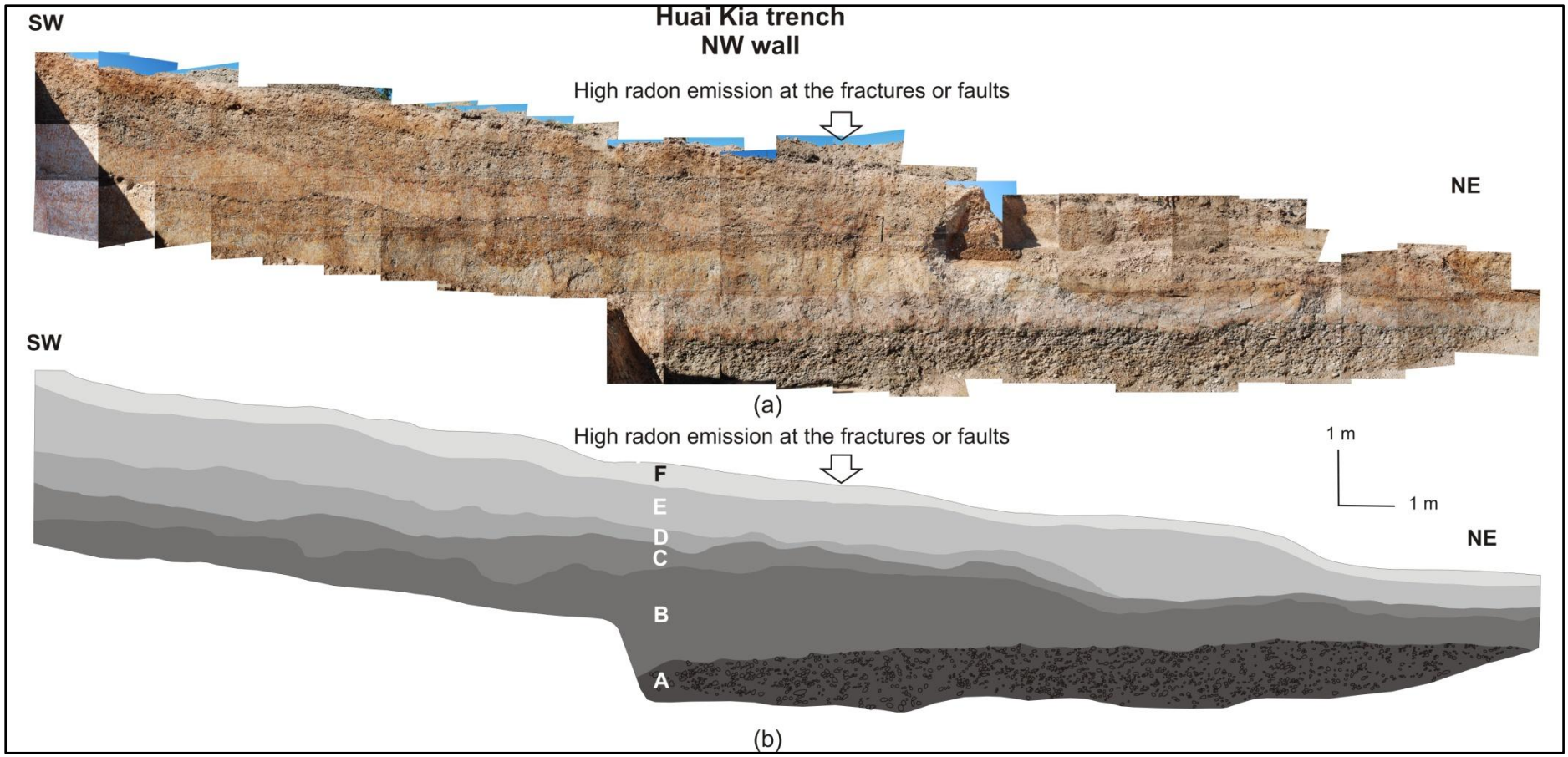

Fig. 38. Stratigraphic units of the Quaternary sediments along the northwest wall of the Huai Kia trench (a–b). The location of the wall is shown in Fig. 19b. Unit A: gravel, sand, and clay; Unit B: reddish-brown to gray sandy clay with a little gravel; Unit C: sand, silt, clay, and gravel; Unit D: reddish-brown sandy clay with a little gravel; Unit E: gravel and sand; Unit F: top soil.

7.1.5. Mok Chum Pae segment

A trench at Ban Mok Chum Pae across the Mok Chum Pae segment of the Mae Hong Son Fault was selected for a paleoearthquake study (Mok Chum Pae trench in Fig. 20b; 19°25'41.19"N, 97°57'25.07"E) on the basis of morphotectonic landforms, detailed topographical and geological maps, and geophysical data (radon and resistivity results). The excavated trench was 22 m long, 3 m wide, and 4 m deep. The sediments exposed in the trench can be divided into six unconsolidated units (excluding sandstone and shale of the basement rock unit), and these sediments are exposed in both sidewalls. The mapped faults (F1 and F2 in Figs 39 and 40) strike N40°E and dip between 50° NW and 80° SE. A detailed trench log is shown in Figs 39 and 40. Details of the individual units are described below.

Unit A, with an average thickness of 20–80 cm, is an alluvial unit composed of gravel, sand, and clay. The unit is clast-supported and consists of subrounded to rounded clasts of quartz, sandstone, and shale (maximum diameter, *ca.*15 cm).

Unit B is an alluvial unit consisting of yellowish-brown to light gray clayey sand with a little gravel. The unit is *ca*. 20–80 cm thick. Most clasts are subrounded and consist of sandstone, shale, and quartz.

Unit C is an alluvial unit composed of gravel, sand, and clay. The gravel clasts are mainly subrounded to rounded, and consist mostly of quartz, sandstone, and shale (maximum diameter, *ca*. 5 cm). The unit is *ca*. 10 cm to 1 m thick.

Unit D is an alluvial unit composed of gravel, sand, and clay. This unit is clast-supported and consists of subangular to rounded clasts of quartz, sandstone, and shale (maximum diameter, *ca.* 5 cm). Lateritic textures can be observed in this unit. The unit is *ca*. 1–1.8 m thick.

Unit E is a clast-supported colluvial unit characterized by gravel and sand. Most clasts in the unit are subangular to subrounded (maximum diameter, *ca*. 10 cm), and the sediments consist of quartz, sandstone, and shale. The unit is approximately 1 m thick.

Unit F, the youngest unit, is the topmost soil layer; it is approximately 10–20 cm thick and consists of an organic rich silt/clay with some gravel and sand.

The sediments of units B and C are poorly sorted and subrounded to rounded, and are characterized by mixtures of sand, silt, clay, and gravel. The geometries of the sedimentary packages and structures indicate that these units were possibly deposited by matrix-rich debris flows, similar to those reported by Shukha [2009] and Rhodes *et al.* [2005]. However, the clast-supported gravels of units A, D, and E mostly contain subangular to subrounded clasts, and the sediments are poorly to moderately sorted. The sediments of units A, D, and E were possibly deposited by clast-rich debris flows similar to those reported by Larsen and Steel [1978] and Steel and Gloppen [1980].

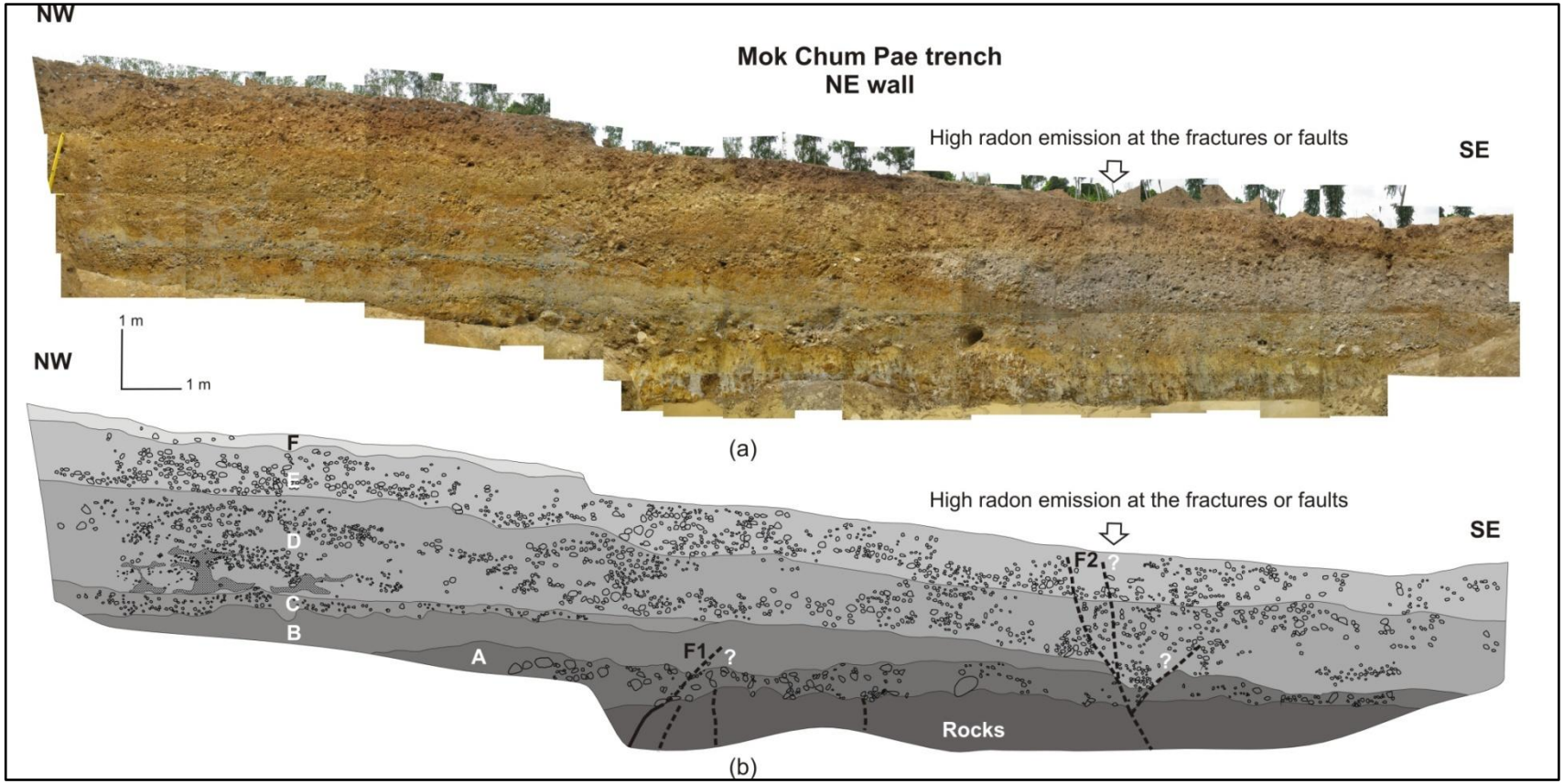

Fig. 39. Stratigraphic units of the Quaternary sediments along the northeast wall of the Mok Chum Pae trench (a–b). Faults indentified in the trench wall are F1 and F2. The location of the wall is shown in Fig. 20b. Unit A: gravel, sand, and clay; Unit B: yellowish-brown to light gray clayey sand with a little gravel; Unit C: gravel, sand, and clay; Unit D: gravel, sand, and clay with a lateritic texture; Unit E: gravel and sand; Unit F: top soil.

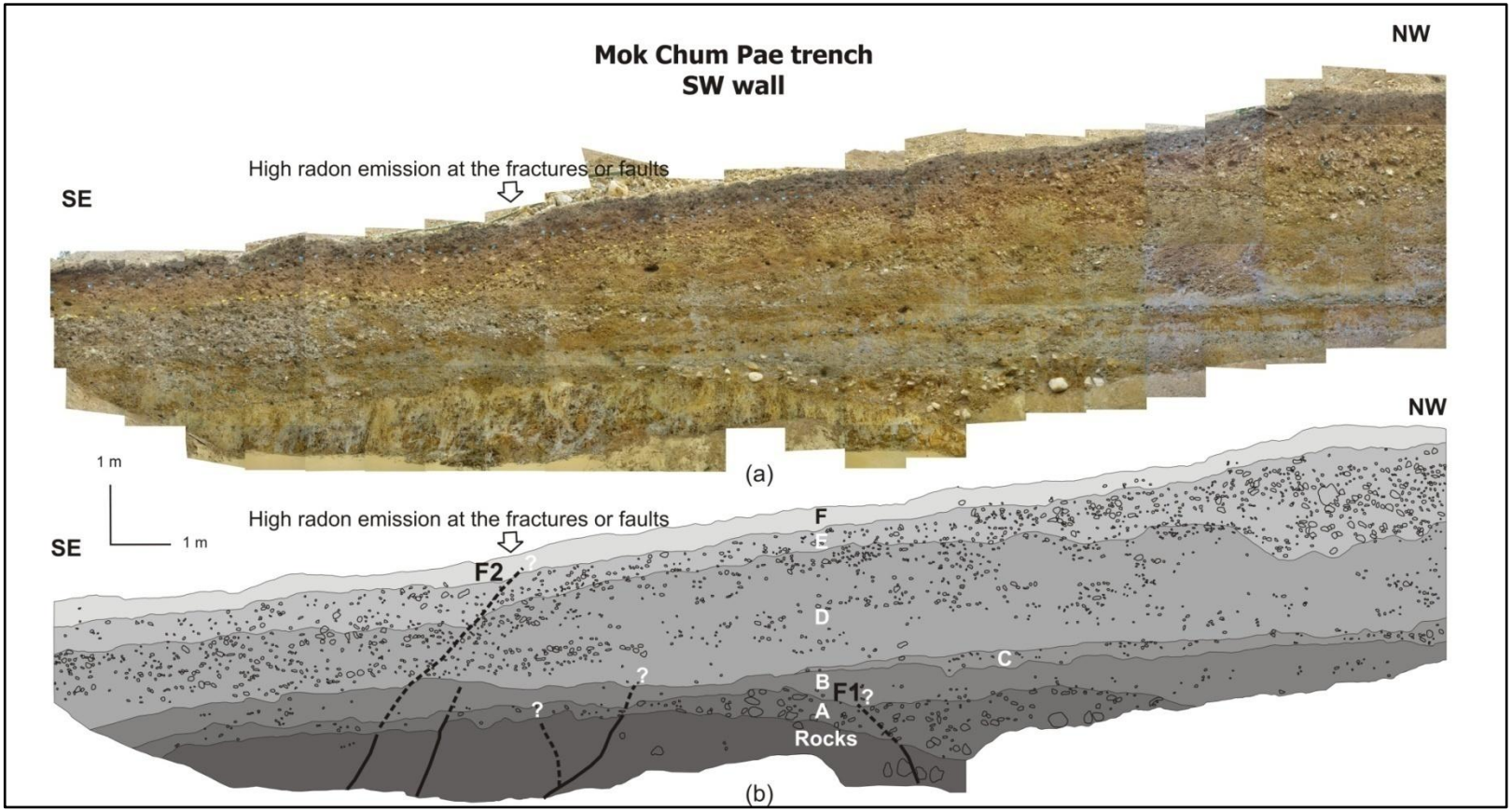

Fig. 40. Stratigraphic units of the Quaternary sediments along the southwest wall of the Mok Chum Pae trench (a–b). Faults indentified in the trench wall are F1 and F2. The location of the wall is shown in Fig. 20b. Unit A: gravel, sand, and clay; Unit B: yellowish-brown to light gray clayey sand with a little gravel; Unit C: gravel, sand, and clay; Unit D: gravel, sand, and clay with a lateritic texture; Unit E: gravel and sand; Unit F: top soil.

7.2. Paleoearthquake investigations of the Thoen Fault

7.2.1. Ban Don Fai segment

Based on morphotectonic landforms, detailed topographical and geological maps, and geomorphic indices [see details in Wiwegwin, 2010; Wiwegwin et al., 2011] developed for the Ban Dan Fai area in the Lampang basin (Fig. 23), a trench at Ban Don Fai across the Ban Don Fai segment of the Thoen Fault was selected for a paleoearthquake study (Ban Don Fai trench no. 2; 18°6′19.042″N, 99°41′14.875″E; location shown in Figs 21c and 23b). The excavated trench was 19 m long, 2 m wide, and 3.5 m deep. The sediments exposed in the trench can be divided into seven unconsolidated units that are exposed in both sidewalls. A detailed trench log is shown in Figs 41 and 42. Details of the individual units are described below.

Unit A, the oldest unit in the trench, is an alluvial unit consisting of gravel, sand, and silt with carbonaceous clay. The gravel beds in unit A are clast-supported. The gravel clasts are mainly subangular to rounded, and most consist of quartz, sandstone, and shale. The unit contains graded beds of 10–50 cm in thickness. A lenticular layer of sand (20 cm thick) occurs between layers of gravel. The total thickness of this unit exceeds 1.5 m.

Unit B is an alluvial unit containing reddish-brown clayey sand, with sparsely distributed pebbles. This unit is limited to the southeastern part of the trench, where it is approximately 30 cm thick.

Unit C is an alluvial unit consisting of sand with gravel. Most of the gravel clasts (of pebble size) are of sandstone and shale. The unit is exposed on the southeastern side of the trench, but it is absent at the point marked ‘x’ in Fig. 41. The thickness of the unit ranges from 10 to 30 cm.

Unit D is an alluvial unit consisting of brown sandy clay, with a little gravel. Most of the gravel clasts are sandstone. The unit is exposed only on the southeastern side of the trench, where its thickness ranges from 10 to 50 cm.

Unit E is an alluvial/colluvial unit containing of brown clayey sand with gravel. Most of the clasts in the gravel are subangular and consist of sandstone, shale, and quartz. The unit is exposed on the southeastern side of the trench, but was not found on the northwestern side. The thickness of the unit ranges from 10 cm to 50 cm.

Unit F is an alluvial/colluvial unit consisting of sand and gravel. The gravels consist mainly of subangular to angular clasts of sandstone and shale, and clast size varies from pebble to cobble. The thickness of this unit ranges from 10 cm to 1 m.

Unit G is a top soil consisting of reddish-brown clayey sand. This is a soil used for agriculture, and organic matter is commonly found. The unit is approximately 30 cm thick.

The grain size of sediment in this trench ranges from clay to coarse gravel. The stratigraphic relationships between unit A and overlying units indicate that the top of unit A is an erosional surface (Figs 41 and 42). The sediments in unit A are poorly sorted. Clasts in gravel layers are subangular to rounded, and the unit contains a lenticular layer of sand and graded beds. The clasts are randomly oriented, with some elongate gravel clasts oriented with their long axes at a high angle to bedding. The sedimentary structures indicate that unit A was deposited by clast-rich debris flows (sediment gravity flows) [Larsen and Steel, 1978; Steel and Gloppen, 1980]. The sediments of units B–F are poorly sorted, and the mixed sand, silt, and gravel of these units was possibly deposited by matrix-rich debris flows (i.e., sandy gravity flows) similar to those reported by Shukha [2009] and Rhodes *et al.* [2005]. The sediments in this trench are laterally continuous, and no faults are observed.

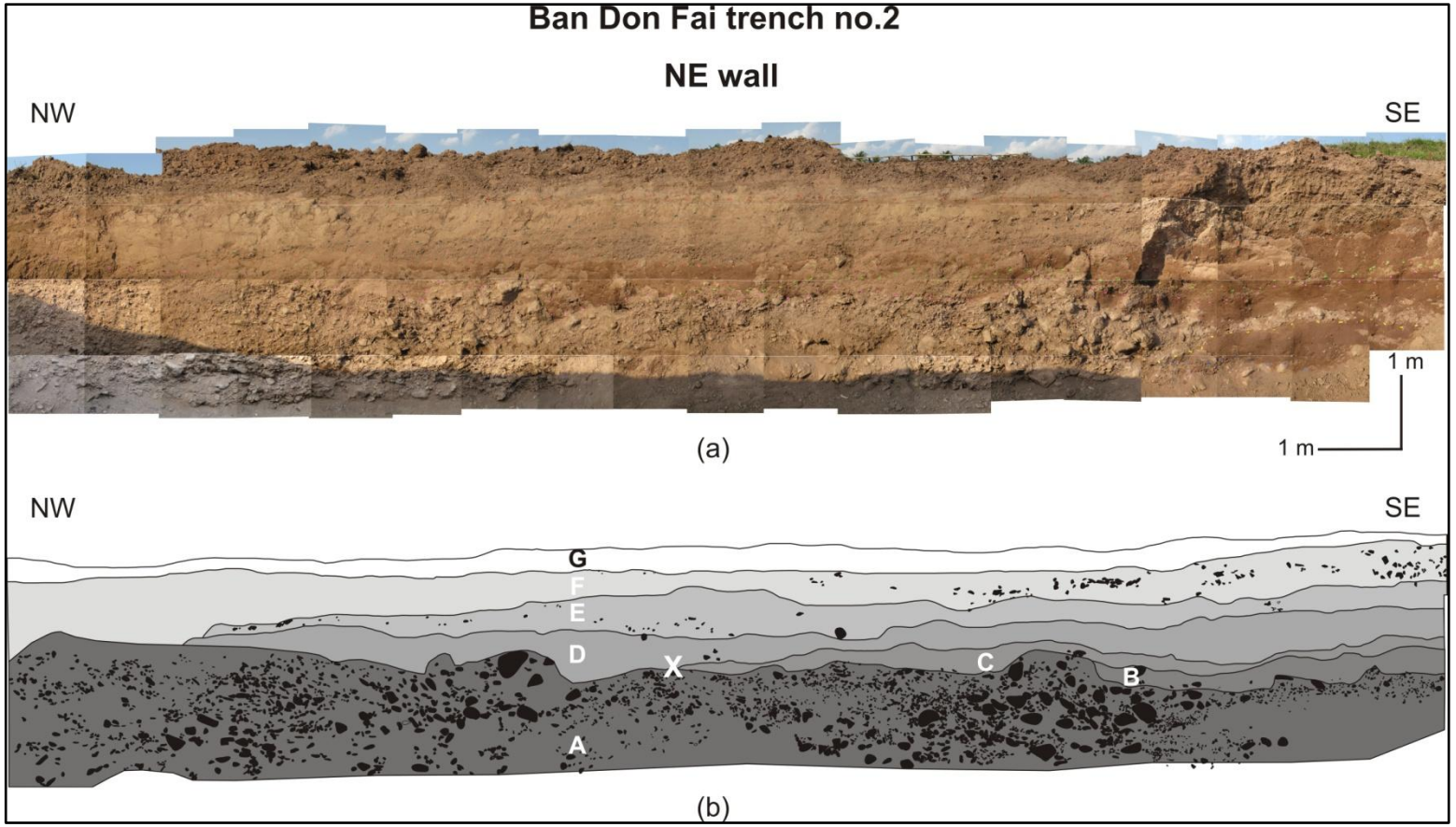

Fig. 41. Stratigraphic units of the Quaternary sediments along the northeast wall of the Ban Don Fai trench no. 2 (a–b). The location of the trench is shown in Figs 21c and 23b. Unit A: gravel, sand, and silt with carbonaceous clay; Unit B: clayey sand; Unit C: sand with gravel; Unit D: sandy clay with minor gravel; Unit E: clayey sand with gravel; Unit F: sand and gravel; Unit G: top soil. The point marked ‘x’ indicates the location where unit C is absent.

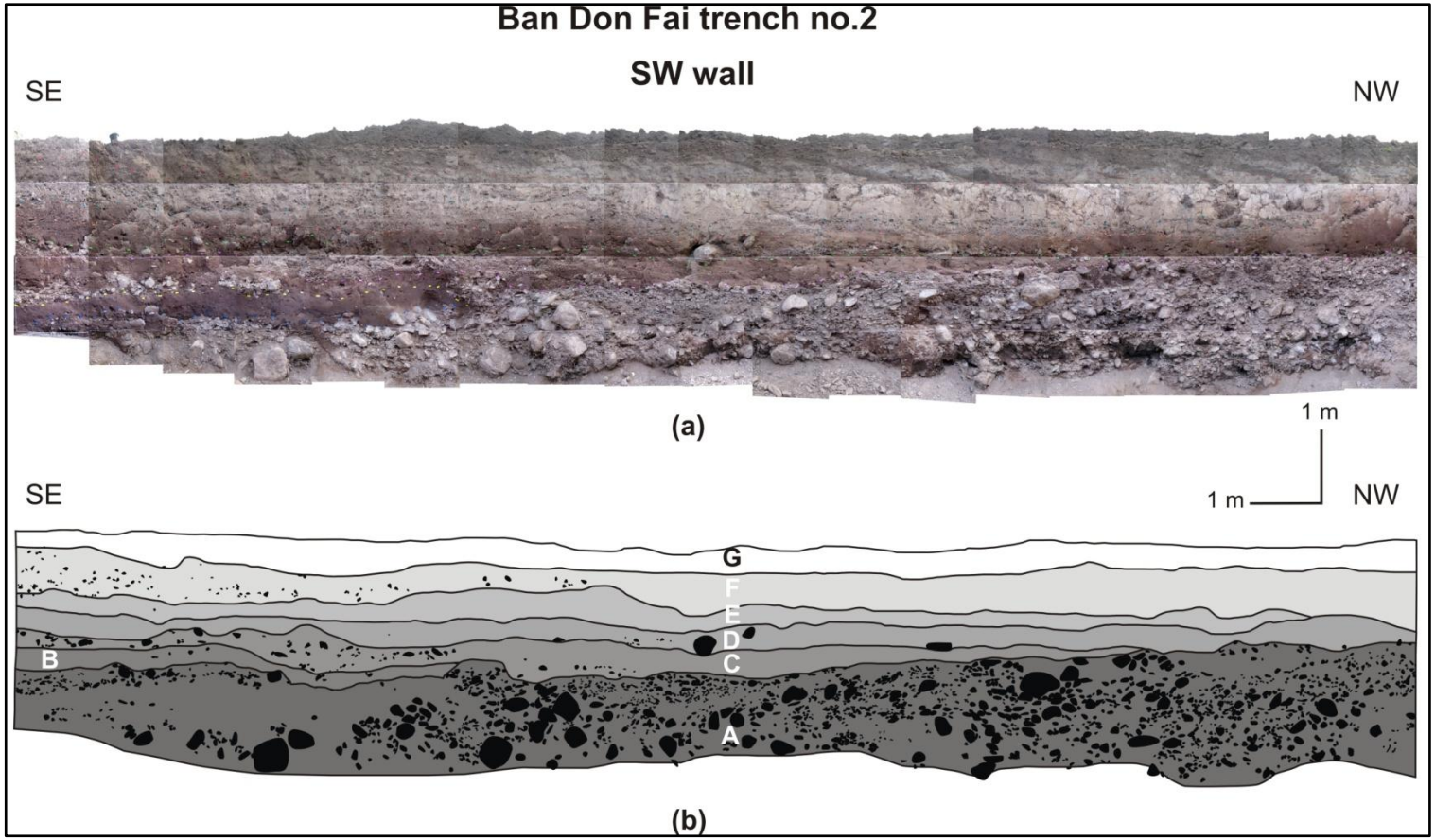

Fig. 42. Stratigraphic units of the Quaternary sediments along the southwest wall of the Ban Don Fai trench no. 2 (a–b). The location of the trench is shown in Figs 21c and 23b. Unit A: gravel, sand, and silt with carbonaceous clay; Unit B: clayey sand; Unit C: sand with gravel; Unit D: sandy clay with minor gravel; Unit E: clayey sand with gravel; Unit F: sand and gravel; Unit G: top soil.

8. Results of geochronological investigations

8.1. Geochronological investigations of the Mae Hong Son Fault

It may be possible to constrain the timing of fault movements if the depositional ages of sedimentary layers, seen to be associated with faults in the quarry, road-cut wall, and trench exposures, can be determined. Unfortunately, no carbonaceous materials suitable for carbon dating were found in any of these exposures, so other geochronological techniques, including optically stimulated luminescence (OSL) and thermoluminescence (TL) dating, have been used to constrain the ages of paleoearthquake events.

8.1.1. Optically Stimulated Luminescence and Thermoluminescence dating

Radioactive isotopes such as uranium (U), thorium (Th), and potassium (K) are present in the Earth's crust and undergo radioactive decay. When minerals such as quartz and feldspar (used as luminescence dosimeters) are exposed to ionizing radiation, electrons may become detached from their parent nuclei in the crystal lattice and diffuse in the vicinity of defects in the lattice where they may become trapped. The number of trapped electrons increases proportionally with the duration and intensity of radiation exposure [Aitken, 1985; Fattahi, 2009]. Natural heating (e.g., sunlight) or artificial heating in the laboratory can free these trapped electrons, and they may return to a vacant position (a "hole") left by a previously displaced electron, where they may emit part of the energy absorbed during irradiation as a photon, or they may become trapped in another defect site [Fattahi, 2009]. For electrons in sediments, the sunlight or illumination of a mineral during a significant tectonic event (and involving, for example, colluviation after the faulting) can free these trapped electrons during the transportation process. However, electrons can be trapped again after deposition of more sediment [Won-in, 2003; Fattahi, 2009]. A convenient way of describing

the luminescence mechanism is to display it on an "energy level diagram", as shown in Fig. 43.

The trapped electrons can be released in the laboratory by artificial heating under controlled conditions. When the trapped electrons recombine at luminescence centres in the crystal (a special type of structural defect or impurity), an emission of light (photon) occurs that is proportional in intensity to the number of trapped electrons. This emission of light is known as thermoluminescence (TL) and it is the basis of thermoluminescence dating [Aitken, 1985; Walker, 2005; Fattahi, 2009]. Alternatively, the electrons can be released from traps by shining a beam of light onto the sample, and the luminescent signal represents the number of electrons trapped within the crystal lattice. This is optically stimulated luminescence, the basis of OSL dating [Walker, 2005]. OSL dating is based on the same principle as TL dating, the difference being that the trapped electrons are released by light rather than by heat.

The OSL and TL dates are based on the amount of luminescence (paleodose or equivalent dose; ED) and the radiation rate (per year) for a radioactive isotope, which yields an annual dose (AD) [Vafiadou *et al.*, 2007]. The OSL and TL methods are widely used in dating sediments such as aeolian quartz-rich sediments, marine sands, and colluvial materials [Murray and Olley, 2002; Fattahi, 2009]. The age of a sample is calculated as follows:

Age (ka) = Paleodose (Gy)/Annual dose (Gy/ka) **(1)**

The paleodose or equivalent dose (ED) is the radiation dose, measured in the laboratory, which has been received by the sediment since some resetting event. The annual dose (AD) is the radiation rate of the radioactive isotope per year. Gray (Gy) is the SI unit of the absorbed radiation.

OSL measurements were made using an OSL/TL instrument (Model OSL/TL-DA-15, RisØ National Laboratory, Denmark) at Chulalongkorn University, Thailand. The instrument

was equipped with a $^{90}Sr/^{90}Y$ beta source delivering 0.14 Gy/sec to the sample. In such a system, the OSL signals from the samples are produced by using Blue-LED arrays (470 ± 30 nm) as stimulation light sources. A single-aliquot regenerative dose (SAR) protocol is applied for measuring a paleodose for all samples, where all the measurements needed to determine a dose are made on one sub-sample (aliquot) of the material to be dated. The natural OSL decay curve and the artificial irradiation decay curve were determined for each sample.

Figure 44 shows an OSL decay curve that represents the relationship between OSL intensity and time. In order to estimate the paleodose, the OSL decay curve was transformed to a growth curve. The growth curve shows the relationship between the OSL ratio (artificial irradiation OSL decay curve/natural OSL decay curve) or the OSL intensity and laboratory irradiation (Gy). For this study, the growth curves were plotted using the relationship between the OSL ratios and laboratory irradiation (Gy), and the paleodose (at point OSL ratio = 1) can be determined, as shown in Fig. 45. The growth curves of OSL samples are shown in appendix A, and the paleodoses of OSL samples are summarized in Table 8.

TL measurements were made using a TL analyzer (C123 photon counter; Hamamatsu Photonics) and an SU-11 temperature controller (Chino Co. Ltd.) with a heating rate of 120 °C per minute under well-designed nitrogen purge conditions at Kasetsart University, Thailand. The TL intensity of sediments is decreased by bleaching from sunlight during transportation of the sediment [Won-in, 2003], although some residual level of TL intensity remains. The TL intensity increases again after deposition of new material [Won-in, 2003] (Fig. 46). Ten hours of natural sunlight bleaching are assumed to result in complete bleaching to residual levels [Pailoplee *et al.*, 2009]. The TL natural and artificial irradiation glow curves were determined for each sample.

Figure 47a shows a glow curve that represents the relationship between TL intensity and temperature. The sediment age calculation is based on a unit of paleodose in Gy. In order

to estimate the paleodose, the glow curve was transformed to a growth curve (Fig. 47b). For this study, the methodology for the TL age calculation mainly follows that described by Takashima and Honda [1989]. The regeneration technique was applied to determine the paleodose, and the technique is based on the straightforward procedure of measuring the natural TL intensity from a natural sample (N) and comparing it with the artificial TL intensity from the same sample with a known dosage (artificial irradiation sample).

For this study, after heating the quartz at 320 °C for 5 hrs, individual samples were separated into four sub-samples. For each sub-sample, artificial irradiation was added with doses of 200, 400, 800, and 1000 Gy (some other samples were also given doses of 50, 100, 200, and 800 Gy: e.g., MLN 11, MLN 12 etc.). The glow curve is shown in Fig. 48; all glow curves for the samples are shown in appendix B. The glow curves were then transformed to growth curves. The growth curve shows the relationship between the TL ratio (artificial irradiation glow curve/natural glow curve) or TL intensity and the laboratory irradiation (Gy). For this study, the growth curves were plotted using the relationship between the TL ratio and the laboratory irradiation (Gy), as shown in appendix B. The paleodose can then be calculated, as shown in Fig. 49, and the paleodoses of the TL samples are summarized in Table 9.

The OSL and TL sample preparation involved drying the samples, and analyzing the water contents. Each sample was sieved using a 0.84 mm mesh filter for annual dose analysis (300 g). Grains between 0.25 and 0.075 mm in size were extracted by re-sieving the remaining sample. Thereafter, these samples were treated with 35% hydrochloric acid (HCl) for at least 30 minutes to remove carbonates and organic material. Ferromagnetic fragments in the samples were separated from quartz using an isodynamic magnetic separator. Feldspar was removed by treating with 24% hydrofluoric acid (HF). X-ray diffraction analysis (XRD) was used to ensure no feldspar remained in the samples; if feldspar was detected, samples were treated again with hydrofluoric acid until all feldspar had been removed.

To determine the annual doses (AD) in the OSL and TL dating samples, the concentrations of U, Th, and K were analyzed using gamma spectrometry at Chulalongkorn University. The annual dose was computed using the concentration of K, U, and Th in the standard table described by Bell [1979], as follows:

Annual dose = Dα + Dβ + Dγ + Dc **(2)**

where $D\alpha = 0.15(2.783U + 0.783Th)/(1 + 1.50W)$

$D\beta = (0.1462U + 0.0286Th + 0.8303K)B/(1 + 1.25W)$

$D\gamma = (0.1148U + 0.514Th + 0.2492K)/(1 + 1.14W)$

Dc = cosmic ray, 0.15

W = water content (%)

B = beta coefficient in the quartz grains, 0.9

The annual dose results for the OSL and TL samples are summarized in Tables 8 and 9.

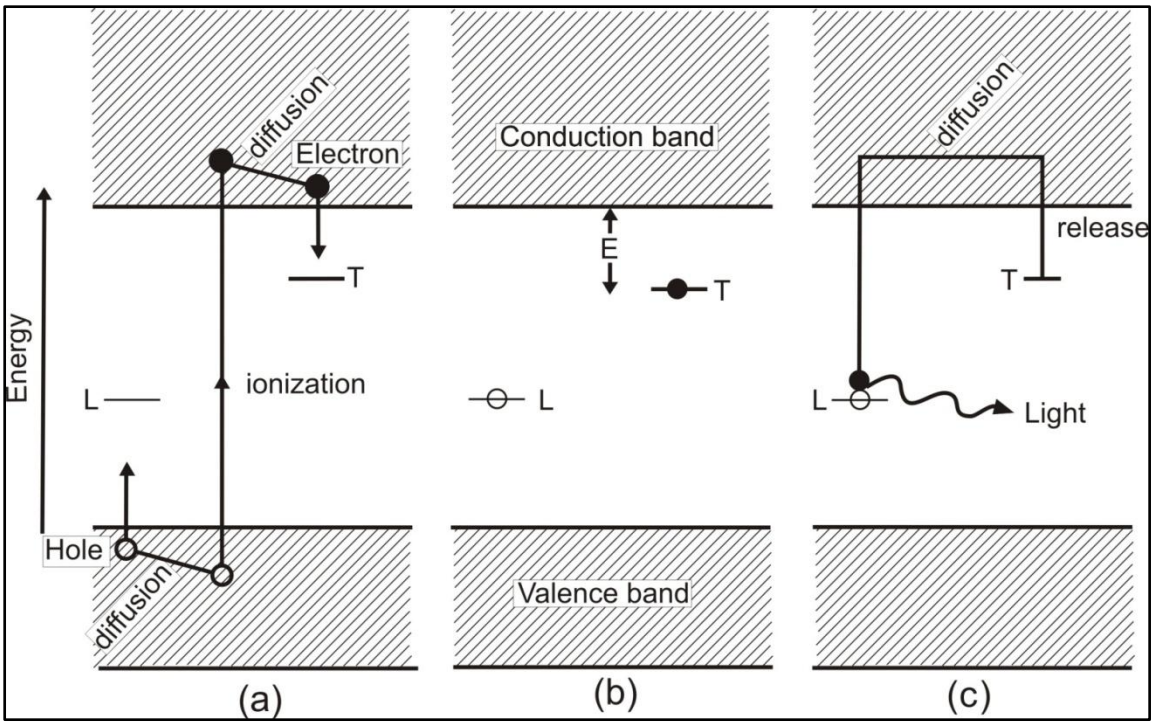

Fig. 43. Luminescence-process diagram showing the energy-level related to three processes: (a) irradiation, caused by exposure of the crystal to nuclear radiation, with ionized electrons trapped in a hole (T); (b) storage, during which the electrons (E) are trapped, but requiring a hole deep enough for storage of the electrons over the geological time period of the sample; and (c) heating to an optimum level of temperature, when electrons are released and recombined at the luminescence centre (L), with the light (TL or OSL) then released [Aitken, 1985].

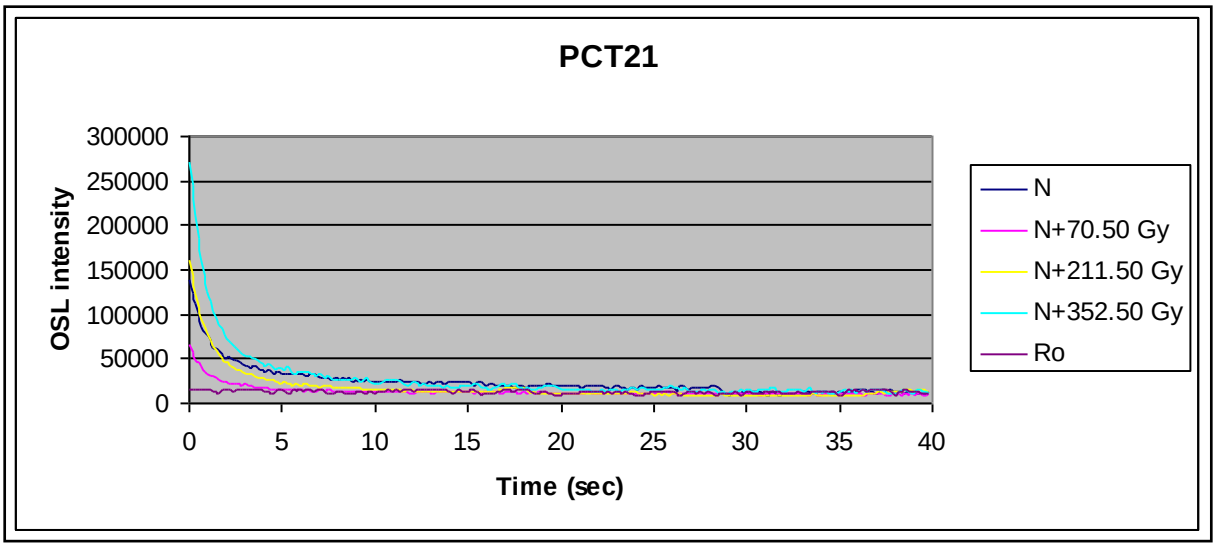

Fig. 44. OSL decay curve that represents the relationship between OSL intensity and time. N: natural sample; Ro: zero-dose sample; N+70.50 Gy, N+211.50 Gy and N+352.50 Gy are artificial irradiation samples

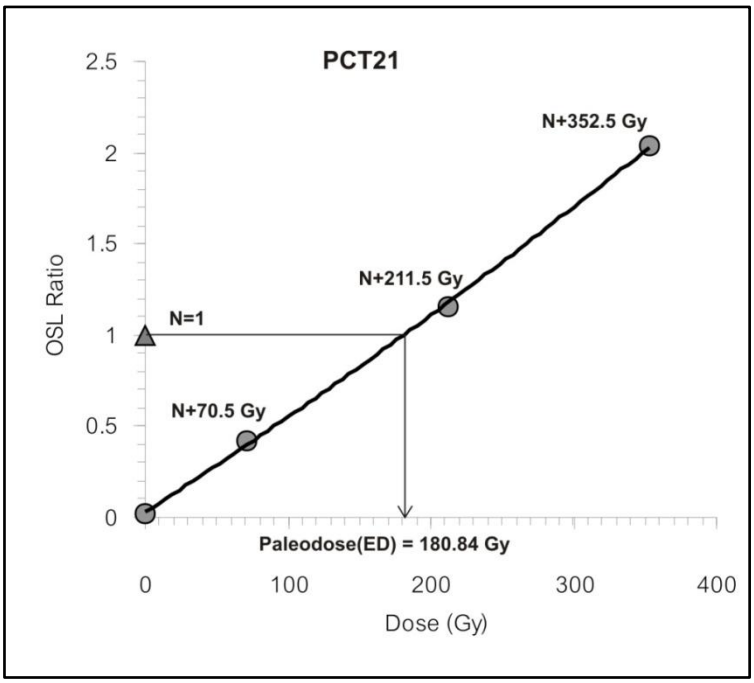

Fig. 45. Growth curve (PCT21) plotted using the relationship between the OSL ratio and the laboratory irradiation (Gy). The paleodose (at point OSL ratio = 1) can be determined from the growth curve.

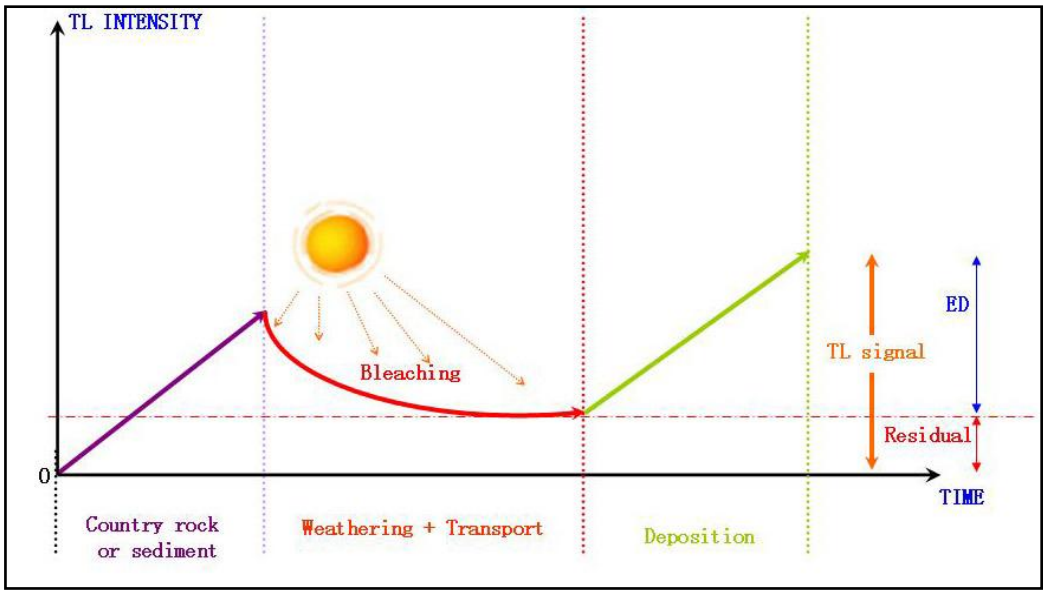

Fig. 46. Relationship between TL intensity and transportation and deposition of sediments. ED is a paleodose [modified from Won-in, 2003].

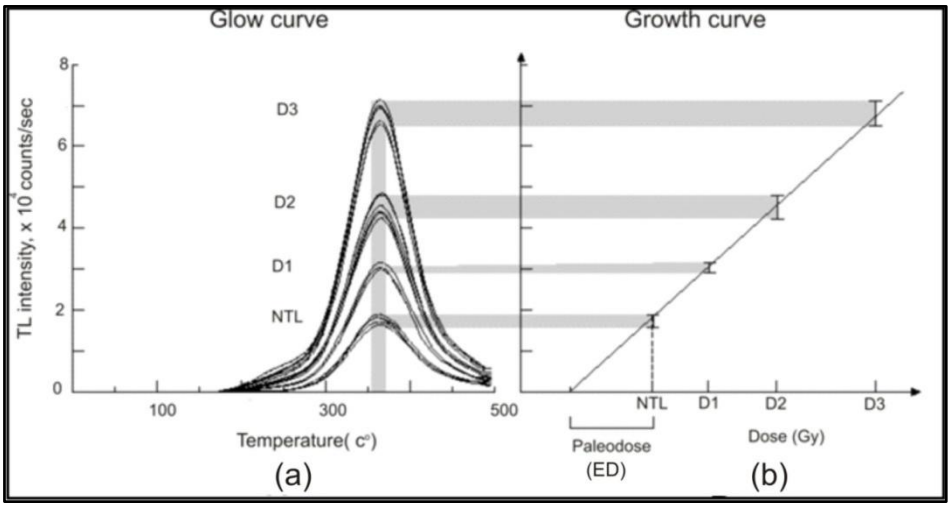

Fig. 47. Idealized graph showing the transformation of a TL glow curve to a TL growth curve. NTL is a natural sample for measuring the paleodose, while D1, D2, and D3 are artificial irradiation samples [modified from Berger, 1988].

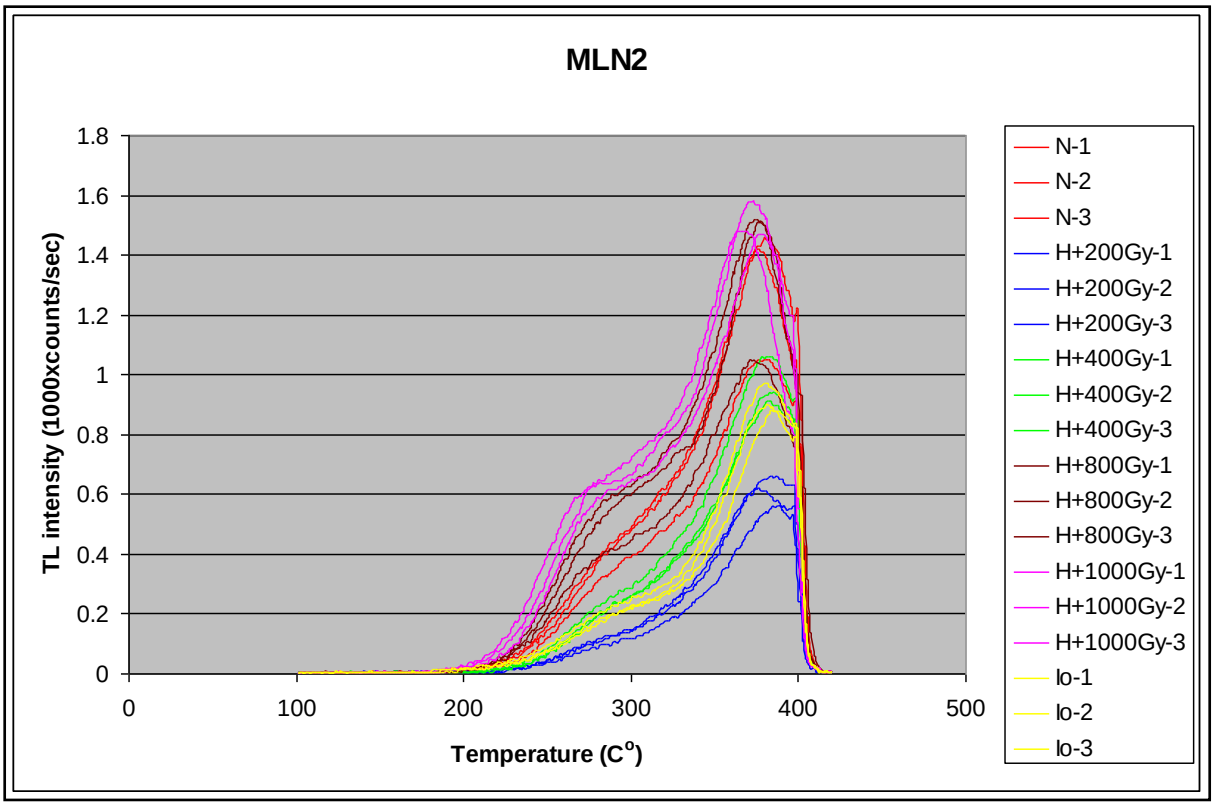

Fig. 48. Thermoluminescence glow curve for sample MLN2 that shows the relationship between the TL intensity and temperature. N: natural sample; Io: residual sample; H+200Gy, H+400Gy, H+800Gy and H+1000Gy are artificial irradiation samples

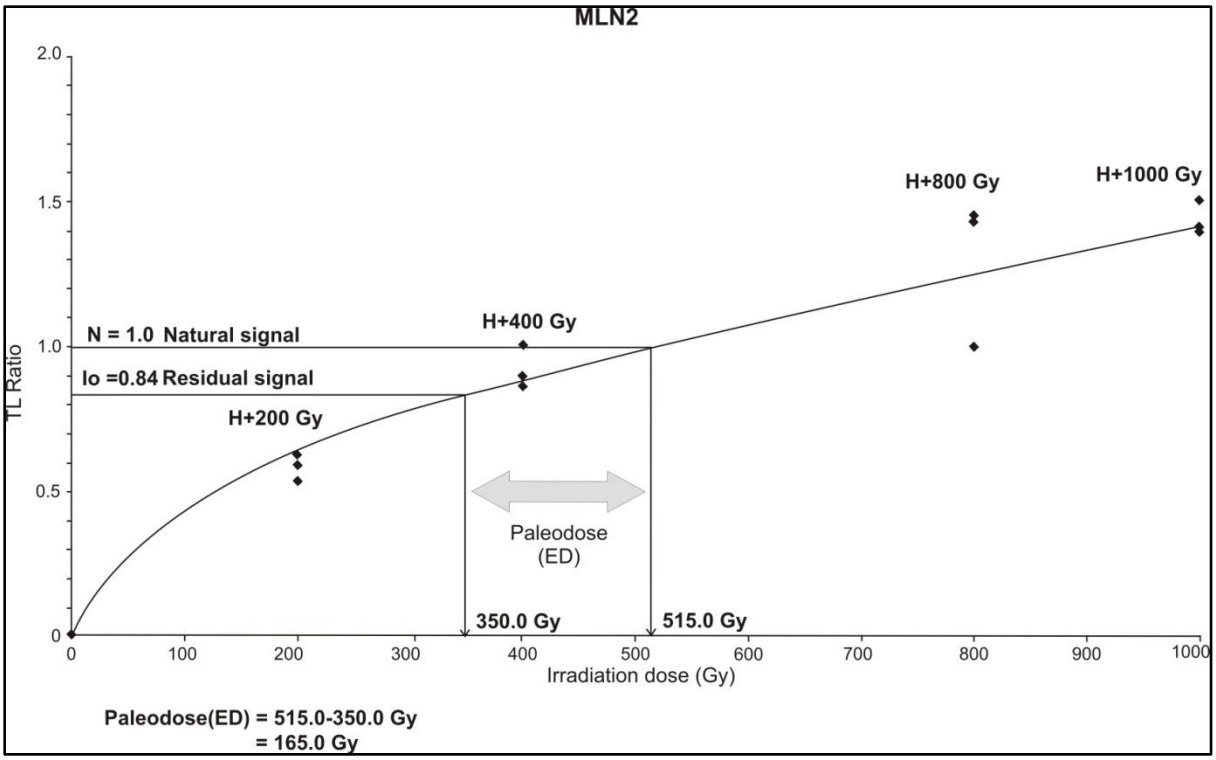

Fig. 49. Growth curve for sample MLN2; the N ratio is 1.0 (as estimated from the ratio between a natural TL sample and a natural TL sample), while the residual TL ratio (Io ratio) is 0.84 (the ratio between a residual TL sample and a natural TL sample). ED can be estimated by subtracting one ratio from the other (N ratio−Io ratio), which here is 515–350 = 165 (Gy).

Table 8. Results of OSL dating of quartz concentrates from sediment samples collected in the Mae La Noi (ML and MLN), Phra That Chom Kitti (PCT), Kon Phung (NML), Huai Kia (HK), and Mok Chum Pae (MCP) areas, Mae Hong Son region, northern Thailand.

Sample No.	U (ppm)	Th (ppm)	K (%)	W (%)	AD (Gy/ka)	ED (Gy)	Age (yr)	Error (yr)
MLN11	3.33	39.02	6.06	17.03	9.58	82.21	8,580	620
MLN12	4.54	38.45	5.97	17.84	9.70	93.21	9,600	720
MLN13	3.26	26.68	4.21	18.96	6.85	81.18	11,840	1,150
MLN14	5.21	65.26	7.10	14.65	12.90	106.49	8,300	640
MLN15	4.56	55.29	6.99	13.94	12.00	112.77	9,400	690
MLN16	3.07	35.6	5.71	14.55	9.02	106.48	11,810	940
MLN2	2.19	28.06	0.73	11.43	3.36	81.61	24,260	1,770
MLN3	1.26	36.73	0.36	17.61	3.27	70.30	21,520	2,010
ML1	2.49	31.29	4.11	13.84	7.01	50.09	7,150	510
ML4	3.17	30.05	4.43	13.85	7.40	48.50	6,550	530
PCT21	1.02	19.49	0.23	9.68	2.02	180.84	89,720	6,460
PCT23	5.23	19.16	0.77	3.45	3.62	181.02	49,980	3,600
PCT25	11.54	32.74	0.44	10.78	5.56	220.87	39,700	2,960
PCT27	11.30	31.15	0.79	9.12	5.80	260.51	44,910	3,220
PCT28	4.02	26.95	1.18	8.38	4.22	154.18	36,540	2,780
PCT29	18.49	33.45	0.63	6.54	7.57	208.94	27,580	2,010
NML1	1.69	14.85	2.55	13.25	4.15	63.50	15,320	1,220
NML2	1.75	12.04	2.23	11.97	3.66	262.47	71,710	5,070

Table 8. (continued)

Sample No.	U (ppm)	Th (ppm)	K (%)	W (%)	AD (Gy/ka)	ED (Gy)	Age (yr)	Error (yr)
NML3	1.86	13.15	2.13	9.59	3.69	61.50	16,660	1,190
NML4	1.48	11.35	1.36	13.39	2.66	159.81	60,070	4,250
NML5	1.58	11.35	2.23	12.39	3.57	276.92	77,600	5,490
NML6	1.75	13.93	2.45	11.13	4.02	52.00	12,920	940
NML7	1.61	11.09	2.32	10.55	3.67	293.09	79,850	5,650
NML8	1.75	13.59	2.43	11.40	3.98	67.00	16,850	1,190
NML9	1.69	11.34	2.06	11.53	3.43	237.19	69,110	4,890
NML10	1.47	10.64	1.78	9.50	3.07	231.77	75,450	5,340
HK1	1.64	21.73	2.02	13.16	4.07	243.27	59,730	4,230
HK2	1.67	21.91	2.17	16.89	4.19	249.33	59,570	4,220
HK3	1.68	12.10	1.36	11.28	2.78	117.12	42,150	2,980
HK6	1.59	20.68	2.33	14.12	4.29	242.12	56,490	4,000
HK7	1.77	21.23	2.14	15.15	4.16	249.18	59,920	4,240
HK8	1.73	14.42	1.42	9.98	3.03	118.44	39,130	2,770
HK9	1.19	16.67	1.57	8.58	3.23	122.91	38,070	2,690
HK10	1.66	12.03	1.13	6.94	2.58	93.50	36,230	2,680
MCP1	1.47	9.15	0.50	5.12	1.70	99.87	58,670	4,150
MCP2	1.90	9.82	1.18	2.69	2.57	148.51	57,670	4,080
MCP3	1.57	11.50	0.64	9.26	2.00	149.37	74,620	5,280
MCP5	1.45	6.59	0.20	5.85	1.20	7.76	6,460	460

Table 8. (continued)

Sample No.	U (ppm)	Th (ppm)	K (%)	W (%)	AD (Gy/ka)	ED (Gy)	Age (yr)	Error (yr)
MCP6	1.48	9.30	0.11	4.91	1.32	79.93	60,670	4,290
MCP9	1.60	9.62	0.79	2.18	2.09	65.26	31,210	2,210
MCP10	1.18	5.89	0.19	11.92	1.05	6.16	5,870	420

Remarks:
Locations of samples are shown on Figs 50–57.

Measurements were performed using a Model OSL/TL-DA-15 analyzer (Risø National Laboratory, Denmark).

The single-aliquot regenerative dose (SAR) protocol technique was applied to measure the paleodose (ED) for each sample.

The annual dose (AD) was computed using the concentrations of K, U, and Th, as shown in the standard table of Bell [1979].

Table 9. Results of TL dating for quartz concentrates from sediment samples collected in the Mae La Noi (ML and MLN) and Phra That Chom Kitti (PCT) areas, Mae Hong Son region, northern Thailand.

Sample No.	U (ppm)	Th (ppm)	K (%)	W (%)	AD (Gy/ka)	ED (Gy)	Age (yr)	Error (yr)
MLN11	3.33	39.02	6.06	17.03	9.58	82.80	8,640	880
MLN12	4.54	38.45	5.97	17.84	9.70	105.00	10,830	1,110
MLN13	3.26	26.68	4.21	18.96	6.85	100.00	14,600	1,490
MLN14	5.21	65.26	7.10	14.65	12.90	107.00	8,300	850
MLN15	4.56	55.29	6.99	13.94	12.00	125.40	10,460	1,080
MLN16	3.07	35.60	5.71	14.55	9.02	126.00	13,980	1,430
MLN 2	4.11	43.84	4.18	23.92	8.01	165.00	20,610	2,250
MLN 3	3.77	34.30	4.13	22.15	7.31	135.00	18,500	2,010
ML1	4.20	45.83	4.46	17.14	8.63	65.00	7,530	650
ML4	4.71	47.47	4.12	20.39	8.41	55.00	6,540	710
PCT21	1.02	38.66	4.11	15.00	7.14	705.00	90,030	7,890
PCT23	13.58	27.42	4.76	13.20	9.94	530.00	53,300	4,760
PCT25	11.70	35.41	5.63	8.88	11.11	400.00	35,990	3,440

Table 9. (continued)

Sample No.	U (ppm)	Th (ppm)	K (%)	W (%)	AD (Gy/ka)	ED (Gy)	Age (yr)	Error (yr)
PCT27	21.57	55.86	4.39	11.58	13.43	554.00	41,240	3,460
PCT28	24.75	37.70	3.50	18.08	11.71	460.00	39,300	3,410
PCT29	23.88	35.68	3.89	13.26	11.98	360.00	30,040	3,200

Remarks:

Locations of samples are shown on Figs 50 and 51.

Measurements were performed using a TL analyzer (C123 photon counter; Hamamatsu Photonics) and an SU-11 temperature controller (Chino Co. Ltd.) with a heating rate of 120 °C per minute under well-designed nitrogen purge conditions. The regeneration technique was applied to measure the paleodose (ED) for each sample. The annual dose (AD) was computed using the concentrations of K, U, and Th, as shown in the standard table of Bell (1979).

8.1.2. Results of Optically Stimulated Luminescence and Thermoluminescence dating

8.1.2.1. Mae La Noi School quarry

Figure 50 shows the stratigraphic units and the measured OSL and TL dates for sediments from the Mae La Noi School quarry. Ten samples were collected for OSL and TL dating (i.e., MLN11–16, MLN2–3, ML1, and ML4 in Fig. 50). The OSL and TL dates from the quartz grains indicate that the sediments in the quarry were deposited from *ca.* 24,260 yr BP to the present day (Tables 8 and 9: unit B was deposited at *ca.* 24,260–18,500 yr BP; unit D was deposited at *ca.* 14,600–11,810 yr BP; unit E was deposited at *ca.* 10,830–9,400 yr BP; unit G was deposited at *ca.* 8,640–7,150 yr BP; and unit H was deposited at *ca.*6,550–6,540 yr BP).

8.1.2.2. Phra That Chom Kitti road-cut wall

Figure 51 shows the stratigraphic units and the measured OSL and TL dates for sediments from the Phra That Chom Kitti road-cut wall. Six samples were collected for OSL and TL dating (i.e., PCT21, PCT23, PCT25, PCT27, PCT28, and PCT29; Fig. 51). The OSL and TL dates from the quartz grains indicate that the sediments in the road-cut wall were deposited from *ca.* 90,030 yr BP to the present day (Tables 8 and 9: unit B was deposited at *ca.* 90,030–89,720 yr BP; unit C was deposited at *ca.* 53,300–49,980 yr BP; unit D was deposited at *ca.* 44,910–41,240 yr BP; unit E was deposited at *ca.* 39,700–35,990 yr BP; F was deposited at *ca.* 39,300–36,540 yr BP; and unit G was deposited at *ca.* 30,040–27,580 yr BP).

8.1.2.3. Nong Mae La trench

Figures 52 and 53 show the stratigraphic units and the measured OSL dates for sediments from the Nong Mae La trench. Ten samples were collected for OSL dating (i.e.,

NML1–10 in Figs 52 and 53). The OSL dates from the quartz grains indicate that the sediments in the trench were deposited from *ca.* 79,850 yr BP to the present day (Table 8: unit B was deposited at *ca.* 79,850–71,710 yr BP; unit D was deposited at *ca.* 69,110–60,070 yr BP; and unit F was deposited at *ca.* 16,850–12,920 yr BP).

8.1.2.4. Huai Kia trench

Figures 54 and 55 show the stratigraphic units and the measured OSL dates for sediments from the Huai Kia trench. Eight samples were collected for OSL dating (i.e., HK1–3 and HK6–10 in Figs 54 and 55). The OSL dates from the quartz grains indicate that the sediments in the trench were deposited from *ca.* 59,920 yr BP to the present day (Table 8: unit B was deposited at *ca.* 59,920–56,490 yr BP; unit D was deposited at *ca.* 42,150–38,070 yr BP; and unit F was deposited at *ca.* 36,230 yr BP to the present day).

8.1.2.5. Mok Chum Pae trench

Figures 56 and 57 show the stratigraphic units and the measured OSL dates for sediments from the Mok Chum Pae trench. Seven samples were collected for OSL dating (i.e., MCP1–3, MCP5–6, MCP9–10 in Figs 56 and 57). The OSL dates from the quartz grains indicate that the sediments in the trench were deposited from *ca.* 74,620 yr BP to the present day (Table 8: unit A was deposited at *ca.* 74,620 yr BP; unit B was deposited at *ca.* 60,670–57,670 yr BP; unit D was deposited at *ca.* 31,210 yr BP; unit E was deposited at *ca.* 6,460 yr BP; and unit F was deposited at *ca.* 5,870 yr BP to the present day).

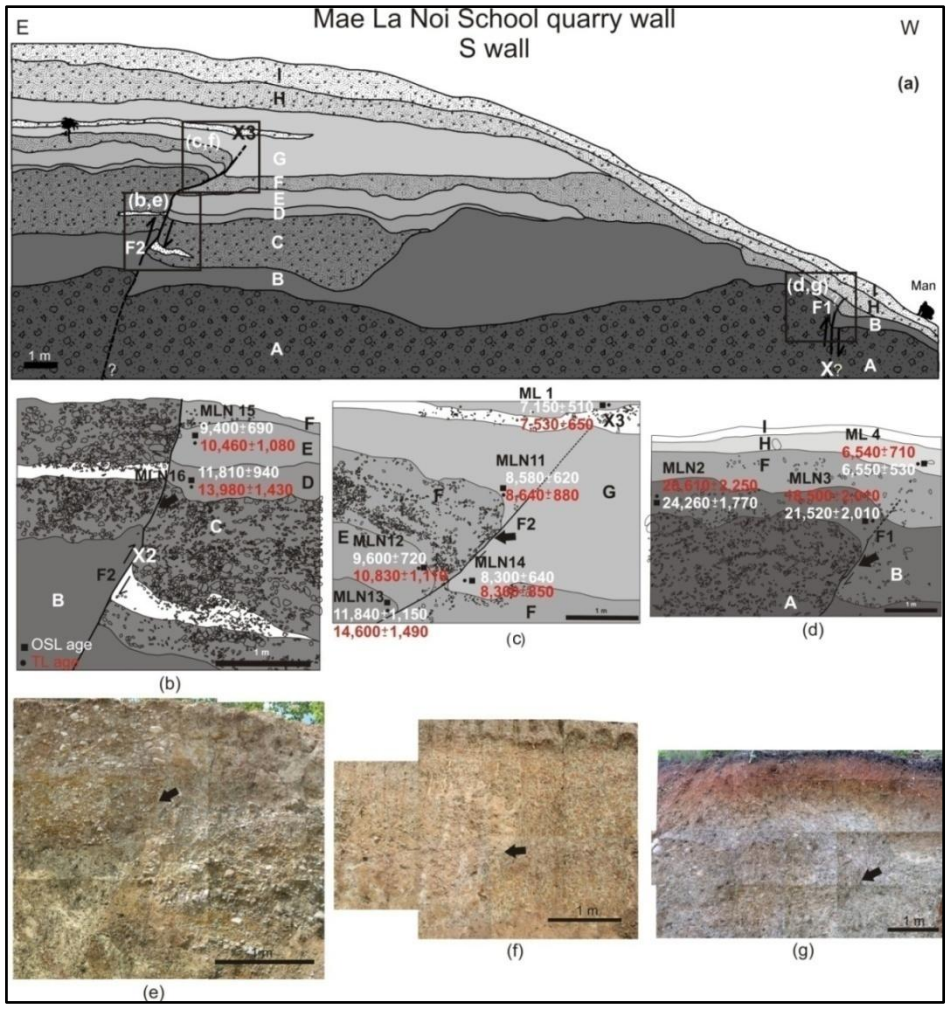

Fig. 50. Stratigraphy and ages of Quaternary sediments along an E–W transect in the Mae La Noi School quarry (a–d). Close-up photographs of plates b, c, and d are presented in plates e, f, and g, respectively. The faults identified in the quarry wall are F1 and F2. Black arrows indicate fault traces and half arrows show sense of movement. Samples MLN11–16, MLN2–3, ML1, and ML4 were collected for OSL and TL dating. The location of the quarry is shown in Figs 13b and 14b. Unit A: gravel sand and clay; Unit B: clay and sand; Unit C: gravel, sand, clay, with sand lens; Unit D: sandy clay with gravel; Unit E: clayey sand with gravel; Unit F: gravel, sand, and clay; Unit G: sandy clay with gravel; Unit H: gravel and sand, and Unit I: top soil. The points marked "X" and "X2" indicate the locations of slickensides on fault planes. The point marked "X3" indicates the location where the fault terminates in unit G.

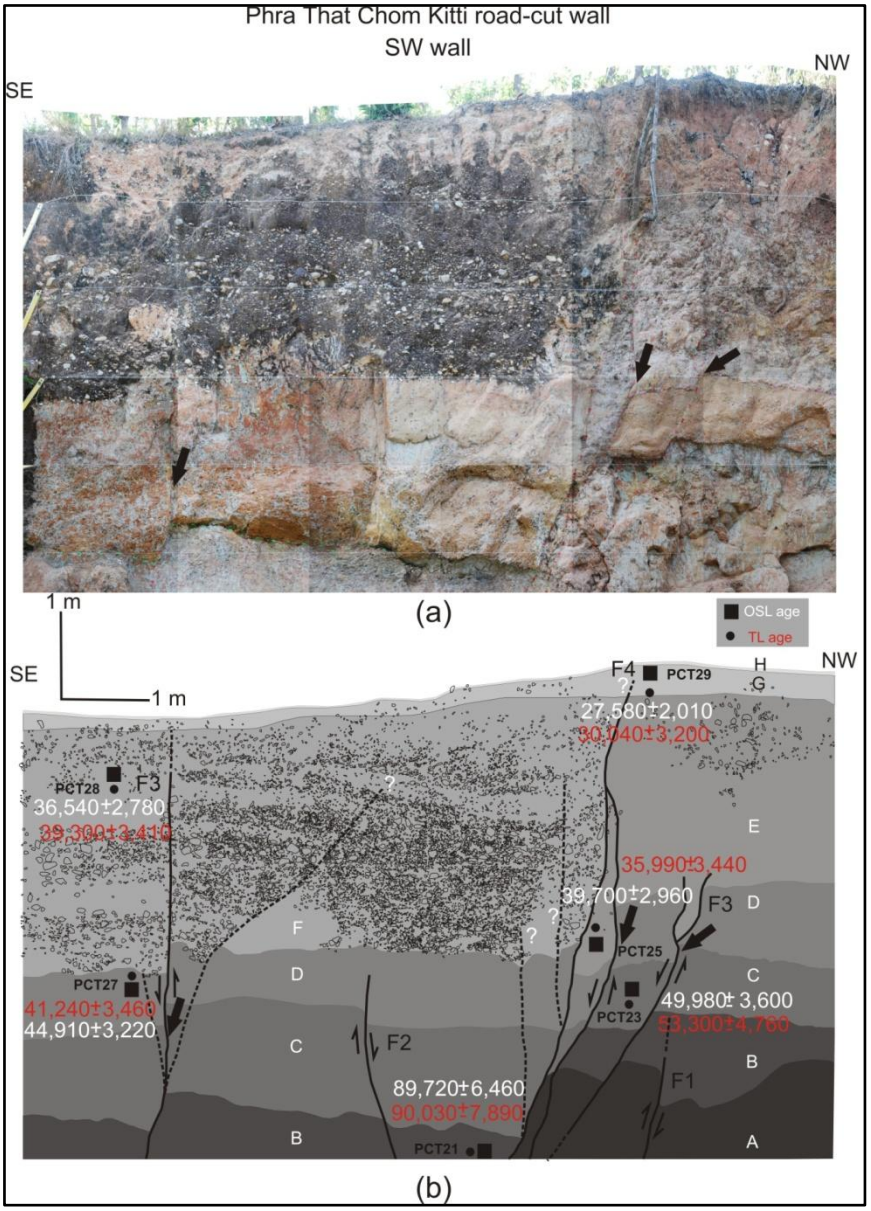

Fig. 51. Stratigraphy and ages of Quaternary sediments along the SE–NW transect in the Phra That Chom Kitti road-cut exposure (a–b). Faults identified in the road-cut wall are F1–F4. Black arrows indicate fault traces and half arrows show the sense of movement. Samples PCT21, PCT23, PCT25, PCT27, PCT28, and PCT29 were collected for OSL and TL dating. The location of the wall is shown in Figs 15b and 16b. Unit A: brown to yellowish sand; Unit B: clay with clasts of feldspar and quartz; Unit C: brown to yellowish sand with gravel; Unit D: light brown to yellowish sand; Unit E: clay, sand and with some gravels; Unit F: gravel, sand, and clay; Unit G: gravel with sand; Unit H: top soil.

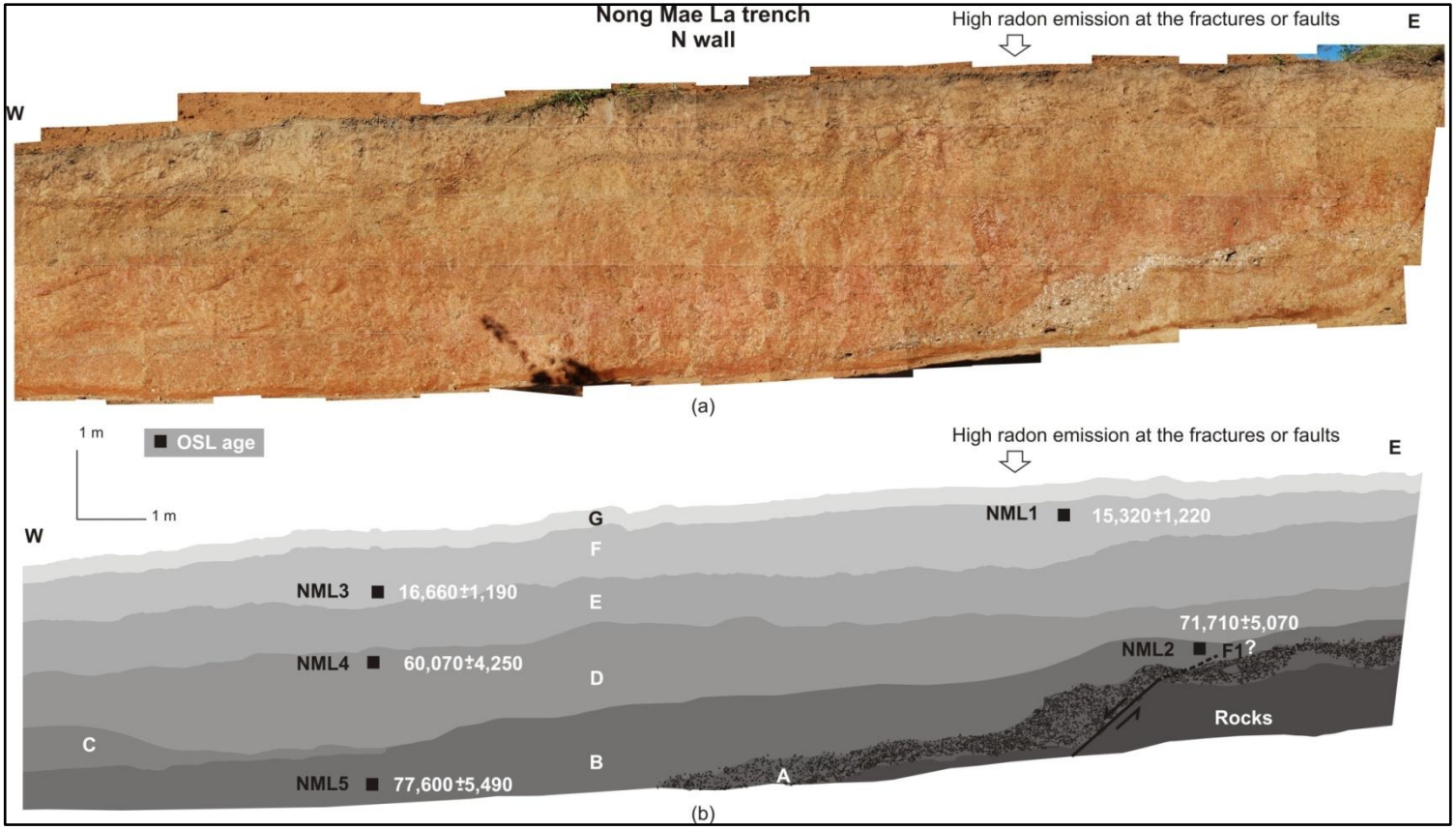

Fig. 52. Stratigraphy and ages of Quaternary sediments along a north wall in the Nong Mae La trench (a–b). Fault indentified in the trench wall is F1. Samples NML1–5 were collected for OSL dating. The location of the wall is shown in Fig. 18b. Unit A: gravel and sand; Unit B: reddish-brown sandy clay; Unit C: reddish-brown sandy clay and gravel; Unit D: reddish-brown sandy clay and gravel with clasts of iron-rich concretions; Unit E: reddish-brown clayey sand and gravel; Unit F: reddish-brown clayey sand with small amounts of gravel; Unit G: top soil.

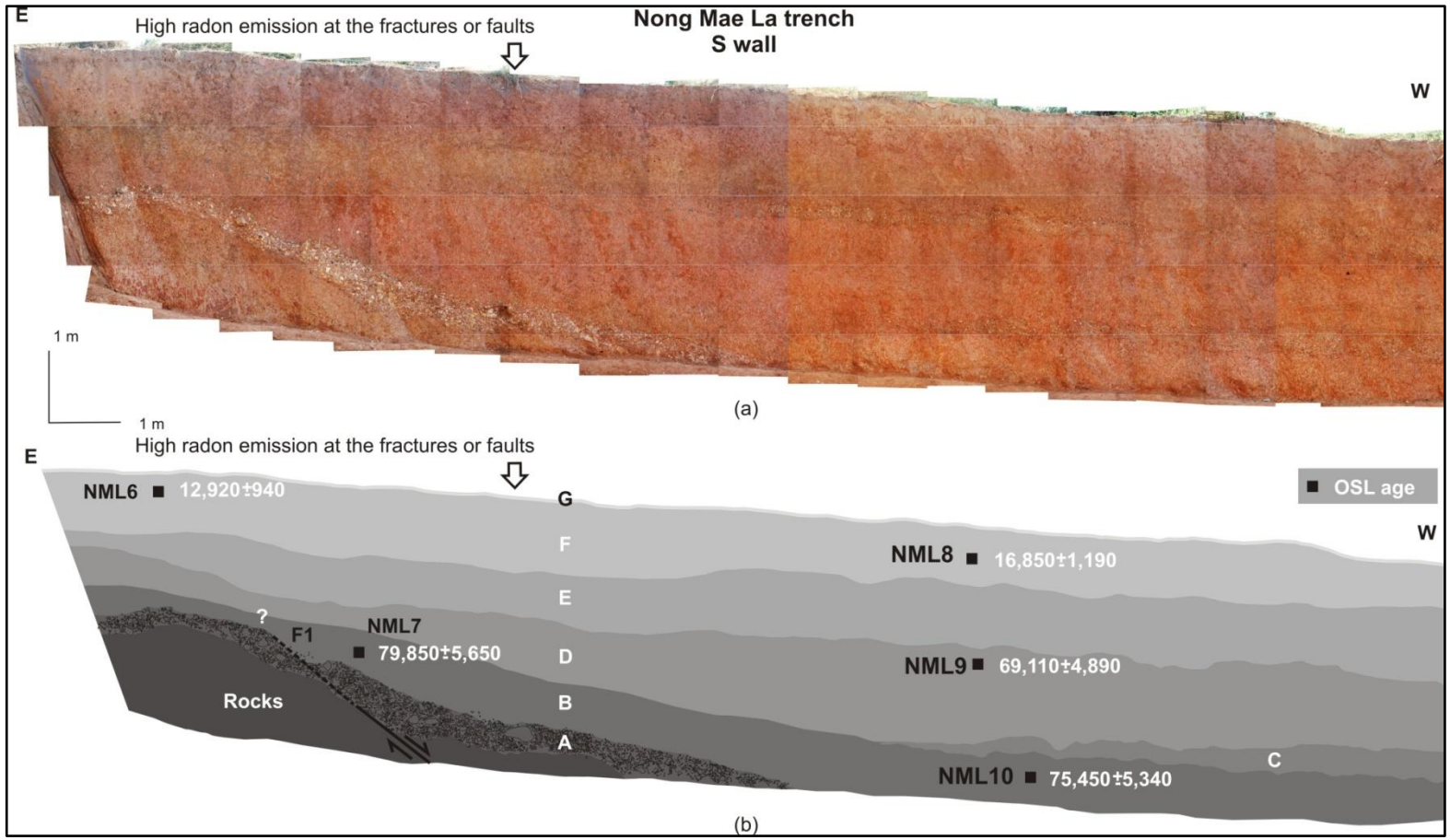

Fig. 53. Stratigraphy and ages of Quaternary sediments along a south wall in the Nong Mae La trench (a–b). Fault indentified in the trench wall is F1. Samples NML6–10 were collected for OSL dating. The location of the wall is shown in Fig. 18b. Unit A: gravel and sand; Unit B: reddish-brown sandy clay; Unit C: reddish-brown sandy clay and gravel; Unit D: reddish-brown sandy clay and gravel with clasts of iron-rich concretions; Unit E: reddish-brown clayey sand and gravel; Unit F: reddish-brown clayey sand with small amounts of gravel; Unit G: top soil.

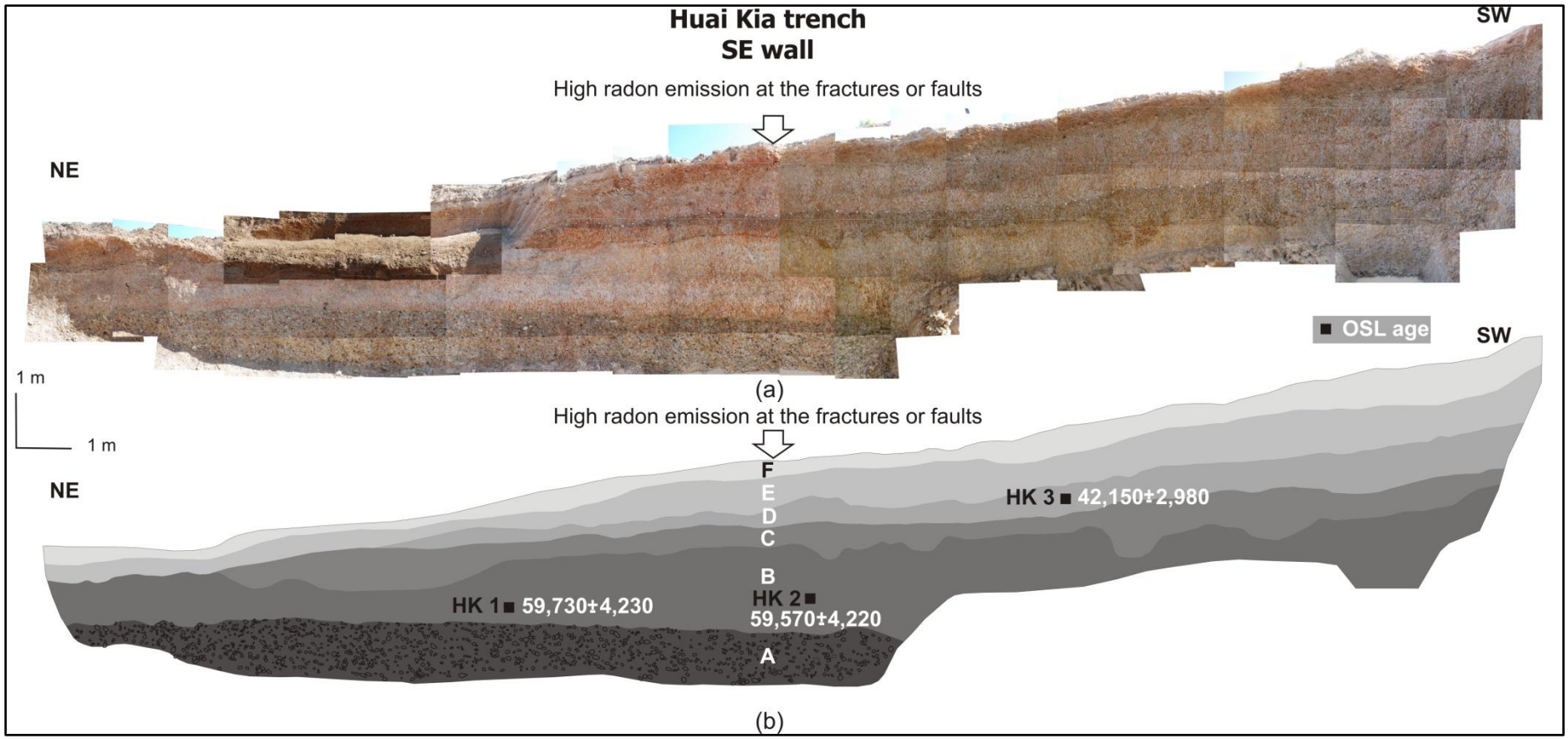

Fig. 54. Stratigraphy and ages of Quaternary sediments along a southeast wall in the Huai Kia trench (a–b). Samples HK1–3 were collected for OSL dating. The location of the wall is shown in Fig. 19b. Unit A: gravel, sand, and clay; Unit B: reddish-brown to gray sandy clay with a little gravel; Unit C: sand, silt, clay, and gravel; Unit D: reddish-brown sandy clay with a little gravel; Unit E: gravel and sand; Unit F: top soil.

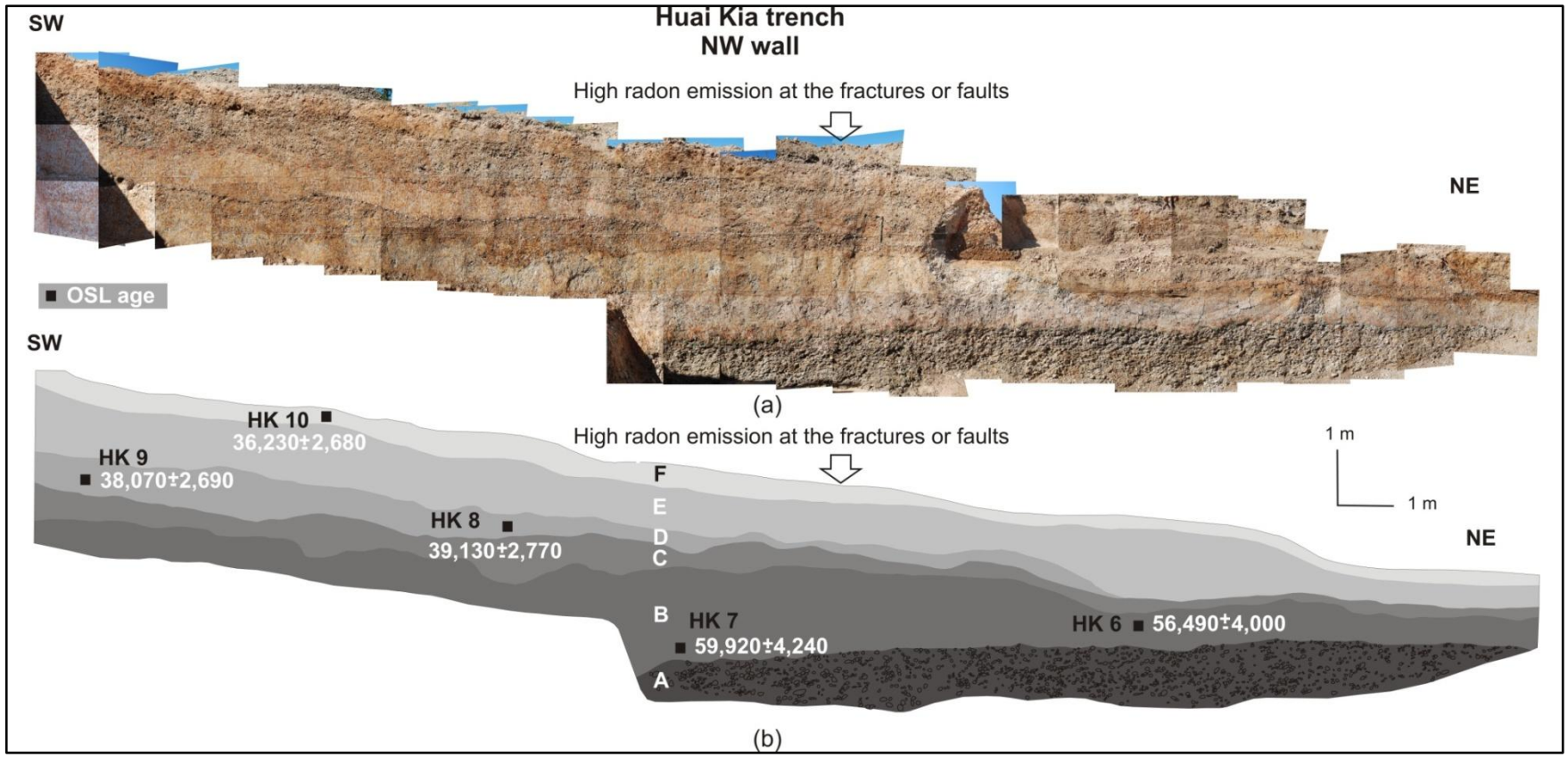

Fig. 55. Stratigraphy and ages of Quaternary sediments along a northwest wall in the Huai Kia trench (a–b). Samples HK6–10 were collected for OSL dating. The location of the wall is shown in Fig. 19b. Unit A: gravel, sand, and clay; Unit B: reddish-brown to gray sandy clay with a little gravel; Unit C: sand, silt, clay, and gravel; Unit D: reddish-brown sandy clay with a little gravel; Unit E: gravel and sand; Unit F: top soil.

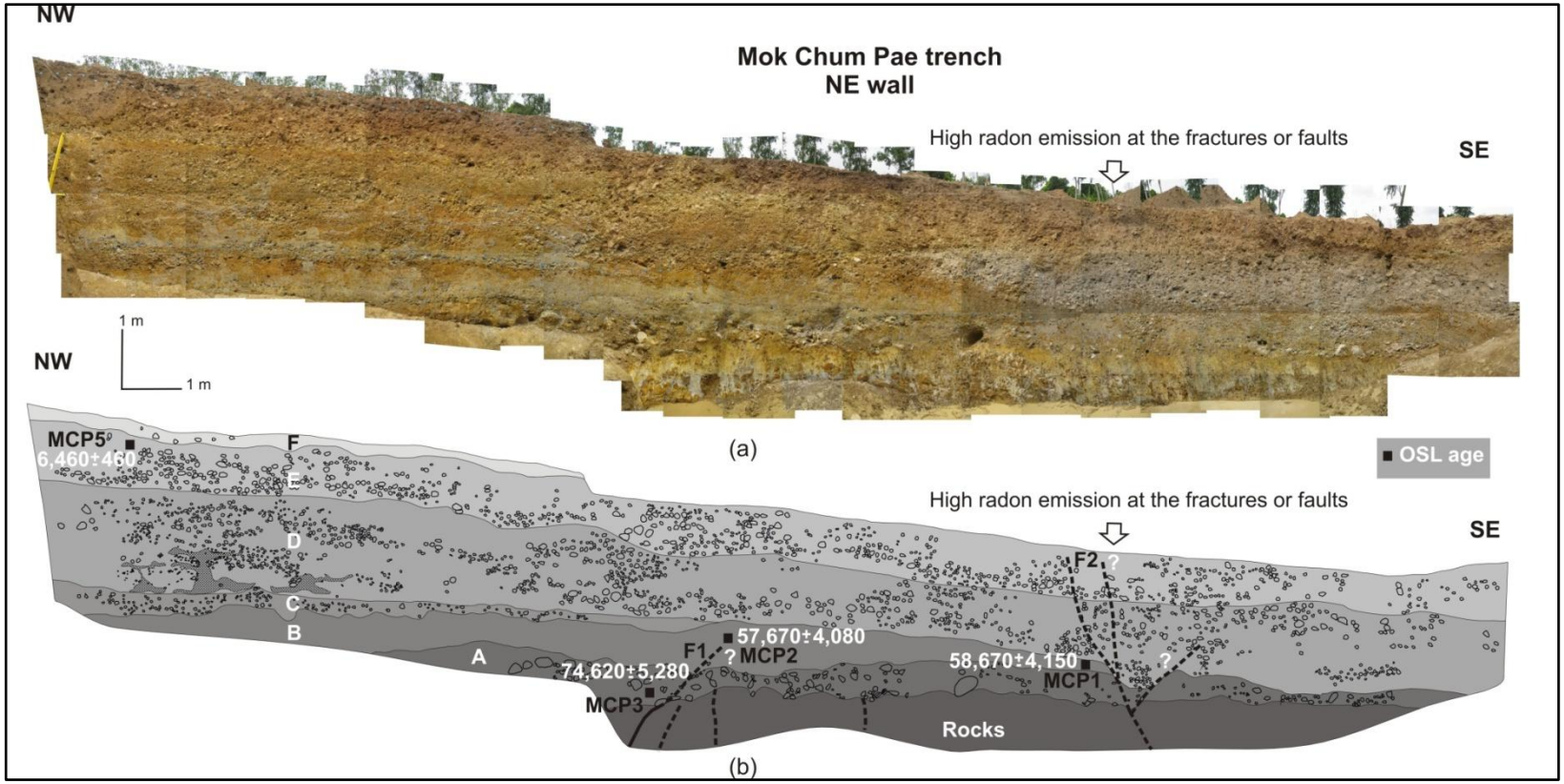

Fig. 56. Stratigraphy and ages of Quaternary sediments along a northeast wall in the Mok Chum Pae trench (a–b). Faults indentified in the trench wall are F1 and F2. Samples MCP1–3, and MCP5 were collected for OSL dating. The location of the wall is shown in Fig. 20b. Unit A: gravel, sand, and clay; Unit B: yellowish-brown to light gray clayey sand with a little gravel; Unit C: gravel, sand, and clay; Unit D: gravel, sand, and clay with a lateritic texture; Unit E: gravel and sand; Unit F: top soil.

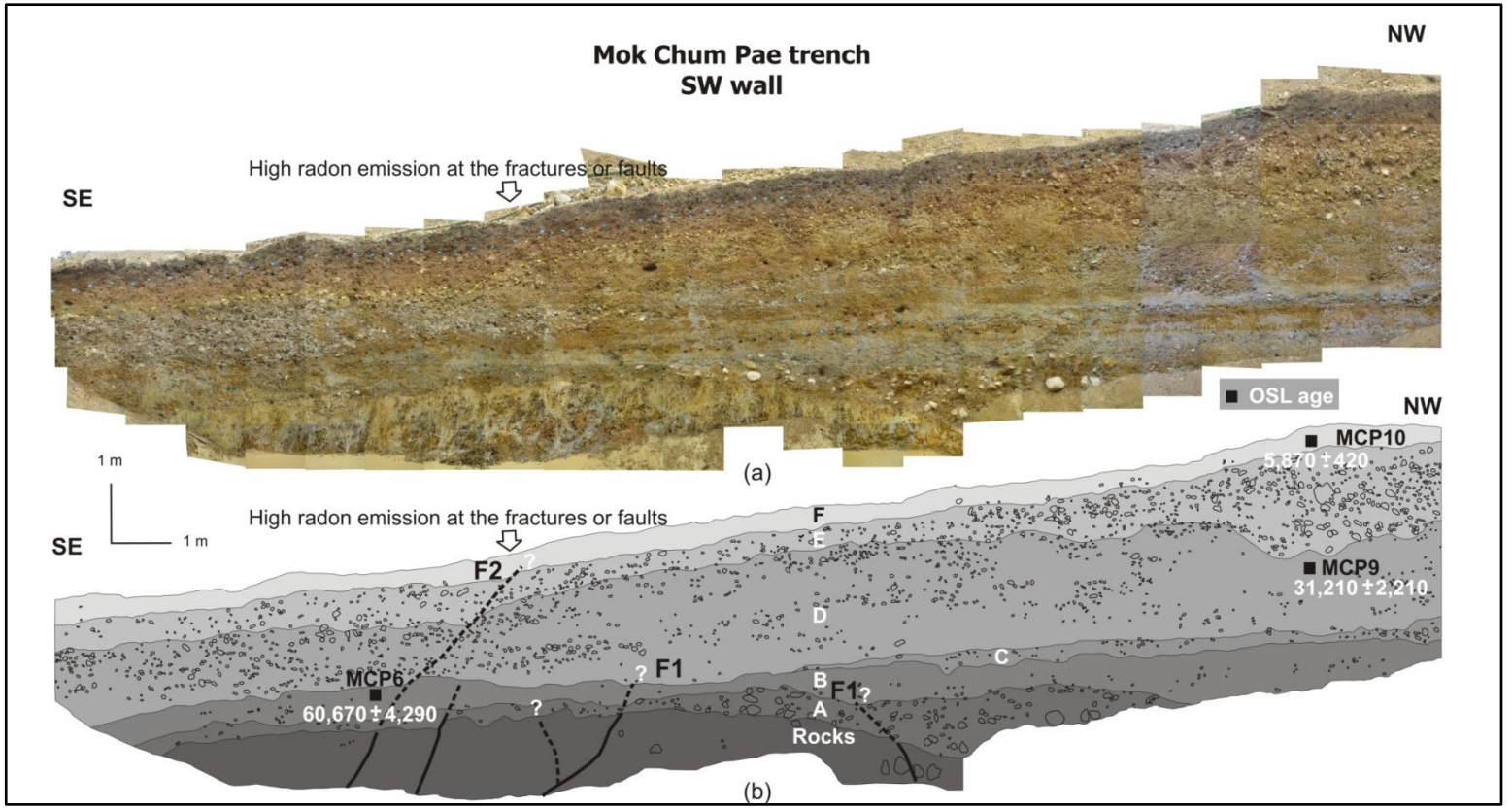

Fig. 57. Stratigraphy and ages of Quaternary sediments along a southwest wall in the Mok Chum Pae trench (a–b). Faults indentified in the trench wall are F1 and F2. Samples MCP6, MCP9, and MCP10 were collected for OSL dating. The location of the wall is shown in Fig. 20b. Unit A: gravel, sand, and clay; Unit B: yellowish-brown to light gray clayey sand with a little gravel; Unit C: gravel, sand, and clay; Unit D: gravel, sand, and clay with a lateritic texture; Unit E: gravel and sand; Unit F: top soil.

8.2. Geochronological investigations of the Thoen Fault

The trench-log stratigraphy in Ban Don Fai trench no. 2 shows no evidence for recent fault movement, but to put this finding in context it is necessary to determine the age of the sediments exposed in the trench. Having established the stratigraphy of the Ban Don Fai trench no. 2, then samples were collected for OSL and AMS radiocarbon dating.

8.2.1. Results of Accelerator Mass Spectrometry radiocarbon (AMS) dating

The ^{14}C method of dating is often applied in archaeology and geology, but the method is only accurate for samples younger than 45,000 years [Roberts *et al.,* 1994]. For paleoearthquakes investigations in Thailand, AMS radiocarbon dating is commonly used for determining the age of sediments in a trench. For example, Pailoplee *et al.* [2009] and DMR [2006] succeeded in dating carbonaceous and charcoal samples, and these ages were then used for estimating the timing of fault movements. In the present study, three carbonaceous clay samples were collected from unit A in the Ban Don Fai trench no. 2 (Figs 58 and 59), and the samples were processed for AMS radiocarbon dating at Beta Analytic Inc. (USA). The dating results are shown in Table 10 and appendix C.

8.2.2. Results of Optically Stimulated Luminescence dating

Six samples from units A, B, and D in Ban Don Fai trench no. 2 were prepared for OSL dating (Figs 58 and 59). Measurements were made using an OSL instrument (Model OSL/TL-DA-15, Risø National Laboratory, Denmark) at Chulalongkorn University, Thailand. The instrument was equipped with a $^{90}Sr/^{90}Y$ beta source delivering 0.14 Gy/sec to the sample. In such a system, the OSL signals from the samples are produced by using Blue-LED arrays (470 ± 30 nm) as stimulation light sources. A single-aliquot regenerative dose (SAR)

protocol is applied to measure a paleodose for all samples. The growth curves of OSL samples are shown in appendix A, and the paleodoses are summarized in Table 11.

For the annual dose, the concentrations of U, Th, and K were analyzed using gamma spectrometry at Chulalongkorn University. The annual dose was computed using the concentration of K, U, and Th in the standard table described by Bell [1979]. The results of annual doses and OSL dating are summarized in Table 11.

Figures 58 and 59 show the stratigraphic units, and the measured OSL and AMS radiocarbon dates for sediments from Ban Don Fai trench no. 2. The OSL ages indicate that the sediments were deposited during the past 910 years. Three AMS radiocarbon dates indicate that the sediments in the lowest unit were deposited from about 960 to 920 yr BP, and these dates are consistent with the OSL ages for sediments in unit A.

Table 10. Result of AMS radiocarbon dating (C-14) of carbonaceous sediments from Ban Don Fai trench no. 2.

Sample No.	^{14}C measured radiocarbon age (yr BP)	$^{13}C/^{12}C$ (per mil)	^{14}C conventional radiocarbon age (yr BP)	Calibration of radiocarbon age (Cal yr BP)
C001	940 ± 40	–25.1	940 ± 40	930–750
C002	940 ± 40	–23.9	960 ± 40	940–780
C003	910 ± 40	–24.6	920 ± 40	930–740

Remarks Method: AMS-Standard ^{14}C

Sample: Organic sediment

Locations of sample sites are shown in Figs 58 and 59.

Table 11. OSL dating results for quartz concentrates from sediment samples collected in the Lampang basin, northern Thailand.

Sample No.	U (ppm)	Th (ppm)	K (%)	W (%)	AD (Gy/ka)	ED (Gy)	Age (yr)	Error (yr)
DF1	3.14	15.07	2.52	1.50	4.66	2.92	630	60
DF2	3.00	15.64	2.87	2.56	5.01	3.67	730	80
DF3	2.59	10.52	1.88	4.06	3.49	1.77	510	40
DF4	2.94	12.21	2.03	7.46	3.80	2.19	580	80
DF5	3.17	15.50	2.35	5.99	4.44	2.73	610	60
DF6	3.51	16.20	2.25	7.79	4.44	4.04	910	40

Remarks

Locations of samples are shown Figs 58 and 59.

Measurements were performed using a Model OSL/TL-DA-15 analyzer (Risø National Laboratory, Denmark).

The single-aliquot regenerative dose (SAR) protocol technique was applied to measure the paleodose (ED) for each sample.

The annual dose (AD) was computed using the concentrations of K, U, and Th, as shown in the standard table of Bell [1979].

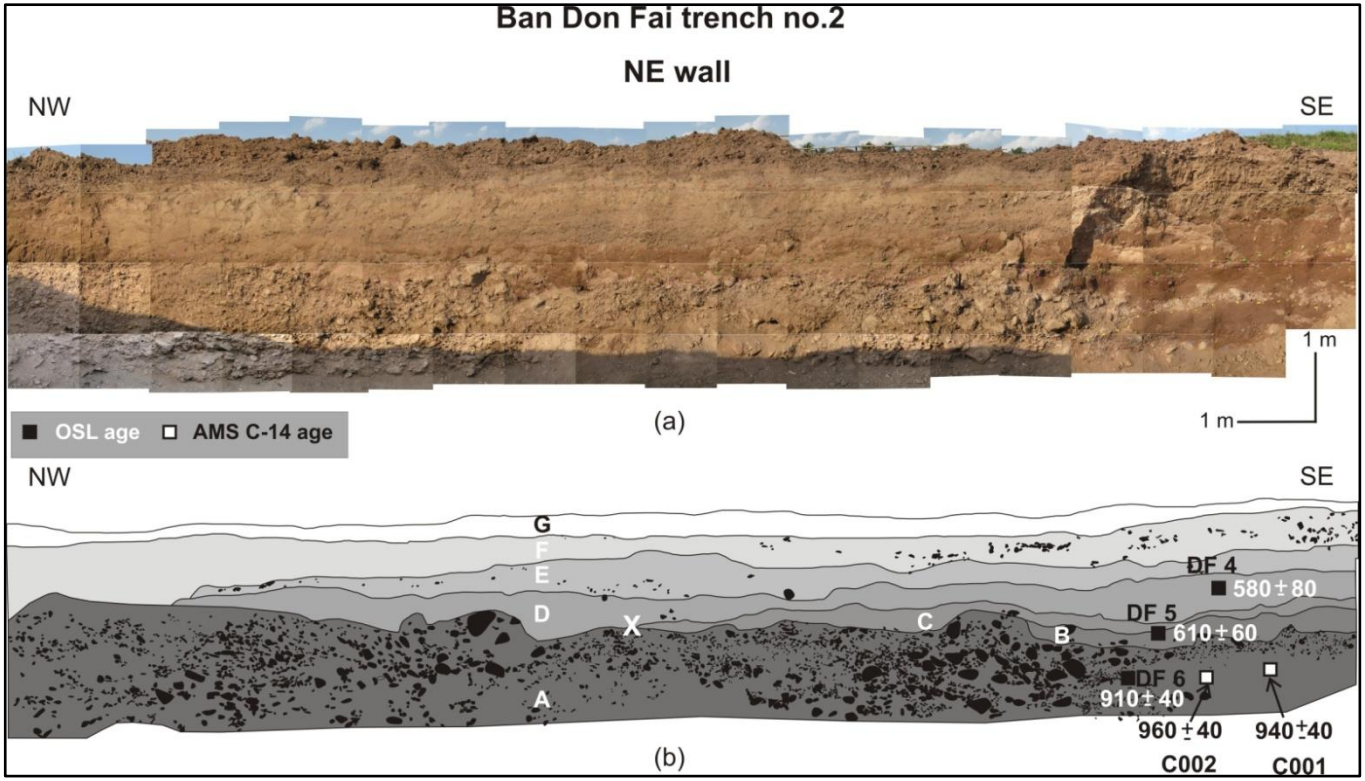

Fig. 58. Stratigraphy and ages of Quaternary sediments along a northeast wall in the Ban Don Fai trench no. 2 (a–b). Samples DF4–6 were collected for OSL dating, while samples C001–002 were also collected for AMS radiocarbon dating. The location of the trench is shown in Figs 21c and 23b. Unit A: gravel, sand, and silt with carbonaceous clay; Unit B: clayey sand; Unit C: sand with gravel; Unit D: sandy clay with minor gravel; Unit E: clayey sand with gravel; Unit F: sand and gravel; Unit G: top soil. The point marked ‘x’ indicates the location where unit C is absent.

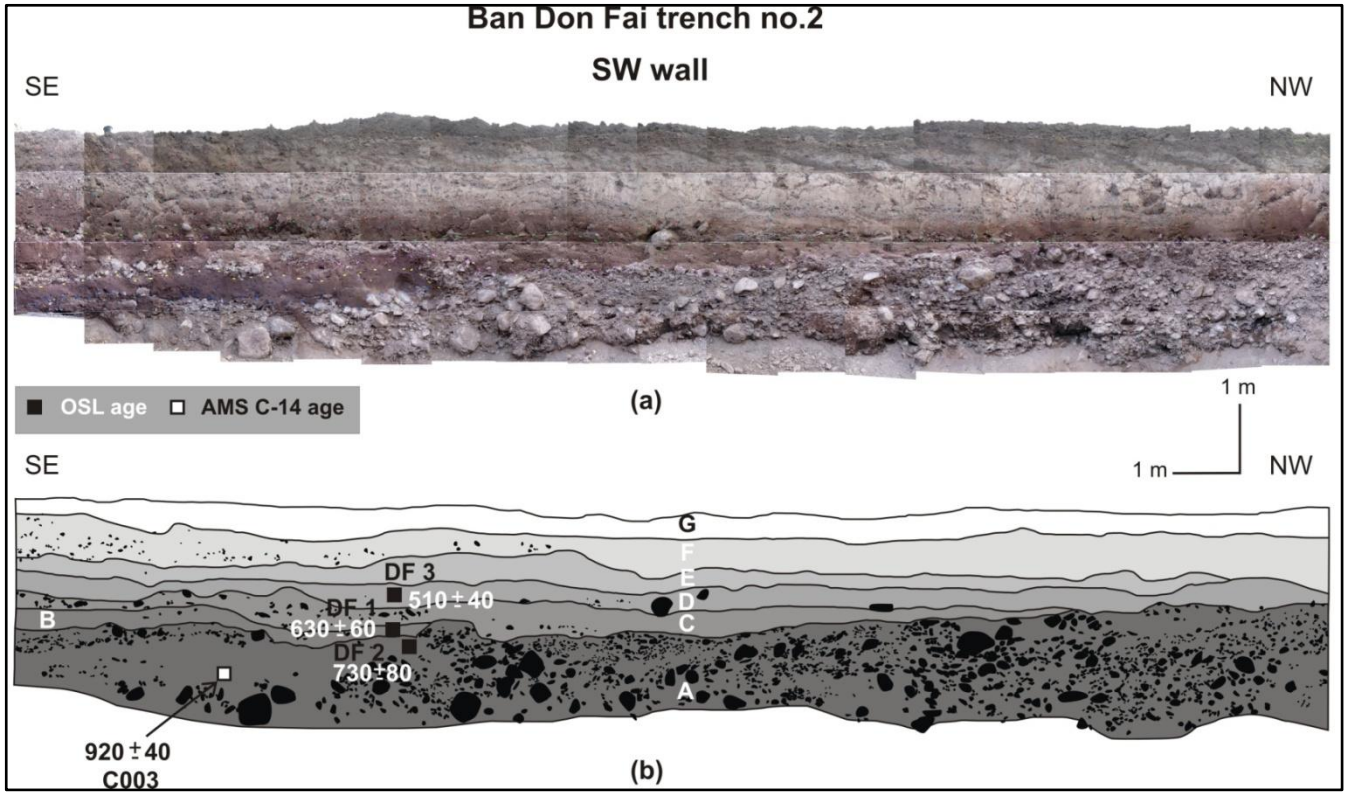

Fig. 59. Stratigraphy and ages of Quaternary sediments along a southwest wall in the Ban Don Fai trench no. 2 (a–b). Samples DF1–3 were collected for OSL dating, while sample C003 was also collected for AMS radiocarbon dating. The location of the trench is shown in Figs 21c and 23b. Unit A: gravel, sand, and silt with carbonaceous clay; Unit B: clayey sand; Unit C: sand with gravel; Unit D: sandy clay with minor gravel; Unit E: clayey sand with gravel; Unit F: sand and gravel; Unit G: top soil.

9. Paleoearthquake Events

9.1. Paleoearthquake events of the Mae Hong Son Fault

On the basis of field and geochronological data, eight paleoearthquake events have been identified along the Mae Hong Son Fault, as shown in Fig. 60. The evidence for these paleoearthquake events consists of offsets of stratigraphic units in the quarry, road cut, and trench walls, as well as geophysical data.

The first paleoearthquake event (F1; Fig. 51) may be related to movement of the Phra That Chom Kitti segment (no. 36 in Fig. 9c). The fault cuts units A and B, and terminates in the upper part of unit B. Unit A is offset vertically by *ca*. 30 cm. The sense of movement was mainly vertical, suggesting this is a normal fault. The fault cuts through a sedimentary unit (unit B) that was deposited at *ca*. 89,720 yr BP, and hence the movement must be younger than the unit. However, no geochronological ages are available to constrain the depositional age of the lower part of unit C. Thus, based on the OSL and TL ages of unit B (Fig. 51), it is possible that this fault was active at *ca*. 78,000 yr BP.

The orientation and location of the Nong Mae La segment (no. 42 in Fig. 9c) are based on the results of radon and resistivity surveys conducted on Quaternary sedimentary strata (Figs 26 and 29). In the Nong Mae La trench, it is possible that this fault cuts unit A, and possibly terminates in the middle part of unit B (Figs 52 and 53). However, evidence for this faulting event is not apparent in the younger sediments (upper part of unit B and units C–G). Based on the OSL ages for unit B, this faulting event might possibly have occurred after 79,850 yr BP (Fig. 53). It is inferred that this faulting was contemporaneous with the first paleoearthquake in the Phra That Chom Kitti segment.

The second paleoearthquake event may be related to movement on the Ban Pae segment (no. 31 in Fig. 9c), as reported by DMR [2007] (although the age of this fault movement has been reassessed here based on data from the trench). The fault cuts through a

sedimentary unit that was deposited at *ca.* 69,740 yr BP (for the depositional ages, see Fig. 60), and the movement must therefore be younger than this unit. However, no geochronological dates are available to constrain the timing of the cessation of fault movement. Thus, based on the OSL age from DMR [2007], the timing of the event is roughly constrained as having occurred at *ca.* 68,000 yr BP.

Data for the third paleoearthquake event, which was identified from radon and resistivity investigations (Figs 28 and 31) and OSL ages from the Mok Chum Pae trench (see Figs 56 and 57), indicate that faulting occurred on the Mok Chum Pae segment (F1 in Figs 56 and 57); the fault cuts through weathered rock and overlying sediments in the trench [EGAT, 2012]. The fault cuts layers of sediment that were deposited during the period 58,670 to 57,670 yr BP (Fig. 56), and this displacement is interpreted as representing a third paleoearthquake event, which might have occurred at *ca.* 58,000 yr BP.

The orientation and location of Huai Kia segment no. 1 (no. 39 in Fig. 9c) are based on the results of radon and resistivity surveys conducted on Quaternary sedimentary strata (Figs 27 and 30). However, evidence for this faulting event is not apparent in the trench. Based on the OSL age for unit B (59,920 ± 4,240 yr BP) and the tilting of the gravel bed (unit A) on the mountain side (Figs 54 and 55), it is assumed that this faulting event might possibly have occurred either before 59,920 yr BP or during the deposition of unit B (59,920–56,490 yr BP). Thus, it is inferred that this faulting was contemporaneous with the third paleoearthquake on the Mok Chum Pae segment.

The fourth paleoearthquake event (F2; Fig. 51) is possibly related to movement on the Phra That Chom Kitti segment. Units B and C and the lower (but not upper) part of unit D are cut by fault F2. The fault cuts layers of sediment deposited during the period 53,300–41,240 yr BP, and this is interpreted as a fourth paleoearthquake event (Fig. 51) that might have occurred at *ca.* 48,000 yr BP.

The fifth paleoearthquake event (F3; Fig. 51) may be related to movement on the Phra That Chom Kitti segment. The fault cuts units A–F, and, except for the youngest unit, all units to the right of the fault (Fig. 51) are offset vertically by *ca*. 30 cm, whereas all units to the left side of the fault are offset vertically by *ca*. 50 cm. It is interpreted that this fault is mainly a normal fault, as the fault cuts the lower part of unit E and terminates in the upper part of unit F. The fault cuts sediment layers that were deposited during the period 39,300–36,540 yr BP, and this is interpreted as a fifth paleoearthquake event (Fig. 51) that might have occurred at *ca.* 38,000 yr BP.

The sixth paleoearthquake event occurred at *ca*. 28,000 yr BP. Evidence for this event was encountered on the Phra That Chom Kitti segment. The fault is observed in the centre of the quarry wall (F4 in Fig. 51); the fault trace cuts units A–F and terminates in the lower part of unit G. Movement of the fault caused displacements of units E and F, and created the sharp contact between these two units. It is interpreted that movement during the sixth event was principally lateral (strike-slip). An offset defined by the shift of a ridge crest suggests a left-lateral strike-slip sense of movement.

Evidence for the seventh paleoearthquake event consists of a fault on the western side of the quarry at Mae La Noi School (F1 in Fig. 50). The fault cuts units A and B, and the latter unit yields an OSL and TL age of 24,260–18,500 yr BP. A well-defined slickenside on the foot wall of the fault, located on the western side of the quarry wall, has a pitch of 15° (Fig. 33a and c). The low pitch (15°) suggests that movement was nearly horizontal. In contrast to the other movements, the vertical offset of units A and B on the western side of the quarry wall is *ca*. 1.0 m; it seems unlikely that a single movement on this fault (F1 in Fig. 50) would generate this amount of offset on the western side of the quarry. Thus, it is interpreted that repeated movements may have occurred along this fault. Because offset is

observed in unit F, it is interpreted that fault movement may post-date the deposition of unit B, and that faulting may have occurred at *ca.* 18,000 yr BP.

The latest recognized paleoearthquake event occurred on the Mae La Noi segment no. 1 (labelled no. 25 in Fig. 9c). Evidence of movement is visible on a fault on the eastern side of the quarry wall (F2 in Fig. 50). Units A–F and the lower part of unit G are displaced along a dipping fault plane. The gravel bed in the upper part of unit G is not cut by the fault (X3 in Fig. 50a and c), which indicates that faulting must have terminated before deposition of the gravel bed. No offsets are observed in younger units (i.e., units H and I). A slickenside on the hanging wall of the fault, on the eastern side of the quarry, has a pitch of 60° (Fig. 33b and c). The pitch angle indicates that fault movement was oblique (i.e., a combination of reverse and sinistral strike-slip movement). Based on the OSL and TL dates of unit G (Fig. 50c), the most recent movement on the fault occurred between 8,300 and 7,150 yr BP. It is inferred that this paleoearthquake occurred at *ca.* 8,000 yr BP. The orientation and location of the Mok Chum Pae segment are based on the results of radon and resistivity surveys conducted on Quaternary sedimentary strata (Figs 28 and 31). However, evidence for this youngest faulting event is not clear in the trench (Figs 56 and 57). However, high radon emissions in the trench may be related to the most recent paleoearthquake on the Mok Chom Pae segment (Figs 28, 56 and 57). It is possible that this faulting was contemporaneous with the most recent paleoearthquake in the Mae La Noi basin.

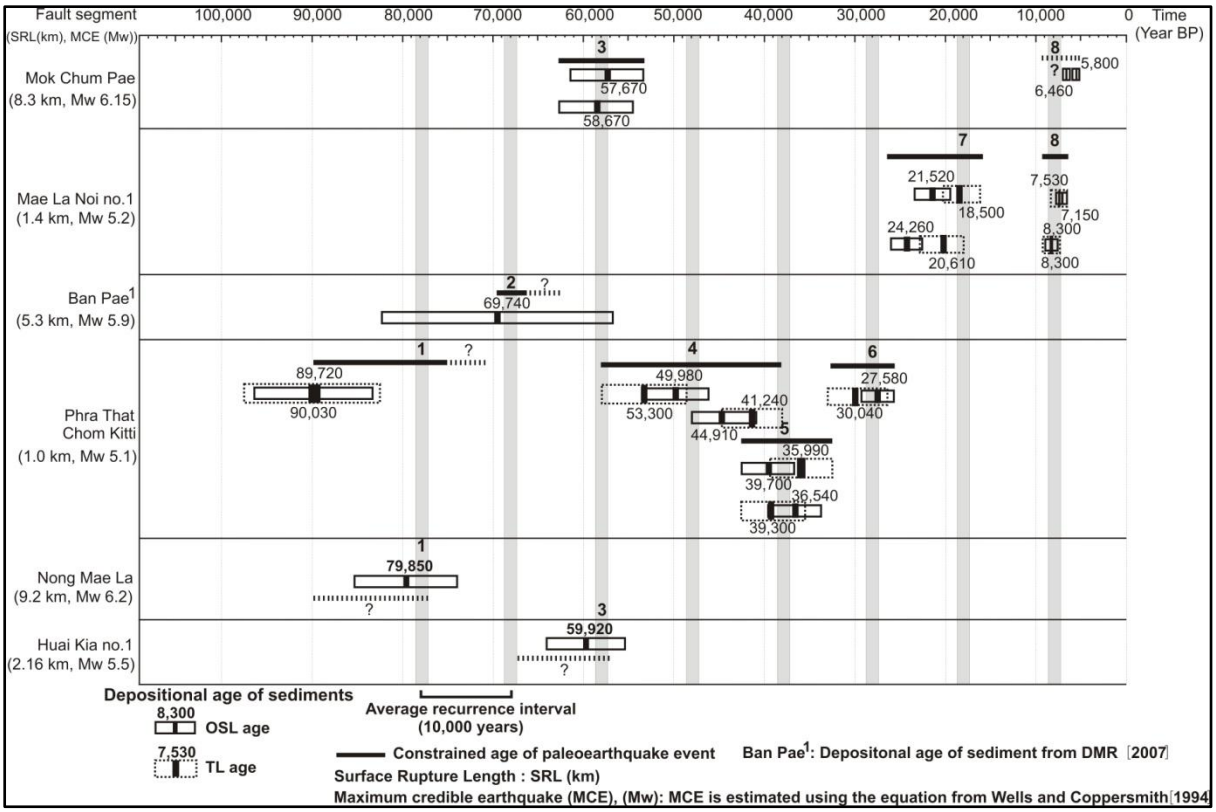

Fig. 60. Diagram showing the depositional ages of sediments in the quarry, the road cut, and the excavated trench walls (see location map, Fig. 9c), the eight paleoearthquake events (Nos 1–8) that occurred during the past 90,000 years on six segments of the Mae Hong Son Fault, and the recurrence interval of faulting on the Mae Hong Son Fault (*ca.* 10,000 years). The OSL and TL ages are used to constrain the ages of the paleoearthquake events.

9.2. Paleoearthquake events of the Thoen Fault

Based on the results of this study and previous trenching studies of Pailoplee *et al.* [2009], three paleoearthquake events have been identified along the Thoen Fault, as shown in Fig. 61.

The first paleoearthquake event may be related to movement of the Ban Mai (no. 2 in Fig. 21c) and Doi Ton Ngun (no. 6 in Fig. 21c) segments of the Thoen Fault in the Lampang basin, as reported by Pailoplee *et al.* [2009]. Pailoplee *et al.* [2009] excavated two trenches on the Ban Mai and Doi Ton Ngun segments. The Ban Mai segment records a single main faulting event, at 3,800 yr BP. To the southwest of the Ban Mai segment, the Doi Ton Ngun segment also records the first faulting event, at 3,500 yr BP. It is inferred that the faulting event occurred on the Doi Ton Ngun segment was contemporaneous with the faulting event on the Ban Mai segment. Based on the AMS radiocarbon and TL ages from Pailoplee *et al.* [2009], the timing of the first paleoearthquake event is roughly constrained as having occurred at *ca.* 3,700 yr BP (Fig. 61).

The second paleoearthquake event may be related to movement on the Doi Ton Ngun segment (no. 6 in Fig. 21c), as reported by Pailoplee *et al.* [2009]. The Doi Ton Ngun segment records an evidence of a second faulting event, at 1,800 yr BP. Thus, based on the AMS radiocarbon and TL ages from Pailoplee *et al.* [2009], the timing of the second event is roughly constrained as having occurred at *ca.* 1,800 yr BP.

The latest recognized paleoearthquake event possibly occurred on the Ban Don Fai segment (1 in Fig. 21c) using results on morphotectonic landforms and geochronological data. Although the geomorphology and geomorphic indices (see details of analyses of geomorphic indices in Wiwegwin [2010]; Wiwegwin *et al.* [2011]) in the study area indicate active normal faulting, sedimentary units exposed in a trench at Ban Don Fai area show no evidence of recent fault movement. At Ban Don Fai trench no. 2, AMS radiocarbon and OSL dates

show that the sediments of the lowest unit (Unit A in Fig. 58 and 59) were deposited between 960 and 910 years ago. The lack of evidence in the trench for recent fault movement indicates that the fault is located below the depth of the trench. The timing of this fault movement might be younger than those of the second paleoearthquake event. Unfortunately, no geochronological ages are available to constrain the maximum age of fault movement in the trench. Thus, it is roughly inferred that the most recent movement upon the Ban Don Fai segment of the Thoen Fault occurred more than 960 years ago.

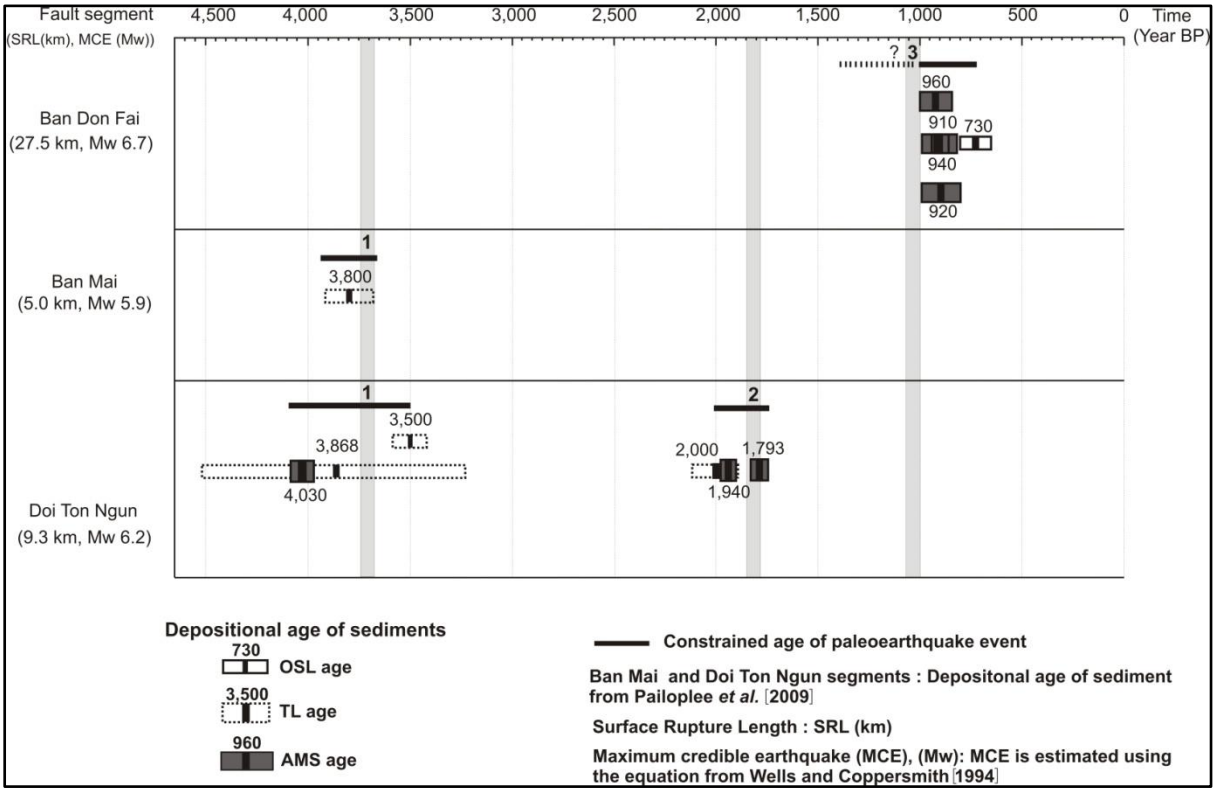

Fig. 61. Diagram showing the depositional ages of sediments in the excavated trench walls (see location map, Fig. 21c), the three paleoearthquake events (Nos 1–3) that occurred during the past 4,500 years on three segments of the Thoen Fault. The AMS radiocarbon, OSL and TL ages are used to constrain the ages of the paleoearthquake events.

10. Discussion

10.1. Timing of Mae Hong Son Fault and Thoen Fault movements

10.1.1. Timing of Mae Hong Son Fault movement

A preliminary study of the timing of movement on the Mae Hong Son Fault revealed that the most recent detected movement of the fault occurred during the period of 890,000–320,000 yr BP, as determined from TL ages on sediments [Takashima and Maneenai, 1995; Hinthong, 1997]; it is possible that this timing is more recent than that proposed by previous researchers. In previous studies, the samples for TL dating may have been collected from fault gouge, in which partial bleaching of the luminescence signal may have occurred; in this case, the TL ages would overestimate the actual age of fault movement. In this study, the quartz grains for OSL and TL dating were collected from young sedimentary strata that are cut by faulting, although the samples themselves are not disturbed by the faulting (Fig. 50). Thus, the measured OSL and TL ages from this study possibly represent the most recent movement of the Mae Hong Son Fault. The most recent movement of the Mae Hong Son Fault might have occurred several thousand years ago. The results of this study are consistent with those of Wiwegwin *et al.* [2014]. On the other hand, if the most recent movement of the Mae Hong Son Fault proposed by Takashima and Maneenai [1995] and Hinthong [1997] is correct, the timing of Mae Hong Son Fault movement as determined in previous studies might represent an early stage of fault activity, which would suggest that the Mae Hong Son Fault has been active since at least the late Pleistocene, as proposed by Takashima and Maneenai [1995] and Hinthong [1997], and that the fault is still active today.

10.1.2. Timing of Thoen Fault movement

Geomorphological features and geomorphic indices (see details of analyses of geomorphic indices in Wiwegwin [2010]; Wiwegwin *et al.* [2011]) in the study area indicate active normal faulting. However, the sediments in the trench at Ban Don Fai area show no clear-cut evidence of recent fault movement. At Ban Don Fai trench no. 2, AMS radiocarbon and OSL dates show that the sediments of the lowest unit (Unit A in Figs 58 and 59) were deposited between 960 and 910 years ago. The lack of evidence in the trench for recent fault movement indicates that the fault is located below the depth of the trench; i.e., the most recent movement upon the fault pre-dates the deposition of the oldest sediments in the trench. In the case that the trench did not intercept the fault trace, the most recent movement on the fault may be younger than the oldest sediments in the trench; however, the location of the trench was decided based on a careful analysis of aerial photographs, and based on the distribution of morphotectonic landforms observed in the field. Thus, it is possible that the most recent movement on the Ban Don Fai segment occurred more than 960 years ago. It is also noted that no geochronological ages are available to constrain the maximum age of fault movement in the trench. Alternatively, the timing of the most recent movement on the Ban Don Fai segment might have occurred after the timing of the second paleoearthquake event (1,800 yr BP) to 960 yr BP. On the other hand, the most recent movement on the Ban Don Fai segment might possibly be the same event as the movement on the Doi Ton Ngun segment (i.e., second paleoearthquake event).

10.2. Average recurrence interval of Mae Hong Son Fault and Thoen Fault activities

10.2.1. Average recurrence interval of Mae Hong Son Fault activity

The average recurrence interval of movement on the Mae Hong Son Fault may be on the order of 10,000 years (Fig. 60). Other active faults in northern Thailand are characterized

by relatively long recurrence intervals of thousands to tens of thousands of years (Table 12) [Bott *et al.*, 1997; Kosuwan *et al.*, 1999; Fenton *et al.*, 2003]. Based on this study, the recurrence interval of the Mae Hong Son Fault is consistent with the results of previous studies on active faults in Thailand.

Wells and Coppersmith [1994] proposed an estimate of paleomagnitude based on surface rupture length,

$$\mathbf{M = 5.08 + 1.16 \log (SRL)} \qquad \mathbf{(3)}$$

where SRL is the surface rupture length determined as the straight-line distance between the rupture endpoints. Using Equation (3), all paleomagnitudes of paleoeartquake events on the studied fault segments of the Mae Hong Son Fault were shown in Fig. 60, and the paleomagnitude of the latest paleoearthquake event (possibly occurring at *ca*. 8,000 yr BP) on the 1.4-km Mae La Noi segment no. 1 was Richter 5.2.

This estimated recurrence interval suggests that Mae La Noi segment no. 1 may have ruptured approximately every 10,000 years. This segment has not ruptured during the last 8,000 years; it is considered that the next earthquake event generated by this fault segment may be of Richter magnitude 5.2. For the Phra Tha Chom Kitti segment, the magnitude of past earthquake events was approximately Richter 5.1, [as derived from equation (3)]. If this estimate of the recurrence interval is correct, the last earthquake event on this segment possibly occurred several thousand years ago. However, the last movement on this segment observed in the road-cut wall was at about 28,000 yr BP. It is possible that a younger fault has not yet been detected, and will be recorded in other areas along the fault trace. These unresolved questions suggest a need to study trenches in young sedimentary deposits in other areas along the fault trace so as to constrain the timing of fault movements on this segment. By contrast, the Phra That Chom Kitti segment has not ruptured in the last 28,000 years.

Table 12. Summary of the characteristics of active faults in northern Thailand, northwestern Laos, and eastern Myanmar.

Fault (length, km)	Segment	Orientation	Sense of movement	Relative age of last movement: Trench investigations (Kyr)	Relative age of last movement: Geomorphic relationships and pedologic development	slip rate (mm/yr)	Recurrence (Kyr)	Maximum credible earthquake (MCE), (Mw)	References
Thoen	Ban Mai	NE–SW	Normal fault and subordinate left-lateral strike-slip fault	3.80	Quaternary	0.06	–	5.9	MCE from this study; Pailoplee *et al.* [2009]
(120 km)	Doi Ton Ngun	ENE–WSW	Normal fault and subordinate left-lateral strike-slip fault	1.80	Quaternary	0.18	1.70	6.2	MCE from this study; Pailoplee *et al.* [2009]
	Ban Don Fai	NE–SW	Normal fault	≥0.96	Holocene	–	–	6.7	This study; Wiwegwin *et al.* [2011]
	–	NE–SW	Normal fault and subordinate left-lateral strike-slip fault	–	Holocene	0.60	1.70–2.50	7.5	Fenton *et al.* [2003]
Uttaradit	Khun Non	NE–SW	Oblique-slip fault	2.50	Quaternary	0.19–0.21	–	6.51	Saithong *et al.* [2011]
(160 km)			(a conbination of normal and left-lateral strike-slip fault)						
Mae Chan	Mae Ai	ENE–WSW	Left-lateral strike-slip fault	17.00	Holocene	0.7	–	–	Kosuwan *et al.* [1999, 2003]
(140 km)	–	ENE–WSW	Left-lateral strike-slip fault	–	Holocene	0.3–3.0	–	7.5	Lacassin *et al.* [1998]; Fenton *et al*. [2003]
	Kio Satai	ENE–WSW	Oblique-slip fault (a conbination of reverse and left-lateral strike-slip fault)	2,000	Holocene	0.15–0.29	1.00	6.8	DMR [2009]
Mae Ping	Khao Mae Song	NW–SE	Right-lateral strike-slip fault	15.00	Pleistocene	0.17–0.73	–	6.7	Saithong [2006]; Saithong *et al.* [2005]
(230 km)	–	NW–SE	Right-lateral strike-slip fault	–	Quaternary	–	–	–	Le Dain et al. [1984]

Table 12. (continued)

Fault (length, km)	Segment	Orientation	Sense of movement	Relative age of last movement		slip rate (mm/yr)	Recurrence (Kyr)	Maximum credible earthquake (MCE), (Mw)	References
				Trench investigations (Kyr)	Geomorphic relationships and pedologic development				
Three Pagoda (350 km)	–	NW–SE	Right-lateral strike-slip fault	–	Holocene	0.5–2.0	–	7.5	Fenton *et al.* [2003]
Mengxian (75 km)	–	ENE–WSW	Left-lateral strike-slip fault	–	Quaternary	4.8 ± 0.2	–	–	Lacassin *et al.* [1998]
Nam Ma (177 km)	–	ENE–WSW	Left-lateral strike-slip fault	–	Quaternary	2.4 ± 0.4	–	–	Lacassin *et al.* [1998]
Sagaing Fault (1000 km)	–	N–S	Right-lateral strike-slip fault	M 7.3 1930 Pegu (Bago) earthquake	Holocene	18.00	≥0.16	–	Tsutsumi and Sato [2009]
Mae Hong Son (202 km)	Mae La Noi no.1	NE–SW	Oblique-slip fault (a conbination of reverse and left-lateral strike-slip fault)	8.00	Holocene	0.05–0.13	10.00	5.2	this study
	Phra That Chom Kitti	NE–SW	Oblique-slip fault (a conbination of normal and left-lateral strike-slip fault)	28.00	Pleistocene	0.03–0.05	10.00	5.1	this study

Table 12. (continued)

Fault (length, km)	Segment	Orientation	Sense of movement	Relative age of last movement		slip rate (mm/yr)	Recurrence (Kyr)	Maximum credible earthquake (MCE), (Mw)	References
				Trench investigations (Kyr)	Geomorphic relationships and pedologic development				
Mae Hon Son (202 km)	Nong Mae La	N–S	Normal fault	78	Pleistocene	–	10(?)	6.2	this study
	Huai Kia no. 1	NW–SE	Right-lateral strike-slip fault	≥58	Pleistocene	–	10(?)	5.5	this study
	Mok Chum Pae	NE–SW	Left-lateral strike-slip fault	58	Pleistocene	–	10(?)	6.1	this study

Remark: MCE is estimated using the equation from Wells and Coppersmith [1994].

10.2.2. Average recurrence interval of Thoen Fault activity

Two paleoearthquake events might have occurred at 3,700 and 1,800 yr BP based on Pailoplee *et al.* [2009] data. The latest paleoearthquake event might have ruptured more than 960 yr BP (Fig. 61). These paleoearthquake data are insufficient in terms of determining the average recurrence interval of movement on the Thoen Fault. Fenton *et al.* [2003] and Pailoplee *et al.* [2009] proposed that the recurrence interval of movement on the Thoen Fault may be on the order of 1,700–2,500 years (Table 12). Therefore, it is possible that the recurrence interval of the Thoen Fault was *ca.* 1,000–1,900 years based on three paleoearthquake events of this study.

Using Equation (3), all paleomagnitudes of paleoeartquake events on the studied fault segments of the Thoen Fault were shown in Fig. 61, and the paleomagnitude of the latest paleoearthquake event (possibly occurring more than 960 yr BP) on the 27.5-km Ban Don Fai segment was Richter 6.7. This segment has not ruptured during the last 1,000 years; it is considered that the next earthquake event generated by this fault segment may be of Richter magnitude 6.7. The next earthquake event on the Doi Ton Ngun segment possibly may be of Richter magnitude 6.2, [as derived from equation (3)]. For the Ban Mai segment, the magnitude of past earthquake events was approximately Richter 5.9, [as derived from equation (3)]. The latest faulting event generated by these fault segments has not yet been detected, and will be recorded in other areas along the fault traces. These unresolved questions suggest a need to study trenches in young sedimentary deposits in other areas along the fault traces so as to constrain the timing of fault movements on these segments. By contrast, the Ban Mai and Doi Ton Ngun segments have not ruptured in the last 3,700 and 1,800 years, respectively.

10.3. Slip rate of the Mae Hong Son and Thoen Faults

10.3.1. Slip rate of the Mae Hong Son Fault

In this study, the slip rate was determined from the vertical offset of stratigraphic units and the ages of sedimentary deposits displaced by the fault. For example, an average slip rate on Mae La Noi segment no. 1 can be estimated using the average or mean offset of the bases of units B–G and a properly estimated age of the base of unit B (Fig.50). The average vertical offset of units B–G is *ca*. 1.0 m. Using 20,000 yr BP as the age of the base of unit B, an average slip rate is *ca.* 0.05 mm/yr.

The slip rate can also be estimated from the amount of displacement during the most recent fault movement, and the age of the movement (8,000 years), which yields a slip rate of *ca.* 0.13 mm/yr. This slip rate is useful in seismological research required to produce seismic hazard maps.

The average slip rate on the Mae Hong Son Fault can also be estimated from

Slip rate = D/R **(4)**

where D is the slip per event and R is the recurrence interval. Based on data of this study, D is in the range of 30 cm to 1 m (determined from the vertical offsets on faults in the quarry and road-cut walls) and R is *ca*. 10,000 years; therefore, the average slip rate is *ca.* 0.03–0.10 mm/yr. These estimates suggest that movements on the Mae Hong Son Fault, particularly on Mae La Noi segment no. 1 and the Phra That Chom Kitti segment, are in the range of *ca.* 0.03–0.13 mm/yr, which is consistent with the slip rate of active faults in northern Thailand (Table 12). On the other hand, DMR [2007] reported that the slip rate on Ban Pae segment no. 31 (Fig. 9c) is *ca*. 0.0028 mm/yr; however, this estimate, which is considerably less than slip rate of this study, was based on data from the second paleoearthquake event (68,000 yr BP), possibly suggesting that the late Quaternary was a period of increased faulting activity in this

region, or that recently renewed activity followed a prolonged period of quiescence. In either case, the slip rate of the Mae Hong Son Fault is quite low (0.03–0.13 mm/yr).

10.3.2. Slip rate of the Thoen Fault

The slip rate of the Thoen Fault from this study cannot be estimated using the results of this study because the sediments in the trench at Ban Don Fai no. 2 show no clear-cut evidence of recent fault movement (i.e., no offset of stratigraphic units). Fenton *et al.* [2003] and Pailoplee *et al.* [2009] proposed that the slip rate of the Thoen Fault was *ca.* 0.06–0.6 mm/yr (Table 12). Therefore, it is inferred that the slip rate of the Thoen Fault might be a *ca.* 0.06–0.6 mm/yr as proposed by them. However, more trenching studies across the fault segments of the Thoen Fault are necessary to estimate its slip rate.

10.4. Neotectonics of the Mae Hong Son and Thoen Faults

The Eocene–Oligocene collision of the Indian and Eurasian plates resulted in N–S compressive stresses in the Indochina region. It is likely that the N–S compressive stresses caused dextral motion on major NW–SE trending faults and sinistral motion on the NE–SW faults in northern Thailand. The movement on faults accompanying regional E–W extension during the late Oligocene–Miocene initiated the formation of Neogene basins. It is possible that the onset of Cenozoic basin formation in the Mae Hong Son region and the Lampang basin occurred during this time. It is also proposed that strike-slip fault movements and E–W extensional tectonics in the Neogene played a critical role in the generation of neotectonic patterns and active faulting. On this basis, the following model for basin development associated with faulting in the Mae Hong Son region and the Lampang basin has proposed (illustrated in Figs 62 and 63).

10.4.1. Neotectonics of the Mae Hong Son Fault

The N–S trending Mae Hong Son Fault (the Mae Yuam Fault), is interpreted as the boundary between the Sibumasu block and the Inthanon zone [Ueno, 1999; Hisada *et al.*, 2004], represents a splay fault of the NW–SE trending Mae Ping Fault to the south [Morley *et al.*, 2007]. Based on remote sensing data, the NW–SE trending Mae Hong Son Fault in the south possibly merges into the Mae Ping Fault. It is possible that dextral movement on the Mae Ping Fault during the Oligocene caused reactivation of Mae Hong Son Fault movement. This movement may also have initiated E–W extension and grabens that developed into sedimentary basins in the Mae Sariang area, as suggested by Uttamo *et al.* [2003]. A series of triangular facets observed along the Nong Mae La and Kon Phung segments may be evidence that vertical dip-slip movement resulted in E–W extension.

During the Miocene, the N–S Sagaing Fault was an active right-lateral strike-slip fault system [Morley, 2002]. The Mae Hong Son Fault possibly shows the same sense of movement as that of the Sagaing Fault. Within the Mae Hong Son Fault zone, two fault strands (zones A and B; Figs 9c and 62) contemporaneously generated the N–S Quaternary Mae Sariang basin during the late Pleistocene. Some faults strands (e.g., zone C) located within zones A and B may also have been generated (Fig. 62). Morphotectonic landforms indicative of active faults also developed at this time, as indicated by features such as offset streams and linear valleys, and the development of scarps related to active faulting. From the late Pleistocene until the present, the region has been influenced by the development of an alluvial plain. However, present-day tectonic processes are still going-on.

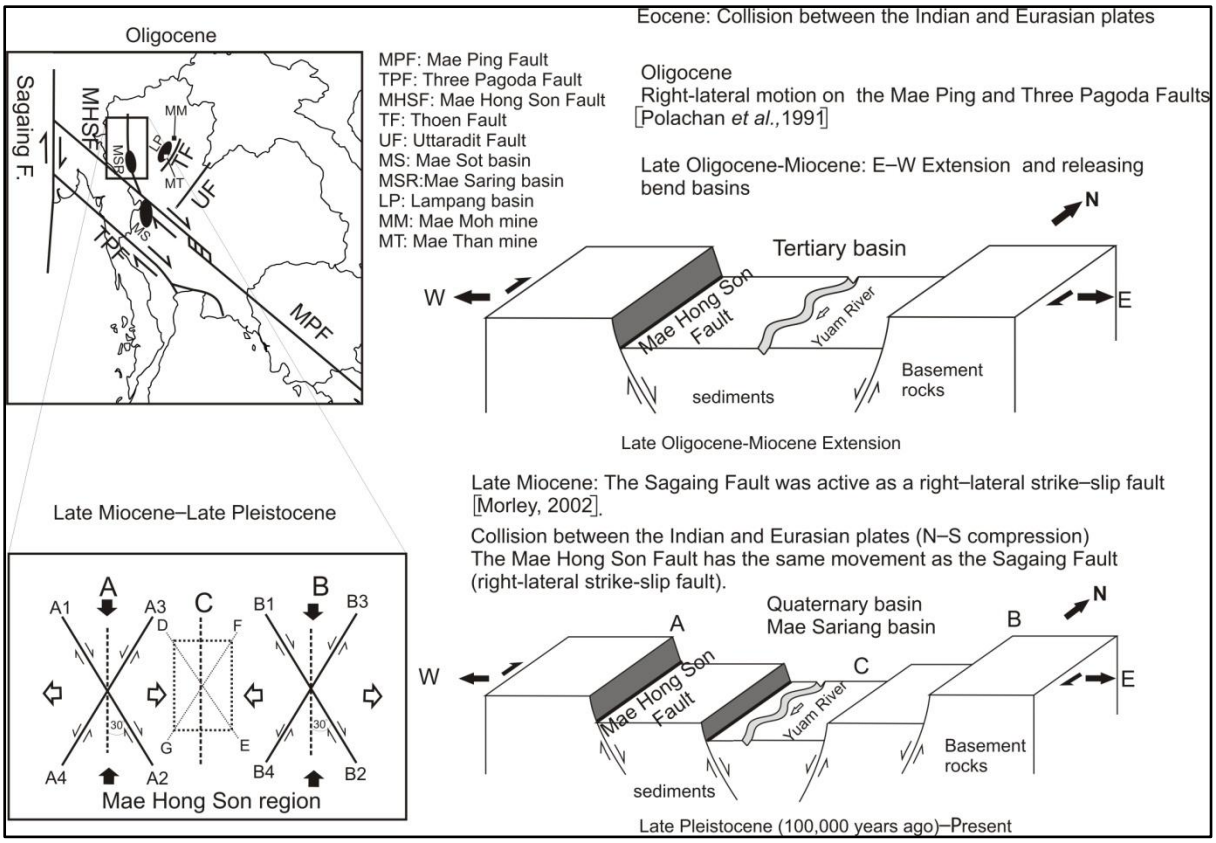

Fig. 62. Simplified model explaining the neotectonics of the Mae Hong Son Fault.

10.4.2. Neotectonics of the Thoen Fault

The NW–SE and NE–SW conjugate strike-slip faults in northern Thailand have been active during Oligocene [Polachan *et al.,* 1991]. This movement may have initiated E–W extension and grabens that developed into several sedimentary basins in the Lampang basin during middle–late Miocene, as suggested by Morley et *al.* [2001]. A series of triangular facets observed along the Sop Prap segments may be evidence that vertical dip-slip movement resulted in E–W extension (Fig. 63).

During the late Miocene–Pliocene, the extension continuously occurred in northern and central Thailand [Morley et *al.,* 2001]. To the northeast of the Lampang basin, fault-slip data indicate that E–W to ENE–WSW extension dominated the evolution of the Mae Moh mine [Morley et *al.,* 2001]. A geological survey performed at the Mae Than mine (MT in Fig.

63) in the northern Sop Prap area confirmed the presence of NE–SW-striking normal faults [Morley *et al.,* 2001]. Inglethorpe *et al.* [1997] also reported the Pliocene diatomite deposits that were cut by normal faults in the Lampang basin. It is possible that the Thoen Fault was an extensional structure during this time.

During the late Quaternary, the NE–SW Thoen Fault shows evidence for predominantly normal displacement [Fenton *et al.,* 2003]. A sequence of alluvial gravels and lacustrine clays is cut by a NE–SW-striking normal fault along Highway 11 (from Lampang to Phrae) at 28 km from Lampang. This offset is exposed on the western side of the main escarpment along the Ban Mai segment. The total vertical displacement is 1.3–1.6 m [Charusiri *et al.,* 1997; Fenton *et al.,* 2003]. The timing of the faulting is interpreted to be Late Quaternary [Fenton *et al.,* 2003]. The relationship between this fault and the Thoen Fault remains unknown, although its location and orientation suggest that it is a synthetic fault (i.e., it has the same dip and sense of movement as the main fault) [Fenton *et al.,* 2003]. Based on seismological analysis, Bott *et al.* [1997] examined the focal mechanisms of three earthquakes in northern Thailand, indicating E–W to NW–SE extension. The remote-sensing data from this study also suggest that the morphotectonic landforms in the Lampang basin were caused only by dip-slip normal fault movements. Morphotectonic landforms indicative of active faults also developed at this time, as indicated by features such as linear valleys, and the development of scarps related to active faulting. From the late Quaternary until the present, the region has been influenced by the development of an alluvial plain. However, present-day tectonic processes are still going-on.

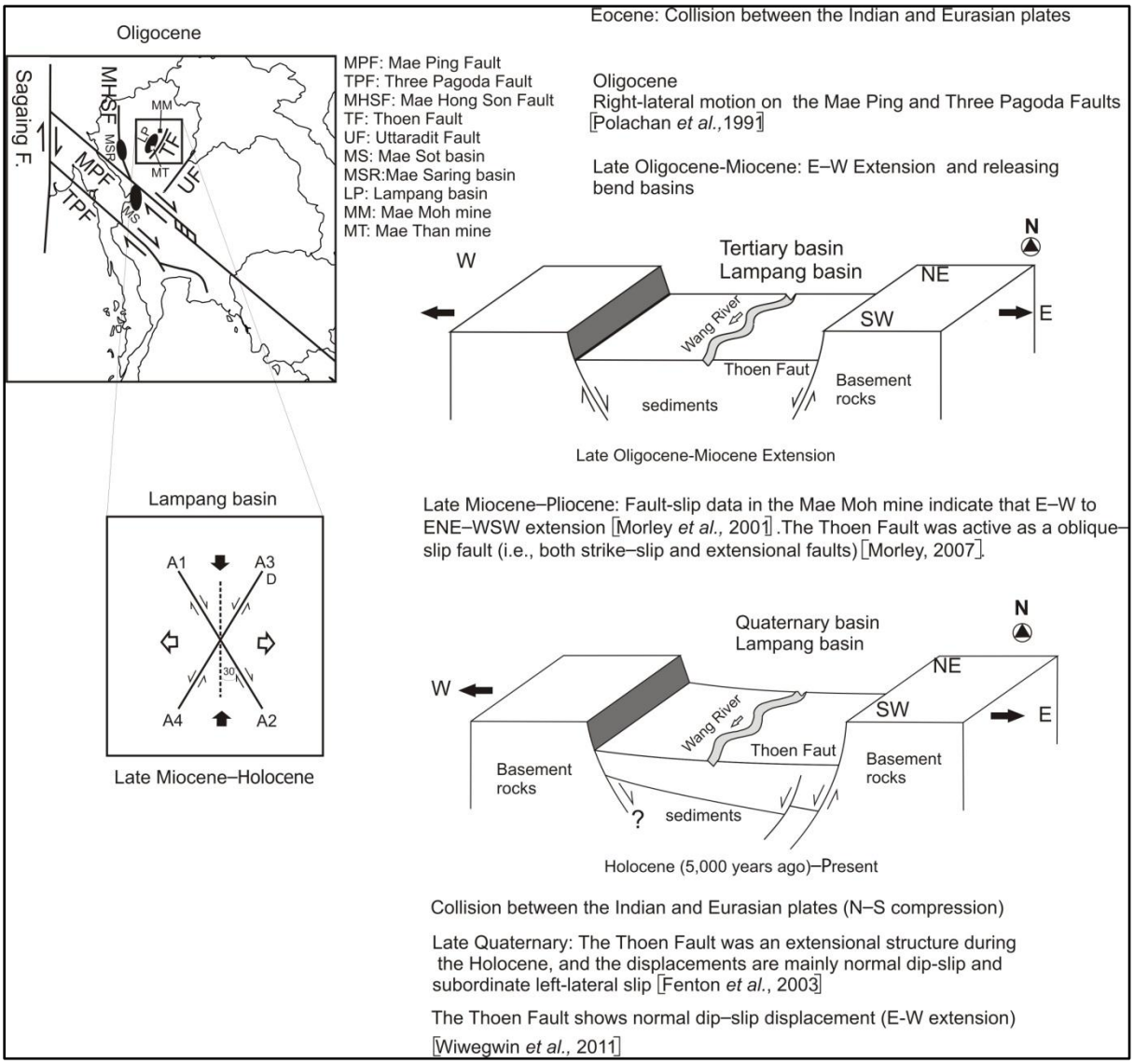

Fig. 63. Simplified model explaining the neotectonics of the Thoen Fault.

10.5. Relationships between neotectoic events and basin formation in the Mae Hong Son region and Lampang basin

The Mae Hong Son and Thoen Faults may possibly be controlled by pre-existing fabrics in basement rocks (e.g., the Mae Hong Son Fault is located on the boundary between the Sibumasu block and the Inthanon zone [Ueno, 1999; Hisada *et al.*, 2004]). The continuous collision between the Indian and Eurasian plates during the Oligocene possibly caused reactivation of faults on pre-existing fabrics in basement rocks of northern Thailand. The Mae Sariang basin might have formed during the Oligocene [Morley *et al.,* 2001]. It is possible that the N–S compression resulted from the collision between the Indian and Eurasian plates, and the accompanying E–W extensional tectonics possibly caused reactivation of the Mae Hong Son Fault movement.

To the east of the Mae Hong Son region, on the western side of Chiang Mai, the Mae Chaem and Li basins are of late Oligocene–late Miocene or Pliocene age [Pradidtan, 1989; Watanasak, 1989, 1990; Morley *et al.,* 2001]. These extensional basins were possibly formed during the uplift of the Doi Inthanon metamorphic core-complex in Chiang Mai area [Upton *et al.,* 1997; Morley *et al.,* 2001]. To the east of Chiang Mai area, extension generally appears to be of middle–late Miocene age. The age of the Cenozoic basins in northern Thailand is possibly young to the east. The Lampang basin may have been active during the middle–late Miocene or Pliocene [Morley *et al.,* 2001]. As explained above, it is possible that the Mae Hong Son Fault might have been reactivated by the E–W extensional tectonics after the Oligocene; subsequently the Thoen Fault might have been reactivated either by the E–W extensional tectonics or metamorphic core-complex activity after the Oligocene. At present, the Mae Hong Son and Thoen Faults are active, and the movement of two active faults might have resulted from the collision between the Indian and Eurasian plates.

10.6. The Mae Hong Son Fault and Thoen Fault activities

In northern Thailand, earthquake events caused by active faults have been reported on the basis of trench investigations (Table 12). However, the level of activity on the Mae Hong Son Fault seems low by comparison with the timing of the latest fault movement and slip rates on and other active faults in northern Thailand (especially comparison with those of the Thoen Fault). The NW–SE trending Mae Ping and Three Pagoda Faults are the principal right-lateral strike-slip faults in the area; however, the NE–SW trending Mae Chan, Thoen and Uttaradit Faults are left-lateral strike-faults which are truncated by the NW–SE trending right-lateral strike-slip faults [Polachan *et al.*, 1991]. To the west of northern Thailand in Myanmar, the N–S Sagaing Fault, which is the most active fault in the region, exhibits dextral displacement [Vigny *et al.*, 2005; Morley *et al.*, 2011]. The Mae Ping Fault extends into Myanmar (Fig. 1), where it either merges with or is cut by the N–S trending Sagaing Fault. Movement on the Sagaing Fault was continuous during collision of the Indian and Eurasian plates [Morley, 2002]. Displacement may also have occurred on the NW–SE trending Mae Ping Fault. Because the Mae Hong Son Fault is probably a splay fault of the Mae Ping Fault [Morley *et al.*, 2007], it may also have moved during this time. However, the NE–SW trending faults on the Mae Hong Son Fault, which are conjugate faults, may have moved slightly as well. Based on Global Position System (GPS) data, Yunnan is experiencing SSW–WSW motions relative to Sundaland (including Thailand) that are associated with clockwise rotation of blocks immediately south of the eastern Himalayan syntaxis [Simons *et al.*, 2007]. Block motion diminishes from *ca.* 12–13 mm/yr SSW in the east of Yunnan, to *ca.* 6 mm/yr WSW in the west of Yunnan, while displacements in northern Thailand are *ca.* 2–3 mm/yr to ENE [Simons *et al.*, 2007]. The ENE–WSW and NE–SW trending faults (i.e., Mae Chan, Thoen and Uttaradit Faults) have been displaced in northern Thailand, and these displacements are consistent with the displacement of northern Thailand as measured from

GPS data. Thus, it is possible that the Thoen Fault is more active than the Mae Hong Son Fault, which locates near the Sagaing Fault in Myanmar.

The numbers and magnitudes of recorded earthquakes decrease southwards towards Thailand [Morley, 2007; Morley *et al.*, 2011], and stress magnitudes in the Yunnan region also progressively diminish to very low levels in northern Thailand [Morley, 2007; Morley *et al.*, 2011]. However, micro-earthquake events recorded from the TMD and RTNSRS have been observed in the northern Thailand (Fig. 3). These micro-earthquakes, which are quite scattered in their distribution, indicate that this region may be in a low-seismicity zone. As explained above, the micro-earthquakes may represent low-level activity on the Mae Hong Son and Thoen Faults.

11. Conclusions

The collision between the Indian and Eurasian plates since the late Paleogene causes the NW–SE and NE–SW strike-slip faults and the N–S dip-slip faults in the Indochina region. In the Mae Hong Son region, northern Thailand, several fault lines trend in the NE–SW, NW–SE and N–S directions. Theses faults are collectively called the Mae Hong Son Fault. In the southeastern margin of the Lampang basin, northern Thailand, fault lines trend in the NE–SW and ENE–WSW directions. Theses faults are called the Thoen Fault. The Mae Hong Son and Thoen Faults are temporally and spatially associated with the Cenozoic basin formation. Previous remote sensing investigation reveals many lines of morphotectonic evidence along the Mae Hong Son and the Thoen Faults which suggest an active tectonic region. In order to clarify tectonic activity of these regions, the Mae Hong Son and Thoen Faults were selected for this study.

The Mae Hong Son Fault in the Mae Hong Son region, trends mainly N–S, and shows conjugate fault sets trending NW–SE and NE–SW. The N–S trending faults show a normal dip-slip sense of motion, and bound the margins of N–S trending elongate basins. The NW–SE and NE–SW trending faults show right-lateral strike-slip and left-lateral strike-slip movements, respectively. Morphotectonic landforms associated with the Mae Hong Son Fault are fault scarps, offset streams, linear valleys, offset ridge crests, triangular facets, beheaded streams, hot springs, and linear mountain fronts.

In this study, a trench, a quarry, and a road cut in Cenozoic strata have been used for fault geometry analysis. Eight paleoearthquake events were identified in the Mae Hong Son region based on trenching data, including offset stratigraphic units in the quarry wall and the road-cut exposure, and OSL and TL ages (first event: 78,000 yr BP; second event: 68,000 yr BP; third event: 58,000 yr BP; fourth event: 48,000 yr BP; fifth event: 38,000 yr BP; sixth event: 28,000 yr BP; seventh event: 18,000 yr BP, and the most recent event: 8,000 yr BP).

The recurrence interval on the Mae Hong Son Fault may be on the order of 10,000 years and the slip rate is estimated as *ca.* 0.03–0.13 mm/yr. It is concluded that the Mae Hong Son Fault is currently active, and that Mae La Noi segment no. 1 and the Phra That Chom Kitti segment are active oblique-slip faults (Mae La Noi segment no. 1 represents combined reverse and left-lateral strike-slip motions, while the Phra That Chom Kitti segment represents combined normal and left-lateral strike-slip motions). However, evidences of the youngest faulting event in trenches across the Mok Chum Pae, Huai Kia no. 1, and Nong Mae La segments are not clear. It is inferred that activity on the Mae Hong Son Fault is low.

The Thoen Fault in the Lampang basin, northern Thailand, strikes principally in the NE–SW direction. Morphotectonic landforms caused by normal faulting in the Lampang basin are well represented by fault scarps, triangular facets, wine-glass canyons, linear valleys, and linear mountain fronts. On the other hand, morphotectonic landforms that would indicate strike-slip faulting are not found.

Two trenches from previous study and one trench of this study have been used for a paleoearthquake study. Three paleoearthquake events were identified in the Lampang basin based on trenching data, AMS radiocarbon, OSL and TL ages (first event: 3,700 yr BP; second event: 1,800 yr BP, and the most recent event: more than 960 yr BP). Geomorphological features in the Lampang basin indicate active normal faulting. However, the sediments exposed in the trench at Ban Don Fai no. 2 provide no clear-cut evidence of recent fault movement. The lack of evidence in the trench for recent fault movement indicates that the fault is located below the depth of the trench; i.e., the most recent movement upon the fault pre-dates the deposition of the oldest sediments in the trench. Thus, it is inferred that activity on the Thoen Fault is low.

The Eocene–Oligocene collision of the Indian and Eurasian plates resulted in N–S compressive stresses in the Indochina region. The N–S compressive stresses possibly caused

dextral motion on major NW–SE trending faults and sinistral motion on the NE–SW trending faults in northern Thailand. The movement on faults accompanying regional E–W extension during the late Oligocene–Miocene initiated the formation of Neogene basins. It is possible that the onset of Cenozoic basin formation in the Mae Hong Son region and the Lampang basin occurred during this time. It is also proposed that strike-slip fault movements and E–W extensional tectonics in the Neogene played a critical role in the generation of neotectonic patterns and active faulting in these areas.

The level of activity on the Mae Hong Son Fault seems low by comparison with the timing of the latest fault movement and slip rates on other active faults in northern Thailand. Moreover, it is inferred that the Thoen Fault is more active than the Mae Hong Son Fault. Although no large earthquake has occurred within the Mae Hong Son region and Lampang basin, micro-earthquakes are recorded by seismographs of the TMD and the RTNSRS. These micro-earthquakes, which are quite scattered in their distribution, indicate that these regions may be in a low-seismicity zone. As explained above, the micro-earthquakes may represent low-level activity on the Mae Hong Son and Thoen Faults.

12. Acknowledgments

I wish to express my sincere gratitude to Professor Ken-ichiro Hisada (Ph.D.), for his helpful comments, advice and encouragement during the entire period of this study, and for his reading of the manuscript. I am deeply grateful to Dr. Punya Charusiri of Chulalongkorn University, Thailand, for his helpful advices, valuable suggestion, and encouragement in completing this study.

I would like to thank the Royal Thai Government for supporting this research, and the Department of Geology, Chulalongkorn University, Thailand, for providing the OSL equipment, and the Department of Earth Sciences, Faculty of Science, Kasetsart University, Thailand for supporting the TL equipment section. I am grateful to the Electricity Generating Authority of Thailand (EGAT) for funding the field work. I also thank the Bureau of Environmental Geology, Department of Mineral Resources (DMR), Thailand, for providing facilities during the fieldwork in Mae Hong Son area.

I extend special thanks to Dr. Yuichi Sugiyama of the National Institute of Advanced Industrial Science and Technology (AIST), Japan, for helpful comments and discussions; Dr. Hidetoshi Hara, Institute of AIST, Japan, for his advice on field work; and Mr. Surun Keawmaungmoon and Mr. Wason Kongpermpool of Chulalongkorn University, Thailand, Mr. Chaiyasit Kruasorn of the Mineral Resources Information Center, DMR, Thailand, Mr. Suwith Kosuwan and Mr. Preecha Saithong of Bureau of Environmental Geology, DMR, Thailand, and Mr. Kitti Khaowiset of Bureau of Geological survey, DMR, Thailand, for their assistance during fieldwork and for managing the collection of samples.

Special thanks extend to Dr. Santi Pailoplee of Chulalongkorn University, Thailand, and Dr. Krit Won-in of Kasetsart University, Thailand, for their advice about OSL and TL dating.

Finally, a very special thank to my family, my mother, my older brother and Ms.Pattharasaya Sanongphan for emotional supports throughout this study.

References

Aitken, M.J. [1985] *Thermoluminescence Dating* (Acadamic Press**,** London).

Atyotha, V. [2007] "Monitoring of radon concentration along active fault: A case study of Klong Marui Fault," M.Sc. thesis, Department of Nuclear Technology, Chulalongkorn University, Thailand.

Abodoh, A. and Pilkington, M. [1989] "Radon emanation studies of the Ile Bizard Fault," *Montreal Geoexploration* **25**, 341–354.

Bal, A.A., Burgisser, H.M., Harris, D.K., Herber, M.A., Rigby, S.M., Thumprasertwong, S. and Winkle, S.J. [1992] "The Tertiary Phitsanulok lacustrine basin, Thailand," *Proc. Natural Conf. Geologic Resources of Thailand: Potential of Future Development*, Department of Mineral Resources, Bangkok, pp. 247–258.

Baum, F., Von Braun, E. and Hahn, L. [1970] "On the geology of northern Thailand," *Beiheft Geolo. Jahrb.* **102**, 1–24.

Bell, W. T. [1979] "Thermoluminescence dating: Radiation dose-rate data," *Archaeometry* **21**, 243–245.

Berger, G.W. [1988] "Dating Quaternary by Luminescence," *in Dating Quaternary Sediments*, ed. Easterbrook, D. J. (The Geological Society of America, Colorado), pp. 13–50.

Bhongsuwan, T., Pispak, P. and Dürrast, H. [2011] "Result of alpha track detection of radon in soil gas in the Khlong Marui Fault Zone, Southern Thailand: A possible earthquake precursor," *Songkhlanakarin J. Sci. Technol.* **33**(5), 606–616.

Biddle, K. T. and Christie–Blick, N. [1985] "Glossary-Strike-Slip Deformation, Basin Formation, and Sedimentation," *Spec. Publ. Soc. Econ. Paleont. Miner.* **37**, 375–385.

Bott, J., Wong, I., Prachuab, S., Wechbunthung, B., Hinthong, C. and Sarapirome, S. [1997] "Contemporary seismicity in northern Thailand and its tectonic implications," *Proc. Int. Conf. Stratigraphy and Tectonic Evolution of Southeast Asia and the South Pacific*, Department of Mineral Resources, Bangkok, Thailand, pp. 453–464.

Bull, W.B. and McFadden, L.D. [1977] "Tectonic geomorphology north and south of the Garlock Fault, California," *Proc. 8th Annual Geomorphology Symposium*, State University New York at Binghamton, pp. 115–137.

Bunkanpai, N. [2005] "Geology of the Mae Sariang district (Scale 1:50,000)," Technical Report, Geological Survey Division, Department of Mineral Resources, Thailand.

Burger, H.R., Sheehan, A.F. and Jones, C.H. [2006] *Introduction to applied geophysics: Exploring the Shallow Subsurface* (W.W.Norton & Company, New York).

Caputo R., Salviulo L., Piscitelli S. and Loperte A. [2007] "Late Quaternary activity along the Scorciabuoi Fault (Southern Italy) as inferred from electrical resistivity tomographies," *Ann. of Geophys*. **50**(2), 213–224.

Carver, G. A. and McCalpin, J. P. [1996] "Paleoseismology of compression tectonic environment," *in Paleoseismology*, ed. McCalpin, J. P. (Academic Press, New York), pp. 183–270.

Charusiri, P., Charusiri, B., Pongsapich, W. and Suwanwerakamtorn, R. [1993] "Applications of enhanced satellite-borne image to the relationship between fracture and mineralization in the Nam Mae Moei-Mae Ping area, northern Thailand," *Nonrenewable Res.* **2**(2), 46–58.

Charusiri, P., Daorerk, V. and Supajanya, T. [1996] "Applications of remote-sensing techniques to geological structures related to earthquakes and earthquake-prone areas in Thailand and neighbouring areas: A preliminary study," *J. Scientific Res. Chula. Univ*. **21**(1), 14–38.

Charusiri, P., Kosuwan, S. Tuteechin, W. Vechbunthoen, B. Suwanwerakamtorn, R. and Jarupongsakul, T. [1997] "Studies on Causes of Earthquakes in Thailand from SE Asian Geology Structures using Landsat TM-5 Images," A final report submitted to National Research Council of Thailand under the research grant from Thailand, Remote sensing center, Bangkok (in Thai, abstract in English).

Charusiri, P., Rhodes, B.P., Saithong, P., Kosuwan, S., Pailoplee, S., Wiwegwin, W., Daorerk, V., Hinthong, C. and Klaipongpan, S. [2007] "Regional tectonic setting and seismicity of Thailand with reference to reservoir construction," *Int. Conf. Geology of Thailand: Towards Sustainable Development and Sufficiency Economy (GEOTHAI'07)*, Bangkok, Thailand, pp. 274–287.

Chindasut, S., Krisadasima, S., Tantiwanich, W. and Wache, M. [1990] "Geology of the Mae La Noi district (Scale 1:50,000)," Technical Report, Geological Survey Division, Department of Mineral Resources, Thailand.

Christie–Blick, N. and Biddle, K. T. [1985] "Deformation and Basin Deformation along Strike-Slip Fault," *Spec. Publ. Soc. Econ. Paleont. Miner.* **37**, 1–34.

Danphaiboonphon, V. [2005] "Neotectonics of the Theon Fault System, Lampang Basin, Northern Thailand," M.Sc. thesis, Department of Geology, Chulalongkorn University, Thailand.

Danphaiboonphon, V., Charusiri, P. and Galong, W. [2007] "Application of enhanced ground geophysical data to active fault analysis in the southern Srisawat Fault segment, South of Srinakarin dam, Western Thailand," *Science Asia* **33**, 257–264.

Department of Mineral Resources [2006] "Active fault map of Thailand," (Online Article, October 2006), available at http://www.dmr.go.th.

Department of Mineral Resources [2007] "Investigation on recurrence interval in areas showing trace of movement along the faults in the Mae Hong Son and Tak provinces (Mae

Hong Son and Mae Ping Faults)," Technical Report, Environmental Geology Division, Department of Mineral Resources, Thailand (in Thai).

Department of Mineral Resources [2009] "Investigation on recurrence interval in areas showing trace of movement along the faults in the Chiang Rai, Chiang Mai and Phayao provinces (Mae Chan and Phayao Faults)," Technical Report, Environmental Geology Division, Department of Mineral Resources, Thailand (in Thai).

Ducrocq, S., Buffetaut, E., Buffetaut-Tong, H., Chimanee, Y., Jaeger, J.J., Lacassin, R. and Suteethorn, V. [1992] "Tertiary continental basins of Thailand as a result of strike-slip motions induced by the India-Asia collision," *J. Southeast Asian Earth Sci.* **7**, 260.

Electricity Generating Authority of Thailand [2012] "Active fault study and seismic hazard analysis in northern and western Thailand (part 1: northern region)," Technical Report, Electricity Generating Authority of Thailand, Thailand.

Fattahi, M. [2009] "Dating past earthquakes and related sediments by thermoluminescence methods: A review," *Quaternary International* **199**, 104–146.

Fenton, C.H., Charusiri, P., Hinthong, C., Lumjuan, A. and Mangkornkarn, B. [1997] "Late Quaternary faulting in northern Thailand," *Proc. Int. Conf. Stratigraphy and Tectonic Evolution of Southeast Asia and the South Pacific*, Department of Mineral Resources, Bangkok, Thailand, pp. 436–452.

Fenton, C. H., Charusiri, P. and Wood, S. H. [2003] "Recent paleoseismic investigations in northern and western Thailand," *Ann. of Geophys.* **46**(5), 957–981.

Fujita, K. and Ikuta, O. [2000] "Resistivity structure of the central part of the Yamasaki Fault studied by the multiple electrodes resistivity method," *Earth Planets Space* **52**, 567–571.

Ganas, A., Shanov, S., Drakatos, G., Dobrev, N., Sboras, S., Tsimi, C., Frangov, G. and Pavlides, S. [2005] "Active fault segmentation in southwest Bulgaria and Coulomb stress triggering of the 1904 earthquake sequence," *J. Geodyn*. **40**, 316–333.

Geological Survey of Japan [1983] "A new series of the neotectonic maps of Japan (1:500,000 scale)," *Bull. Geol. Surv. Jpn.* **34**(1), 27–37.

Hahn, L., Koch, K.E. and Wittekindt, H. [1986] "Outline of the geology and mineral potentials of Thailand," *Geol. Jahrb. Reihe. B* **59**, 3–49.

Hamblin, B.K. [1976] "Patterns of displacement along the Wasatch Fault," *Geology* **4**, 619–622.

Hinthong, C. [1995] "The study of active faults in Thailand," *Technical Conference on the Progression and Vision of Mineral Resources Development (Department of Mineral Resources)*, Bangkok, Thailand, pp. 129–140.

Hinthong, C. [1997] "The study of active faults in Thailand," Report of EANHMP, An approach to natural hazards in Eastern Asia, Eastern Asia Natural Hazards Mapping Project, Thailand.

Hisada, K., Sugiyama, M., Ueno, K., Charusiri, P. and Arai, S. [2004] "Missing Ophiolitic rocks along the Mae Yuam Fault as the Gondwana-Tethys divide in north-west Thailand," *Island Arc* **13**, 119–127.

Huchon, P., Le Pichon, X. and Rangin, C. [1994] "Indochina peninsula and the collision of India and Eurasia," *Geology* **22**, 27–30.

Inglethorpe, S.D.J., Utha-aroon, C. and Chanyavanich, C. [1997] "An inventory of diatomite of the Lampang basin, northern Thailand," *Proc. of the International Conference on Stratigraphy and Tectonic Evolution of Southeast Asia and South Pacific*, Department of Mineral Resources , Bankok, Thailand, pp. 669–685.

Israel, H. and Bjornsson, S. [1967] "Radon (Rn-222) and thoron (Rn-220) in soil air over faults," *Geophys.* **33**, 48–64.

Keller, E. A. and Pinter, N. [1996] *Active Tectonics: Earthquake, Uplift, and Landscape* (Prentice-Hall, New Jersey).

King, C.Y., King, B.S., Evans, W.C. and Zhang, W. [1996] "Spatial radon anomalies on active faults in California," *Applied Geochemistry* **11**, 947–510.

Kosuwan, S., Saithong, P. and Lumjuan, A. [2003] "Paleoearthquake on the Mae Ai segment of the Mae Chan Fault Zone, Chiang Mai, northern Thailand," Technical Report, Geological Survey Division, Department of Mineral Resources (in Thai with English abstract).

Kosuwan, S., Saithong, P., Lumjuan, A., Takashima, I. and Charusiri, P. [1999] "Preliminary results of studies on the Mae Ai segment of the Mae Chan Fault Zone, Chiang Mai, northern Thailand," *The CCOP Meeting on Exodynamic Geohazards in East and Southeast Asia*, Pattaya, Thailand, pp. 1–8.

Lacassin, R., Hinthong, C., Siribhakdi, K., Chauviroj, S., Charoenravat, A., Maluski, H., Leloup, P.H. and Tapponnier, P. [1997] "Tertiary diachronic extrusion and deformation of western Indochina: Structure and $^{40}Ar/^{39}Ar$ evidence from NW Thailand," *J. Geophys. Res.* **102**(5), 10013–10037.

Lacassin, R., Replumaz, A. and Leloup, P.H. [1998] "Hairpin river loops and slip-sense inversion on Southeast Asia strike-slip faults," *Geology* **26**, 703–706.

Larsen, V. and Steel, R.J. [1978] "The sedimentary history of a debris-flow dominated, Devonian alluvial fan-a study of textural inversion," *Sedimentology* **25**, 37–59.

Le Dain, A.Y., Tapponnier, P. and Molnar, P. [1984] "Active faulting and tectonics of Burma and surrounding regions," *J. Geophys. Res.* **89**, 453–472.

Longley, I.M. [1997] "The tectonostratigraphic evolution of SE Asia," *Geol. Soc. Spec. Publ.* **126**, 311–339.

MacDonald, A.S., Barr, S.M., Dunning, G.R. and Yaowanoiyothin, W. [1993] "The Doi Inthanon metamorphic core complex in NW Thailand: Age and tectonic significance," *J. Southeast Asian Sci.* **8**(1–4), 117–125.

McCalpin, J.P. [2009] *Paleoseismology: International geophysics* (Elsevier Inc., Burlington, MA, USA).

Morley, C. K. [2002] "A tectonic model for the Tertiary evolution of strike–slip faults and rift basins in SE Asia," *Tectonophysics* **347**(4), 189–215.

Morley, C.K. [2007] "Variations in Late Cenozoic-Recent strike slip and oblique- extensional geometries, within Indochina: The influence of pre-existing fabrics," *J. Struct. Geol.* **29**, 36–58.

Morley, C. K., Charusiri, P. and Watkinson, I.K. [2011] "Structural geology of Thailand during the Cenozoic," *in The Geology of Thailand*, eds. Ridd, M.F., Barber, A.J. and Crow, M.J. (The Geological Society, London), pp. 273–334.

Morley, C. K., Haranya, C., Phoosongsee, W., Pongwapee, S., Kornsawan, A. and Wonganan, N. [2004] "Activation of rift oblique and rift parallel pre-existing fabrics during extension and their effect on deformation style: Examples from the rifts of Thailand," *J. Struct. Geol.* **26**(10), 1803–1829.

Morley, C.K., Smith, M., Carter, A., Charusiri, P. and Chantraprasert, S. [2007] "Evolution of deformation styles at a major restraining bend, constrains from cooling histories, Mae Ping Fault Zone, western Thailand," *Geol. Soc. Lond. Spec. Publ*. **290**, 325–349.

Morley, C. K., Woganan, N., Sankumarn, N., Hoon, T. B., Alief, A. and Simmons, M. [2001] "Late Oligocene–Recent stress evolution in rift basins of northern and central Thailand: Implications for escape tectonics," *Tectonophysics* **334**, 115–150.

Moussa, M.M. and El Arabi, M.A. [2003] "Soil radon survey for tracing active fault: A case study along Qena-Safaga road, Eastern desert, Egypt," *Radiation Measurements* **37**, 211–216.

Murray, A.S. and Olley, J.M. [2002] "Precision and accuracy in the optically stimulated luminescence dating of sedimentary quartz," *Geochronometria* **21**, 1–16.

Nutalaya, P., Sodsri, S. and Arnold, E.P. [1985] "Series on seismology Vol. II – Thailand," Technical report, Southeast Asia Association of Seismology and Earthquake Engineering Project, USGS.

O'Leary, J. and Hill, G.S. [1989] "Tertiary basin development in the southern plains Thailand," *The Int. Symp. Intermountane Basins: Geology and Resources*, Chiang Mai University, pp. 254–264.

Pailoplee, S., Takashima, I., Kosuwan, S. and Charusiri, P. [2009] "Earthquake activities along the Lampang - Thoen Fault Zone, northern Thailand: Evidence from paleoseismological and seismicity data," *J. Applied Sci. Res.* **5**(2), 168–180.

Peltzer, G. and Tapponnier, P. [1988] "Formation and evolution of strike-slip fault, rift, and basin during the India-Asia collision: An experimental approach," *J. Geophys. Res.* **93**(B12), 15,085–15,117.

Philip, H., Rogozhin, E., Cisternas, A., Bousquet, J. C., Borisov, B. and Karakhanian, A. [1992] "The Armenian earthquake of 1988 December 7: faulting and folding, neotectonics and paleoseismicity," *Geophys. J. Int*. **110**, 141–158.

Picotti, V., Alessio, P. and Frank, P. J. [2009] "Topographic expression of active faults in the foothills of the northern Apennines," *Tectonophysics* **474**, 285–294.

Pispak, P., Dürrast, H. and Bhongsuwan, T. [2010] “Soil-gas radon as a possible earthquake precursor: A case study from the Klong Marui Fault Zone,” *Kasetsart J. (Nat.Sci.)* **44**, 1079–1093.

Polachan, S., Pradidtan, S., Tongtaow, C., Janmaha, S., Intarawijitr, K. and Sangsuwan, C. [1991] “Development of Cenozoic basins in Thailand,” *Mar.Petroleum Geol.* **8**, 84–97.

Pradidtan, S. [1989] “Characteristics and controls on lacustrine deposits of some Tertiary basins in Thailand,” *The Int. Symp. Intermountane Basins: Geology and Resources*, Chiang Mai University, pp. 133–145.

Reading, H. G. [1980] “Characteristics and recognition of strike-slip fault system,” *Spec. Publ. Int. Ass. Sediment.* **4**, 7–26.

Reynolds, J.M. [2011] *An Introduction to Applied and Environmental Geophysics* (John Wiley & Sons, Chichester, UK).

Rhodes, B.P., Conejo, R., Benchawan, T., Titus, S. and Lawsan, R. [2005] “Paleocurrents and provenance of the Mae Rim Formation, northern Thailand: Implications for tectonic evolution of the Chiang Mai basin,” *J. Geol. Soc., Lond*. **162**, 51–63.

Rhodes, B.P., Perez, R., Lamjuan, A. and Kosuwan, S. [2004] “Kinematics and tectonic implications of the Mae Kuang Fault, northern, Thailand,” *J. Southeast Asian Earth Sci*. **24,** 79–89.

Roberts, R.G., Jones, R. and Smith, M.A. [1994] “Beyond the radiocarbon barrier in Australian prehistory,” *Antiquity J*. **68**, 611–616.

Royal Thai Navy Seismic Research Station [2012] “Earthquake statistics of Thailand,” available at http://www.hdrtnsrs.com (in Thai).

Saithong, P. [2006] “Characteristics of the Moei-Mae Ping Fault Zone, Changwat Tak, northwestern Thailand,” M.Sc. thesis, Department of Geology, Chulalongkorn University, Thailand.

Saithong, P., Kosuwan, S., Won-in, K., Takashima, I. and Charusiri, P. [2005] “Late Quaternary paleoseismic history and surface rupture characteristics of the Moei-Mae Ping Fault Zone in Tak area, northwestern Thailand,” *Proc. Int. Conf. Geology, Geotechnology and Mineral Resources of INDOCHINA: November 28–30, 2005*, Khon Kaen, Thailand, pp. 511–516.

Saithong, P., Pananont, P., Kosuwan, S., Kaowiset, K., Won-in, K. and Charusiri, P. [2011] “Neotectonics along the Uttaradit Fault Zone, northern Thailand: Evidence from remote sensing and thermoluminescence dating,” *Proc. GEOINDO 2011*, Khon Kaen University, Khon Kaen, Thailand, pp. 512.

Sasada, M., Chaturongkawanich, S., Soponpongpipat, P., Obara, K. and Ochi, M. [1987] “Structural control the hot springs of northern Thailand based on the analysis of Landsat imagery,” *Bull. Geol. Surv. Jpn.* **38**(1), 1–6.

Shukha, U.K. [2009] “Sedimentation model of gravel-dominated alluvial piedmont fan, Ganga Plain, India,” *Int. J. Earth Sci. (Geol Rundsch.)* **98**, 443–459.

Simons, W.J.F., Socquet, A., Vigny, C., Ambrosius, B.A.C., Abu, S.H., Promthong, C., SubaryaSarsito, D.A., Matheussen, S., Morgan, P. and Spakman, W. [2007] “A decade of GPS in Southeast Asia: resolving Sundaland motion and boundaries,” *J. Geophys. Res.* **112,** (B06420), doi:10.1029/2005JB003868.

Siribhakdi, K. [1986] "Seismogenic of Thailand and periphery," *Proc. 1st Workshop on Earthquake Engineering and Hazard Mitigation*, Bangkok: Chulalongkorn University, pp. 151–158.

Slemmons, D.B. [1982] "Determination of design earthquake magnitudes for microzonation," *3rd Int. Earthquake Microzonation Conf. Proc*., pp. 119–130.

Slemmons, D.B. [1991] "Introduction," *in Neotectonics of North America*, eds. Slemmons, D.B., Engdahl, E.R., Zoback, M.D. and Blackwell, D.D. (The Geological Society of America, Colorado), pp. 1–20.

Srinak, N., Charusiri, P., Hisada, K. and Daorerk, V. [2003] "Marine Triassic lithostratigraphy of Mae Hong Son area, NW Thailand," *29th Congr. Science and Technology of Thailand*, Khon Kaen, Thailand.

Srinak, N., Hisada, K., Kamata, Y. and Charusiri, P. [2007] "Stratigraphy of the Mae Sariang Group of northwestern Thailand: Implication for paleoenvironment and tectonic setting," *Nat. Hist. J. Chula. Univ*. **7**(2), 87–108.

Srisuwan, P. [2002] "Structural and sedimentological evolution of the Phrae basin, northern Thailand," Ph.D. thesis, Department of Geology, Royal Holloway, University of London.

Steel, R. and Gloppen, T.G. [1980] "Late Caledonian (Devonian) basin formation, western Norway: sign of strike-slip tectonics during infillings," *Spec. Publ. Int. Ass. Sediment.* **4**, 79–103.

Sylvester, A. G. [1988] "Strike-Slip Faults," *Geol. Soc. Am. Bull*. **100**, 1666–1703.

Takashima, I. and Honda, S. [1989] "Comparison between K-Ar and TL Dating results of pyroclastic flow deposits in the Aizutajima area, northeast Japan," *J. Geol. Soc.* **95**, 807–816.

Takashima, I. and Maneenai, D. [1995] "Result of analyses of TL dating of some faults from Thailand: Preliminary TL age dates from fault samples of Thailand," Preliminary data personally conveyed to DMR staff, Nov. 1991.

Tanner, A. B. [1980] "Radon migration in the ground: A supplementary review," *The Natural Radiation Environment III, Symp. Proc*., Houston Texas, 23–28 April 1978, Washington, D. C., pp. 5–56.

Tapponnier, P., Peltzer, G. and Armijo, R. [1986] "On the mechanism of collision between India and Asia," *Geol. Soc. Lond. Spec. Publ*. **19**, 115–157.

Thailand Meteorological Department [2012] "Earthquake statistics of Thailand," available at http://www.seismology.tmd.go.th (in Thai).

Thiramongkol, N. [1986] "Neotectonism and Rate of Uplift in the Eastern Margin of the Lower Central Plain of Thailand," *Proc. Workshop on Economic Geology Tectonics, Sedimentary Processes and Environment of Quaternary of SE Asia,* Had Yai, IGCP, pp. 35–44.

Tsutsumi, H. and Sato, T. [2009] "Tectonic geomorphology of the southernmost Sagaing Fault and surface rupture associated with the May 1930 Pego(Bago) earthquake, Myanmar," *Bull. Seismol. Soc. Am.* **99**, 2155–2168.

Ueno, K. [1999] "Gondwana/Tethys divide in east Asia: solution from Late Paleozoic foraminiferal paleobiogeography," *Proc. Int. Symp. Shallow Tethys 5*, Department of Geological Sciences, Chiang Mai University, Chiang Mai, Thailand, pp. 45–54.

Upton, D., Bristow, C., Hurford, A.J. and Carter, A. [1997] "Tertiary tectonic denudation in northwestern Thailand: Provisional results from apatite fission-track analysis," *Proc.*

Int. Conf. Stratigraphy and Tectonic Evolution of Southeast Asia and South Pacific, Department of Mineral Resources, Bankok, Thailand, pp. 421–433.

United States Geological Survey [2006] "Earthquake Data Base", available at http://neic.usgs.gov / neis/ epic/ epic_global.html (2006, November 22).

Uttamo, W., Elders, C. and Nichols, G. [2003] "Relationship between Cenozoic strike-slip faulting and basin opening in northern Thailand," *Geol. Soc. Lond. Spec. Publ.* **210**, 89–108.

Uttamo, W., Nichols, G. and Elders, C. [1999] "The Tertiary sedimentary basins of northern Thailand," *Symp. Mineral, Energy and Water Resources of Thailand: Towards the Year 2000*, Chulalongkorn University, Bangkok, Thailand, pp. 71–93.

Vafiadou, A., Murray, A.S. and Liritzis, I. [2007] "Optically stimulated luminescence (OSL) dating investigations of rock and underlying soil from three case studies," *J. Archaeol. Sci.* **34**, 1659–1669.

Vigny, C., Simons, W.J.F., Abu, S., Bamphenyu, R., Satirapod, C., Choosakul, N., Subarya, C., Socquet, A., Omar, K., Abdin, H.Z. and Ambrosius, A.A.C. [2005] "Insight into the 2004 Sumatra-Andaman earthquake from GPS measurements in southeast Asia," *Nature* **436**, 201–206.

Walker, M.J.C. [2005] *Quaternary dating methods* (John Wiley & Son Ltd, The Atrium, Southern Gate, Chichester, West Sussex PO19 8SQ, England).

Wallace, R. E. [1978] "Geometry and rates of change of fault-related fronts, north-central Nevada," *J. Res. US. Geol.* Surv. **6**, 637–650.

Wang C., Li, X. and Wei, B. [1991] "Applications of measurement of fracture gases in seismological Sciences," Seismology Press, Beijing, China.

Watanasak, M. [1989] “Palynological zonation of Mid-tertiary intermontane basins in northern Thailand,” *The Int. Symp. Intermountane Basins: Geology and Resources*, Chiang Mai University, pp. 215–224.

Watanasak, M. [1990] “Mid-Tertiary palynostratigraphy of Thailand,” *J. Southeast Asian Earth Sci.* **4**, 203–218.

Wells, D.L. and Coppersmith, K.J. [1994] “New empirical relationships among magnitude, rupture length, rupture area, and surface rupture displacement,” *Bull. Seismol. Soc. Am.* **84**, 974–1002.

Wiwegwin, W. [2010] “Reevaluation of the Thoen Fault Activity in the Lampang Basin, Northern Thailand,” M.Sc. thesis, Earth Evolution Sciences, Life and Environmental Sciences, University of Tsukuba, Japan.

Wiwegwin, W., Hisada, K., Charusiri, P. Kosuwan, S., Pailoplee, S., Saithong, P., Khaowiset, K. and Won-in, K. [2014] “Paleoearthquake investigations of the Mae Hong Son Fault, Mae Hong Son region, northern Thailand,” *JET* **8**(2), 1450007-1–145007-35.

Wiwegwin, W., Sugiyama,Y., Hisada, K. and Charusiri, P. [2011] “Re-evaluation of the activity of the Thoen Fault in the Lampang basin, northern Thailand, based on geomorphology and geochronology,” *Earth Planets Space* **63**, 975–990.

Won-in, K. [2003] “Quaternary geology of the Phrae Basin, northern Thailand and application of thermoluminescence technique for Quaternary chronology,” Ph.D. thesis, Graduate School of Mining and Engineering, Akita University, Japan.

Wood, R. and Mallard, D.J. [1992] “When a fault is extinct?,” *J. Geol Soc. Lond.* **149**, 251–255.

Woodward-Clyde Federal Services [1996] “Seismic hazards evaluation, Environmental Impact Assessment: Geological Aspect, Kaeng Sua Ten Dam Project Changwat

Phrae," Unpublished report prepared by GMT Corporation and other for the Department of Mineral Resources, Thailand.

Appendix A

OSL glow and OSL growth curves

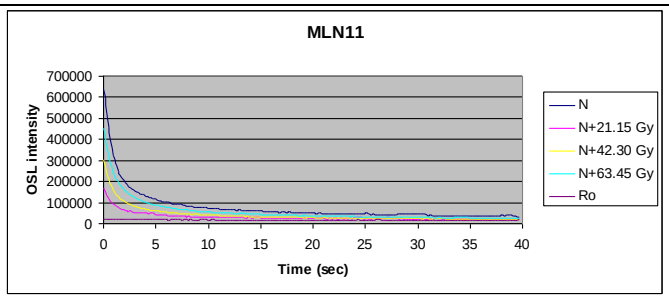

MLN11

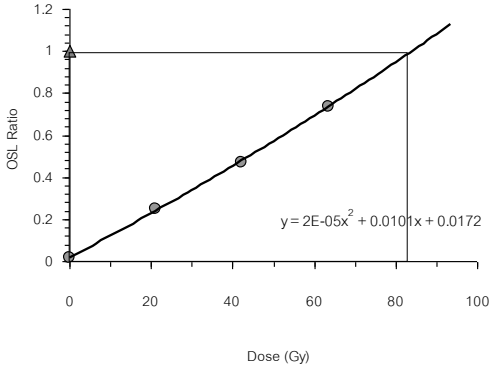

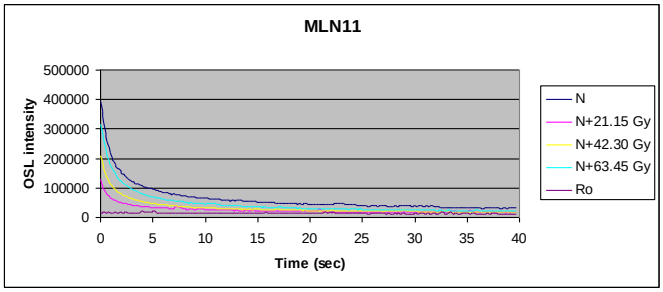

MLN11

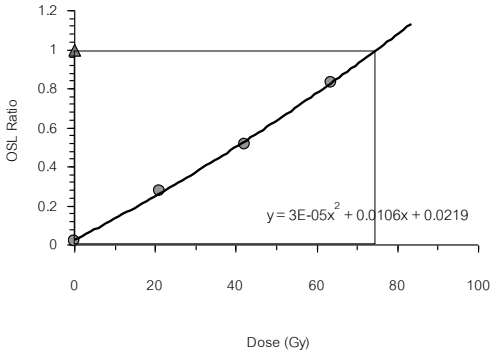

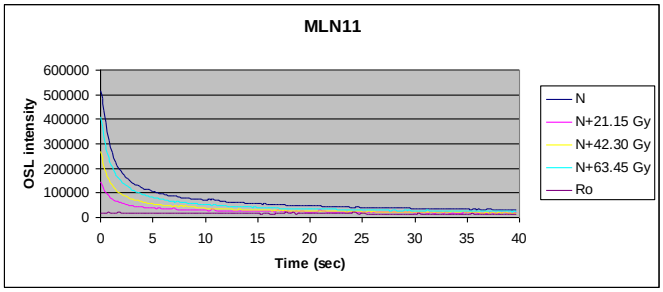

MLN11

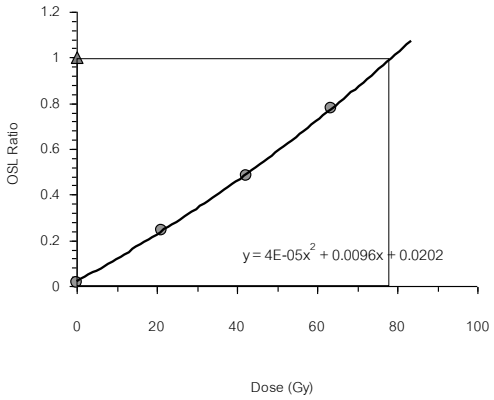

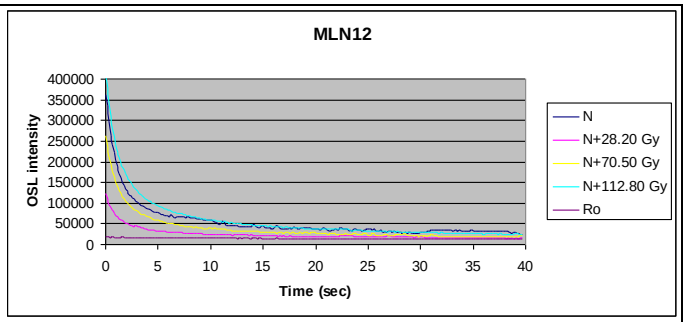

MLN12-

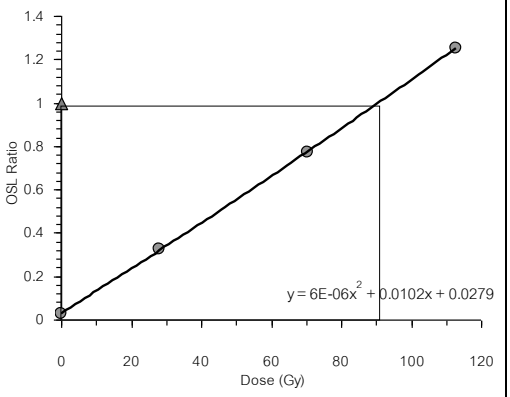

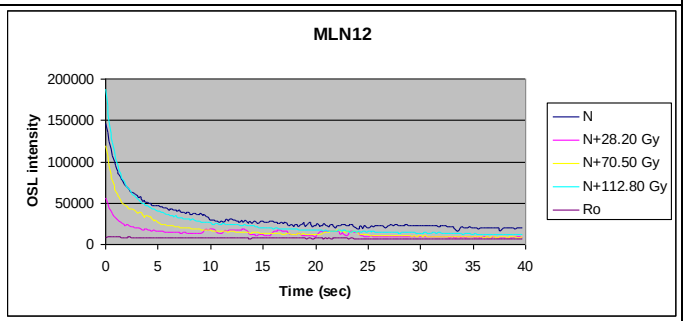

MLN12

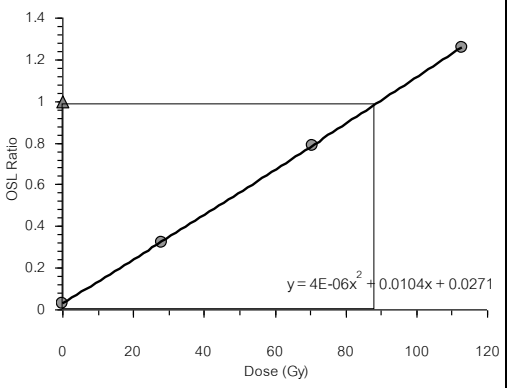

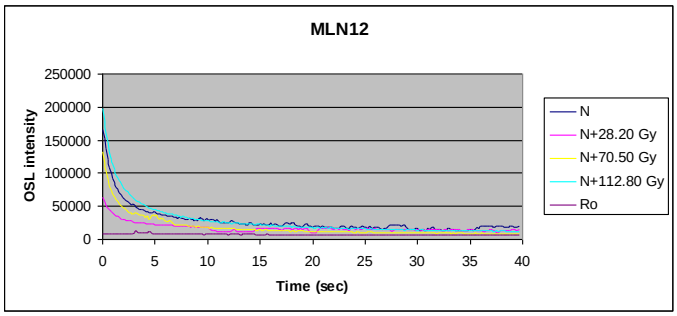

MLN12

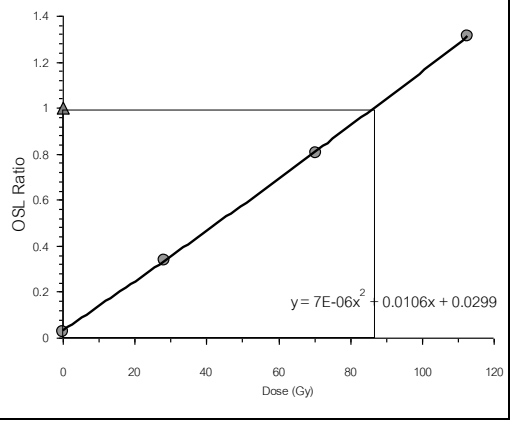

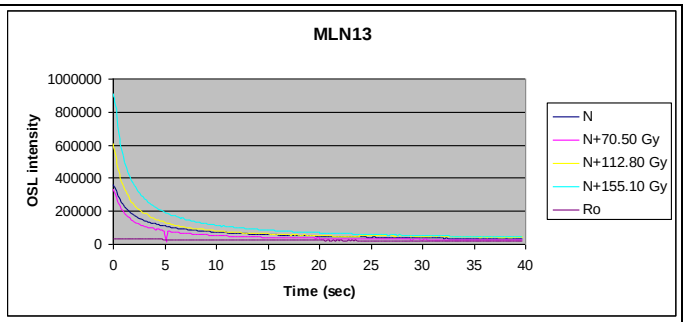

MLN13

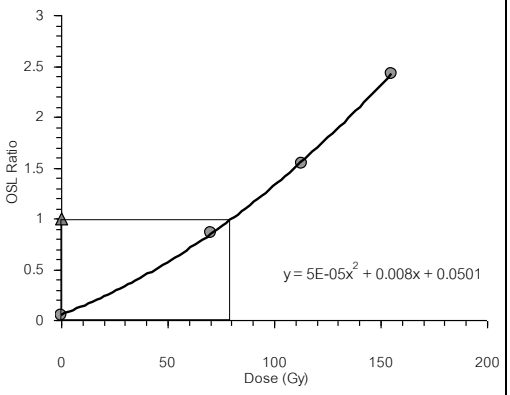

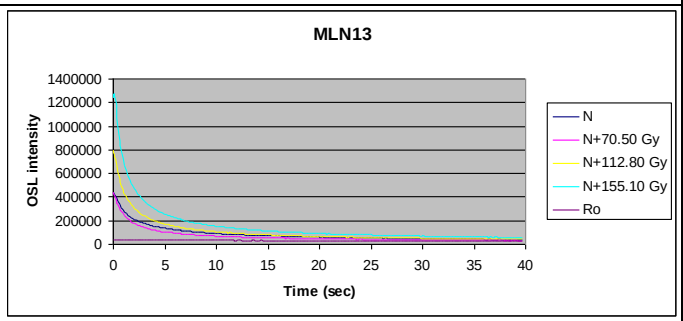

MLN13

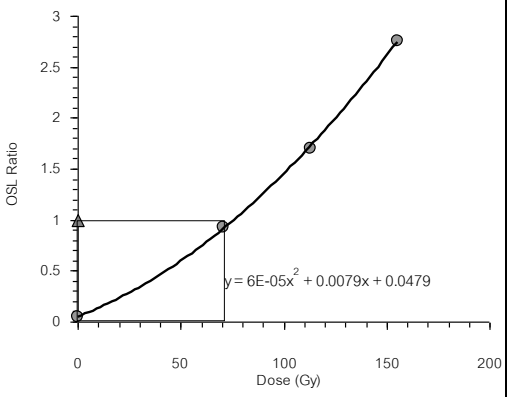

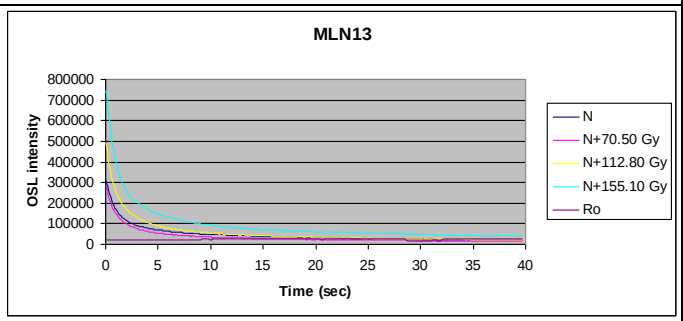

MLN13

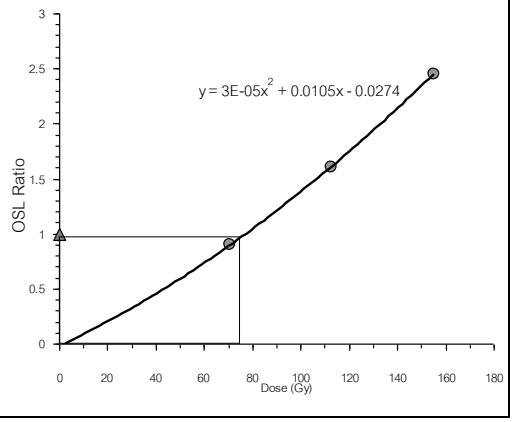

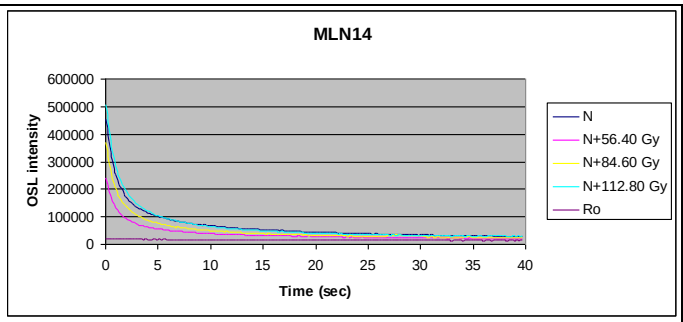

MLN14

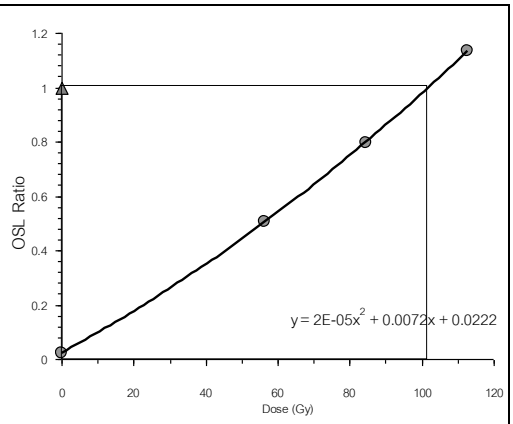

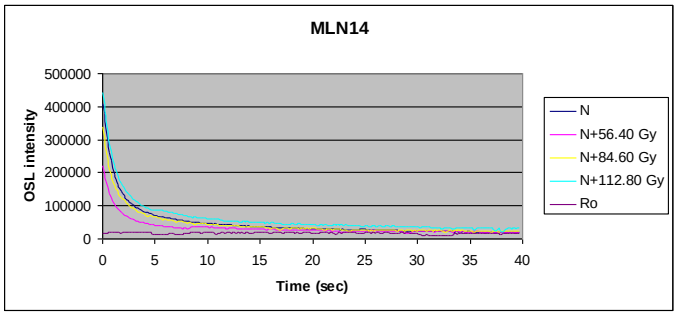

MLN14

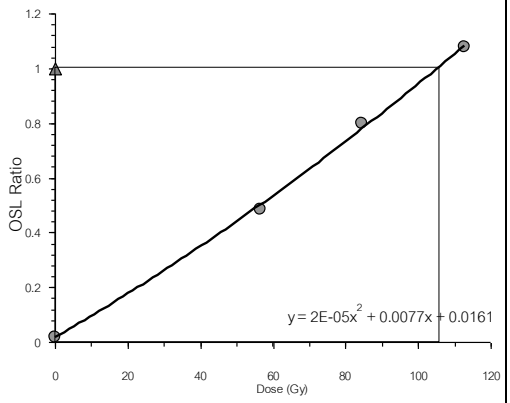

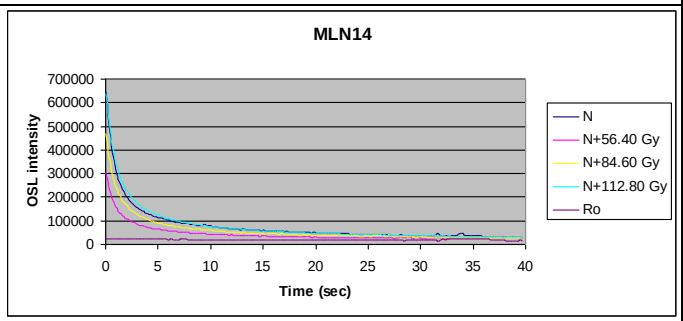

MLN14

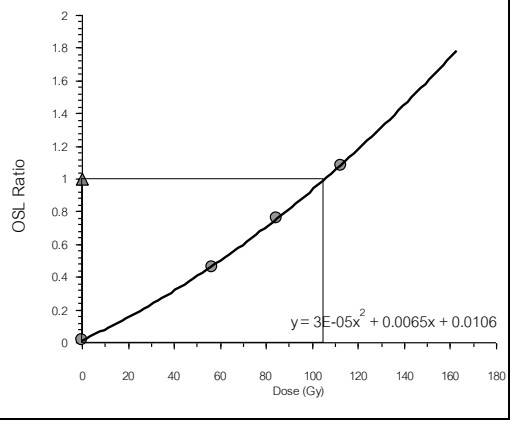

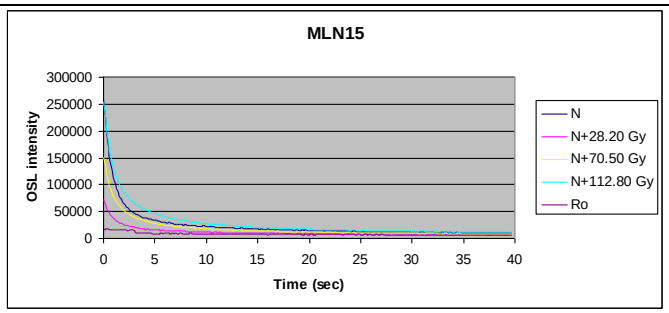

MLN15

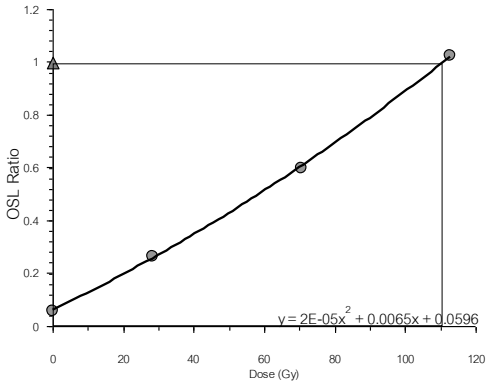

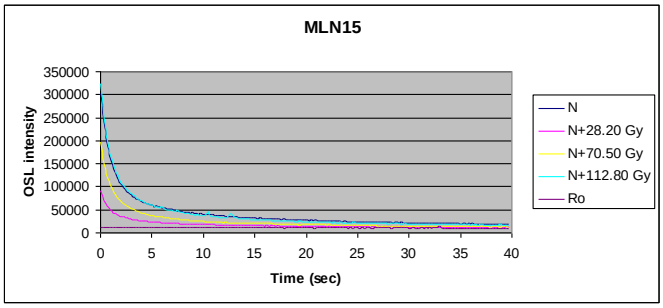

MLN15

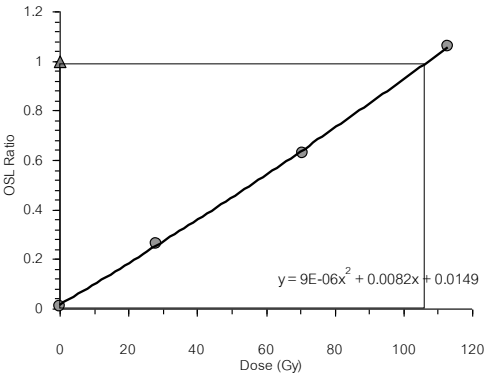

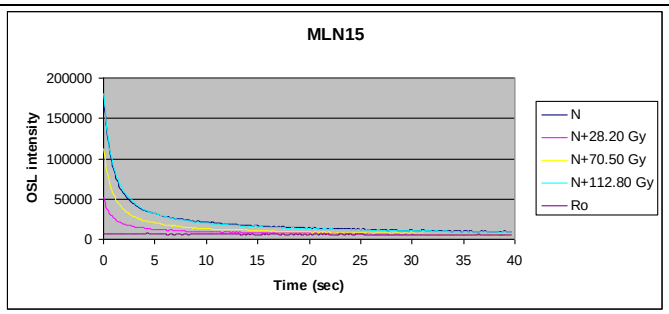

MLN15

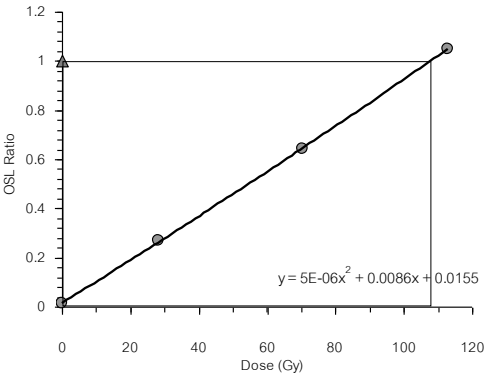

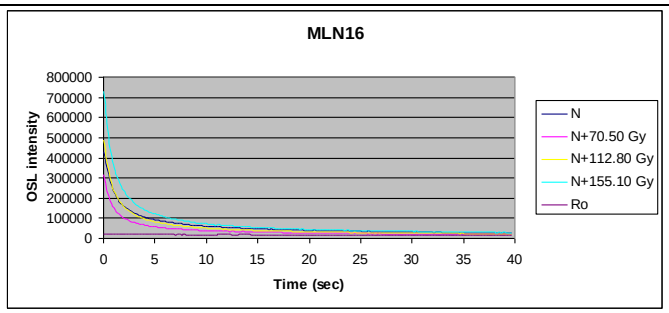

MLN16

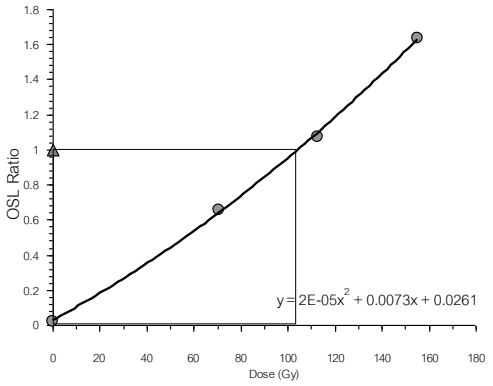

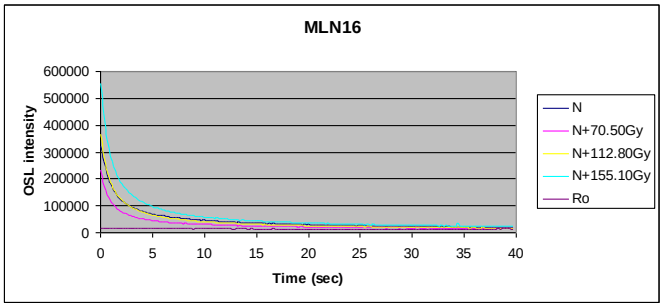

MLN16

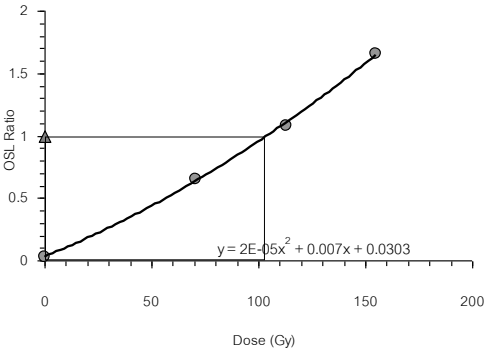

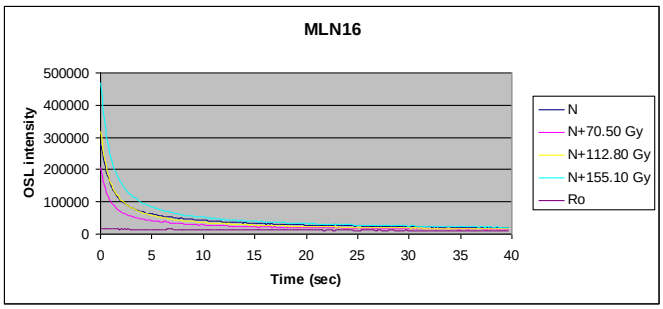

MLN16

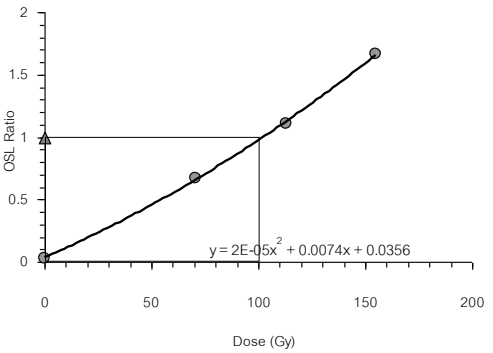

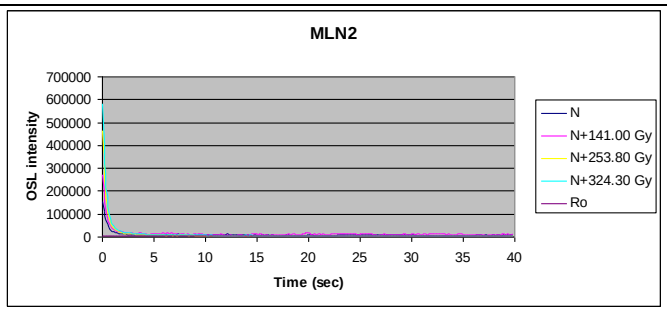

MLN2

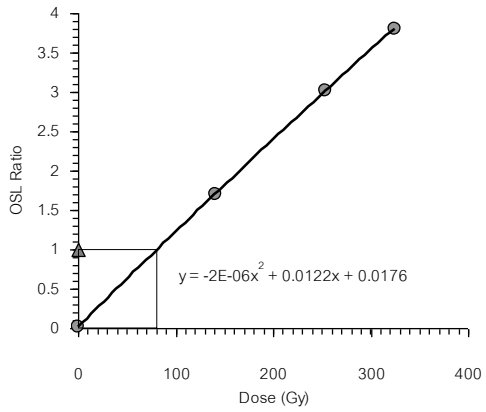

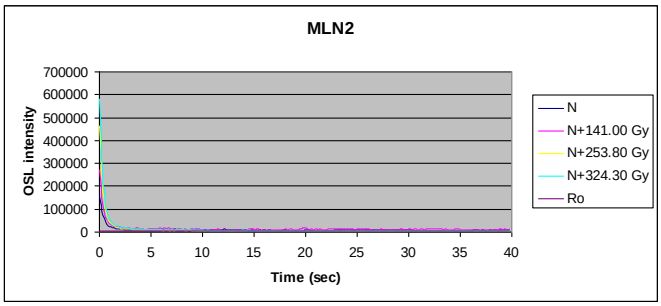

MLN2

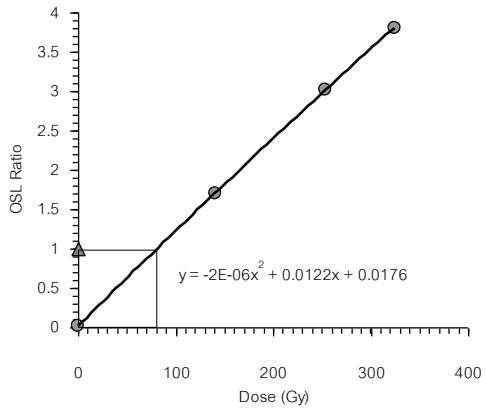

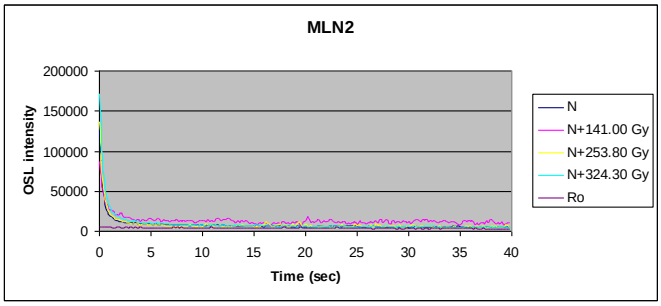

MLN2

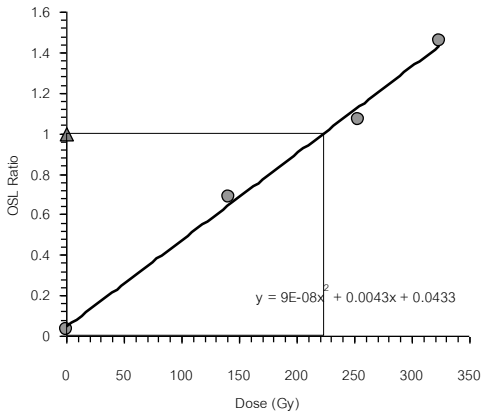

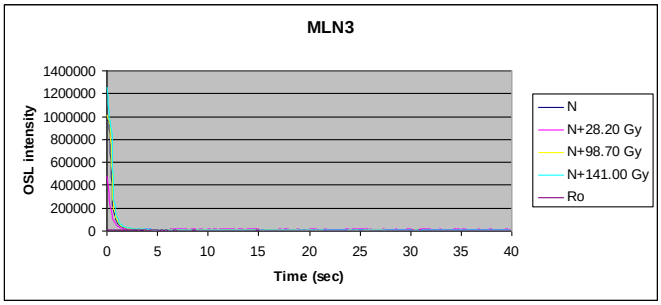

MLN3

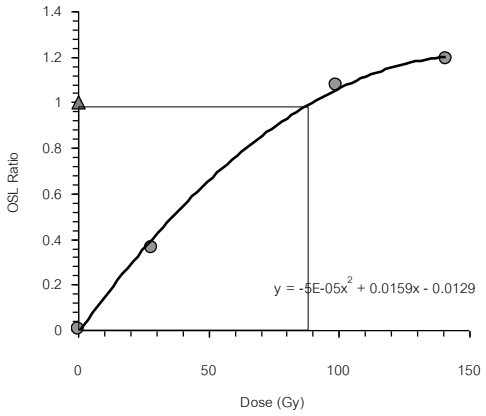

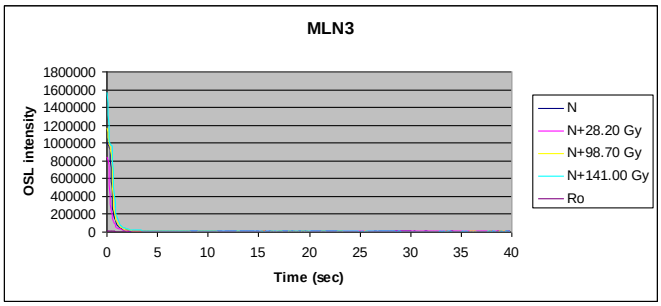

MLN3

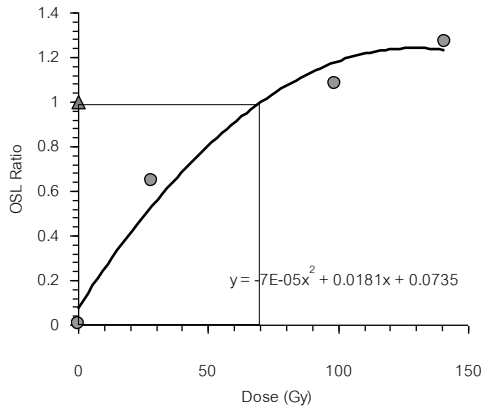

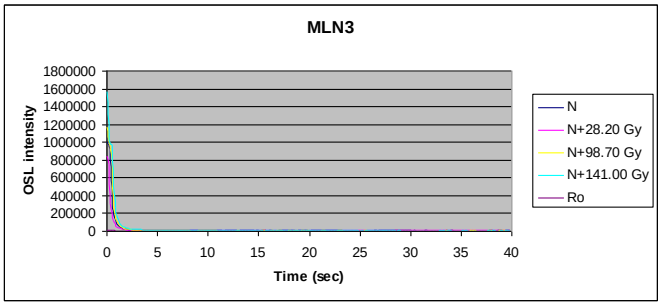

MLN3

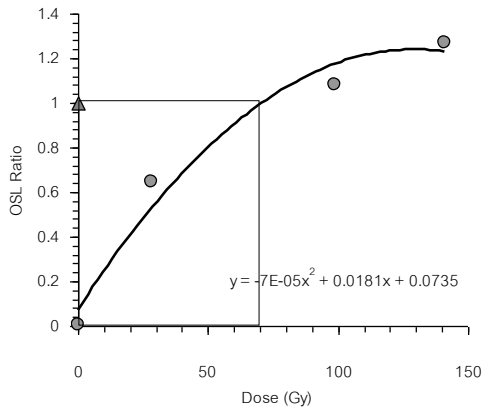

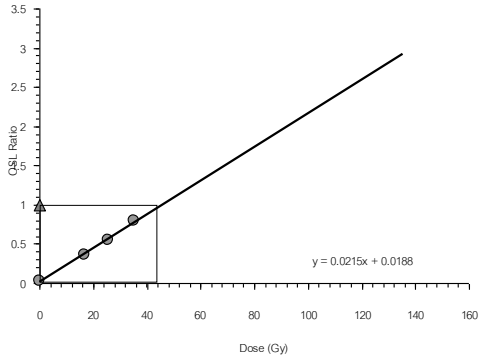 ML1	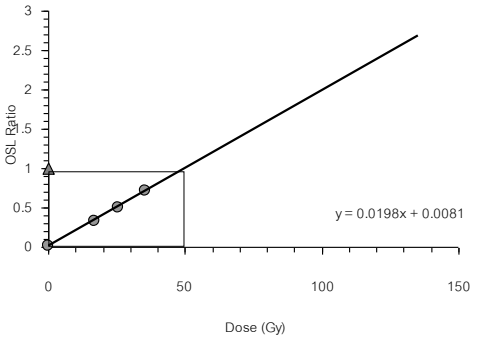 ML1
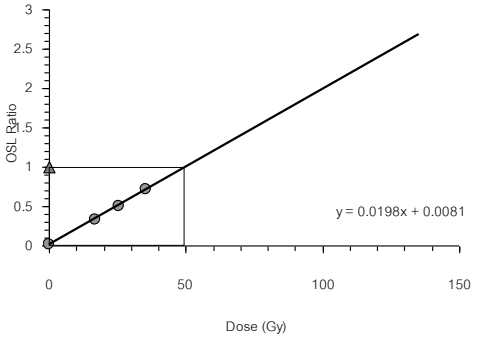 ML1	Remark: The original glow curves of this sample are available in EGAT [2012]. For this study, the growth curves were only permitted to reassess.
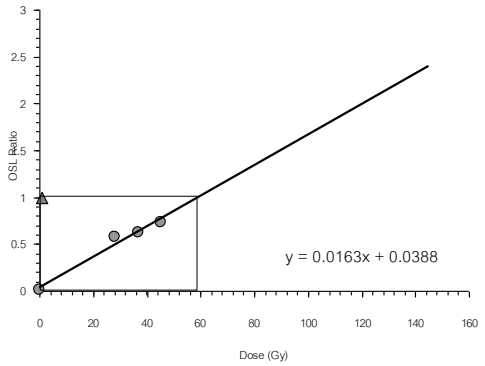 ML4	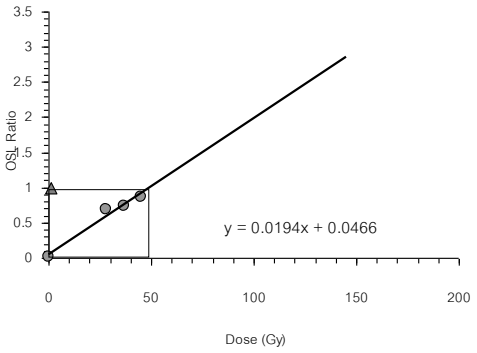 ML4
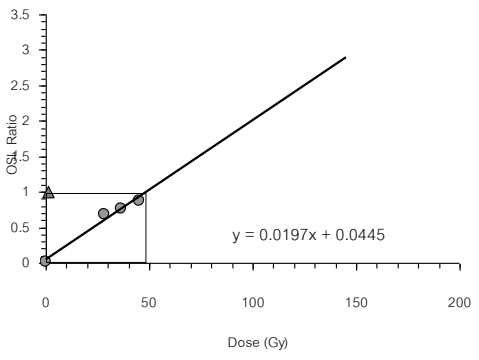 ML4	Remark: The original glow curves of this sample are available in EGAT [2012]. For this study, the growth curves were only permitted to reassess.

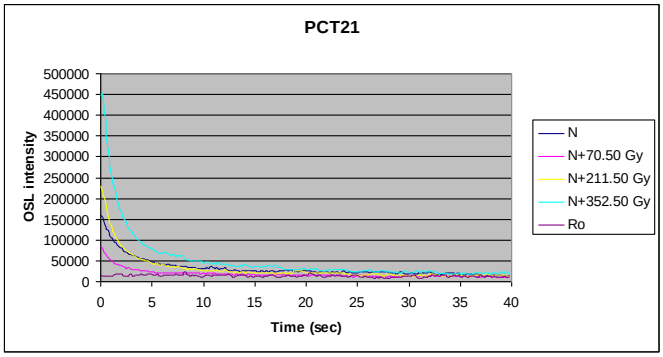

PCT21

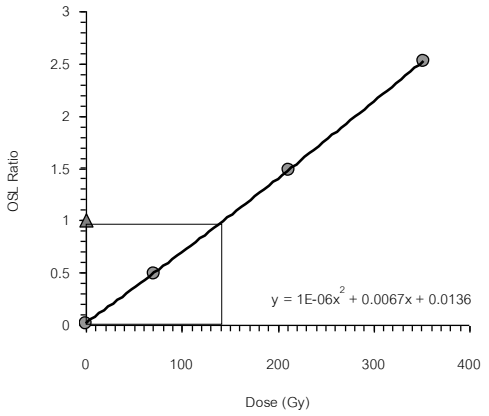

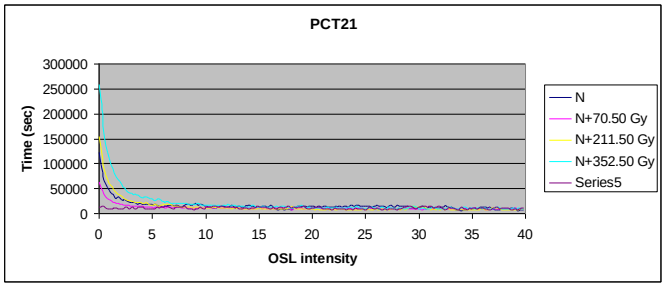

PCT21

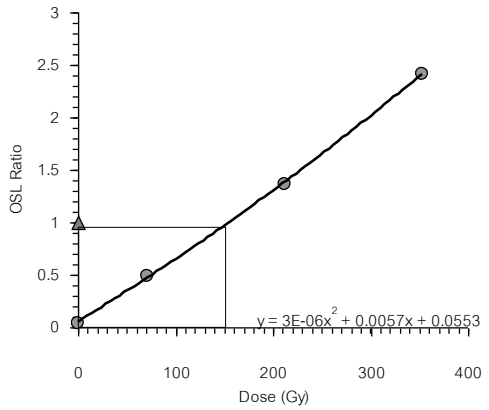

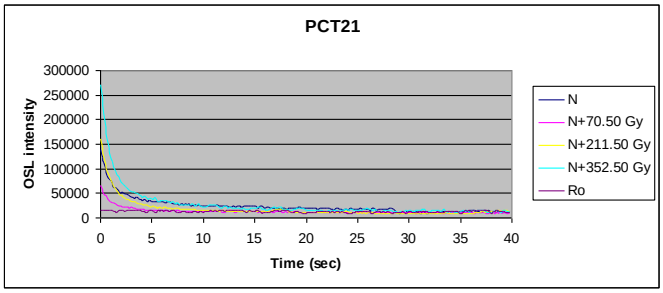

PCT21

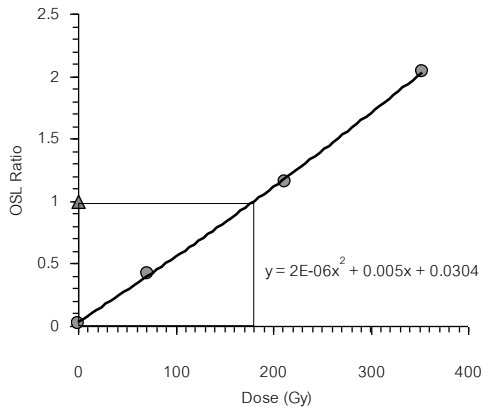

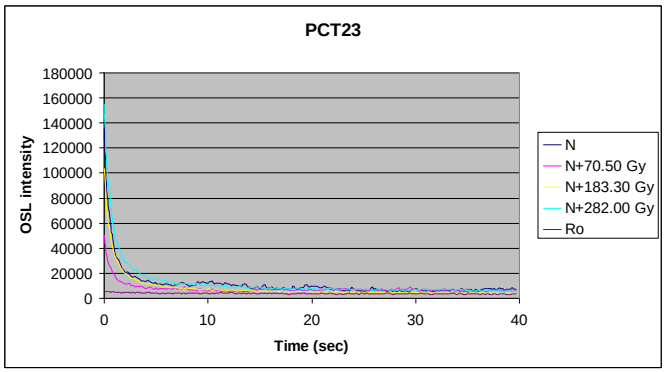

PCT23

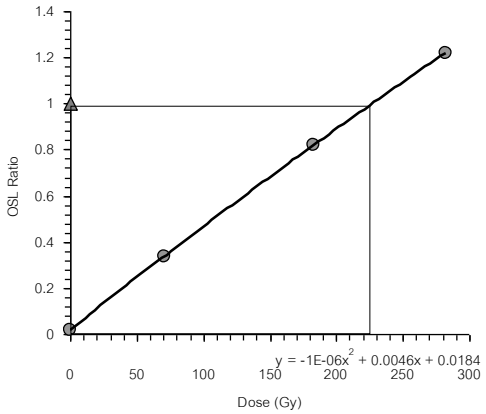

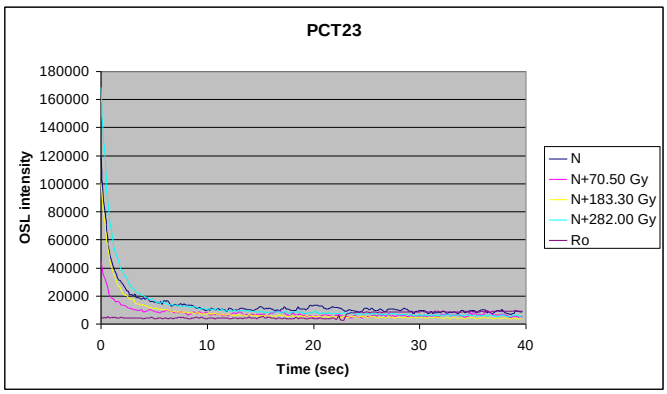

PCT23

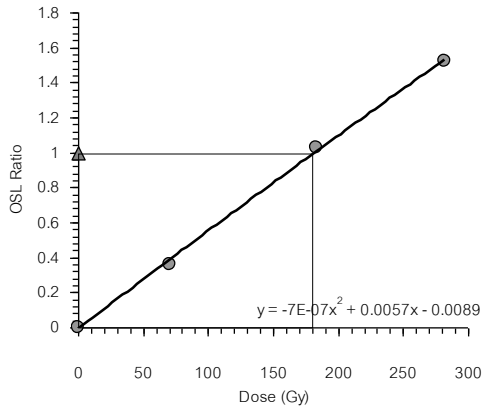

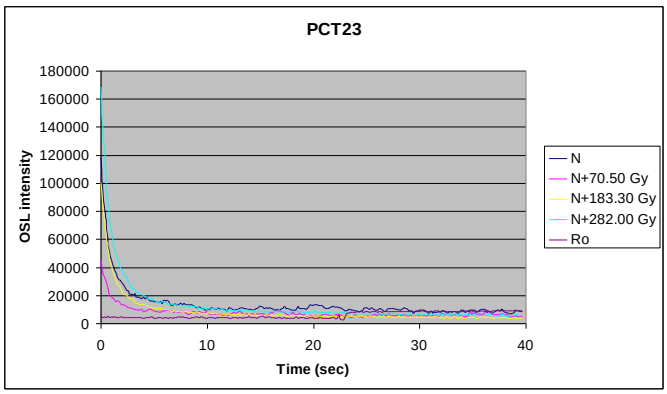

PCT23

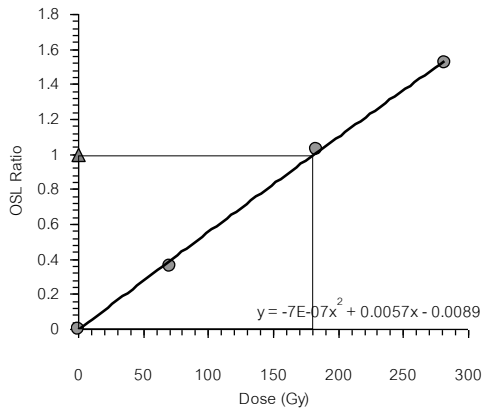

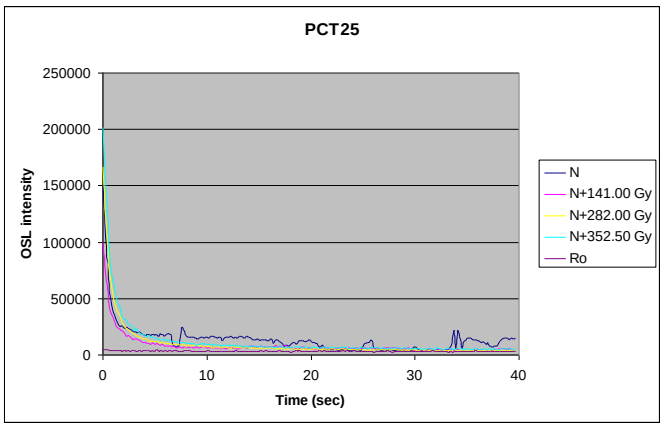

PCT25

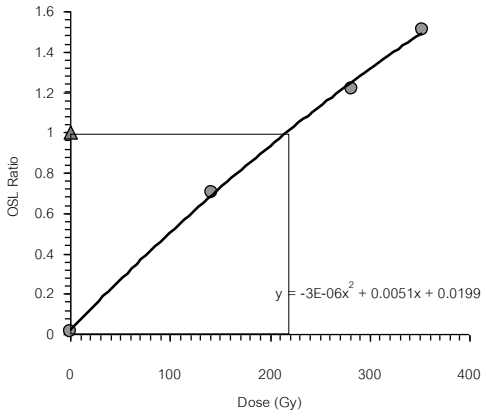

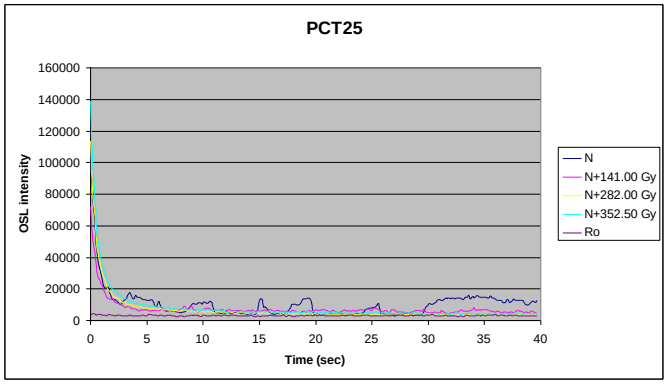

PCT25

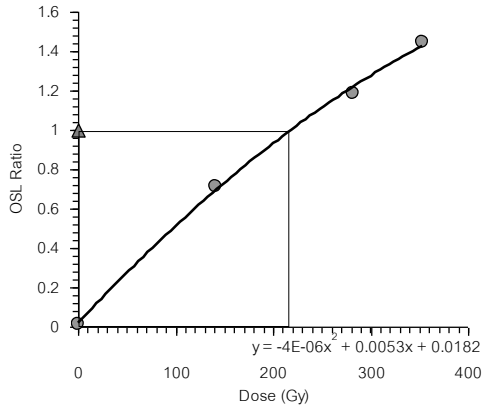

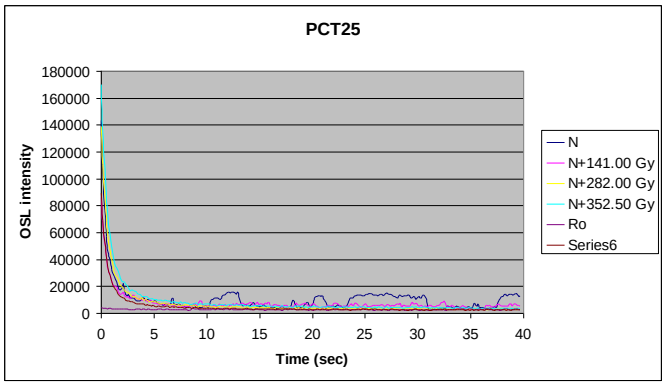

PCT25

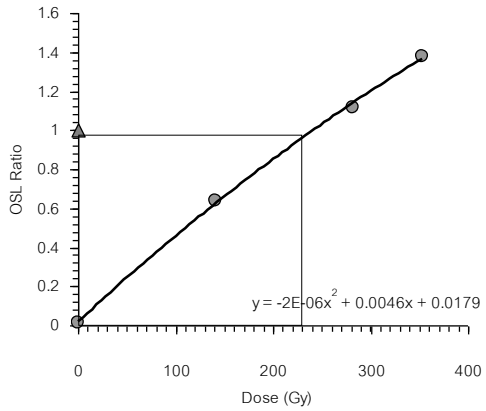

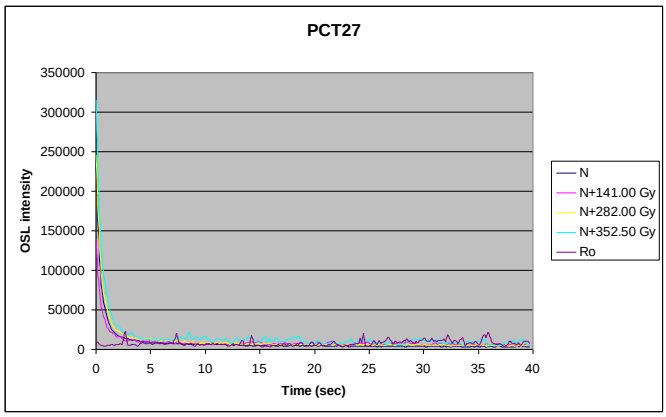

PCT27

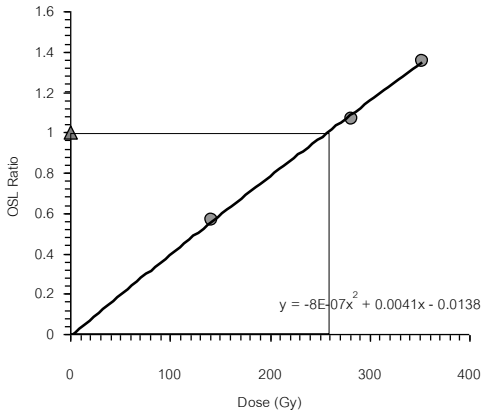

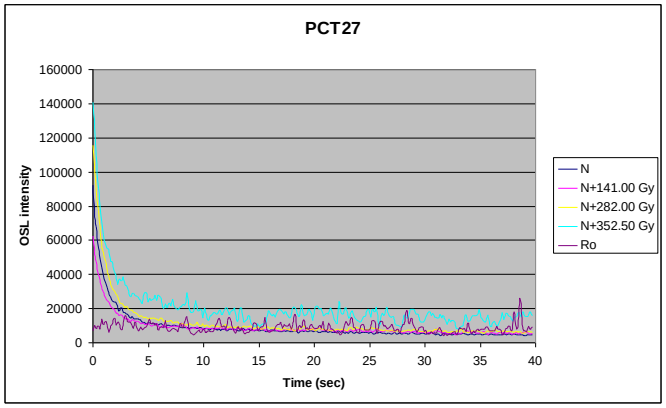

PCT27

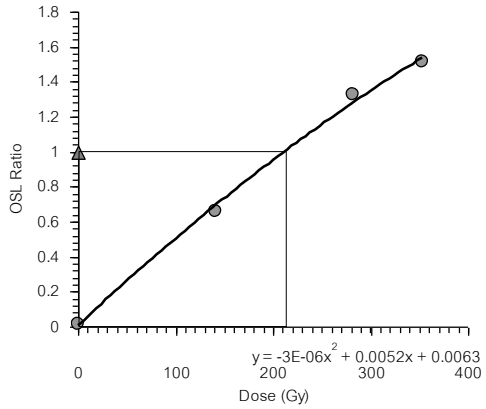

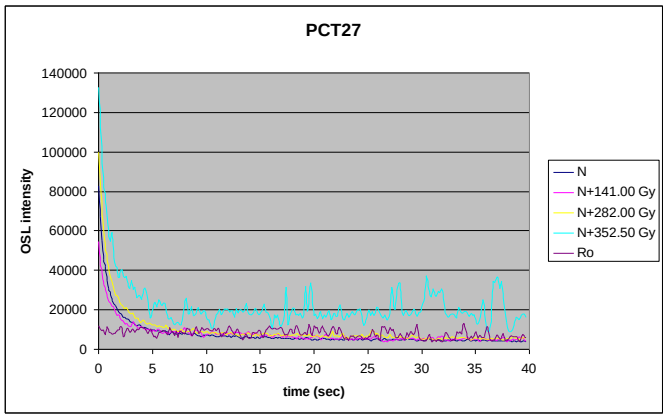

PCT27

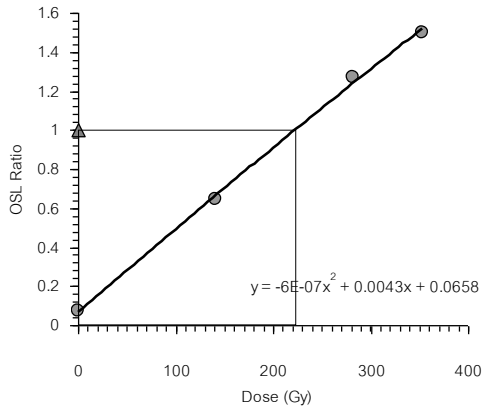

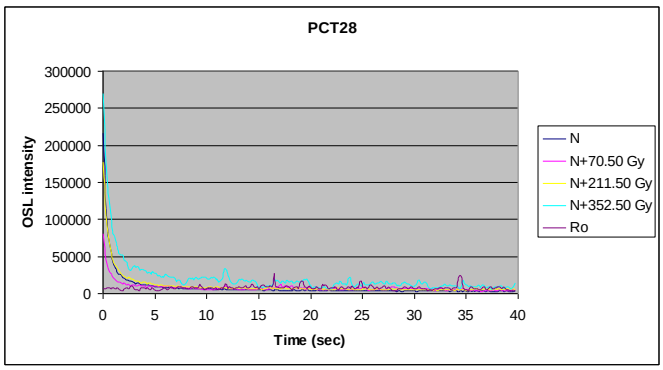

PCT28

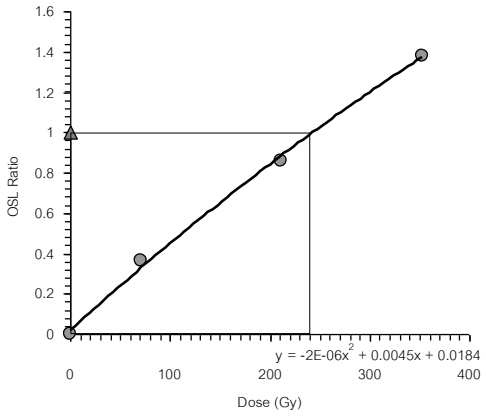

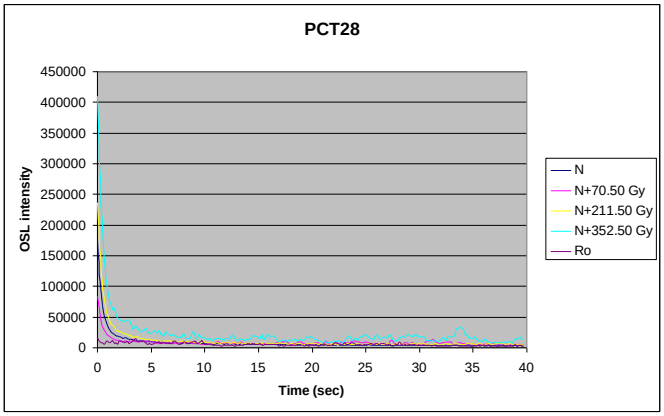

PCT28

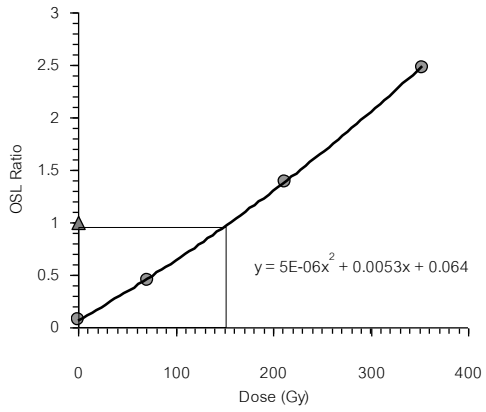

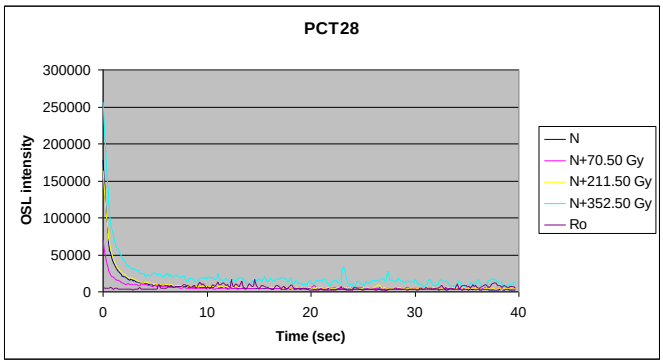

PCT28

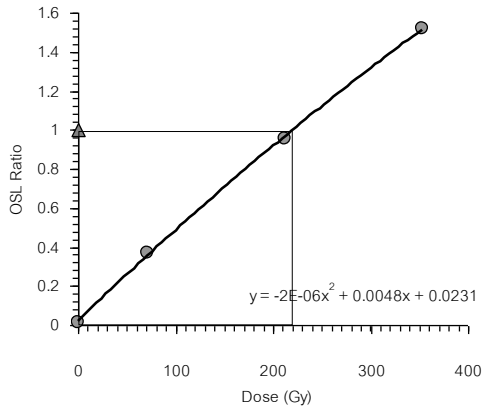

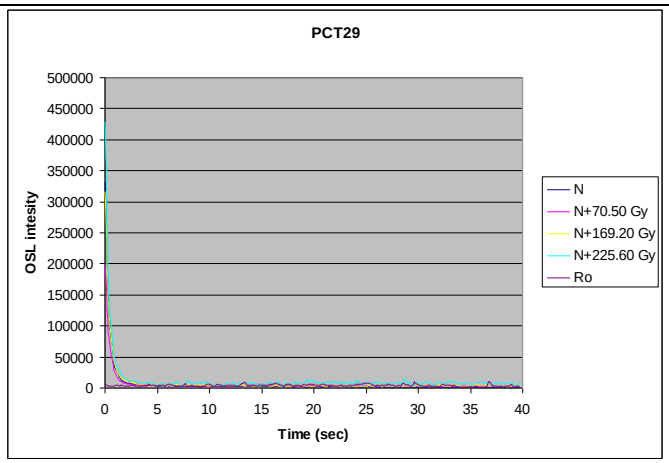

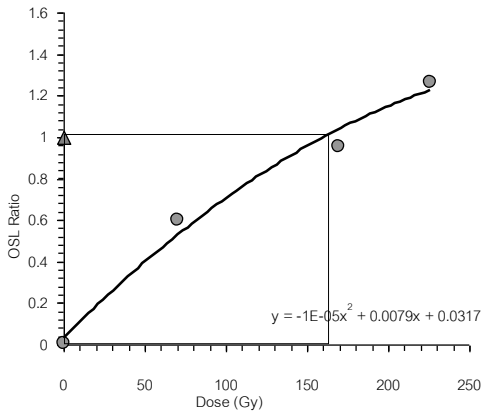

PCT29

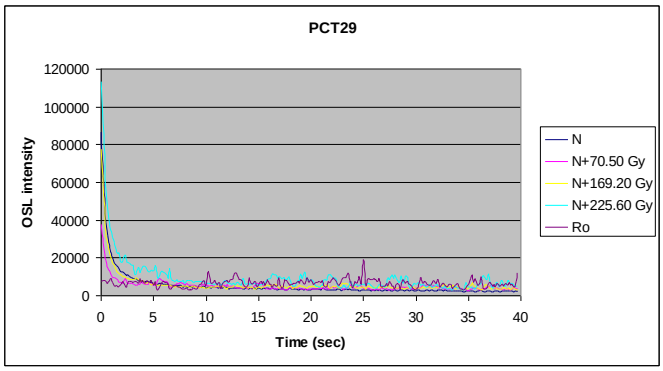

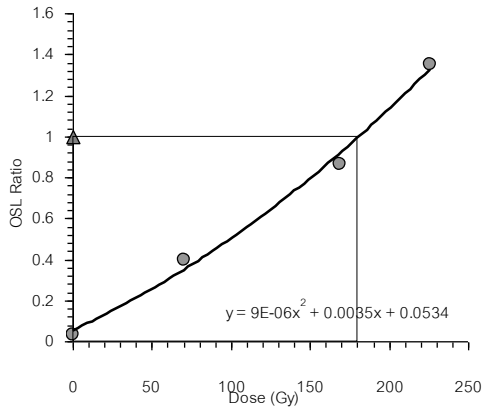

PCT29

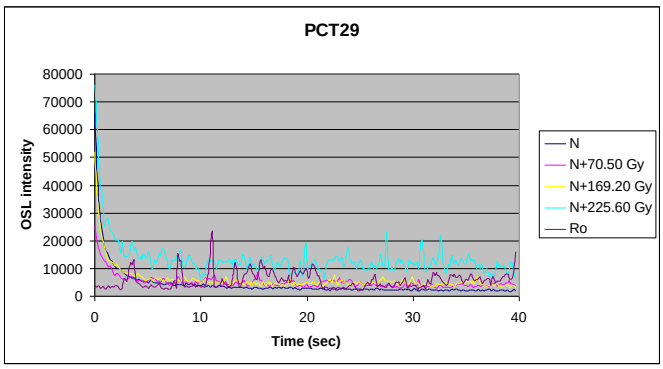

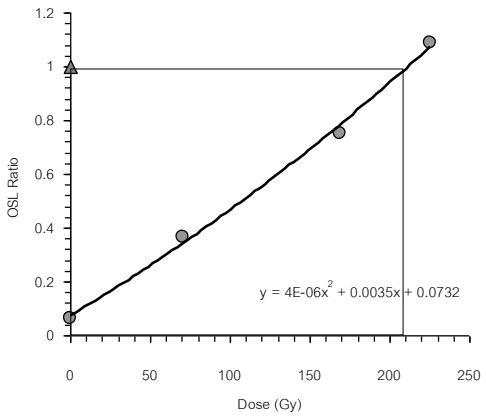

PCT29

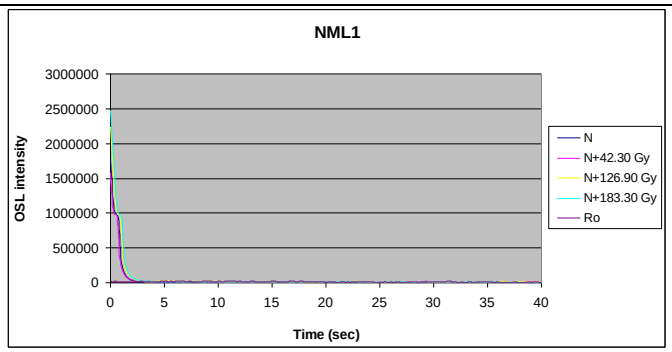

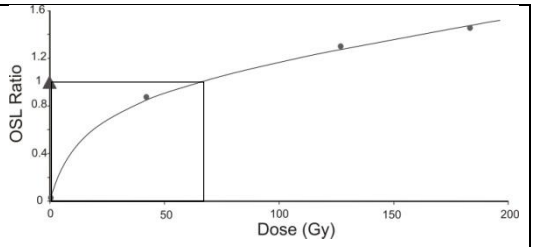

NML1

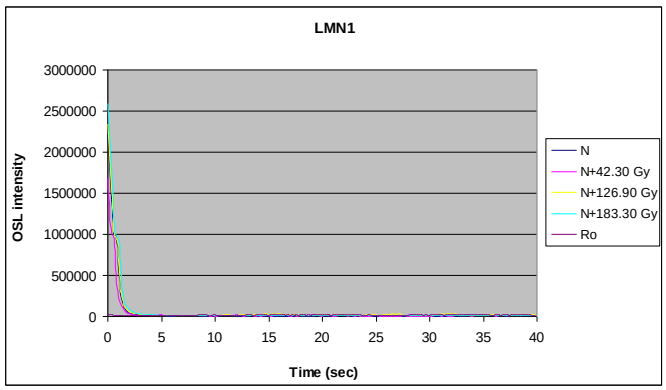

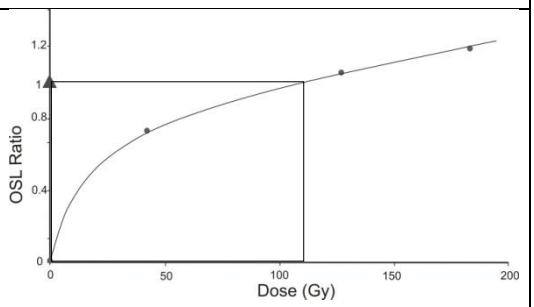

NML1

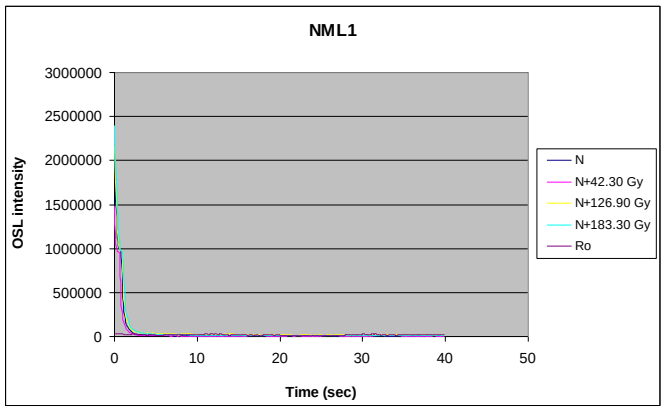

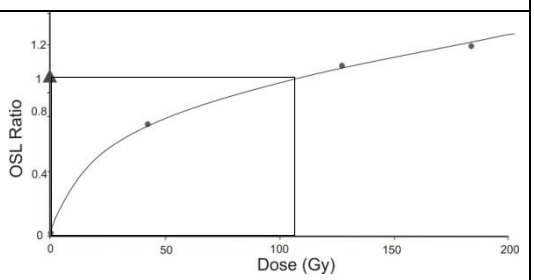

NML1

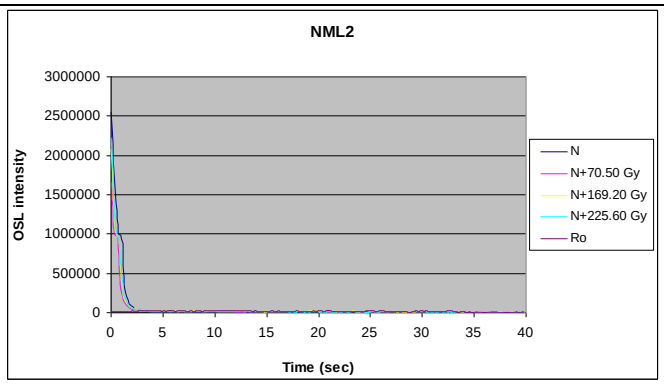

NML2

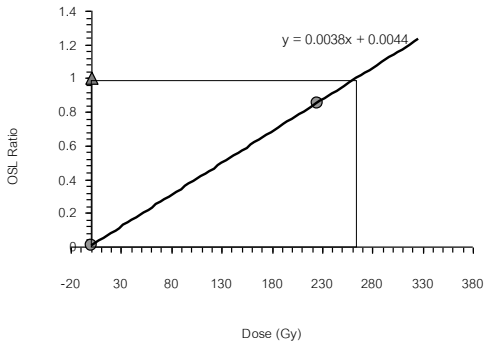

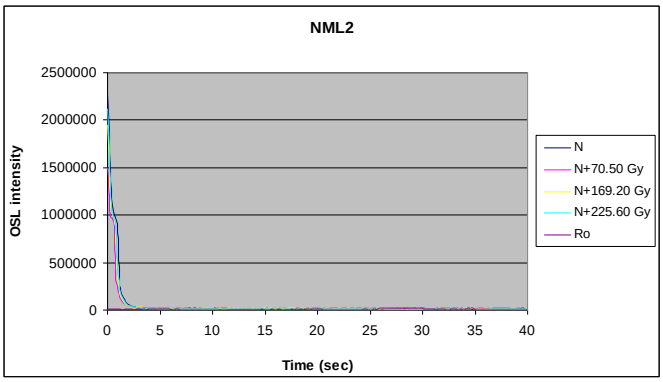

NML2

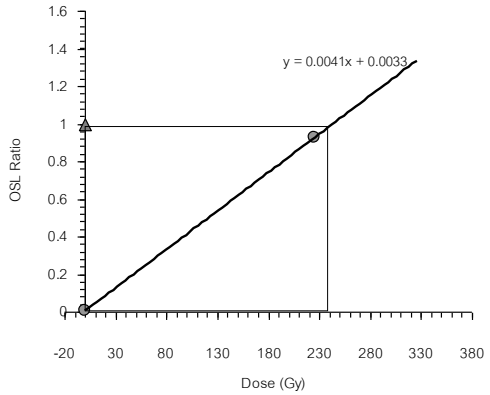

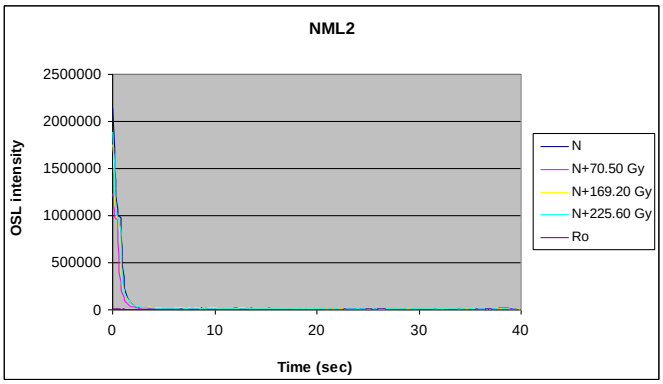

NML2

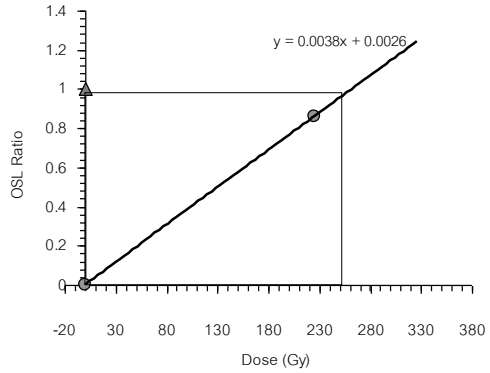

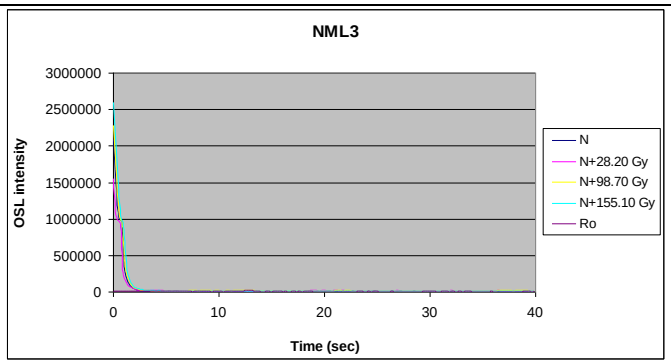

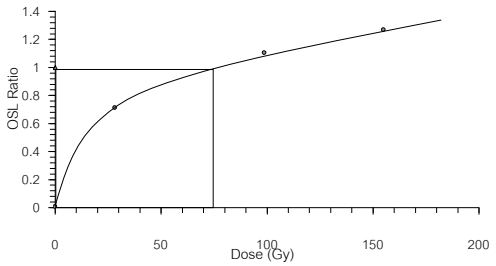

NML3

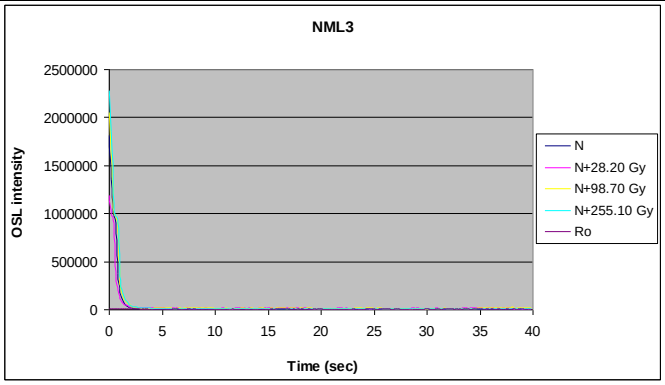

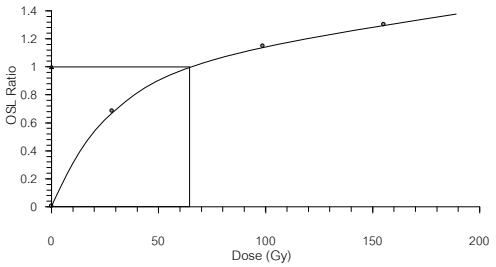

NML3

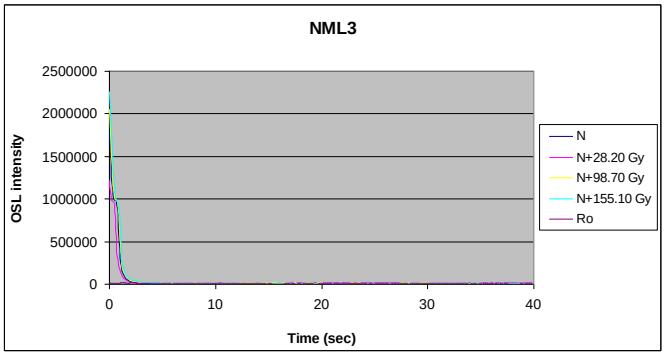

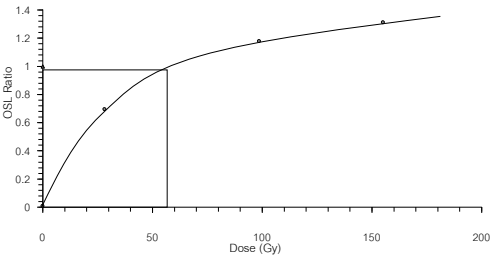

NML3

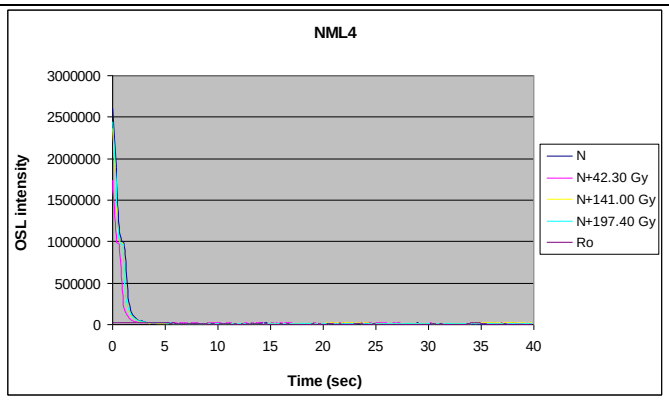

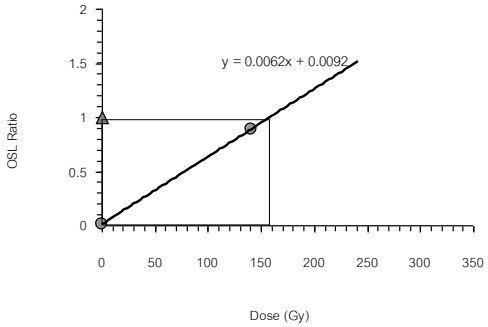

NML4

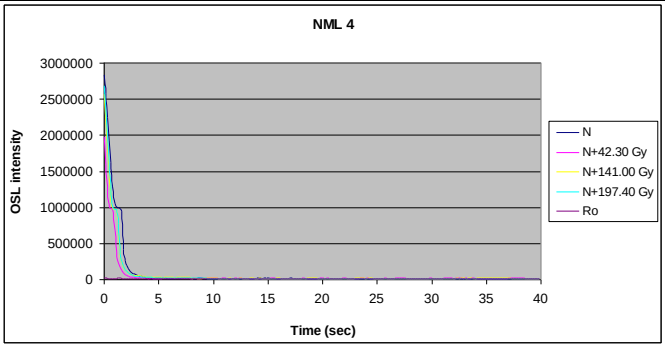

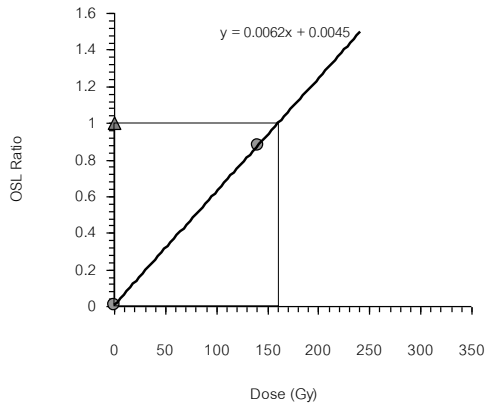

NML4

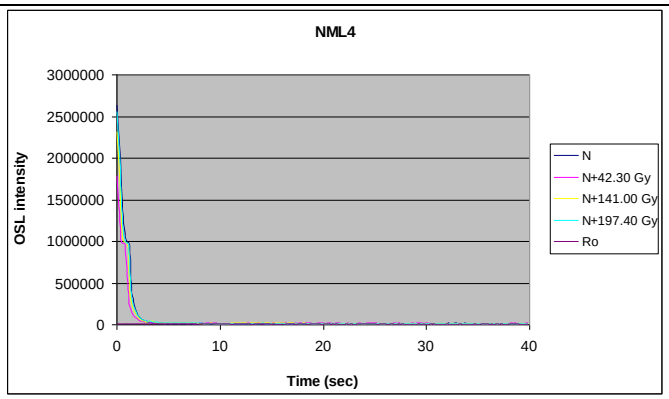

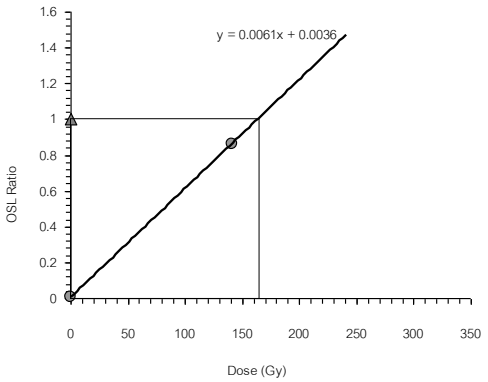

NML4

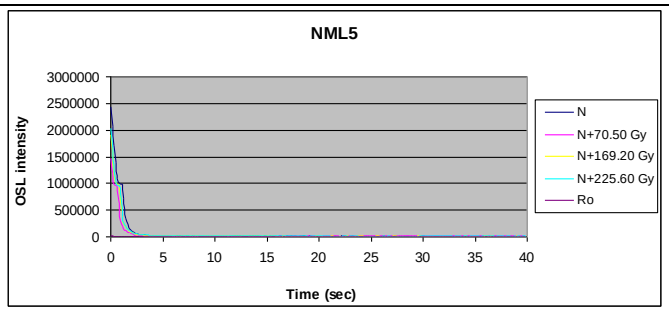

NML5

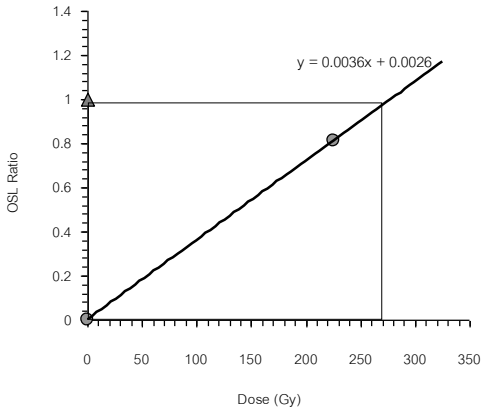

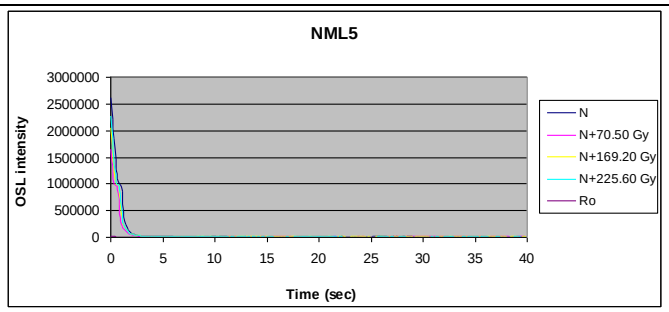

NML5

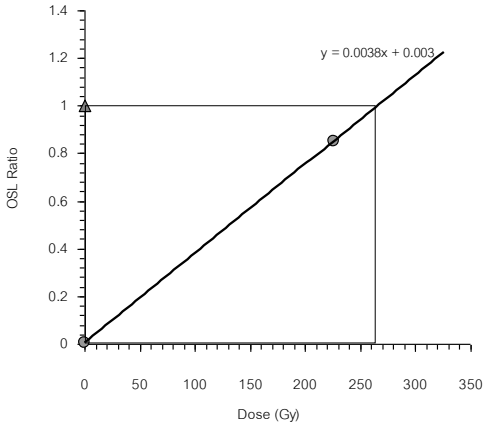

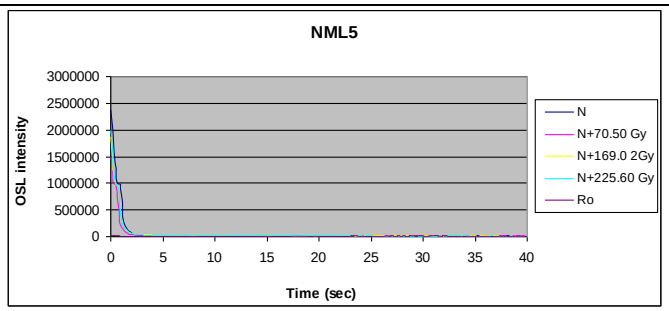

NML5

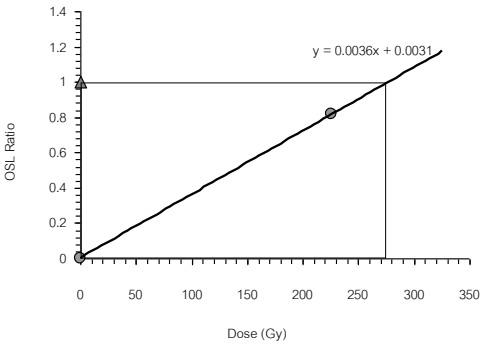

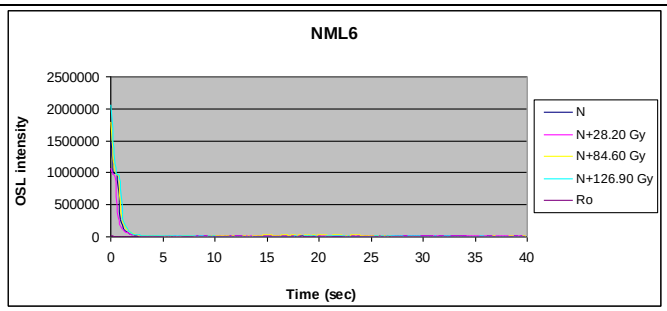

NML6

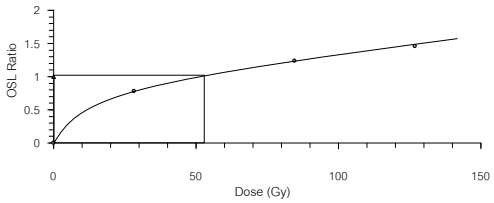

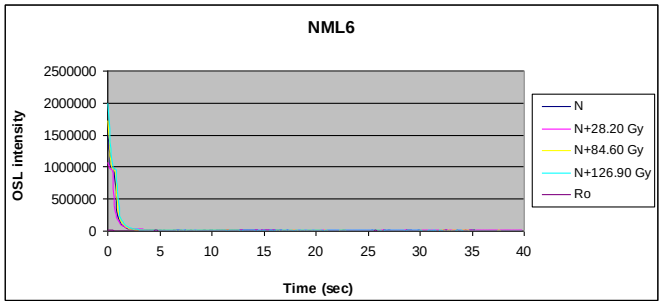

NML6

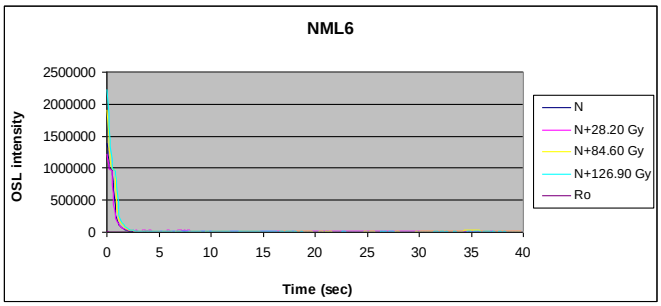

NML6

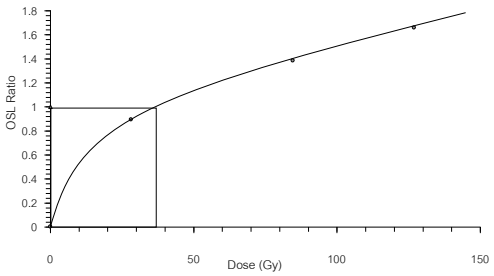

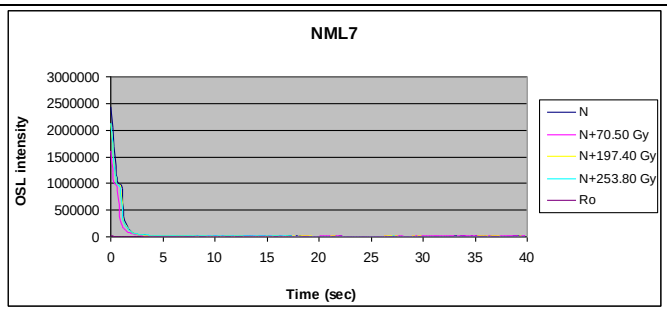

NML7

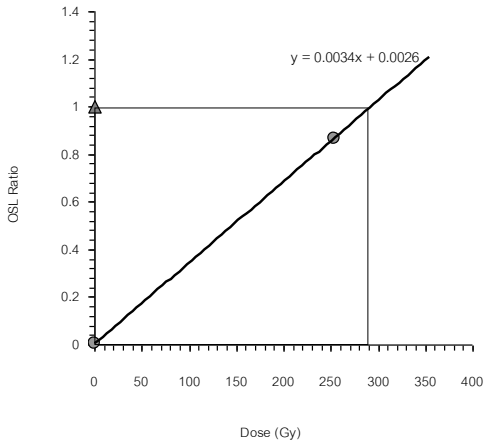

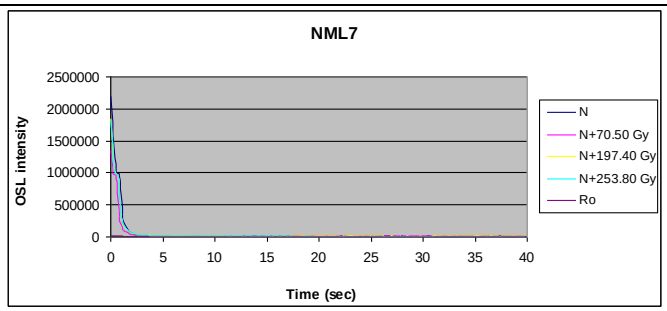

NML7

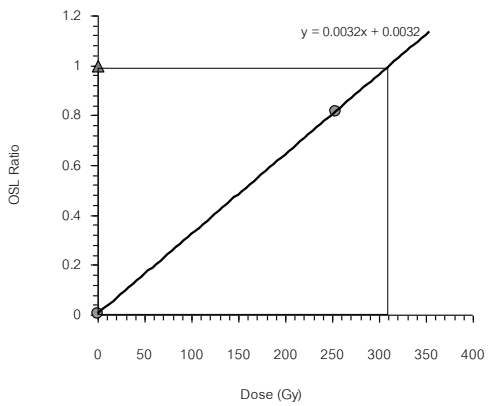

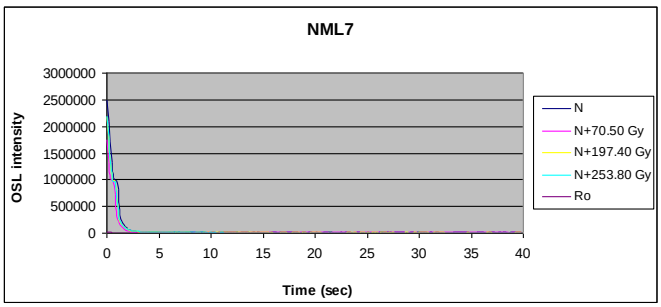

NML7

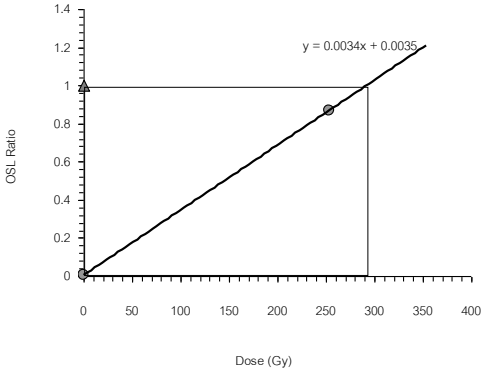

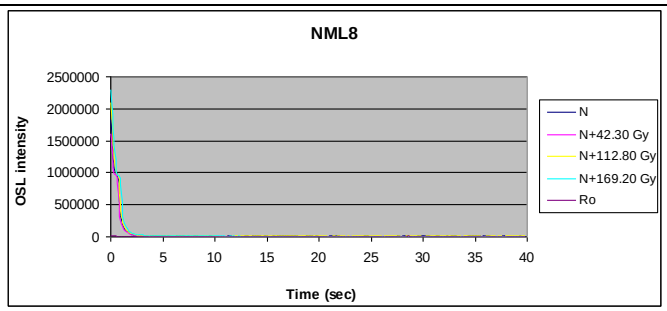

NML8

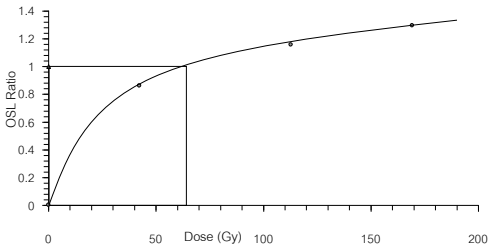

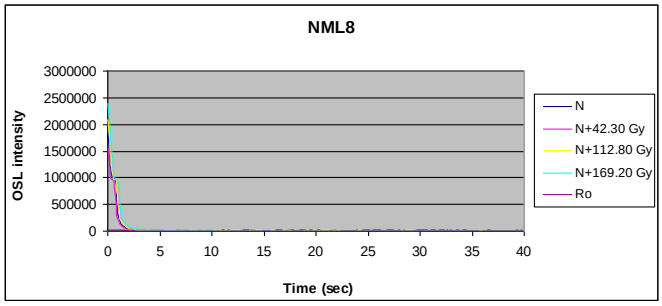

NML8

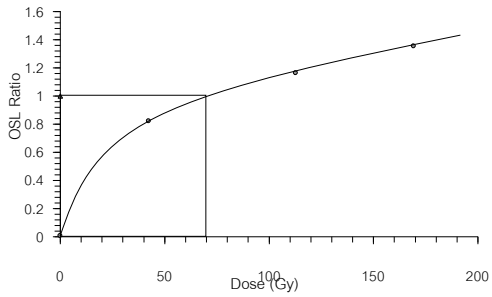

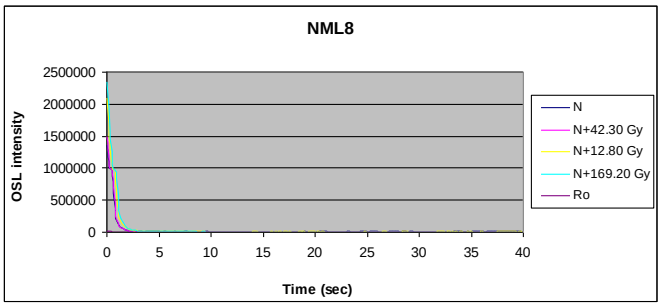

NML8

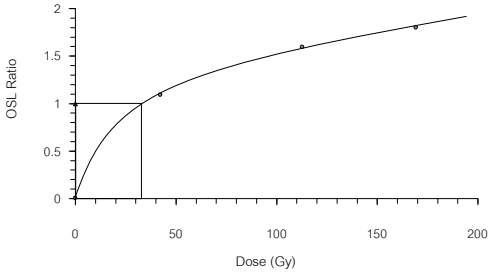

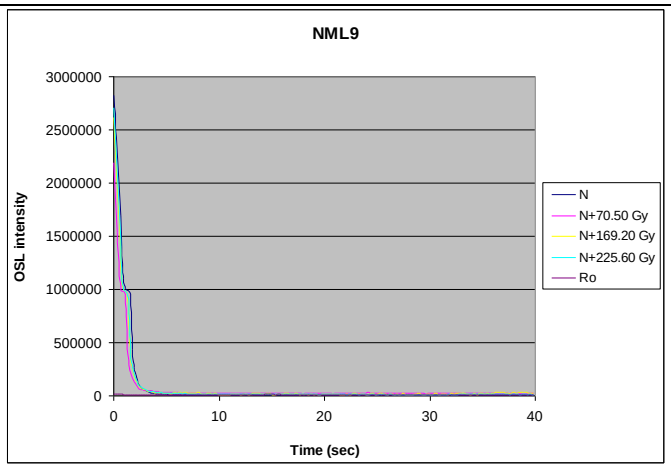

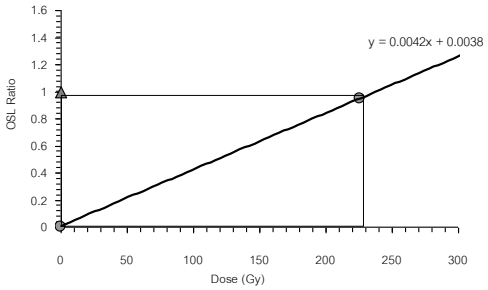

NML9

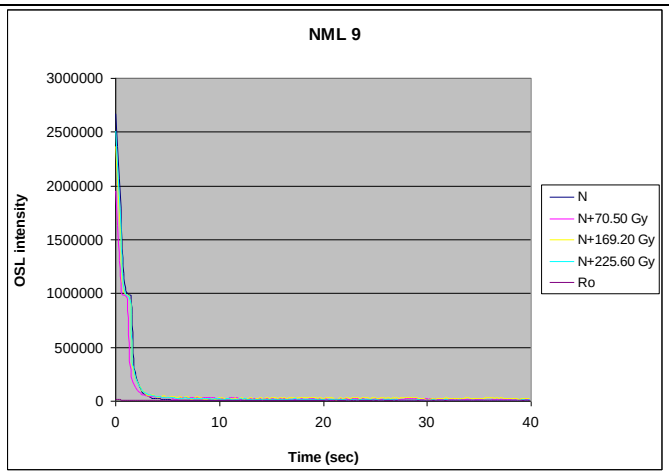

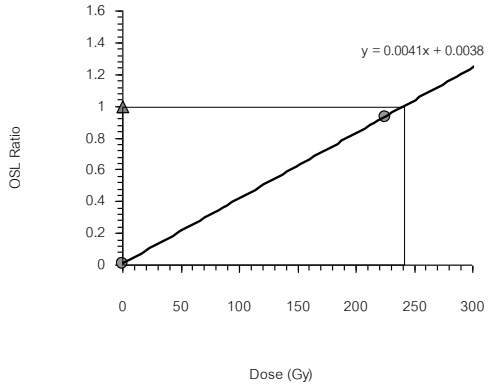

NML9

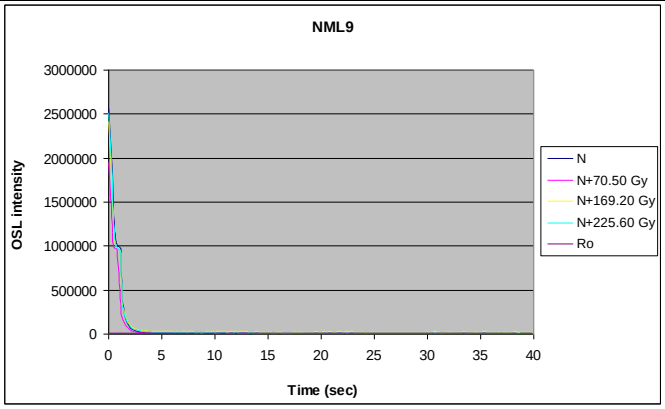

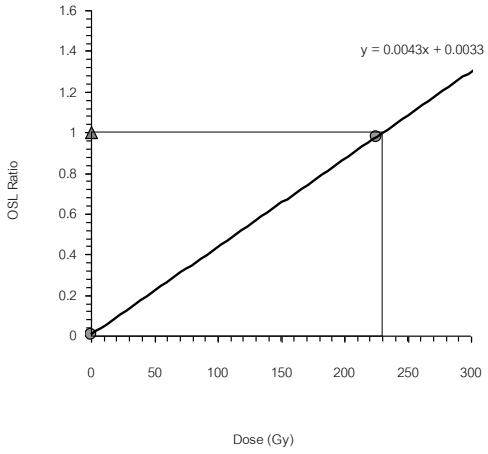

NML9

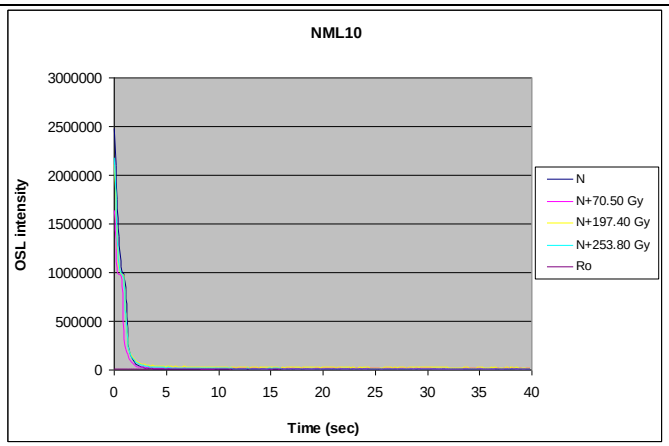

NML10

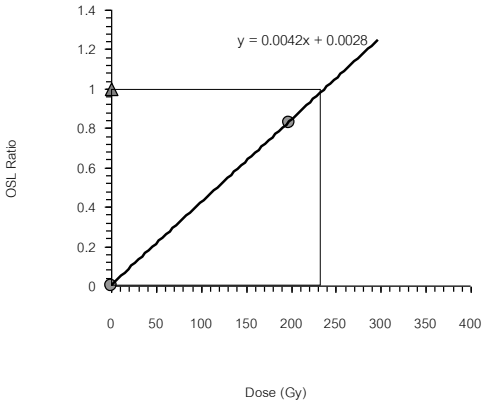

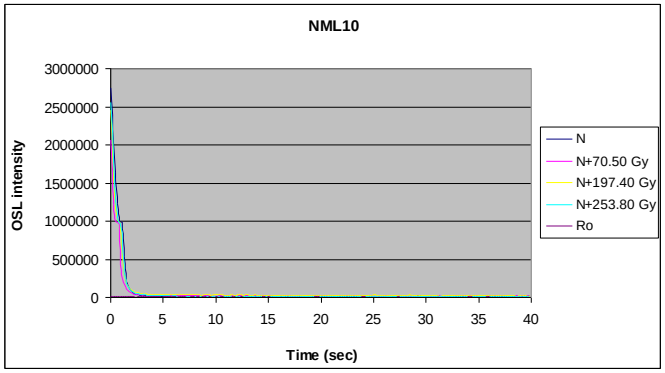

NML10

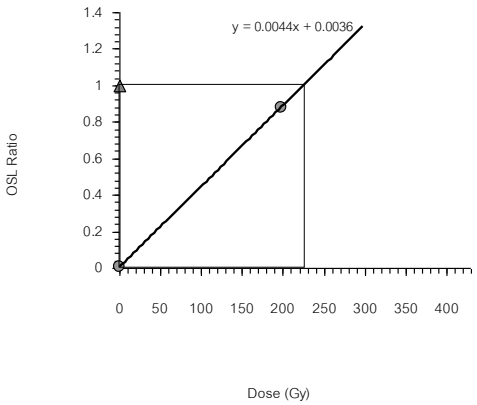

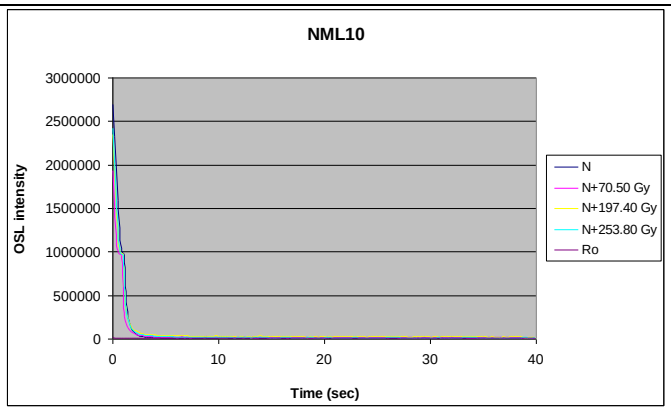

NML10

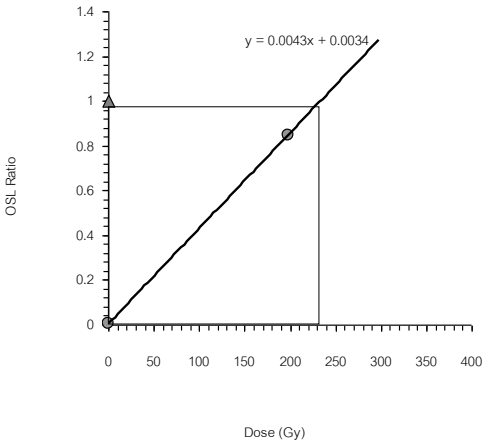

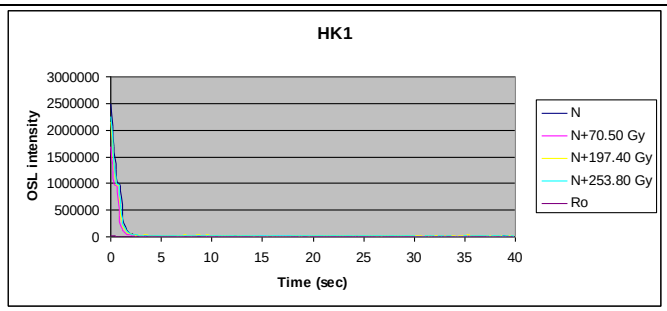
HK1
OSL intensity
3000000
2500000
2000000
1500000
1000000
500000
0
0 5 10 15 20 25 30 35 40
Time (sec)
N
N+70.50 Gy
N+197.40 Gy
N+253.80 Gy
Ro

HK1

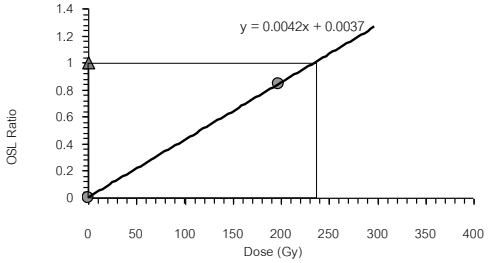
y = 0.0042x + 0.0037
OSL Ratio
1.4
1.2
1
0.8
0.6
0.4
0.2
0
0 50 100 150 200 250 300 350 400
Dose (Gy)

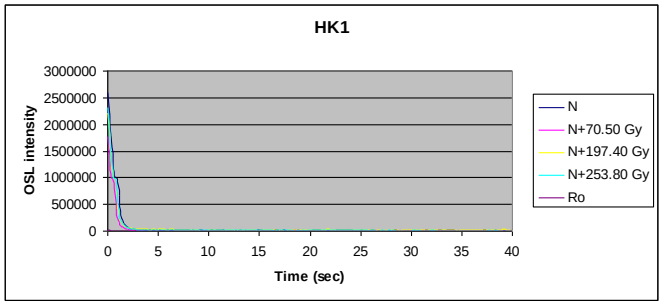
HK1
OSL intensity
3000000
2500000
2000000
1500000
1000000
500000
0
0 5 10 15 20 25 30 35 40
Time (sec)
N
N+70.50 Gy
N+197.40 Gy
N+253.80 Gy
Ro

HK1

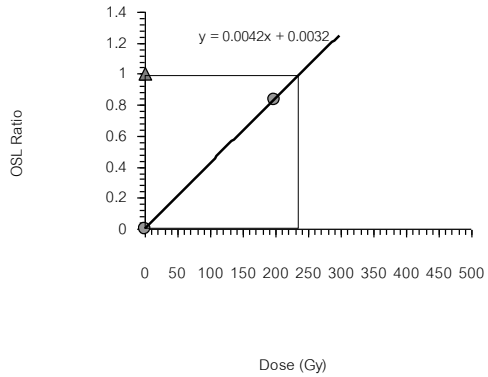
y = 0.0042x + 0.0032
OSL Ratio
1.4
1.2
1
0.8
0.6
0.4
0.2
0
0 50 100 150 200 250 300 350 400 450 500
Dose (Gy)

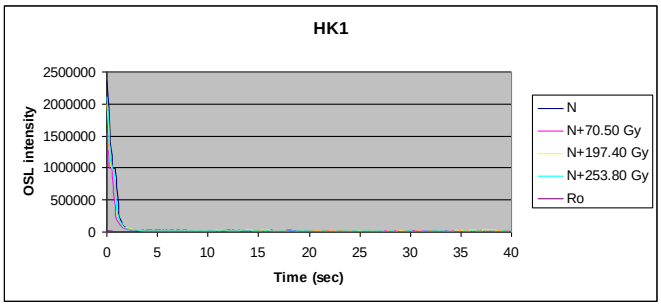
HK1
OSL intensity
2500000
2000000
1500000
1000000
500000
0
0 5 10 15 20 25 30 35 40
Time (sec)
N
N+70.50 Gy
N+197.40 Gy
N+253.80 Gy
Ro

HK1

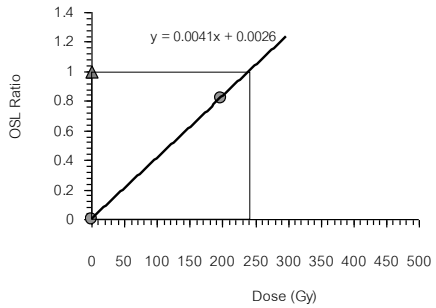
y = 0.0041x + 0.0026
OSL Ratio
1.4
1.2
1
0.8
0.6
0.4
0.2
0
0 50 100 150 200 250 300 350 400 450 500
Dose (Gy)

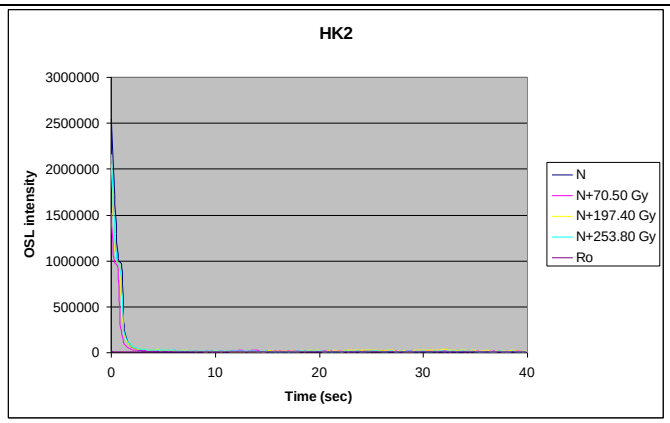
HK2
OSL intensity
Time (sec)
N
N+70.50 Gy
N+197.40 Gy
N+253.80 Gy
Ro

HK2

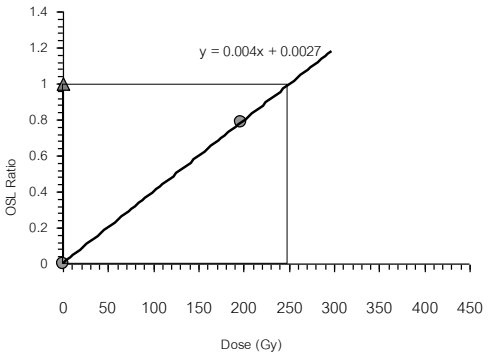
y = 0.004x + 0.0027
OSL Ratio
Dose (Gy)

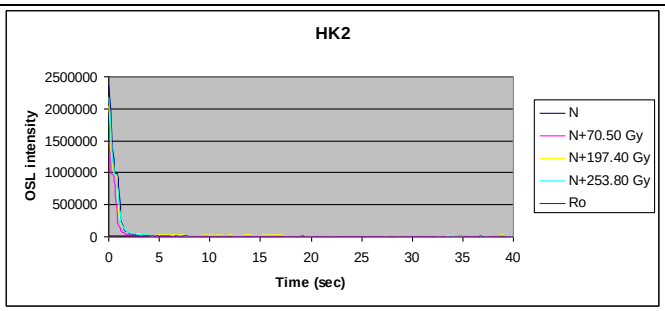
HK2
OSL intensity
Time (sec)
N
N+70.50 Gy
N+197.40 Gy
N+253.80 Gy
Ro

HK2

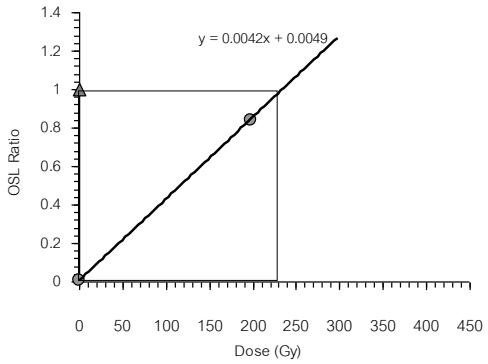
y = 0.0042x + 0.0049
OSL Ratio
Dose (Gy)

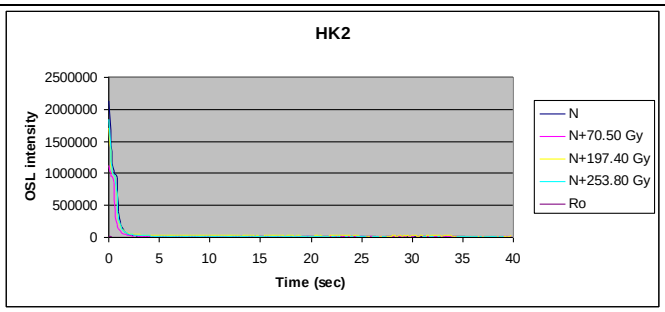
HK2
OSL intensity
Time (sec)
N
N+70.50 Gy
N+197.40 Gy
N+253.80 Gy
Ro

HK2

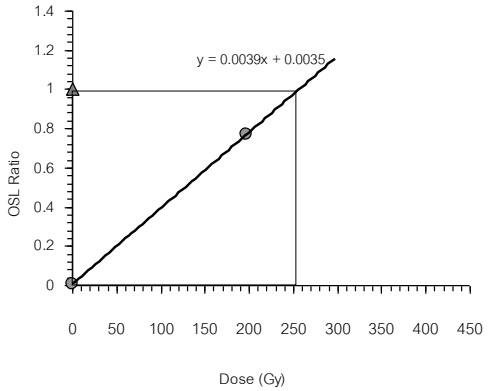
y = 0.0039x + 0.0035
OSL Ratio
Dose (Gy)

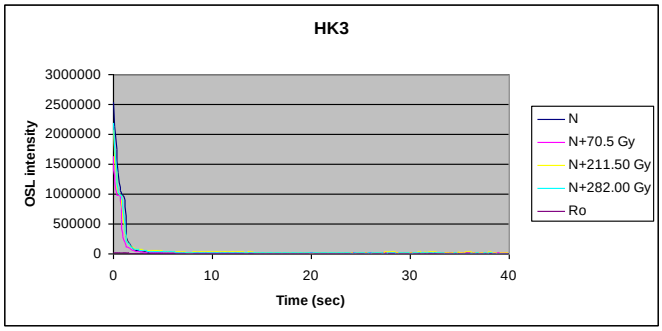
HK3
OSL intensity
3000000
2500000
2000000
1500000
1000000
500000
0
0
10
20
30
40
Time (sec)
N
N+70.5 Gy
N+211.50 Gy
N+282.00 Gy
Ro

HK3

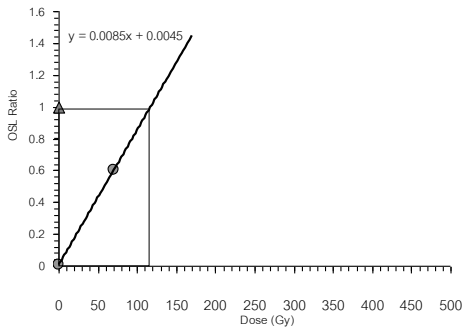
y = 0.0085x + 0.0045
OSL Ratio
1.6
1.4
1.2
1
0.8
0.6
0.4
0.2
0
0
50
100
150
200
250
300
350
400
450
500
Dose (Gy)

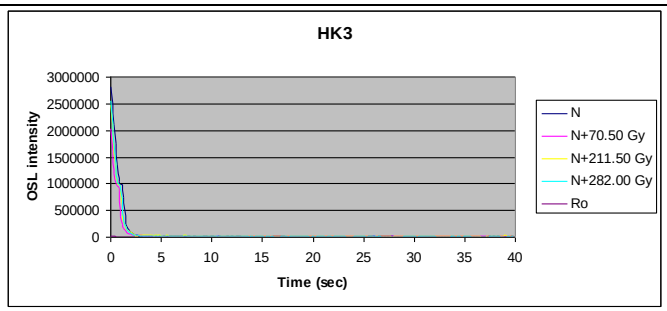
HK3
OSL intensity
3000000
2500000
2000000
1500000
1000000
500000
0
0
5
10
15
20
25
30
35
40
Time (sec)
N
N+70.50 Gy
N+211.50 Gy
N+282.00 Gy
Ro

HK3

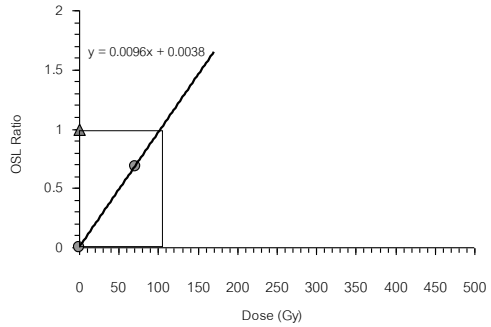
y = 0.0096x + 0.0038
OSL Ratio
2
1.5
1
0.5
0
0
50
100
150
200
250
300
350
400
450
500
Dose (Gy)

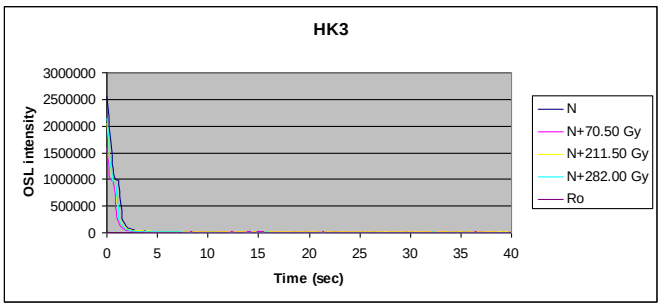
HK3
OSL intensity
3000000
2500000
2000000
1500000
1000000
500000
0
0
5
10
15
20
25
30
35
40
Time (sec)
N
N+70.50 Gy
N+211.50 Gy
N+282.00 Gy
Ro

HK3

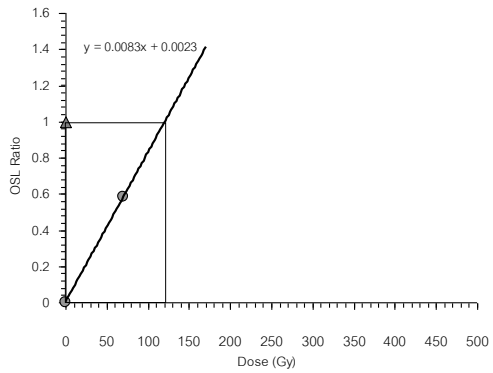
y = 0.0083x + 0.0023
OSL Ratio
1.6
1.4
1.2
1
0.8
0.6
0.4
0.2
0
0
50
100
150
200
250
300
350
400
450
500
Dose (Gy)

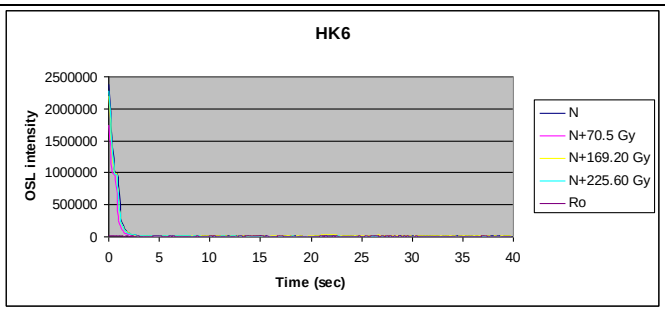
HK6
OSL intensity
2500000
2000000
1500000
1000000
500000
0
0 5 10 15 20 25 30 35 40
Time (sec)
N
N+70.5 Gy
N+169.20 Gy
N+225.60 Gy
Ro

HK6

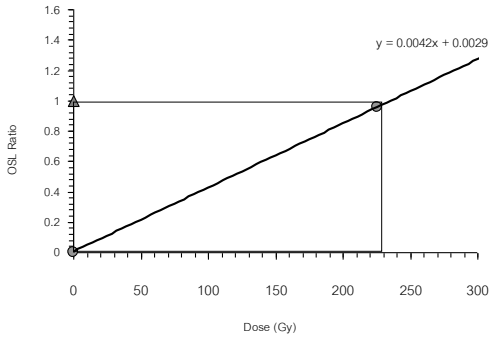
y = 0.0042x + 0.0029
OSL Ratio
1.6
1.4
1.2
1
0.8
0.6
0.4
0.2
0
0 50 100 150 200 250 300
Dose (Gy)

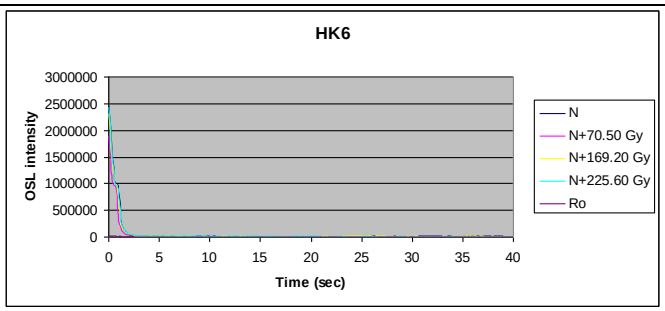
HK6
OSL intensity
3000000
2500000
2000000
1500000
1000000
500000
0
0 5 10 15 20 25 30 35 40
Time (sec)
N
N+70.50 Gy
N+169.20 Gy
N+225.60 Gy
Ro

HK6

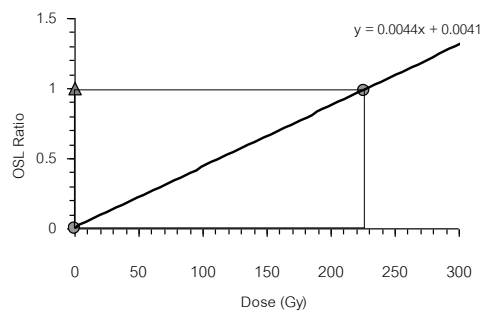
y = 0.0044x + 0.0041
OSL Ratio
1.5
1
0.5
0
0 50 100 150 200 250 300
Dose (Gy)

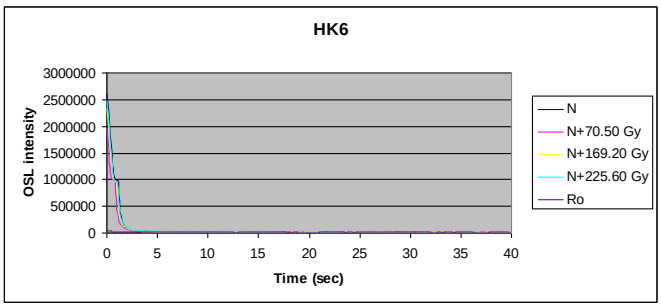
HK6
OSL intensity
3000000
2500000
2000000
1500000
1000000
500000
0
0 5 10 15 20 25 30 35 40
Time (sec)
N
N+70.50 Gy
N+169.20 Gy
N+225.60 Gy
Ro

HK6

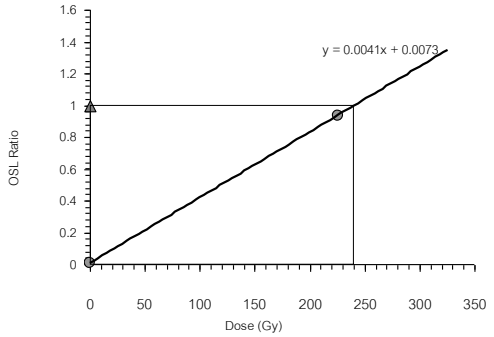
y = 0.0041x + 0.0073
OSL Ratio
1.6
1.4
1.2
1
0.8
0.6
0.4
0.2
0
0 50 100 150 200 250 300 350
Dose (Gy)

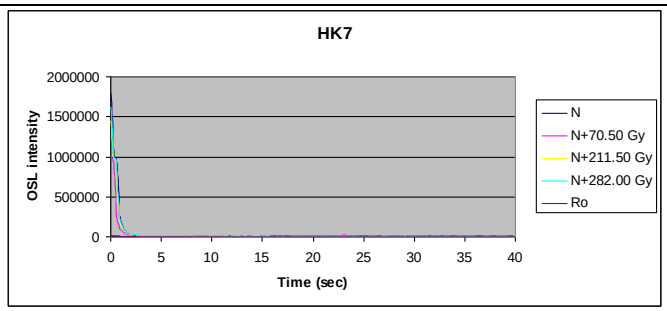
HK7
OSL intensity
2000000
1500000
1000000
500000
0
0 5 10 15 20 25 30 35 40
Time (sec)
N
N+70.50 Gy
N+211.50 Gy
N+282.00 Gy
Ro

HK7

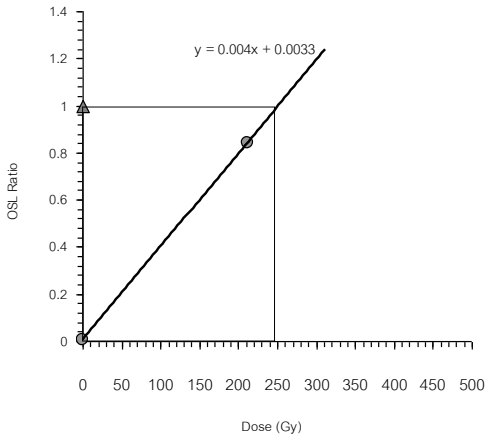
y = 0.004x + 0.0033
OSL Ratio
1.4
1.2
1
0.8
0.6
0.4
0.2
0
0 50 100 150 200 250 300 350 400 450 500
Dose (Gy)

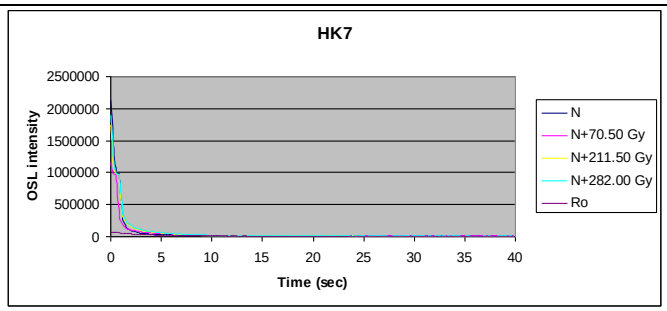
HK7
OSL intensity
2500000
2000000
1500000
1000000
500000
0
0 5 10 15 20 25 30 35 40
Time (sec)
N
N+70.50 Gy
N+211.50 Gy
N+282.00 Gy
Ro

HK7

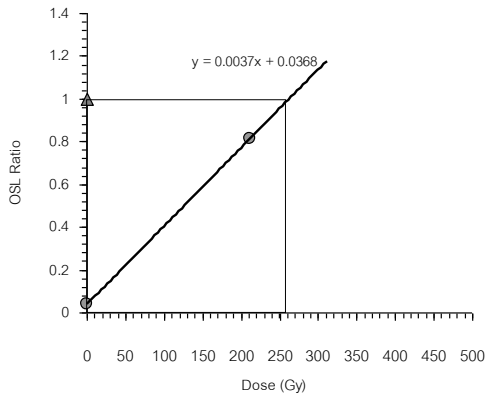
y = 0.0037x + 0.0368
OSL Ratio
1.4
1.2
1
0.8
0.6
0.4
0.2
0
0 50 100 150 200 250 300 350 400 450 500
Dose (Gy)

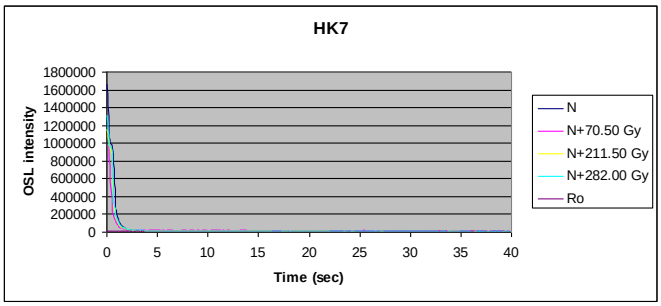
HK7
OSL intensity
1800000
1600000
1400000
1200000
1000000
800000
600000
400000
200000
0
0 5 10 15 20 25 30 35 40
Time (sec)
N
N+70.50 Gy
N+211.50 Gy
N+282.00 Gy
Ro

HK7

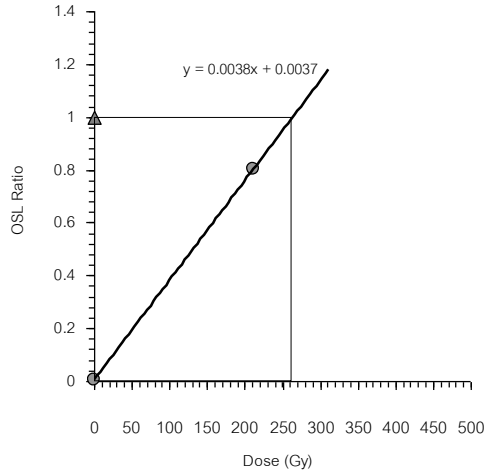
y = 0.0038x + 0.0037
OSL Ratio
1.4
1.2
1
0.8
0.6
0.4
0.2
0
0 50 100 150 200 250 300 350 400 450 500
Dose (Gy)

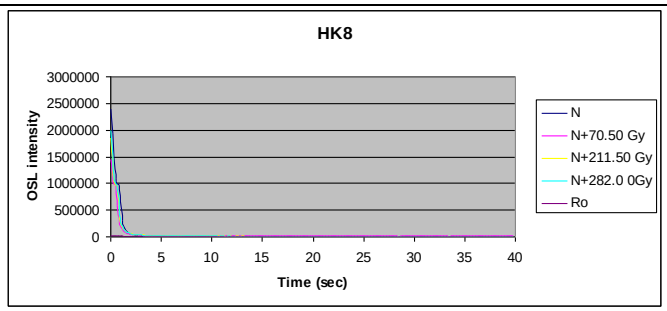
HK8
OSL intensity
3000000
2500000
2000000
1500000
1000000
500000
0
0 5 10 15 20 25 30 35 40
Time (sec)
N
N+70.50 Gy
N+211.50 Gy
N+282.0 0Gy
Ro

HK8

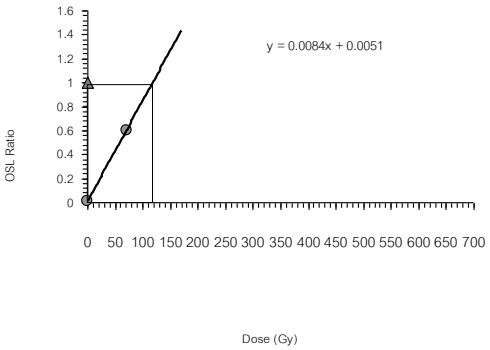
y = 0.0084x + 0.0051
OSL Ratio
1.6
1.4
1.2
1
0.8
0.6
0.4
0.2
0
0 50 100 150 200 250 300 350 400 450 500 550 600 650 700
Dose (Gy)

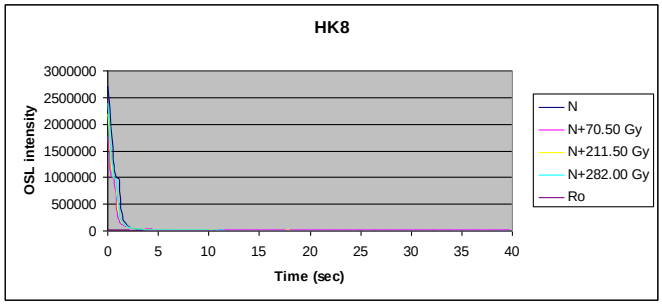
HK8
OSL intensity
3000000
2500000
2000000
1500000
1000000
500000
0
0 5 10 15 20 25 30 35 40
Time (sec)
N
N+70.50 Gy
N+211.50 Gy
N+282.00 Gy
Ro

HK8

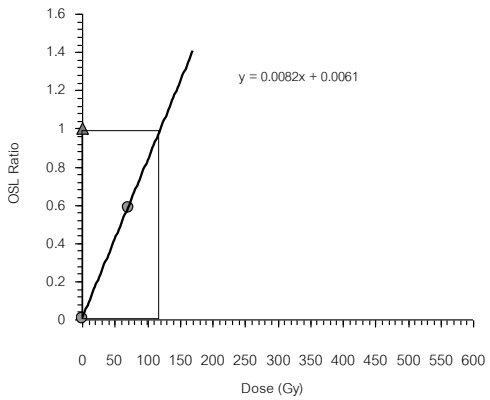
y = 0.0082x + 0.0061
OSL Ratio
1.6
1.4
1.2
1
0.8
0.6
0.4
0.2
0
0 50 100 150 200 250 300 350 400 450 500 550 600
Dose (Gy)

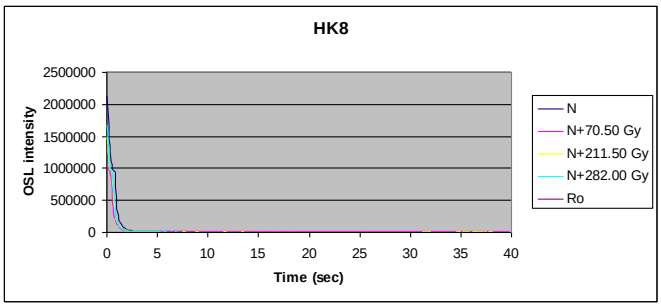
HK8
OSL intensity
2500000
2000000
1500000
1000000
500000
0
0 5 10 15 20 25 30 35 40
Time (sec)
N
N+70.50 Gy
N+211.50 Gy
N+282.00 Gy
Ro

HK8

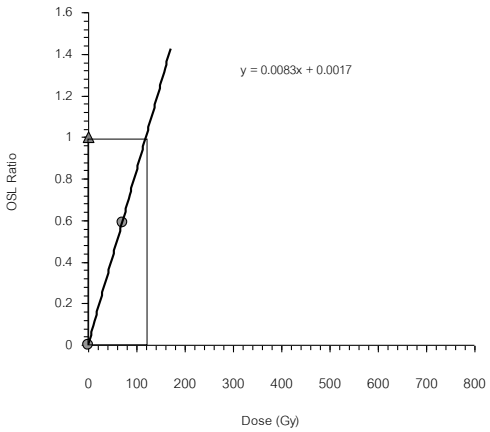
y = 0.0083x + 0.0017
OSL Ratio
1.6
1.4
1.2
1
0.8
0.6
0.4
0.2
0
0 100 200 300 400 500 600 700 800
Dose (Gy)

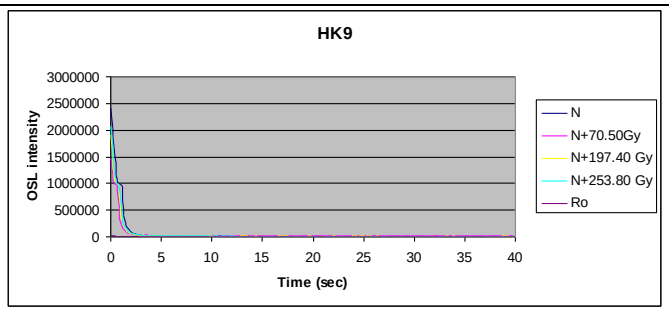
HK9
OSL intensity
Time (sec)
N
N+70.50Gy
N+197.40 Gy
N+253.80 Gy
Ro

HK9

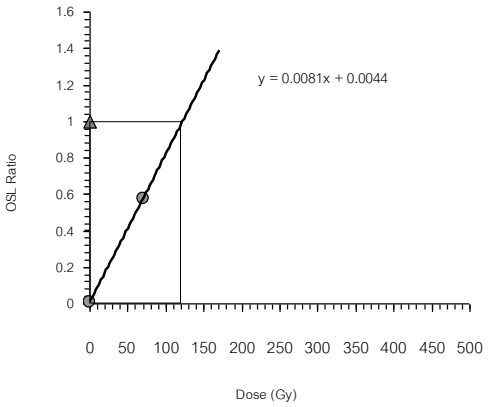
y = 0.0081x + 0.0044
OSL Ratio
Dose (Gy)

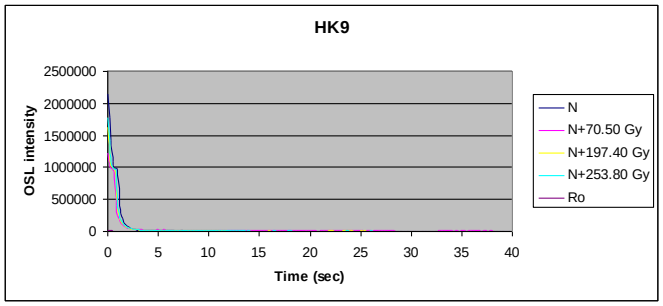
HK9
OSL intensity
Time (sec)
N
N+70.50 Gy
N+197.40 Gy
N+253.80 Gy
Ro

HK9

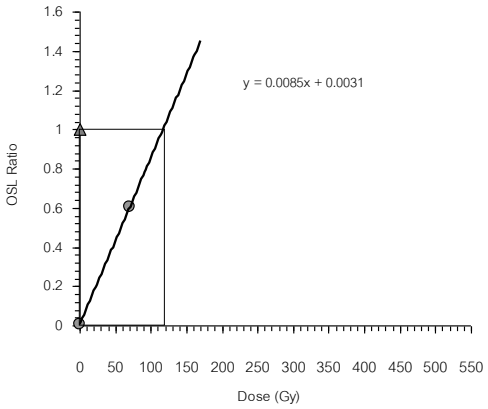
y = 0.0085x + 0.0031
OSL Ratio
Dose (Gy)

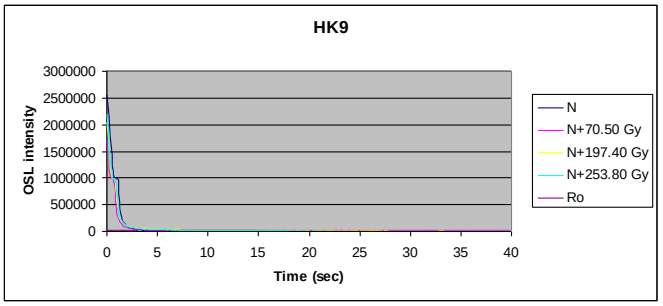
HK9
OSL intensity
Time (sec)
N
N+70.50 Gy
N+197.40 Gy
N+253.80 Gy
Ro

HK9

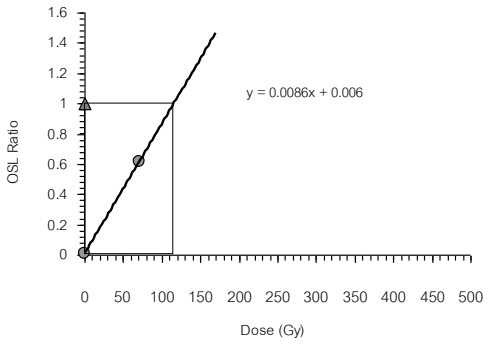
y = 0.0086x + 0.006
OSL Ratio
Dose (Gy)

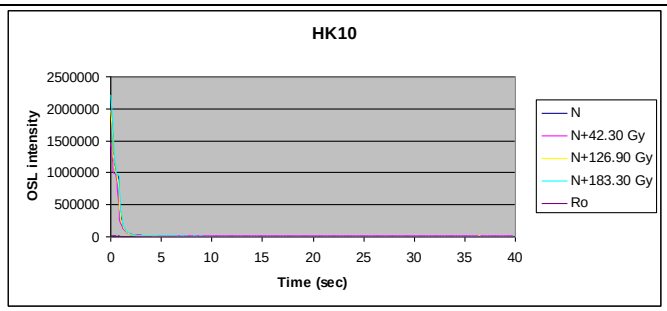

HK10

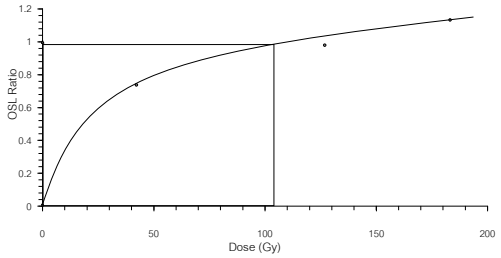

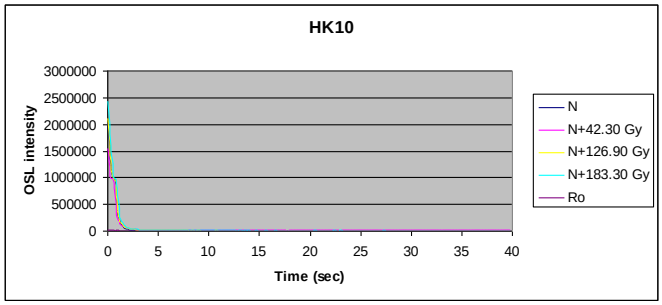

HK10

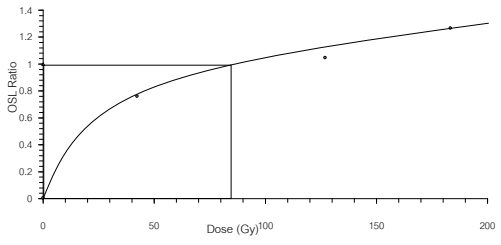

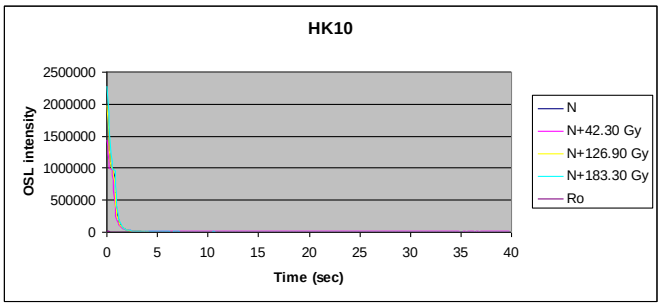

HK10

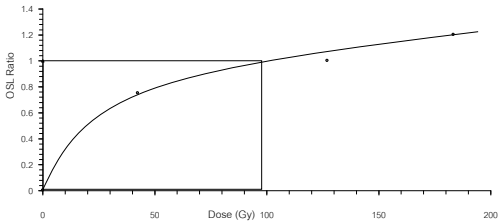

<table>
<tr>
<td> 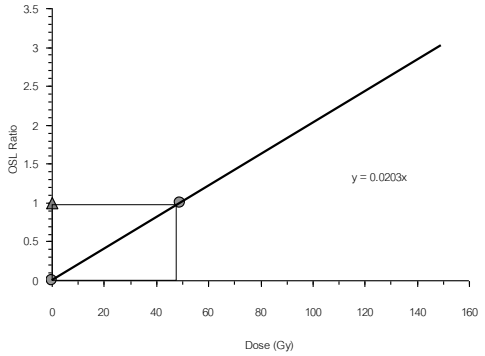

MCP1</td>
<td> 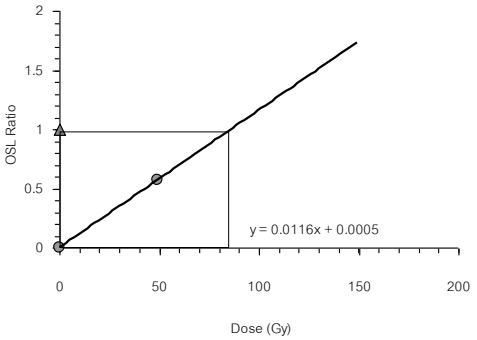

MCP1</td>
</tr>
<tr>
<td> 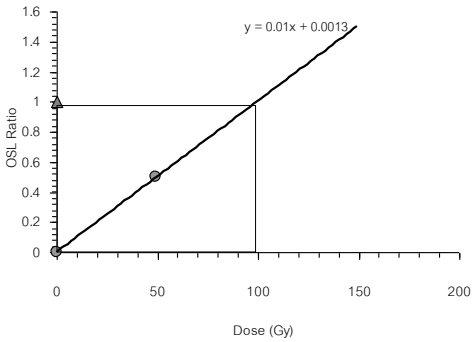

MCP1</td>
<td>Remark:
The original glow curves of this sample are available in EGAT [2012]. For this study, the growth curves were only permitted to reassess.</td>
</tr>
<tr>
<td> 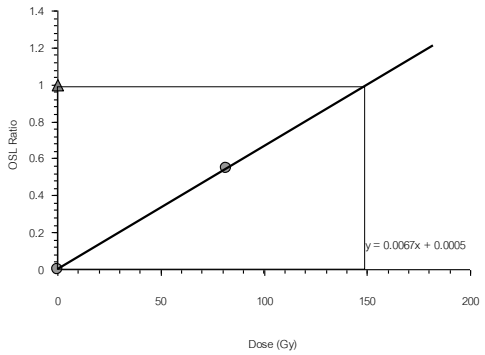

MCP2</td>
<td> 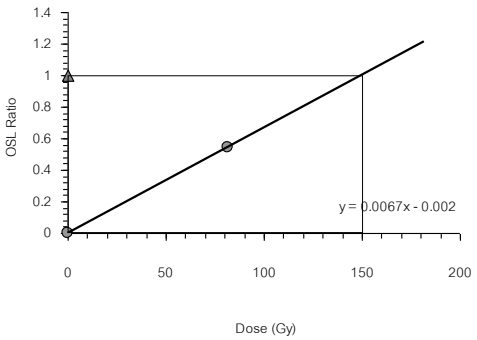

MCP2</td>
</tr>
<tr>
<td> 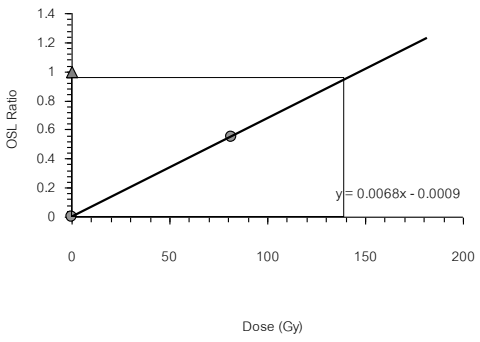

MCP2</td>
<td>Remark:
The original glow curves of this sample are available in EGAT [2012]. For this study, the growth curves were only permitted to reassess.</td>
</tr>
</table>

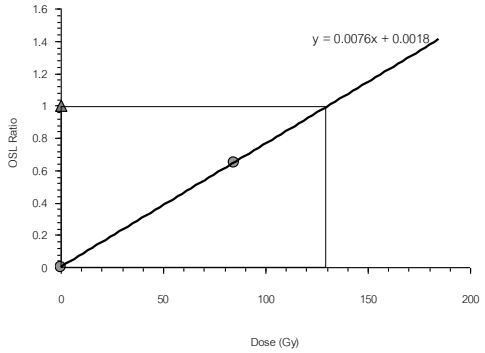 MCP3	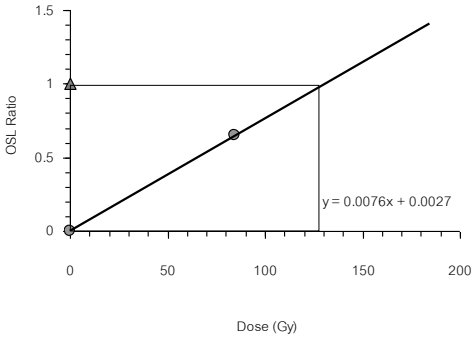 MCP3
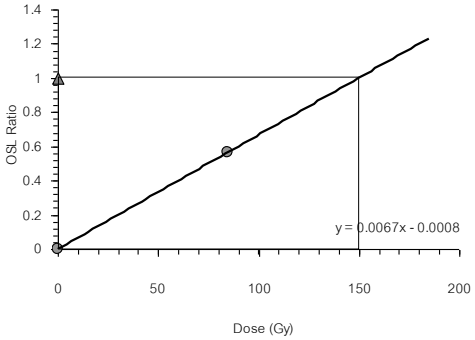 MCP3	Remark: The original glow curves of this sample are available in EGAT [2012]. For this study, the growth curves were only permitted to reassess.
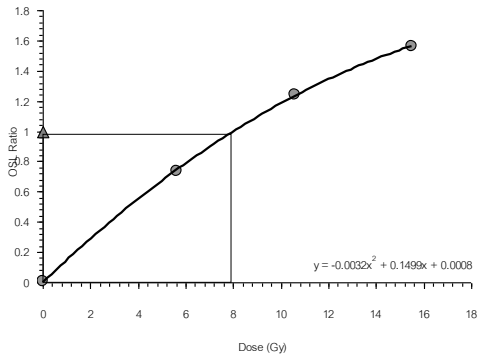 MCP5	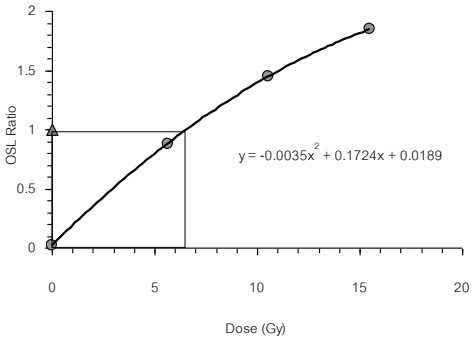 MCP5
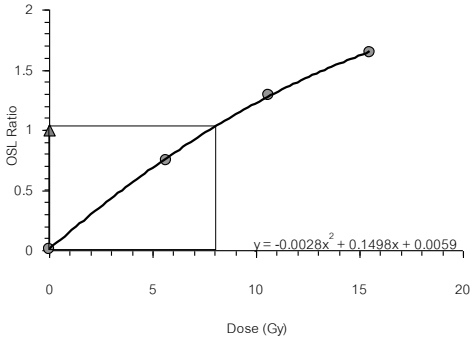 MCP5	Remark: The original glow curves of this sample are available in EGAT [2012]. For this study, the growth curves were only permitted to reassess.

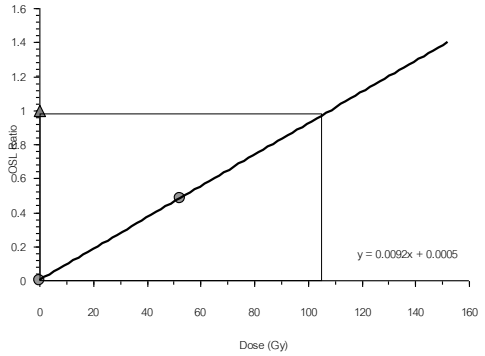	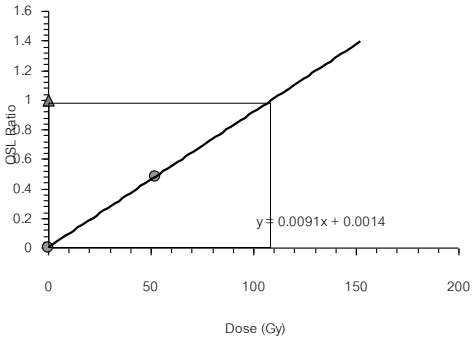
MCP6	MCP6
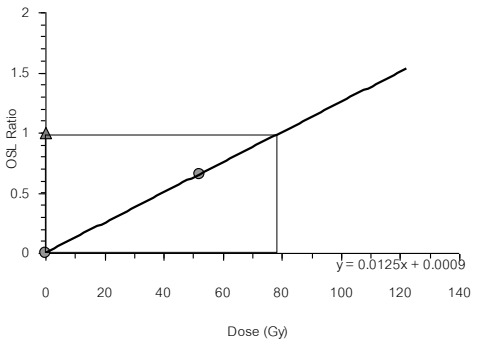	Remark: The original glow curves of this sample are available in EGAT [2012]. For this study, the growth curves were only permitted to reassess.
MCP6	
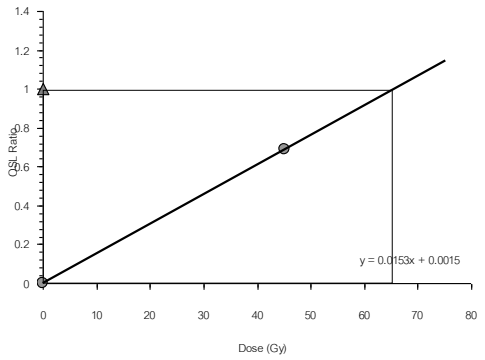	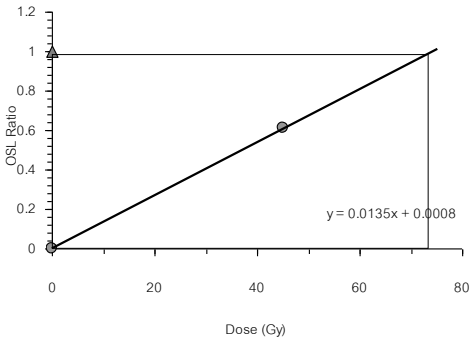
MCP9	MCP9
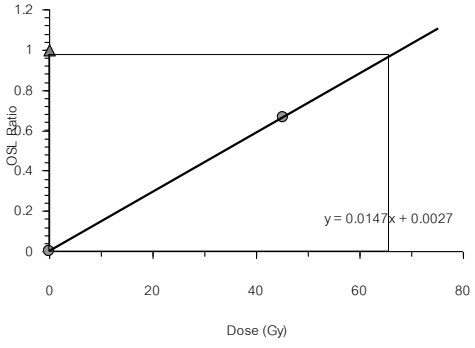	Remark: The original glow curves of this sample are available in EGAT [2012]. For this study, the growth curves were only permitted to reassess.
MCP9	

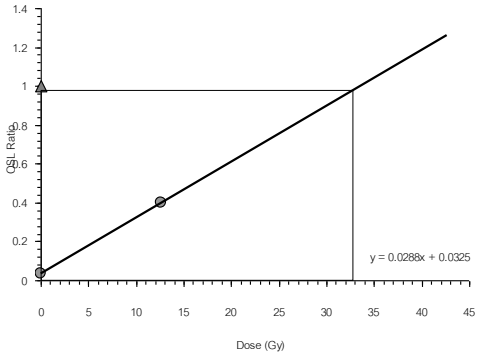 MCP10	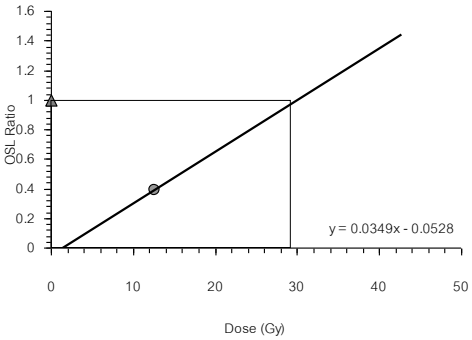 MCP10
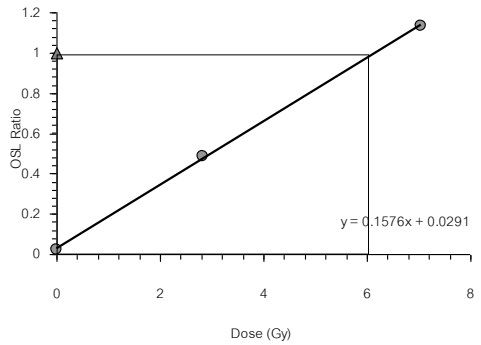 MCP10	Remark: The original glow curves of this sample are available in EGAT [2012]. For this study, the growth curves were only permitted to reassess.

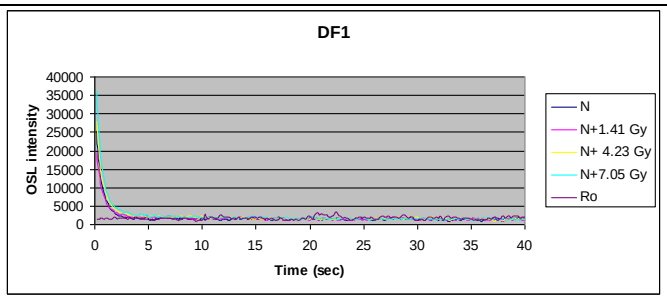
DF1
OSL intensity
Time (sec)
N
N+1.41 Gy
N+ 4.23 Gy
N+7.05 Gy
Ro

DF1

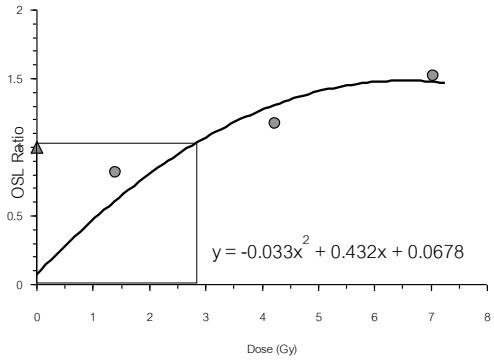
OSL Ratio
Dose (Gy)
y = -0.033x2 + 0.432x + 0.0678

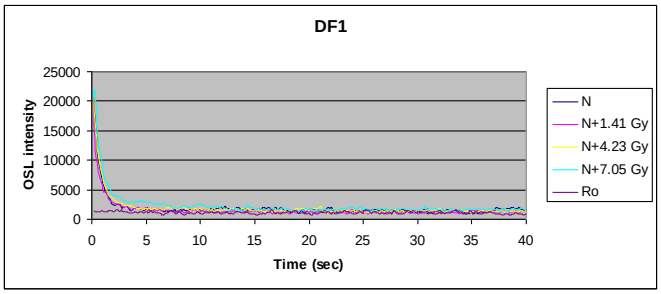
DF1
OSL intensity
Time (sec)
N
N+1.41 Gy
N+4.23 Gy
N+7.05 Gy
Ro

DF1

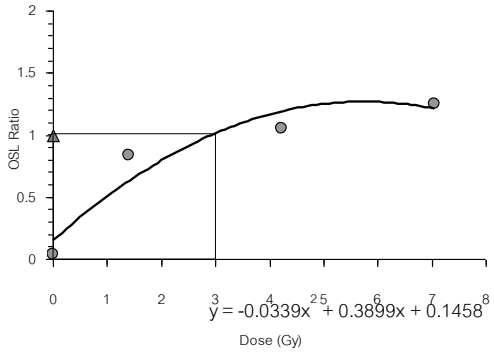
OSL Ratio
Dose (Gy)
y = -0.0339x2 + 0.3899x + 0.1458

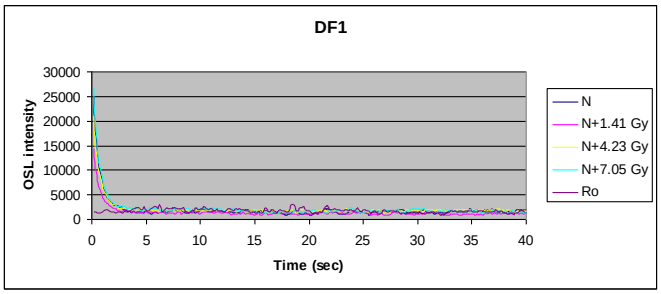
DF1
OSL intensity
Time (sec)
N
N+1.41 Gy
N+4.23 Gy
N+7.05 Gy
Ro

DF1

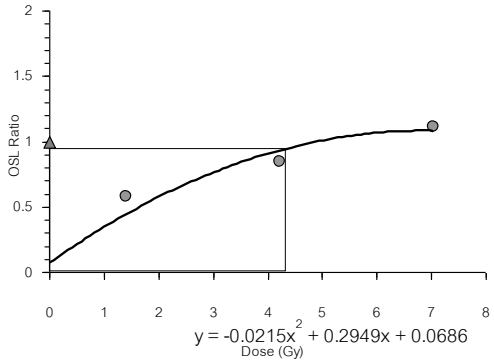
OSL Ratio
Dose (Gy)
y = -0.0215x2 + 0.2949x + 0.0686

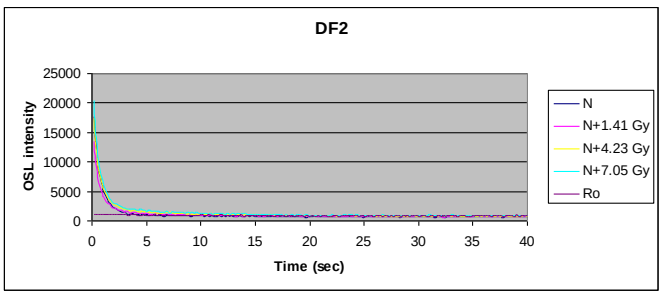
DF2
OSL intensity
25000
20000
15000
10000
5000
0
0
5
10
15
20
25
30
35
40
Time (sec)
N
N+1.41 Gy
N+4.23 Gy
N+7.05 Gy
Ro

DF2

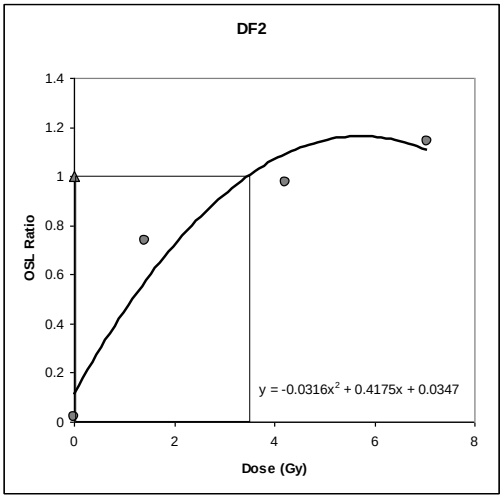
DF2
OSL Ratio
1.4
1.2
1
0.8
0.6
0.4
0.2
0
0
2
4
6
8
Dose (Gy)
y = -0.0316x² + 0.4175x + 0.0347

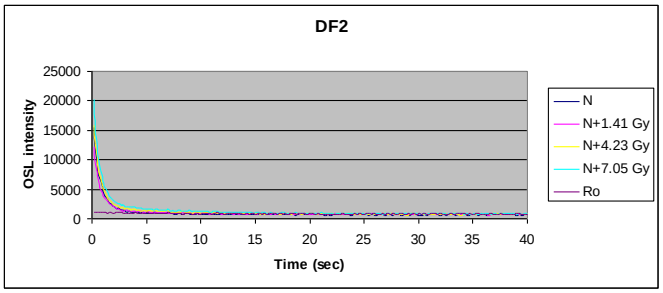
DF2
OSL intensity
25000
20000
15000
10000
5000
0
0
5
10
15
20
25
30
35
40
Time (sec)
N
N+1.41 Gy
N+4.23 Gy
N+7.05 Gy
Ro

DF2

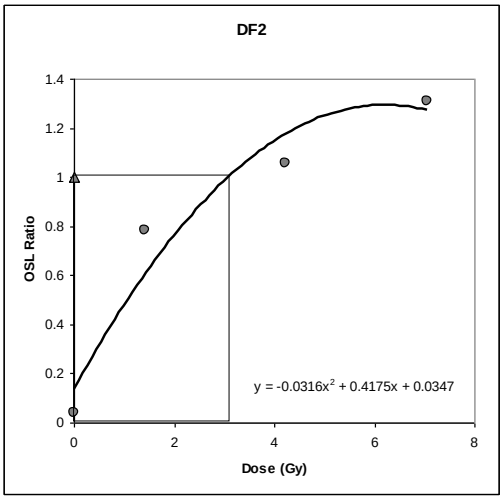
DF2
OSL Ratio
1.4
1.2
1
0.8
0.6
0.4
0.2
0
0
2
4
6
8
Dose (Gy)
y = -0.0316x² + 0.4175x + 0.0347

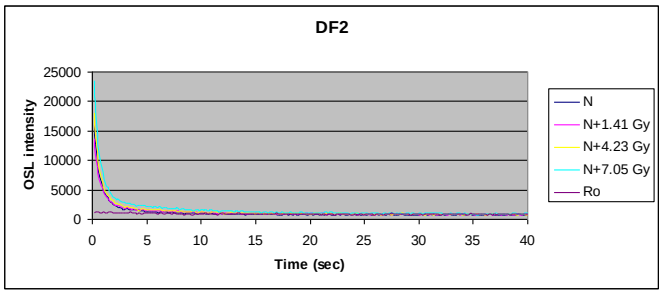
DF2
OSL intensity
25000
20000
15000
10000
5000
0
0
5
10
15
20
25
30
35
40
Time (sec)
N
N+1.41 Gy
N+4.23 Gy
N+7.05 Gy
Ro

DF2

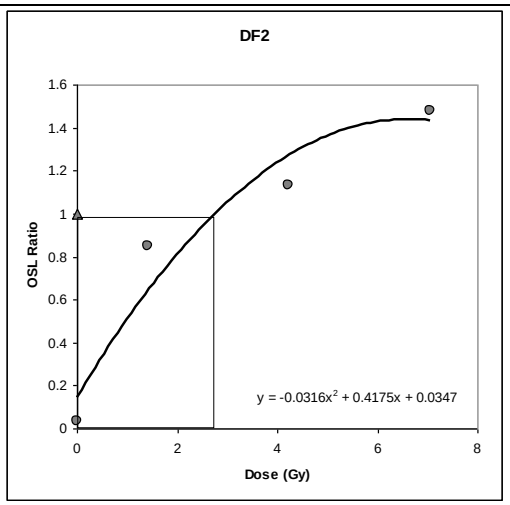
DF2
OSL Ratio
1.6
1.4
1.2
1
0.8
0.6
0.4
0.2
0
0
2
4
6
8
Dose (Gy)
y = -0.0316x² + 0.4175x + 0.0347

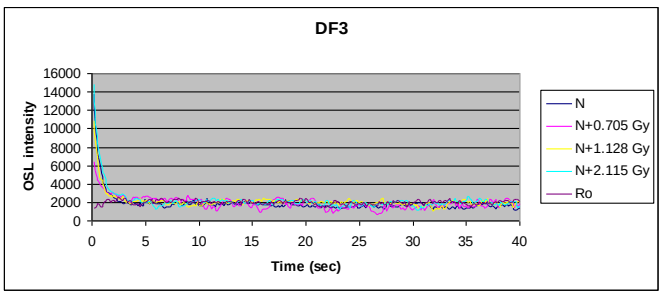
DF3
OSL intensity
Time (sec)
N
N+0.705 Gy
N+1.128 Gy
N+2.115 Gy
Ro

DF3

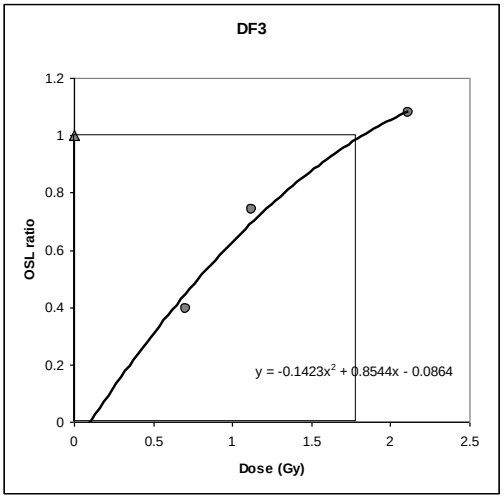
DF3
OSL ratio
Dose (Gy)
y = -0.1423x² + 0.8544x - 0.0864

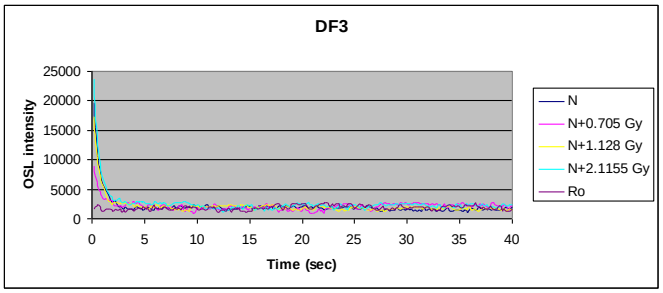
DF3
OSL intensity
Time (sec)
N
N+0.705 Gy
N+1.128 Gy
N+2.1155 Gy
Ro

DF3

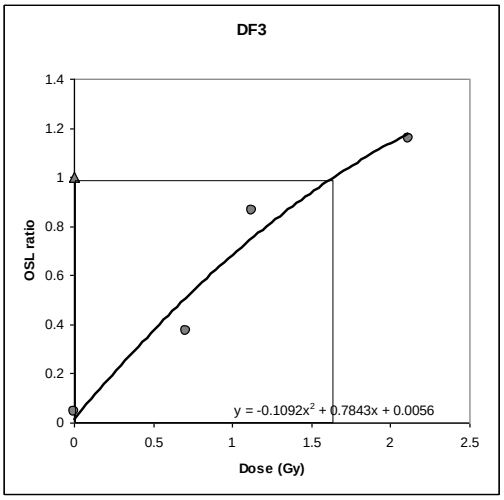
DF3
OSL ratio
Dose (Gy)
y = -0.1092x² + 0.7843x + 0.0056

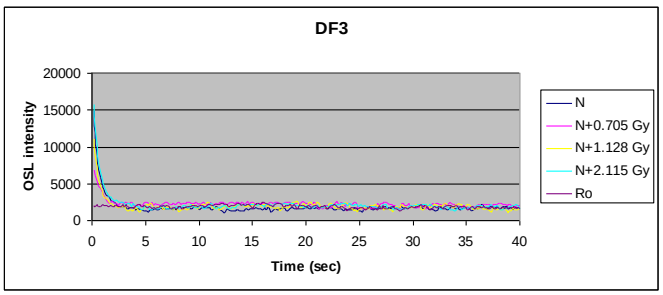
DF3
OSL intensity
Time (sec)
N
N+0.705 Gy
N+1.128 Gy
N+2.115 Gy
Ro

DF3

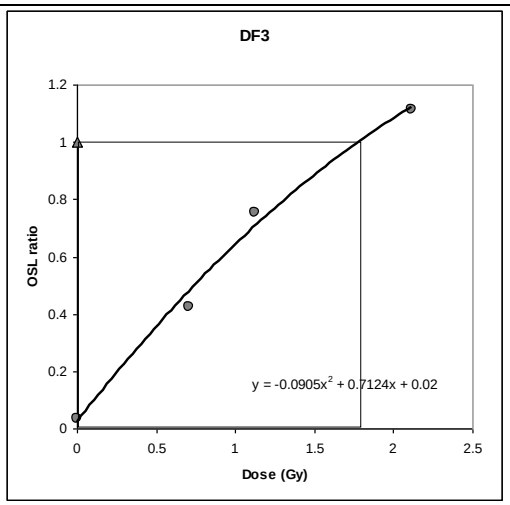
DF3
OSL ratio
Dose (Gy)
y = -0.0905x² + 0.7124x + 0.02

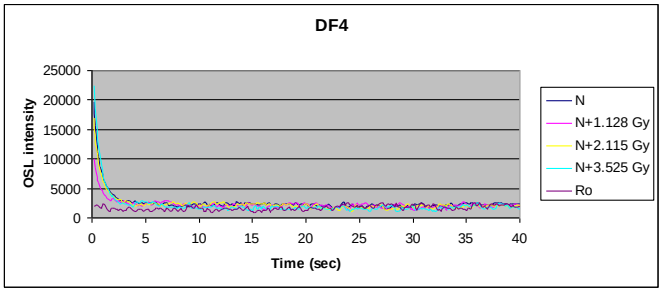
DF4
OSL intensity
Time (sec)
N
N+1.128 Gy
N+2.115 Gy
N+3.525 Gy
Ro

DF4

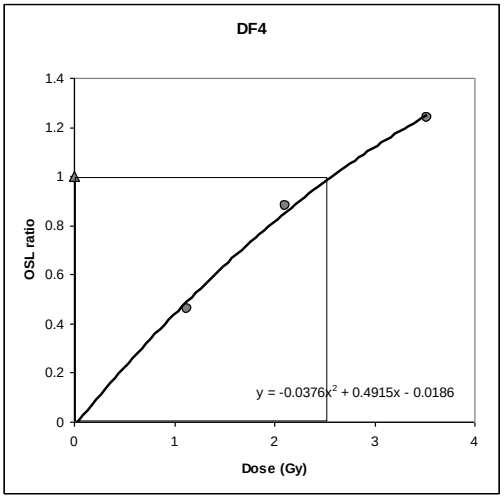
DF4
OSL ratio
Dose (Gy)
y = -0.0376x² + 0.4915x - 0.0186

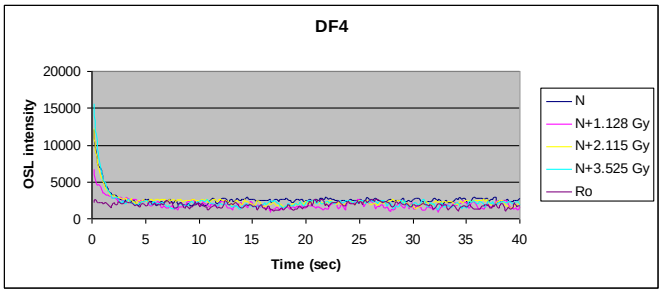
DF4
OSL intensity
Time (sec)
N
N+1.128 Gy
N+2.115 Gy
N+3.525 Gy
Ro

DF4

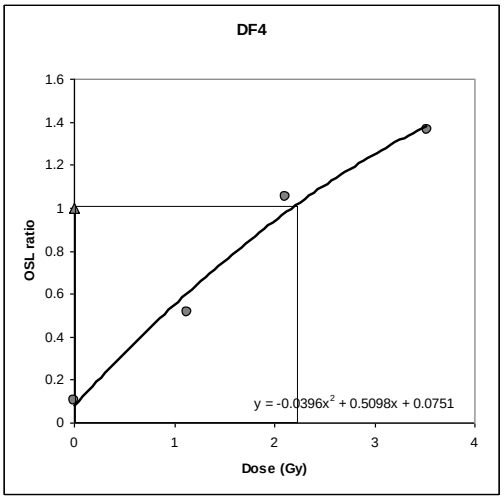
DF4
OSL ratio
Dose (Gy)
y = -0.0396x² + 0.5098x + 0.0751

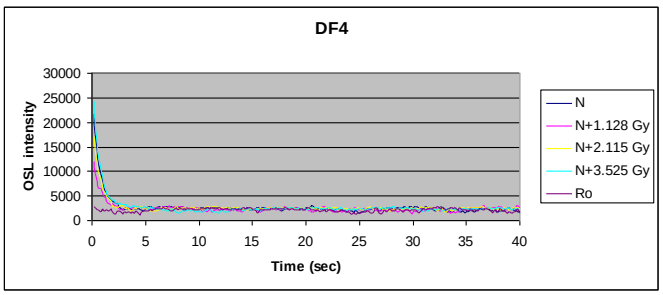
DF4
OSL intensity
Time (sec)
N
N+1.128 Gy
N+2.115 Gy
N+3.525 Gy
Ro

DF4

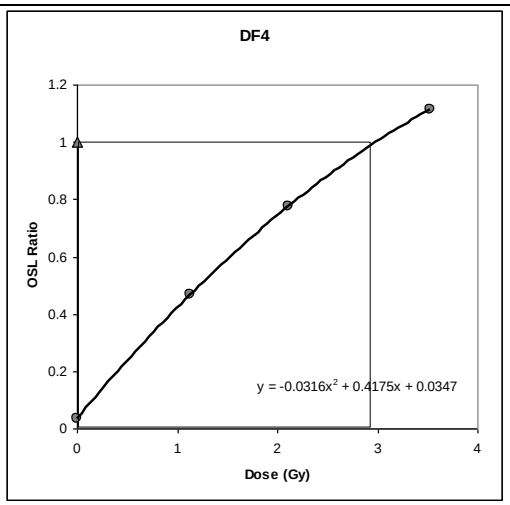
DF4
OSL Ratio
Dose (Gy)
y = -0.0316x² + 0.4175x + 0.0347

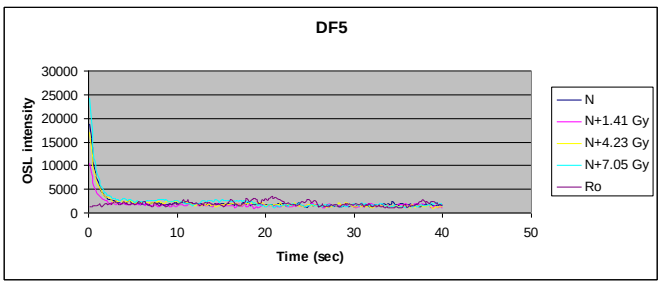
DF5
OSL intensity
Time (sec)
N
N+1.41 Gy
N+4.23 Gy
N+7.05 Gy
Ro

DF5

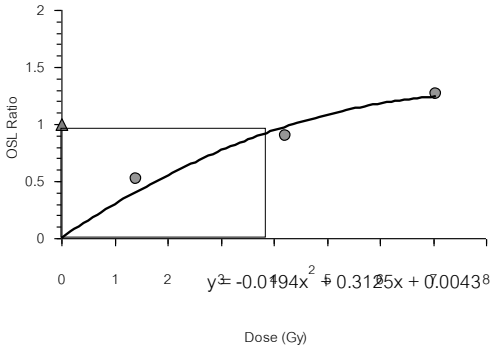
OSL Ratio
Dose (Gy)
y = -0.0194x2 + 0.3125x + 0.0043

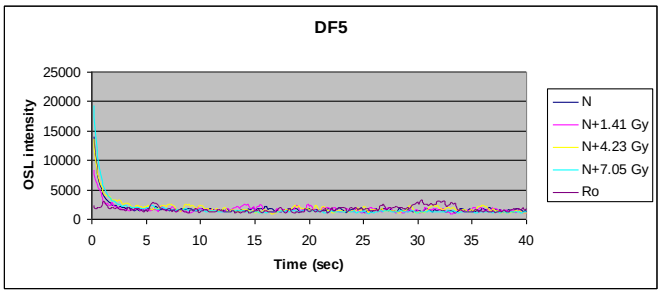
DF5
OSL intensity
Time (sec)
N
N+1.41 Gy
N+4.23 Gy
N+7.05 Gy
Ro

DF5

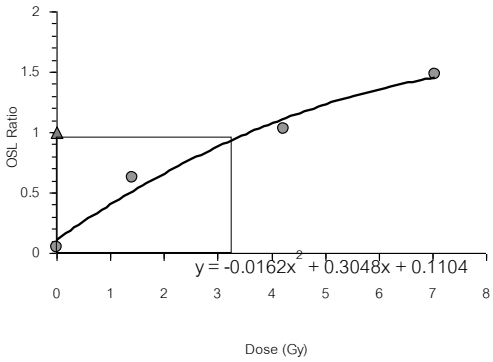
OSL Ratio
Dose (Gy)
y = -0.0162x2 + 0.3048x + 0.1104

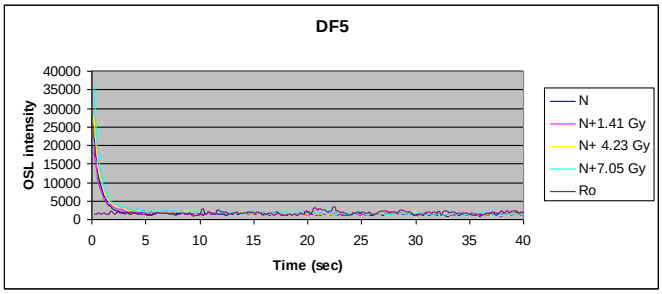
DF5
OSL intensity
Time (sec)
N
N+1.41 Gy
N+ 4.23 Gy
N+7.05 Gy
Ro

DF5

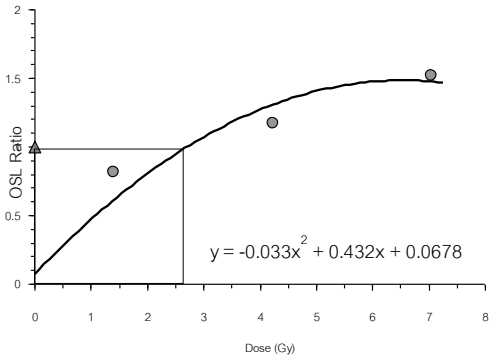
OSL Ratio
Dose (Gy)
y = -0.033x2 + 0.432x + 0.0678

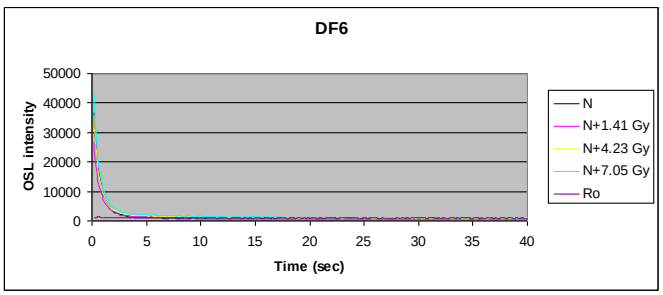
DF6
OSL intensity
50000
40000
30000
20000
10000
0
0 5 10 15 20 25 30 35 40
Time (sec)
N
N+1.41 Gy
N+4.23 Gy
N+7.05 Gy
Ro

DF6

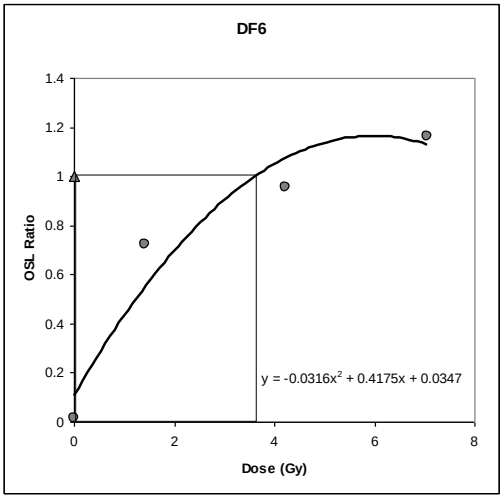
DF6
OSL Ratio
1.4
1.2
1
0.8
0.6
0.4
0.2
0
0 2 4 6 8
Dose (Gy)
y = -0.0316x² + 0.4175x + 0.0347

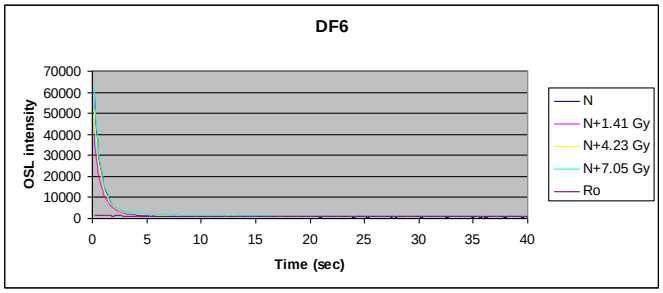
DF6
OSL intensity
70000
60000
50000
40000
30000
20000
10000
0
0 5 10 15 20 25 30 35 40
Time (sec)
N
N+1.41 Gy
N+4.23 Gy
N+7.05 Gy
Ro

DF6

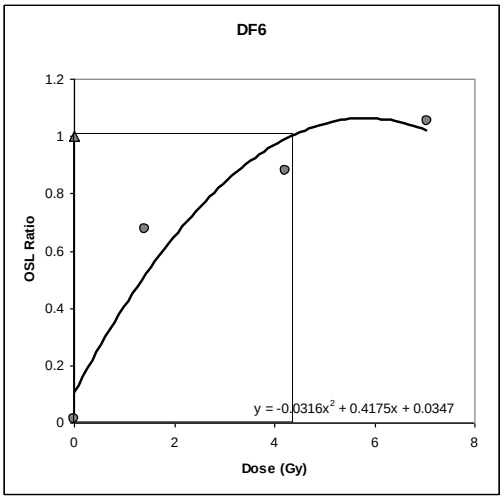
DF6
OSL Ratio
1.2
1
0.8
0.6
0.4
0.2
0
0 2 4 6 8
Dose (Gy)
y = -0.0316x² + 0.4175x + 0.0347

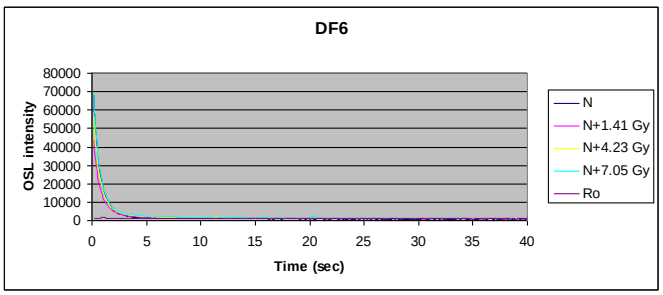
DF6
OSL intensity
80000
70000
60000
50000
40000
30000
20000
10000
0
0 5 10 15 20 25 30 35 40
Time (sec)
N
N+1.41 Gy
N+4.23 Gy
N+7.05 Gy
Ro

DF6

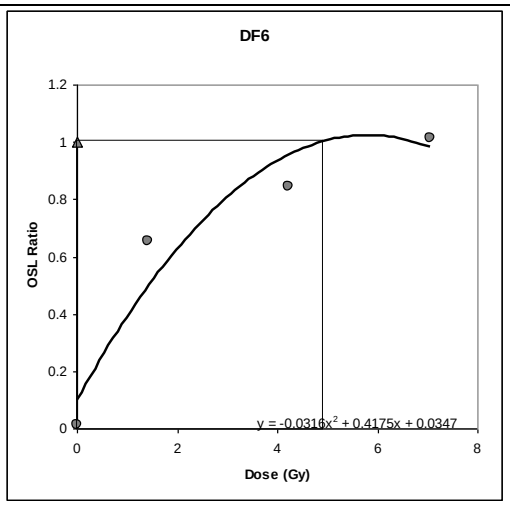
DF6
OSL Ratio
1.2
1
0.8
0.6
0.4
0.2
0
0 2 4 6 8
Dose (Gy)
y = -0.0316x² + 0.4175x + 0.0347

Appendix B

TL glow and TL growth curves

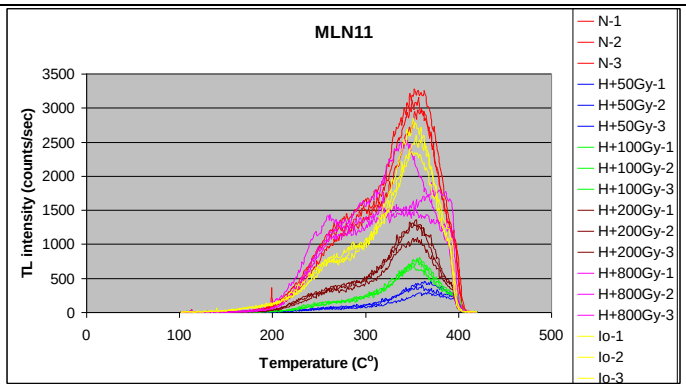
MLN11
TL intensity (counts/sec)
Temperature (C°)
N-1
N-2
N-3
H+50Gy-1
H+50Gy-2
H+50Gy-3
H+100Gy-1
H+100Gy-2
H+100Gy-3
H+200Gy-1
H+200Gy-2
H+200Gy-3
H+800Gy-1
H+800Gy-2
H+800Gy-3
Io-1
Io-2
Io-3

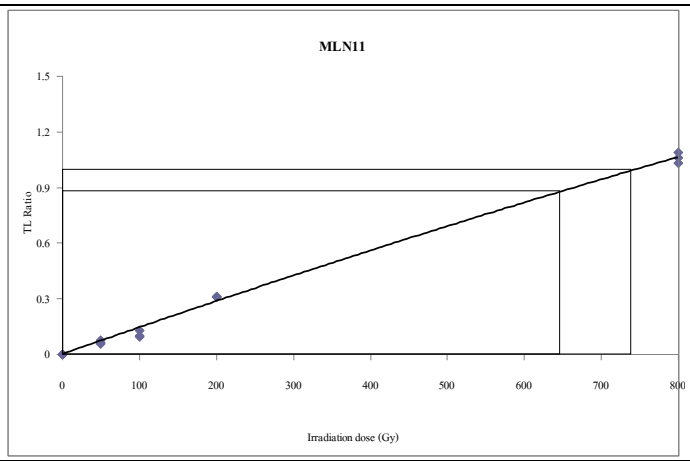
MLN11
TL Ratio
Irradiation dose (Gy)

MLN11

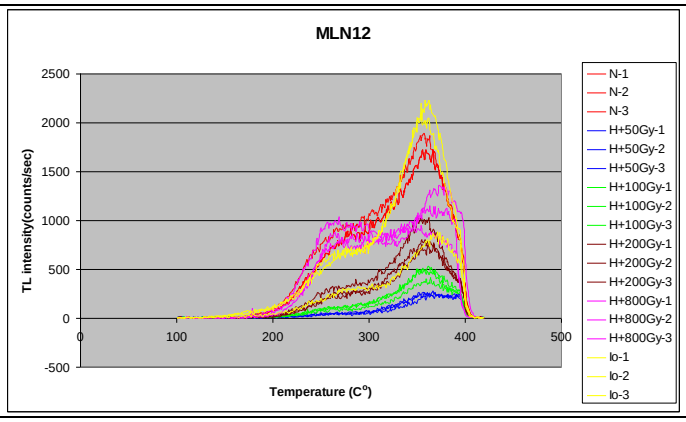
MLN12
TL intensity(counts/sec)
Temperature (C°)
N-1
N-2
N-3
H+50Gy-1
H+50Gy-2
H+50Gy-3
H+100Gy-1
H+100Gy-2
H+100Gy-3
H+200Gy-1
H+200Gy-2
H+200Gy-3
H+800Gy-1
H+800Gy-2
H+800Gy-3
Io-1
Io-2
Io-3

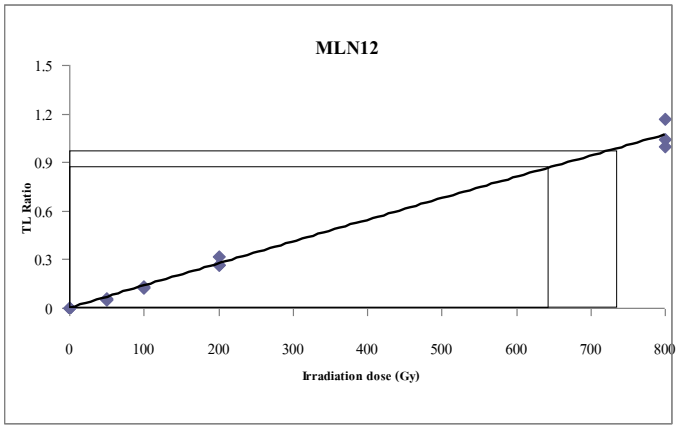
MLN12
TL Ratio
Irradiation dose (Gy)

MLN12

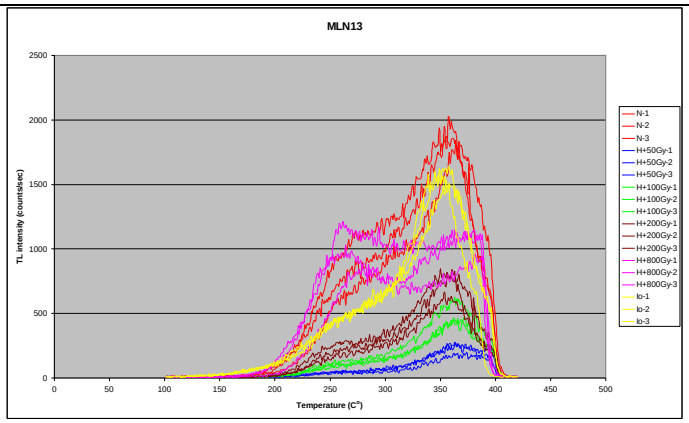
MLN13
TL intensity (counts/sec)
Temperature (C°)
N-1
N-2
N-3
H+50Gy-1
H+50Gy-2
H+50Gy-3
H+100Gy-1
H+100Gy-2
H+100Gy-3
H+200Gy-1
H+200Gy-2
H+200Gy-3
H+800Gy-1
H+800Gy-2
H+800Gy-3
lo-1
lo-2
lo-3

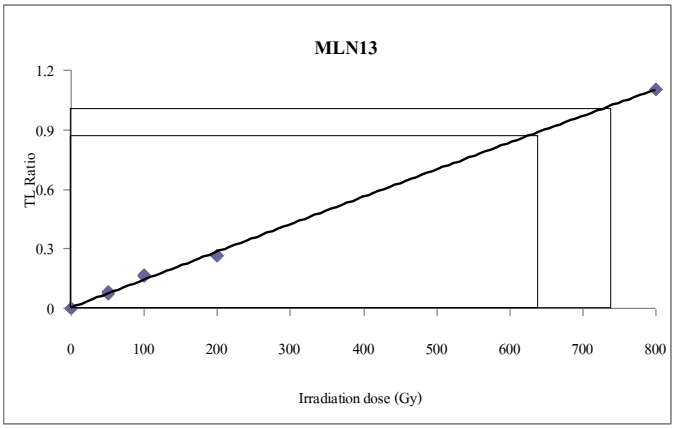
MLN13
TL Ratio
Irradiation dose (Gy)

MLN13

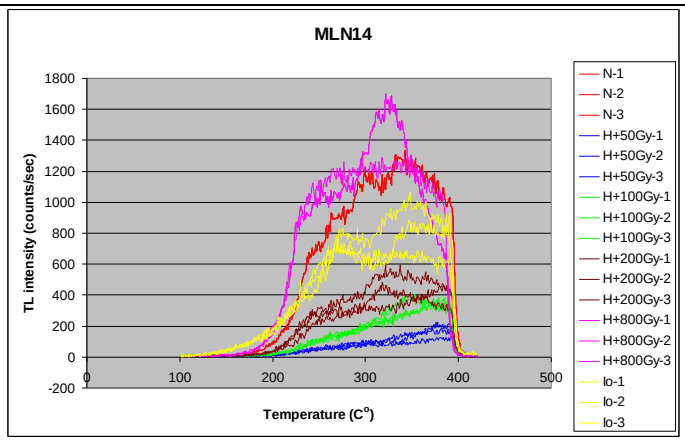
MLN14
TL intensity (counts/sec)
Temperature (C°)
N-1
N-2
N-3
H+50Gy-1
H+50Gy-2
H+50Gy-3
H+100Gy-1
H+100Gy-2
H+100Gy-3
H+200Gy-1
H+200Gy-2
H+200Gy-3
H+800Gy-1
H+800Gy-2
H+800Gy-3
lo-1
lo-2
lo-3

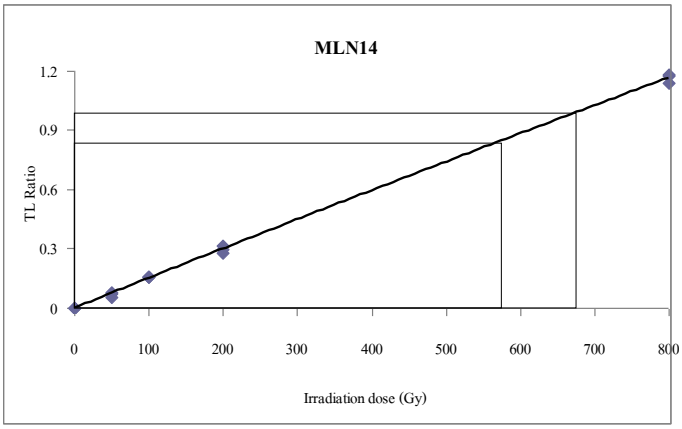
MLN14
TL Ratio
Irradiation dose (Gy)

MLN14

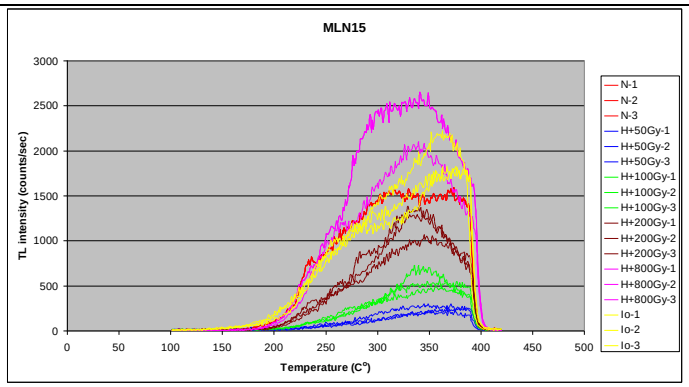
MLN15
TL intensity (counts/sec)
Temperature (C°)
N-1
N-2
N-3
H+50Gy-1
H+50Gy-2
H+50Gy-3
H+100Gy-1
H+100Gy-2
H+100Gy-3
H+200Gy-1
H+200Gy-2
H+200Gy-3
H+800Gy-1
H+800Gy-2
H+800Gy-3
Io-1
Io-2
Io-3

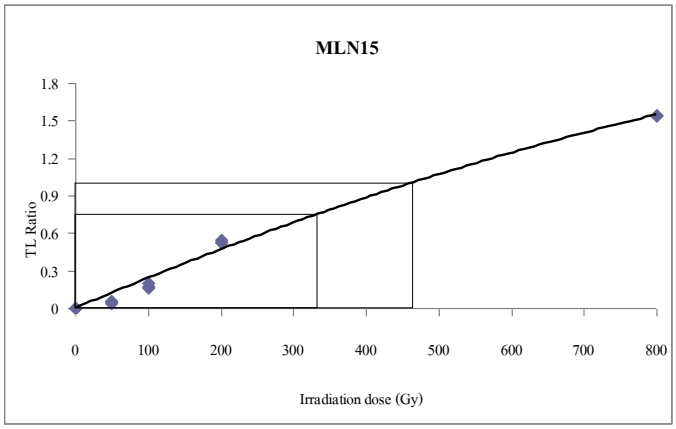
MLN15
TL Ratio
Irradiation dose (Gy)

MLN15

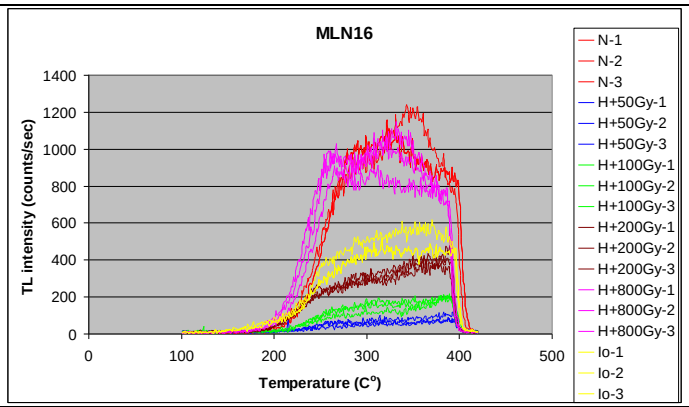
MLN16
TL intensity (counts/sec)
Temperature (C°)
N-1
N-2
N-3
H+50Gy-1
H+50Gy-2
H+50Gy-3
H+100Gy-1
H+100Gy-2
H+100Gy-3
H+200Gy-1
H+200Gy-2
H+200Gy-3
H+800Gy-1
H+800Gy-2
H+800Gy-3
Io-1
Io-2
Io-3

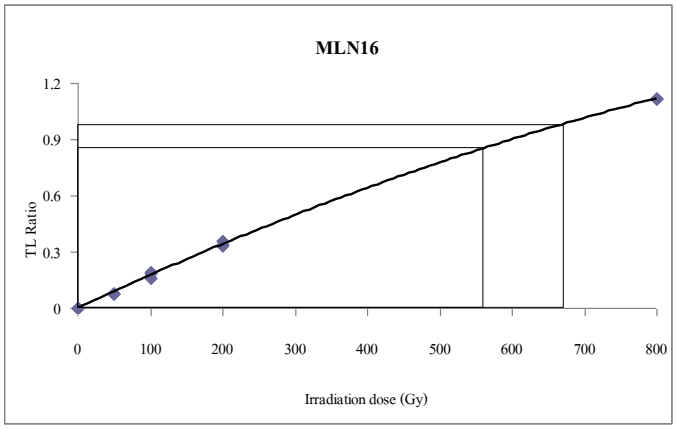
MLN16
TL Ratio
Irradiation dose (Gy)

MLN16

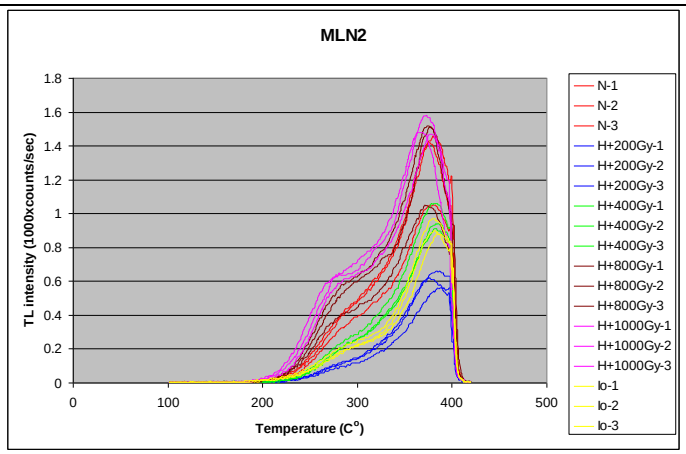
MLN2
TL intensity (1000xcounts/sec)
Temperature (C°)
N-1
N-2
N-3
H+200Gy-1
H+200Gy-2
H+200Gy-3
H+400Gy-1
H+400Gy-2
H+400Gy-3
H+800Gy-1
H+800Gy-2
H+800Gy-3
H+1000Gy-1
H+1000Gy-2
H+1000Gy-3
lo-1
lo-2
lo-3

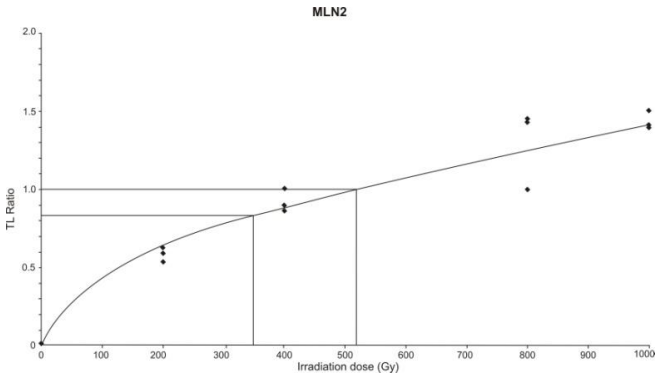
MLN2
TL Ratio
Irradiation dose (Gy)

MLN2

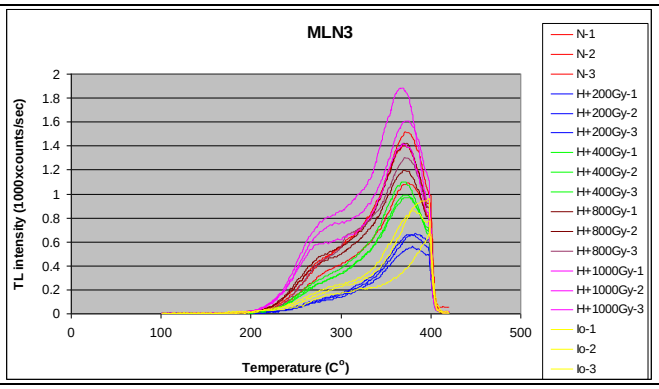
MLN3
TL intensity (1000xcounts/sec)
Temperature (C°)
N-1
N-2
N-3
H+200Gy-1
H+200Gy-2
H+200Gy-3
H+400Gy-1
H+400Gy-2
H+400Gy-3
H+800Gy-1
H+800Gy-2
H+800Gy-3
H+1000Gy-1
H+1000Gy-2
H+1000Gy-3
lo-1
lo-2
lo-3

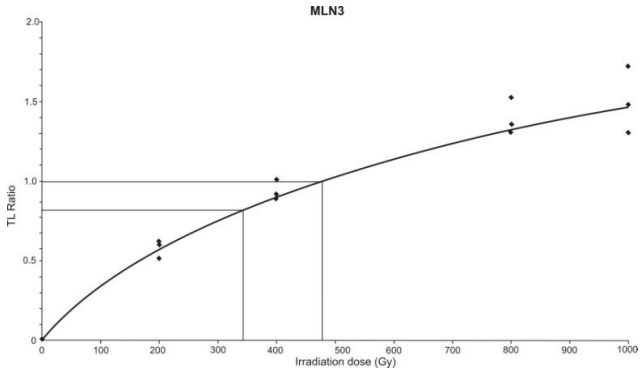
MLN3
TL Ratio
Irradiation dose (Gy)

MLN3

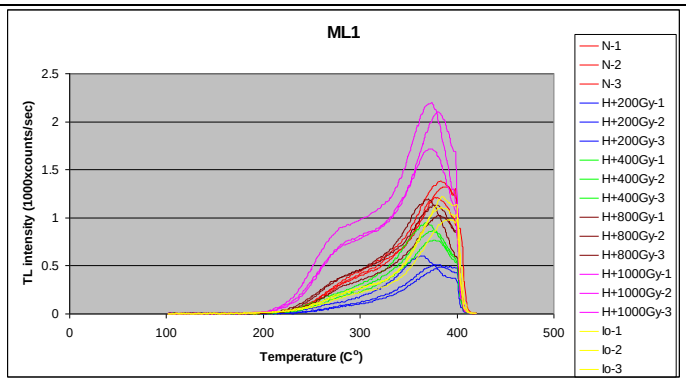
ML1
TL intensity (1000xcounts/sec)
Temperature (C°)
N-1
N-2
N-3
H+200Gy-1
H+200Gy-2
H+200Gy-3
H+400Gy-1
H+400Gy-2
H+400Gy-3
H+800Gy-1
H+800Gy-2
H+800Gy-3
H+1000Gy-1
H+1000Gy-2
H+1000Gy-3
Io-1
Io-2
Io-3

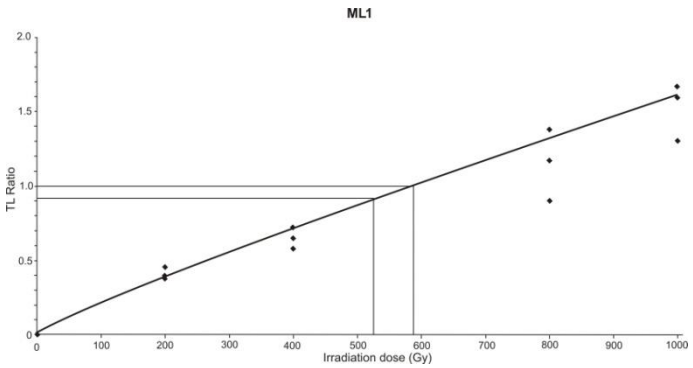
ML1
TL Ratio
Irradiation dose (Gy)

ML1

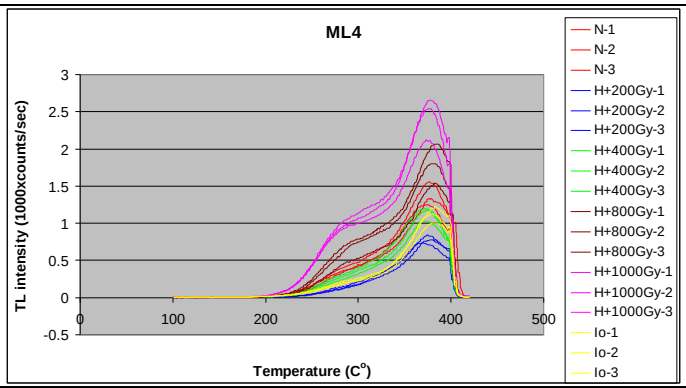
ML4
TL intensity (1000xcounts/sec)
Temperature (C°)
N-1
N-2
N-3
H+200Gy-1
H+200Gy-2
H+200Gy-3
H+400Gy-1
H+400Gy-2
H+400Gy-3
H+800Gy-1
H+800Gy-2
H+800Gy-3
H+1000Gy-1
H+1000Gy-2
H+1000Gy-3
Io-1
Io-2
Io-3

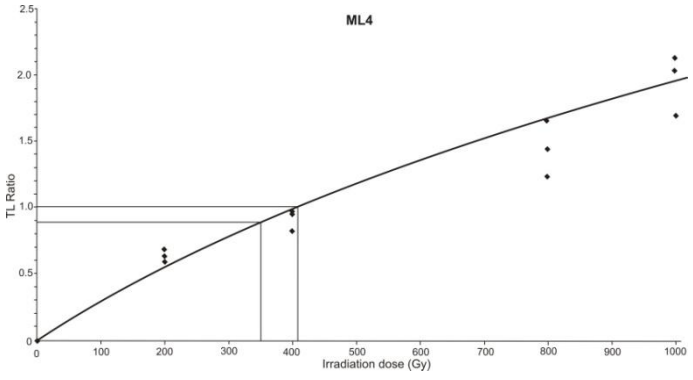
ML4
TL Ratio
Irradiation dose (Gy)

ML4

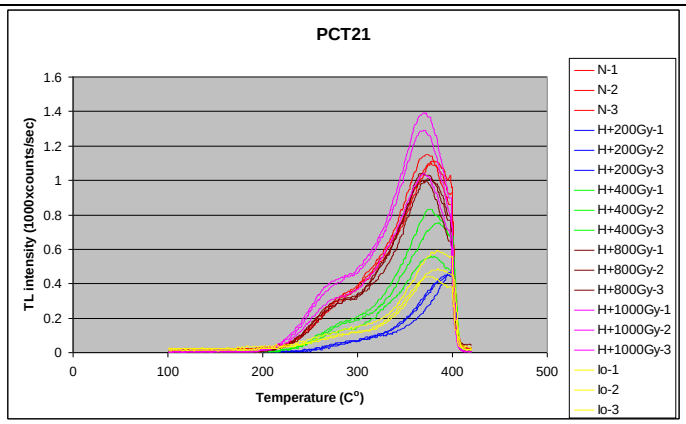
PCT21
TL intensity (1000xcounts/sec)
Temperature (C°)
N-1
N-2
N-3
H+200Gy-1
H+200Gy-2
H+200Gy-3
H+400Gy-1
H+400Gy-2
H+400Gy-3
H+800Gy-1
H+800Gy-2
H+800Gy-3
H+1000Gy-1
H+1000Gy-2
H+1000Gy-3
lo-1
lo-2
lo-3

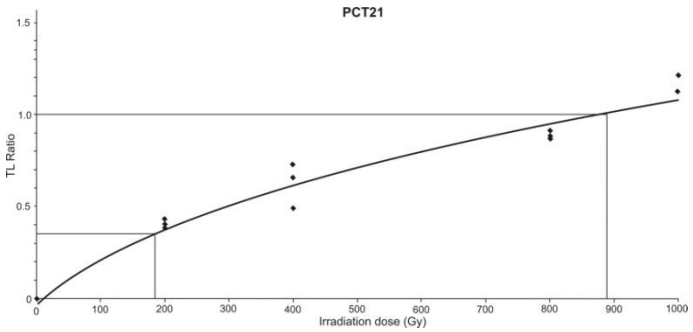
PCT21
TL Ratio
Irradiation dose (Gy)

PCT21

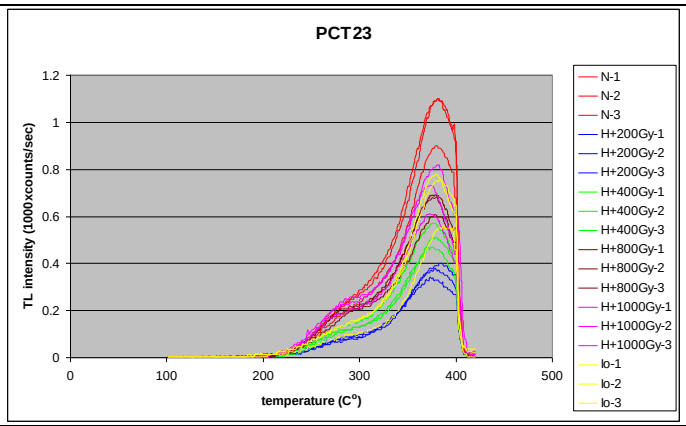
PCT23
TL intensity (1000xcounts/sec)
temperature (C°)
N-1
N-2
N-3
H+200Gy-1
H+200Gy-2
H+200Gy-3
H+400Gy-1
H+400Gy-2
H+400Gy-3
H+800Gy-1
H+800Gy-2
H+800Gy-3
H+1000Gy-1
H+1000Gy-2
H+1000Gy-3
lo-1
lo-2
lo-3

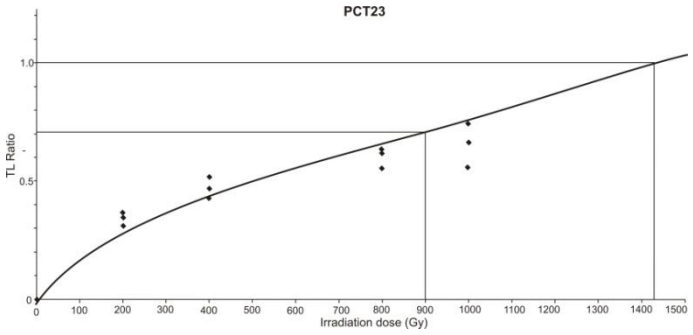
PCT23
TL Ratio
Irradiation dose (Gy)

PCT23

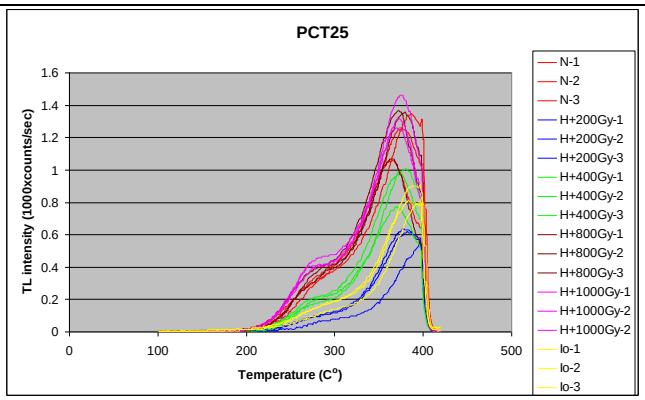
PCT25
TL intensity (1000xcounts/sec)
Temperature (C°)
N-1
N-2
N-3
H+200Gy-1
H+200Gy-2
H+200Gy-3
H+400Gy-1
H+400Gy-2
H+400Gy-3
H+800Gy-1
H+800Gy-2
H+800Gy-3
H+1000Gy-1
H+1000Gy-2
H+1000Gy-2
lo-1
lo-2
lo-3

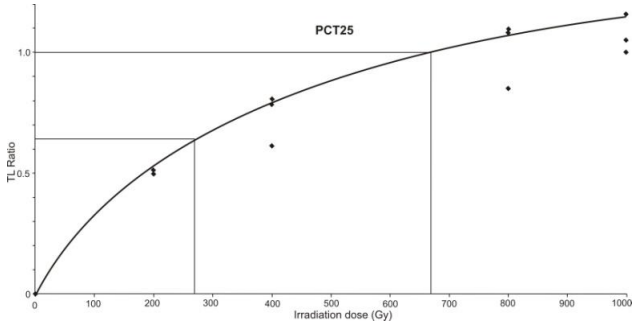
PCT25
TL Ratio
Irradiation dose (Gy)

PCT25

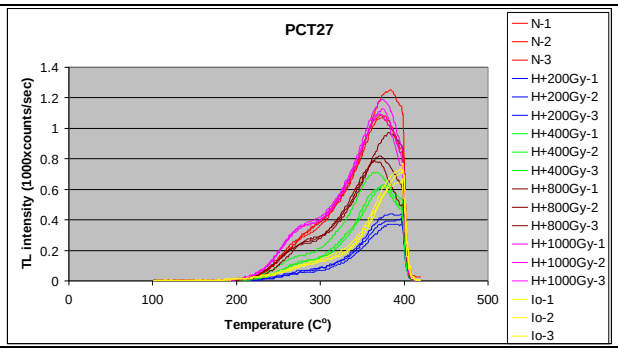
PCT27
TL intensity (1000xcounts/sec)
Temperature (C°)
N-1
N-2
N-3
H+200Gy-1
H+200Gy-2
H+200Gy-3
H+400Gy-1
H+400Gy-2
H+400Gy-3
H+800Gy-1
H+800Gy-2
H+800Gy-3
H+1000Gy-1
H+1000Gy-2
H+1000Gy-3
lo-1
lo-2
lo-3

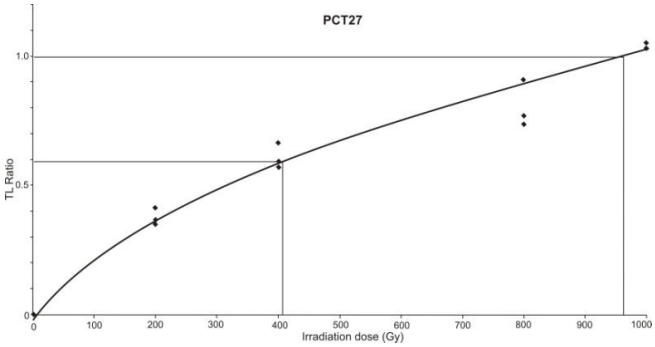
PCT27
TL Ratio
Irradiation dose (Gy)

PCT27

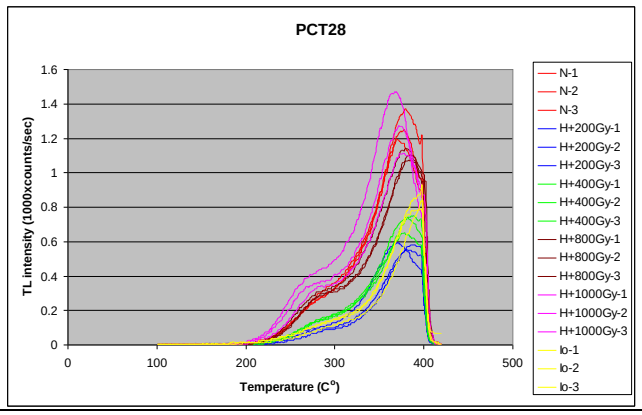
PCT28
TL intensity (1000xcounts/sec)
Temperature (C°)
N-1
N-2
N-3
H+200Gy-1
H+200Gy-2
H+200Gy-3
H+400Gy-1
H+400Gy-2
H+400Gy-3
H+800Gy-1
H+800Gy-2
H+800Gy-3
H+1000Gy-1
H+1000Gy-2
H+1000Gy-3
lo-1
lo-2
lo-3

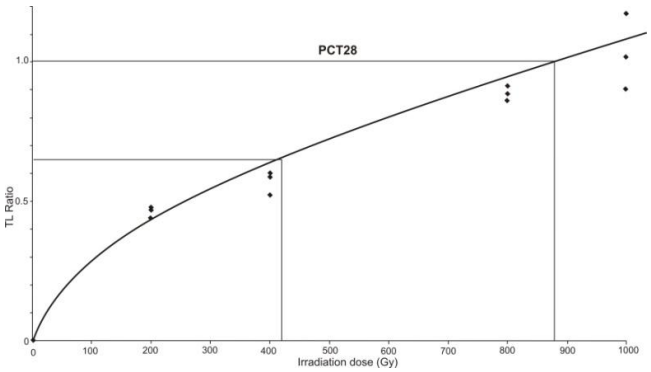
PCT28
TL Ratio
Irradiation dose (Gy)

PCT28

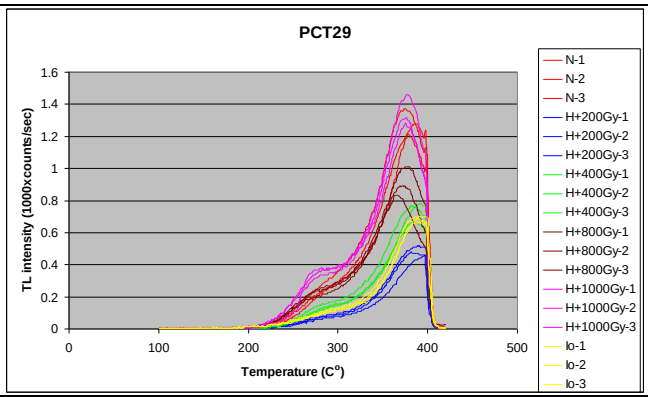
PCT29
TL intensity (1000xcounts/sec)
Temperature (C°)
N-1
N-2
N-3
H+200Gy-1
H+200Gy-2
H+200Gy-3
H+400Gy-1
H+400Gy-2
H+400Gy-3
H+800Gy-1
H+800Gy-2
H+800Gy-3
H+1000Gy-1
H+1000Gy-2
H+1000Gy-3
lo-1
lo-2
lo-3

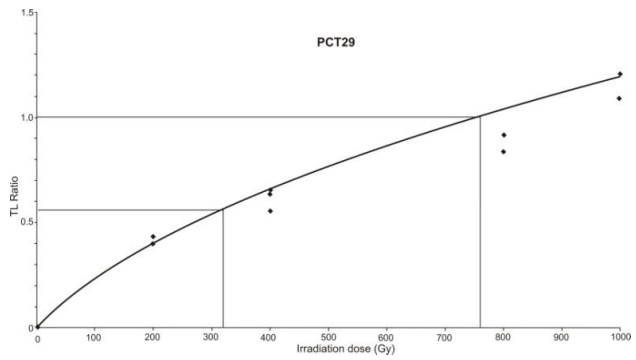
PCT29
TL Ratio
Irradiation dose (Gy)

PCT29

Appendix C

AMS radiocarbon dating

CALIBRATION OF RADIOCARBON AGE TO CALENDAR YEARS

(Variables: C13/C12=-25.1:lab. mult=1)

Laboratory number: **Beta-261128**

Conventional radiocarbon age: **940±40 BP**

2 Sigma calibrated result: (95% probability) **Cal AD 1020 to 1200 (Cal BP 930 to 750)**

Intercept data

Intercepts of radiocarbon age with calibration curve: Cal AD 1040 (Cal BP 910) and
Cal AD 1100 (Cal BP 850) and
Cal AD 1120 (Cal BP 830)

1 Sigma calibrated result: (68% probability) Cal AD 1030 to 1160 (Cal BP 920 to 790)

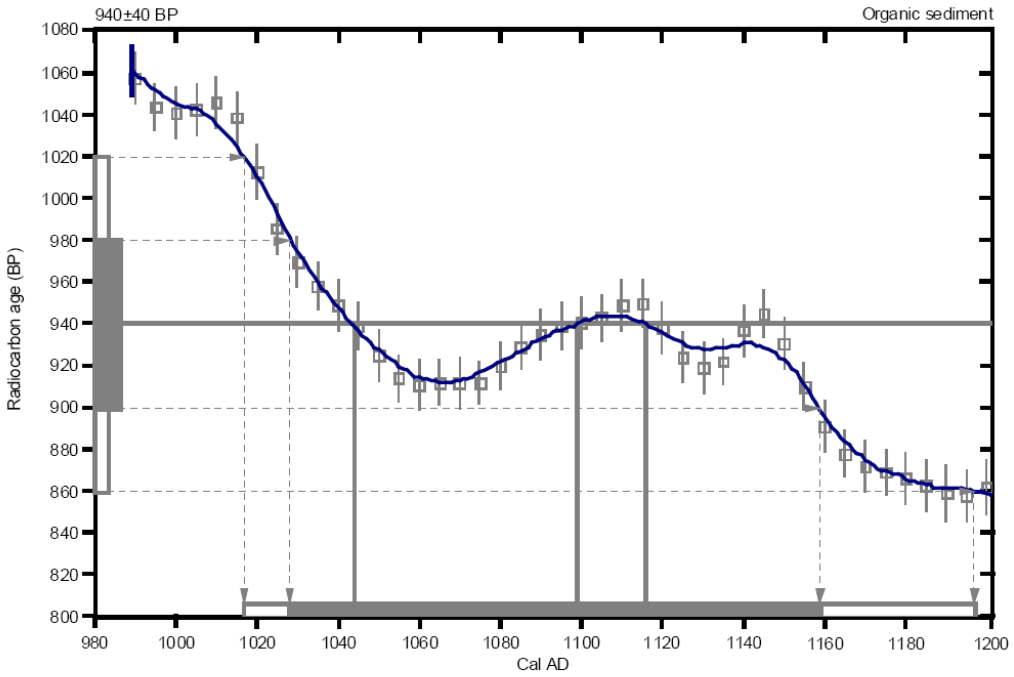

References:

Database used

INTCAL04

Calibration Database

INTCAL04 Radiocarbon Age Calibration

IntCal04: Calibration Issue of Radiocarbon (Volume 46, nr 3, 2004).

Mathematics

A Simplified Approach to Calibrating C14 Dates

Talma, A. S., Vogel, J. C., 1993, Radiocarbon 35(2), p317-322

Beta Analytic Radiocarbon Dating Laboratory

4985 S.W. 74th Court, Miami, Florida 33155 • Tel: (305)667-5167 • Fax: (305)663-0964 • E-Mail: beta@radiocarbon.com

CALIBRATION OF RADIOCARBON AGE TO CALENDAR YEARS

(Variables: C13/C12=-23.9:lab. mult=1)

Laboratory number: **Beta-261129**

Conventional radiocarbon age: **960±40 BP**

2 Sigma calibrated result: (95% probability) **Cal AD 1010 to 1170 (Cal BP 940 to 780)**

Intercept data

Intercept of radiocarbon age with calibration curve: Cal AD 1040 (Cal BP 920)

1 Sigma calibrated results: (68% probability) Cal AD 1020 to 1060 (Cal BP 930 to 900) and Cal AD 1080 to 1150 (Cal BP 870 to 800)

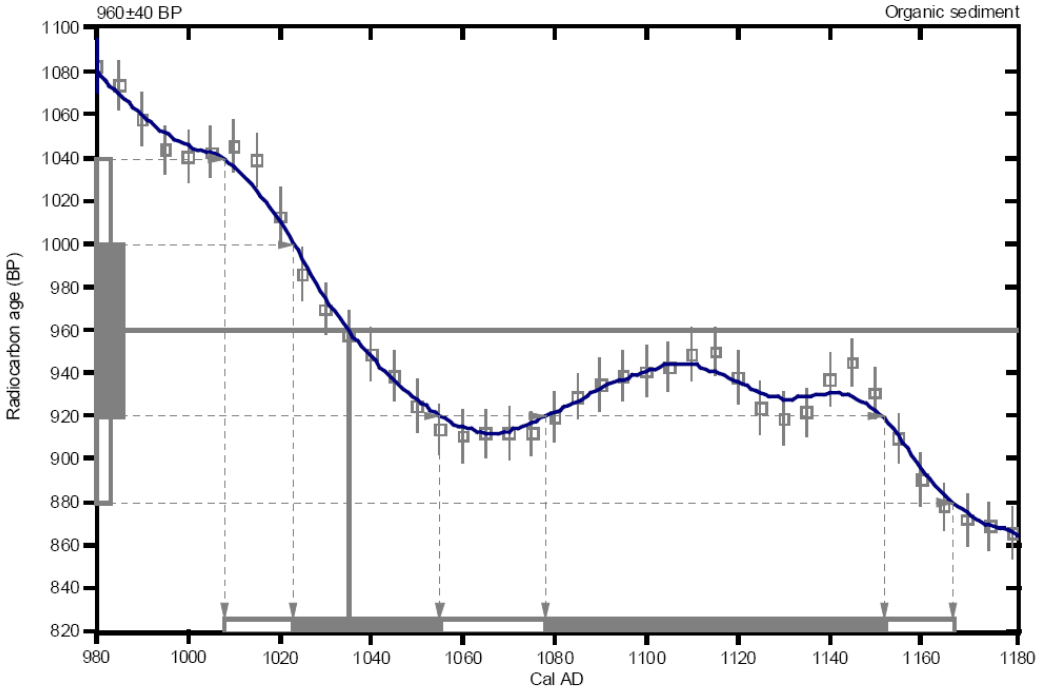

References:

Database used

INTCAL04

Calibration Database

INTCAL04 Radiocarbon Age Calibration

IntCal04: Calibration Issue of Radiocarbon (Volume 46, nr 3, 2004).

Mathematics

A Simplified Approach to Calibrating C14 Dates

Talma, A. S., Vogel, J. C., 1993, Radiocarbon 35(2), p317-322

Beta Analytic Radiocarbon Dating Laboratory

4985 S.W. 74th Court, Miami, Florida 33155 • Tel: (305)667-5167 • Fax: (305)663-0964 • E-Mail: beta@radiocarbon.com

CALIBRATION OF RADIOCARBON AGE TO CALENDAR YEARS

(Variables: C13/C12=-24.6:lab. mult=1)

Laboratory number: **Beta-261130**

Conventional radiocarbon age: **920±40 BP**

2 Sigma calibrated result: (95% probability) **Cal AD 1020 to 1210 (Cal BP 930 to 740)**

Intercept data

Intercepts of radiocarbon age with calibration curve: Cal AD 1060 (Cal BP 900) and
Cal AD 1080 (Cal BP 870) and
Cal AD 1150 (Cal BP 800)

1 Sigma calibrated result: (68% probability) Cal AD 1040 to 1170 (Cal BP 920 to 780)

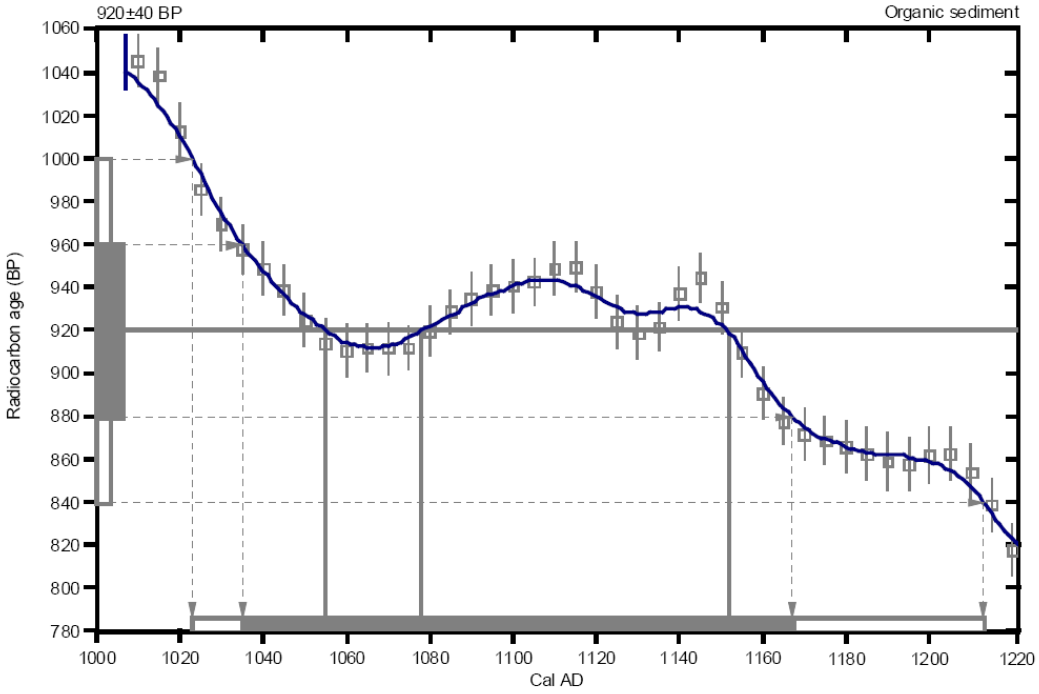

References:

Database used

INTCAL04

Calibration Database

INTCAL04 Radiocarbon Age Calibration

IntCal04: Calibration Issue of Radiocarbon (Volume 46, nr 3, 2004).

Mathematics

A Simplified Approach to Calibrating C14 Dates

Talma, A. S., Vogel, J. C., 1993, Radiocarbon 35(2), p317-322

Beta Analytic Radiocarbon Dating Laboratory

4985 S.W. 74th Court, Miami, Florida 33155 • Tel: (305)667-5167 • Fax: (305)663-0964 • E-Mail: beta@radiocarbon.com